SHAPING AND ANALYSIS OF LASER SPECKLE FOR IMAGING APPLICATIONS

A Thesis submitted

in partial fulfillment for the Degree of

Doctor of Philosophy

by

VINU R.V

Department of Physics

INDIAN INSTITUTE OF SPACE SCIENCE AND TECHNOLOGY

Thiruvananthapuram-695547

August, 2016

CERTIFICATE

This is to certify that the thesis entitled **Shaping and Analysis of Laser Speckle for Imaging Applications,** submitted by **Vinu R.V,** to the Indian Institute of Space Science and Technology, Thiruvananthapuram, in partial fulfillment for the award of the degree of **Doctor of Philosophy,** is a *bona fide* record of research work carried out by him under my supervision. The contents of this thesis, in full or in parts, have not been submitted to any other Institution or University for the award of any degree or diploma.

<div align="right">

Dr. Rakesh Kumar Singh

Supervisor

Associate Professor

Department of Physics

</div>

Thiruvananthapuram   Counter signature of HOD with seal

August, 2016

DECLARATION

I declare that this thesis entitled **Shaping and Analysis of Laser Speckle for Imaging Applications** submitted in partial fulfillment of the degree of **Doctor of Philosophy** is a record of original work carried out by me under the supervision of **Dr. Rakesh Kumar Singh**, and has not formed the basis for the award of any other degree or diploma, in this or any other Institution or University. In keeping with the ethical practice in reporting scientific information, due acknowledgements have been made wherever the findings of others have been cited.

<div align="right">

Vinu R.V
SC12D008

</div>

Thiruvananthapuram - 695 547

August, 2016

ACKNOWLEDGEMENTS

ABSTRACT

The potential of laser speckle pattern as a versatile tool in numerous application regimes in science and engineering secure interest of researchers to explore different application based scenarios where speckle effects can be implemented. Advancements towards this direction of using the speckle pattern leads to new application areas such as surface roughness estimation, speckle interferometry, speckle photography, astronomy, laser speckle contrast imaging, optical manipulation, correlation imaging etc. The randomness associated with speckle pattern provides the potential to treat speckle pattern as a part of statistical optics, and the theoretical and experimental progresses in the field of statistical optics give new opportunities in the study of random fluctuations in the speckle pattern. The main objectives of this thesis are shaping and analysis of laser speckle pattern and the effective utilization of their randomness for optical manipulation and imaging through scattering layers.

Active shaping approach for shaping the laser speckle size based on correlation of the amplitude and intensity of the speckle pattern has been developed and successfully demonstrated. The use of diffractive optical elements such as holograms, phase gratings, Dammann gratings, apertures etc in active shaping of the speckle pattern is discussed and demonstrated by developing field and intensity based interferometers. A single-shot correlation analysis is performed by relying on the spatial averaging (rather than temporal averaging) and demonstrated applications of spatial stationarity feature of random fields in different applications ranging from characterization to imaging. Initial part of the thesis focus on the shaping of the speckle pattern with various diffractive optical elements and its analysis using field and intensity based interferometers. Final part of the thesis focuses on the applications of the active shaping approach in imaging through the complex scattering layers.

A polarization sensitive interferometer capable of single-shot detection of orthogonal polarization components is developed and experimentally demonstrated. The efficient execution of diffractive optical element such as Dammann phase type grating by exploiting the characteristic feature of phase only SLM and polarization sensitive interferometer provides the potential to control the orthogonal polarization components of the fluctuating field. This potential is effectively implemented to generate uniform array of spatial coherence points both in 1D and 2D with desired spacing. The technique offers a new method for synthesis and analysis of laser speckle pattern and consequently controls the coherence and polarization properties of the random field. The speckle holographic approach combined with two point intensity correlation is implemented to retrieve the complex information of the random field in scalar and vectorial cases. A singular point array generation with desired densities is

efficiently demonstrated in spatially fluctuating random field by utilizing the concepts of two point intensity correlation and spatial average approach. An experimental technique for the determination of generalized Stokes parameters or coherence-polarization matrix elements is experimentally demonstrated by making use of the speckle holographic approach in combination with the intensity correlation. Applicability of this technique is demonstrated in the controlled synthesis of coherence and polarization properties of random light field.

The active shaping approach used for speckle (or correlation function) is efficiently applied in the optical imaging through random scattering layers. The complex valued object lying behind the scattering layer is recovered by making use of speckle holographic approach in combination with two point intensity correlation. By efficiently implementing this approach, a single-shot imaging technique is demonstrated for the recovery of an off-axis hologram hidden by a scattering layer. The technique has unique ability to retrieve the 3D complex field behind a scattering medium resulting into the reconstruction of actual position of the object. The potential of the technique is validated to more real time situation where the holographic diffraction is dominant by the recovery of in-line hologram through scattering layer. The depth resolved imaging of reflecting type and transmitting type object hidden by the scattering layer are efficiently demonstrated and analyzed quantitatively by presenting the reconstruction parameters. These imaging technique has a remarkable achievement in true non-invasive single-shot and depth resolved 3D imaging through complex scattering layers, and have robust practical applications in biomedical imaging, imaging through turbid media, astronomy etc

TABLE OF CONTENTS

LIST OF FIGURES

LIST OF TABLES

ABBREVIATIONS

BS	Beam Splitter
CCD	Charge Coupled Device
CP	Coherence-Polarization
DOE	Diffractive Optical Element
GG	Ground Glass
GSP	Generalized Stoke Parameter
HBT	Hanbury Brown-Twiss
He-Ne	Helium - Neon
HWP	Half Wave Plate
L	Lens
LP	Linear Polarizer
M	Mirror
MO	Microscope Objective
PBS	Polarization Beam Splitter
QWP	Quarter Wave Plate
SF	Spatial Filter
SLM	Spatial Light Modulator
SPP	Spiral Phase Plate

NOTATIONS

$|.|$ - Absolute value

θ - Angle of rotation

δ - Delta function

$\langle . \rangle$ - Ensemble average

f - Focal length of lens

k - Propagation factor

φ - Random phase from scattering layer

η - Reconstruction efficiency

$\langle . \rangle_S$ - Spatial average

$\boldsymbol{r}$ - Spatial co-ordinates in observation plane

$\hat{\boldsymbol{r}}$ - Spatial co-ordinates in source plane

σ - Standard deviation

$\boldsymbol{t}$ - Time

Tr - Trace of the matrix

v - Visibility

λ - Wavelength of light source

CHAPTER 1
INTRODUCTION

Light scattering from optically complex media generates speckles, a high-contrast, and fine-scale granular pattern with well defined statistical properties (Dainty, 1984; Goodman, 2007). This phenomenon got attention since the invention of laser in the early 1960s as a nuisance that to be minimized for coherent optical imaging applications. These speckle patterns arises from the coherent superposition of the wavelets emanating from the scattering spots in the rough surface that are on the scale of wavelength. The speckle pattern also plays a decisive role in other fields such as images in synthetic aperture radar in microwave region and also ultrasound medical imagery of organs in the human body where it destroys the contrast of the images obtained (Goodman, 2007). In this respect speckle reduction technologies have increasing interest in areas where laser is used as a light source such as in interferometry, holography, microscopy, optical coherence tomography and projection displays. A number of methods have been developed for speckle elimination or reduction starting from the classical way of putting a moving diffuser in laser beam(Lowenthal and Joyeux, 1971). Some of the recently introduced techniques are based on multimode optical fibers(Manni and Goodman, 2012; Mehta et al., 2012), by tailoring the structure of a random laser beam(Redding et al., 2011, 2012), using phase only spatial light modulator(Y. Wang et al., 2013), by using dynamic deformable mirror(Tran et al., 2014) etc

In recent years interest has turned in the direction of using speckle pattern as a versatile tool for a wide variety of applications such as surface roughness estimation, speckle interferometry, speckle photography, astronomy, laser speckle contrast imaging, optical manipulation, correlation imaging etc. The statistical analysis of speckle pattern generating from a random diffuser is developed by Goodman and Dainty by considering a monochromatic light source illumination on the diffuser. These statistical properties associated with the speckle field play a central role in determining the coherence and polarization properties of the randomly fluctuating field. The pioneering works in unified theory of coherence

and polarization of randomly fluctuating field opens up new opportunities in treating coherence and polarization together in terms of cross spectral density matrix in space-frequency domain or beam coherence-polarization matrix in space-time domain (Gori, 1998; Mandel and Wolf, 1995; Wolf, 2007). The statistical features of optical field fluctuations are too rapid to be directly measurable and the randomness of the optical field is characterized by the concept of ensemble average. Usually in experimental implementation the ensemble average is replaced with the time average by assuming that statistical field is stationary and ergodic in time (Goodman, 2000). However, recently practical interests are in the direction of replacing ensemble average with space average under the assumption of spatial stationarity and spatial ergodicity, and thereby introduced the concept of spatial statistical optics (Takeda et al., 2014; Takeda, 2013). This progress in the correlation holography based on spatial statistical optics provides new opportunities to control and synthesize the optical fields with desired statistical properties in space, thereby have applications in the field of optical coherence tomography, lithography, profilometry, correlation imaging, physical optics etc.

The shaping and analysis of laser speckle pattern by giving emphasis on spatial statistical optics and its applications in imaging is the main theme of the thesis. The research work focuses on the development of theoretical basis and experimental techniques for shaping and analysis of laser speckle pattern thereby tailoring the spatial coherence function of the random field in a desired fashion to explore its strength in imaging based applications. Statistical properties of the laser speckle field is studied by considering the second order and fourth order correlation functions for two space points at an instant of time and influence of diffractive optical elements in shaping these statistical properties are explored. Synthesis and analysis of statistical properties of random fluctuating field is implemented by developing field and intensity based interferometers. The use of fourth order correlation or two point intensity correlation for the measurement of coherence and polarization properties of random field is investigated. An experimental determination of generalized Stokes parameters using fourth order correlation based on spatial averaging is described and its potential in characterizing the inhomogeneous polarization states is demonstrated. Finally in the applied domain, imaging techniques were developed for the non-invasive

imaging through complex scattering layers by utilizing the controlled synthesis and analysis of spatial coherence function. In the remainder of this introduction we describe the propagation of light beam through scattering layers and the physical origin of laser speckle pattern. Later a brief literature review exploiting the randomness of speckle pattern for various applications is described.

1.1.   Origin of Speckle

The invention of laser-the generation of coherent light by Maimann in 1960 opens up the wide door of optics applications in scientific and engineering world (Maiman, 1960). Along with the development of the generation of coherent light, researchers noticed the presence of granular appearance later named as 'speckle' when the light illuminates rough objects (Ridgen and Gordon, 1962).When the coherent beam either reflects from a rough surface or propagates through an inhomogeneous medium with refractive index variation, the wave emerges from the surface contains contributions from many independent scattering spots. Propagation of this light to an observation plane forms the random interference pattern that contains superposition of scattered components with relative phase delays. This addition of the scattered components at an observation plane can be considered as a random walk and the resultant sum will produce constructive or destructive interference depending up on the relative phases of the various components of the sum. A schematic representation of the origin of speckle pattern from a scattering medium when a coherent light transmits through the medium is shown in Fig.1.1.
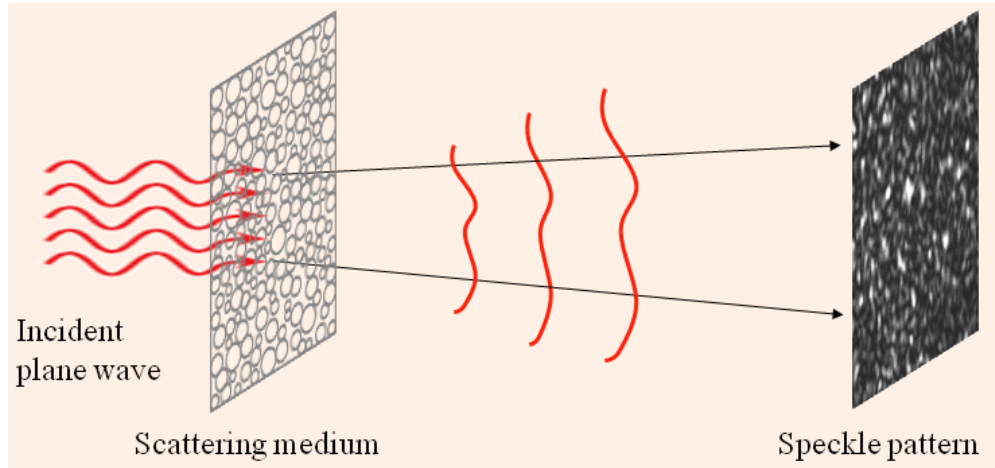
Figure 1.1: Schematic representation of the origin of speckle pattern from a scattering medium

This random speckle pattern is considered as a nuisance in coherent imaging applications and there after techniques where developed to eliminate or reduce the speckle pattern in the images to improve the quality of the images like in synthetic aperture radar (SAR) imaging, ultrasound imaging and optical coherence tomography (OCT) (Porcello et al., 1976; Schmitt et al., 1999). Later the investigations on the fundamental statistical properties of the speckle pattern (Angel et al., 2001; Dainty, 1970; Goodman, 1976; Ohtsubo and Asakura, 1975) and possibilities in synthesizing the speckle pattern turned interest from undesirable aspects of the speckle pattern to utilize the speckle pattern as a flexible tool in different applications.

Propagation of coherent light through multiple scattering medium got increasing attention in recent years due its practical importance in biomedical optics (Davis et al., 2014; Li et al., 2002; Schmidt et al., 2015; Tchvialeva et al., 2013). This multiple scattering from random media generates in homogeneously polarized light and it plays a significant role in controlling the depolarization of light. The speckle pattern arising from such a random media has a spatially fluctuating state of polarization and is referred as the polarization speckles (R. K. Singh et al., 2014; Takeda et al., 2010; W. Wang et al., 2009). The polarization speckles results from the vectorial addition of a number of randomly phased complex distributions with different polarization states. The random vectorial field at each position has well defined polarization state with its degree of polarization

4

equal to one and the polarization state fluctuate in space. A schematic representation of the origin of polarization speckle pattern from a multiple scattering when a coherent light transmits through the random medium is shown in Fig.1.2.
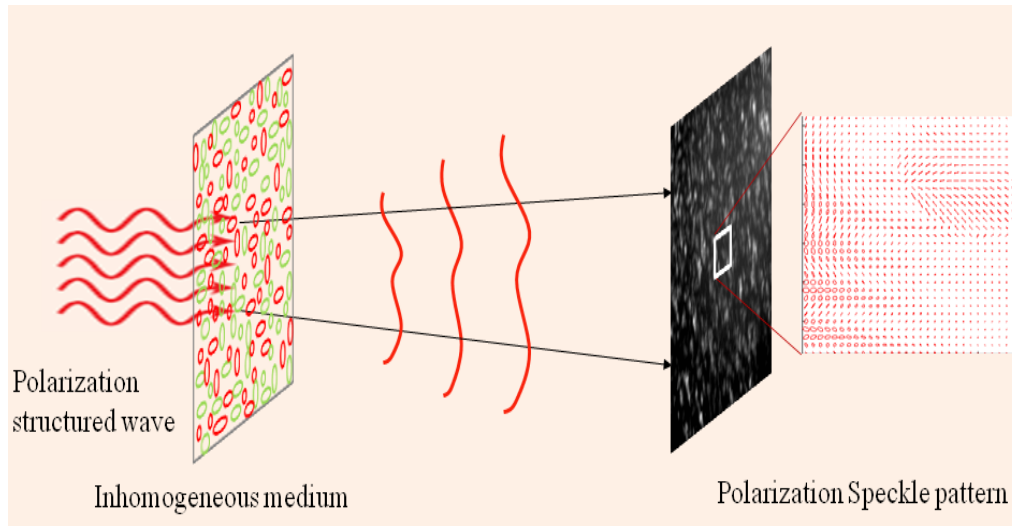
Figure 1.2: Schematic representation of the generation of polarization speckle pattern from an inhomogeneous scattering medium

1.2. Exploiting the Laser Speckle Pattern

The potential of speckle pattern as a versatile tool in different application regimes in science and engineering attains interest of researchers to explore different application based scenarios where speckle effects can be implemented. Investigations on the development of techniques to use the speckle pattern for imaging were started after the pioneering work of Leith and Upatneik in holography (Leith and Upatnieks, 1963). Later techniques were developed to image through random or diffusing media by utilizing the random feature of the speckle pattern (Goodman et al., 1966; Leith and Upatnieks, 1964). The field of speckle photography and speckle interferometry became an intense research area in 1970s due to its potential applications in engineering metrology and stellar astrophysics (Dainty, 1984; L. EK, 1971; Labeyrie, 1975; Schneiderman et al., 1975). The reconstruction of high resolution images were achieved by combining speckle interferometry with speckle holography techniques (Liu and Lohmann, 1973; Weigelt, 1978). Information processing ability of the speckle pattern is made use in speckle photography and innovative techniques were developed recently to detect the surface tampering effects (Angel et al., 2000; Shih et al.,

2012; Tebaldi et al., 2000). Phase object detection by using double exposure fringe modulated speckle patterns and with a speckle interferometer is demonstrated (Angel et al., 2002; Tebaldi et al., 2003). A detailed exploration of the statistical properties of the laser speckle pattern received interests in surface inspection of the materials and experimental demonstrations showed that an inspection of laser speckle contrast can give the roughness and correlation length of the rough surface object (Curry et al., 2011; Kodono et al., 1987). The statistical properties of speckle pattern generated through multiple apertures were studied and the possibility of synthesizing the speckle distribution is investigated (Angel et al., 2001). Recently laser speckle contrast imaging emerged as a powerful tool in biomedical optics especially in full-field imaging of blood flow (Boas and Dunn, 2010; Briers et al., 2013; Richards et al., 2013). Very recently the role of speckle fields in efficient manipulation tasks such as trapping, guiding and sorting is demonstrated by introducing the speckle optical tweezers (Volpe et al., 2014). Speckle imaging and speckle correlation techniques were effectively implemented in developing laser speckle strain gauge which find applications in non-destructive surface deformation measurements and vascular applications (Kirkpatrick and Cipolla, 2000; Takai and Asakura, 1983; Yamaguchi, 1987).

Polarization properties associated with the laser speckle pattern arising from a multiple scattering medium has increasing interest in researches as it has potential applications in the field of biomedical imaging and diagnostics (Davis et al., 2014; Li et al., 2002; Tchvialeva et al., 2013), dynamic spectroscopy (Pecora, 1985), remote sensing (Carswell and Pal, 1980) etc. An investigation on the statistical properties of polarization-related speckle phenomena by introducing polarization speckles and their spatial degree polarization is described recently (Takeda et al., 2010; W. Wang et al., 2009). Spatial dynamics of polarization fluctuation is investigated very recently by extending the concept of Poincare vector correlation for characterization of fluctuating scattered field and by designing polarization interferometer to detect the instantaneous polarization state (R. K. Singh et al., 2014). The spatial non-stationarities in random electromagnetic field is identified from single realization of speckle pattern by appropriate statistical analysis (Broky et al., 2008). Investigations on the statistical signature of random media and loss of polarization of light scattered from rough surfaces were reported recently (Soriano et al., 2014; Sorrentini et al., 2009; Zerrad et al., 2010).

An experimental description to measure the polarization degree within each grain of the speckle pattern is proposed very recently (Ghabbach et al., 2014).

Imaging and focusing in turbid media by exploiting the randomness of the speckle field is a celebrated area in optics due to its importance in biomedical imaging, astronomy etc. A significant number of techniques for imaging through random media based on holographic principles were introduced by using the random nature of the speckle pattern (Chen et al., 1993; Goodman et al., 1966; Kogelnik and Pennington, 1968; A. K. Singh et al., 2014). The advances in the use of scattering medium to focus, shape and compress waves by controlling the many degrees of freedom of incident waves gives a new potential in imaging and focusing in turbid media (Mosk et al., 2012; Yu et al., 2015). The turbidity of the scattering layer is exploited to improve the focusing and spatial resolution beyond the diffraction limit (Choi et al., 2011; Vellekoop and Aegerter, 2010). Very recently techniques with speckle correlation approach are employed for the non-invasive imaging through scattering layers. A fluorescent object inside an opaque layer is reconstructed by angular speckle correlation by exploiting the speckle memory effect (Bertolotti et al., 2012). The angular scanning of speckle pattern results in a long acquisition time of images and limits the object to be stationary for the complete acquisition period. An innovative non-invasive single shot imaging technique is demonstrated that is capable to overcome the limitation of long acquisition period by capturing the single shot speckle pattern (Katz et al., 2014). The technique is limited by actual depth information behind the scattering medium and iterative approach supported by complicated image processing.

The relationship between speckle theory and coherence theory attains a significant attention to many of the researchers in the later part of the 1970 itself (Carter and Wolf, 1977; Leader, 1980). The equivalency exist in the autocorrelation function of the speckle field to the van Cittert-Zernike theorem of classical coherence theory give way to engineer the speckle pattern for applications in coherence theory (Goodman, 2007). Correlation of light field plays a fundamental role in characterization of the optical field from statistical point of view. Significant developments on coherence theory lead foundation to various new areas of research activities in the statistical optics. The quantitative treatment of the concepts of correlation lies in the measurement of statistical similarity between the interfering beams or vibration at two points in terms of

degree of coherence of light (Angelsky et al., 2009; Tervo et al., 2003). Field based measurements for second order correlation is the widely used technique to analyze the coherence phenomena associated with fluctuations in the field. However the interests in Hanbury Brown-Twiss intensity interferometer draw attention to higher order correlations at two space-time points or two frequency-time (Brown and Twiss, 1956). This measures the two point intensity correlation or fourth order correlation, which is directly related to the coherence and polarization properties of the field (Hassinen et al., 2011). Statistical properties of light field and their efficient control to obtain desired coherence-polarization properties have potential role in applications related to correlation induced spectral changes (Wolf, 2003a, 2007). The unified theory of coherence and polarization provides the basis to examine the coherence and polarization of random electromagnetic beam together and to investigate the controlled synthesize using polarization dependent devices. Techniques were developed in recent years to modulate the coherence and polarization properties of the random electromagnetic field by random phase screens and by using phase sensitive liquid crystal spatial light modulator. (Ostrovsky et al., 2009; Shirai and Wolf, 2004).

Recent experimental interests are in the direction of replacing ensemble average with space average under the assumption of spatial stationarity and spatial ergodicity and thereby provide opportunity for single shot measurement technique (Broky et al., 2008; Georges et al., n.d.; Réfrégier et al., 2012; R. K. Singh et al., 2013; Sorrentini et al.,; Takeda et al., 2014; Takeda, 2013; Zerrad et al., 2014, 2015). The coherence and polarization studies of light scattered from rough surfaces using spatial or angular average process attains a significant amount of practical interest in recent years (Georges et al.,; Réfrégier et al., 2012; Sorrentini et al.,; Zerrad et al., 2014, 2015).The formal analogy between correlation function and optical field has been exploited from speckle field to develop correlation holography based techniques. An unconventional holography technique called coherence holography is developed to shape the spatial coherence of light in a desired fashion and to reconstruct the object information (Takeda et al., 2005). A three dimensional (3D) object reconstruction is made possible in photon correlation holography from intensity correlation or fourth order correlation by illumination through a random phase screen (Naik et al., 2011). Recently, extension of the coherence holography to the vectorial domain is carried out and

techniques such as vectorial coherence holography and Stokes holography are developed (R. K. Singh et al., 2011, 2012). These practical interests in correlation based holographic techniques by exploiting the randomness of the speckle pattern by replacing ensemble average with space average under the assumption of spatial stationarity and spatial ergodicity, provides potential developments in the concept of spatial statistical optics (Takeda et al., 2014; Takeda, 2013). This progress in spatial averaging based techniques provides new opportunities to control and synthesize the optical fields with desired statistical properties in space and thereby providing new realms to the field of spatial statistical optics. In the present research work our main interest is to investigate shaping and analysis of laser speckle pattern by developing experimental techniques based on spatial averaging. We have carried out this work by considering uniformly and non-uniformly polarized random fields. New techniques have been developed to shape and analyze such random fields. Also single-shot imaging techniques for non-invasive imaging through a scattering medium by employing the spatial average approach and shaped spatial correlation function is investigated and experimentally demonstrated.

1.3.   Outline of the Thesis

The whole thesis is split into 6 chapters. The significance of shaping the laser speckle pattern and its importance in various applications is described in chapter2. In chapter 3 and 4 we describe the different experimental techniques developed for shaping and analysis of laser speckle pattern based on amplitude/field and intensity interferometers. Chapter 5 focuses on the application of shaped correlation function in non-invasive imaging through complex scattering layers and in chapter 6, we conclude by pointing out the major outcomes of the research work.

Chapter 2 describes the need for shaping the laser speckle pattern by discussing the applications in various fields. The significance of correlation of light field in optical characterization and its importance in shaping the laser speckle pattern are discussed by giving emphasis on van Cittert Zernike theorem. Also discuss the concept of ensemble average in characterization of the randomness of optical field and its experimental implementation by considering

temporal average and spatial average as replacement of ensemble average. The shaping of laser speckle pattern with different apertures as source structure is demonstrated.

In chapter 3 we discuss the diffractive optics element such as Dammann phase grating and its role to shape the laser speckle pattern. Detection and analysis of complex field of laser speckle patterns were experimentally demonstrated by designing amplitude sensitive interferometer. Generation of one dimensional and two dimensional uniform spatial coherence points were experimentally demonstrated by shaping the laser speckle pattern with Dammann phase type grating. This chapter also discusses random polarization fluctuations and its characterization by using the 2X2 coherence polarization matrix with help of field based polarization interferometer.

The role of intensity based interferometers in the analysis of laser speckle pattern is discussed in chapter 4. The use of two point intensity correlation for the generation of singular point array is investigated and experimentally demonstrated. A new experimental approach to retrieve the complex coherence function from two point intensity correlation by making use of speckle holography technique is developed and experimentally demonstrated. Also the extension of the idea to vectorial domain is developed by describing a new experimental technique for the determination of generalized Stokes parameters (GSP) or coherence-polarization (CP) matrix elements and demonstrates its application in the synthesis of statistical properties of light field.

Imaging through scattering media by using two point intensity correlation measurement techniques were investigated and experimentally demonstrated in chapter 5. Recovery of complex valued object behind the scattering layer using two point intensity correlation and speckle holographic technique is described and experimentally demonstrated. Extension of this technique for the depth resolved 3D non-invasive single shot imaging through scattering layers is proposed and experimentally demonstrated. Also a digital holographic imaging through scattering layers is investigated and experimentally demonstrated.

In concluding chapter 6, we summarize the research work by pointing out key research outcomes and take a look on to the future scope of the work. Followed by this chapter bibliography, appendices and the list of publications are provided.

CHAPTER 2
SHAPING OF LASER SPECKLE PATTERN

Speckle pattern is a part of statistical optics; the theoretical and experimental progresses in the field of statistical optics give new potentials in the study of random fluctuations in a speckle pattern (Dainty, 1970; Goodman, 1976; Vry and Fercher, 1986). These developments provide new ways to use speckle pattern as a versatile tool in various applications in science and technology. The prediction of memory effect in coherent wave propagation through disordered media (Feng et al., 1988) and its experimental validation (Freund et al., 1988) in later years provides fundamental basis to use the randomness of speckle pattern. A number of techniques have been introduced on the laser speckle contrast which has significant applications in biomedical optics (Boas and Dunn, 2010; Briers et al., 2013; Richards et al., 2013). Advances in the correlation based studies on speckle field and speckle intensity turned the attention to use the speckle pattern to investigate the statistical properties of the scattered optical field (Dainty, 1984; Goodman, 2007). Recently the possibility of synthesizing the image speckle distribution by multiple apertures is demonstrated and the first and second order statistical properties of the speckle pattern are investigated using mutual intensity and autocorrelation of intensity (Angel et al., 2001). The similarity in correlation function of speckle field to the van Cittert-Zernike theorem in classical coherence theory provide the potential to shape the speckle pattern in a desired fashion to control and synthesize the statistical properties of the light and in correlation based imaging (Takeda et al., 2005, 2008, 2009).

In the present chapter we focus on the preliminary mathematical basis required for the thesis by giving emphasis on the first order and second order statistical properties of speckle pattern. In the following section the importance of $f - f$ geometry in shaping the speckle pattern is discussed by focusing on spatial averaging as replacement of ensemble averaging. Also an extension of the concepts to vectorial domain is presented for investigating the coherence and polarization properties of the scattered optical field.

2.1. First order statistics of speckle pattern

The first order statistical properties of the laser speckle pattern deals with the properties of the scattered field at a single point in space and time. Consider the case of a coherent beam illuminating a rough surface and generates random speckle pattern with well defined statistical properties. The statistical properties of speckle patterns were investigated by considering an ensemble of scattering point contribution from the rough surfaces. A schematic representation of the formation of speckle pattern at an observation plane and the corresponding spatial coordinate representation are shown in Fig. 2.1.
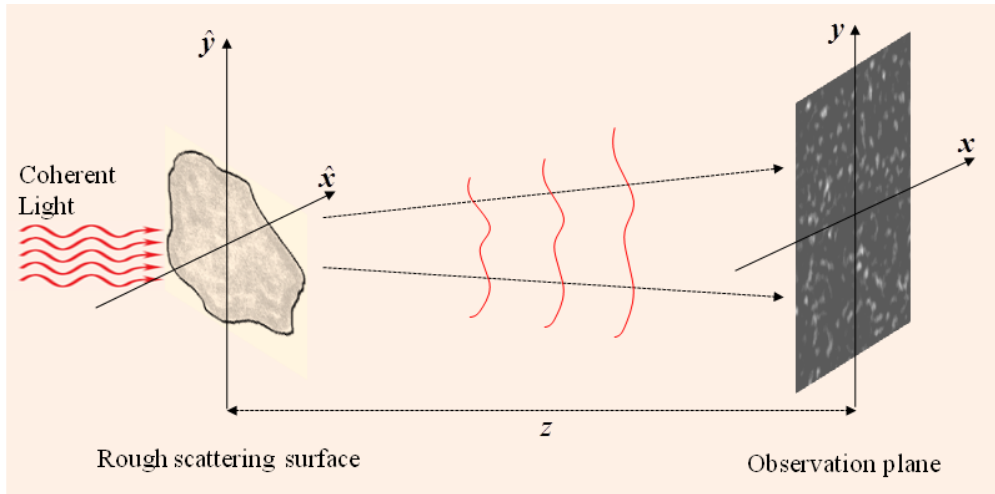
Figure 2.1: Schematic representation of the formation of speckle pattern at an observation plane

The speckle pattern at any plane after the rough surface is the superposition of the field contribution from different scattering points in the rough surface. At a point in the observation plane, the resultant field consists of a multitude of de-phased contributions from different scattering points of the rough surface. The resultant field at this plane is given by

$$U(\boldsymbol{r},t) = \sum_{k=1}^{N} |u_k| e^{i\varphi_k} \tag{2.1}$$

where u_k and φ_k are the amplitude and phase contribution from the kth scattering point in the rough surface and N is the total number of scattering points in the rough surface. This resultant field at each point in the speckle pattern can be

12

considered as a random walk phenomena similar to the well known classical problem of the random walk (Goodman, 1976).

The statistical properties of the complex speckle field is investigated by Goodman by assuming that (a) amplitude u_k and phase φ_k of the resultant field from each scattering point are statistically independent of each other and are independent of amplitude and phase of the field of all other components (b) the phase φ_k are uniformly distributed on the interval $-\pi$ to π, such that the surface is considered to be rough in comparison with wavelength of the illuminating light. Using these assumptions and by considering large number of scattering points (i.e large N value) in a rough surface Goodman showed that the real and imaginary part of the complex field are identically distributed Gaussian random variables and the intensity at any point in the speckle pattern obeys negative exponential statistics. These predicted results were experimentally verified in later years (Dainty, 1970). In most of the practical applications the intensity of the speckle pattern is of main interest. The probability density function of the intensity of the speckle pattern is given by

$$p(I) = \begin{cases} \dfrac{1}{\langle I \rangle} \exp\left(\dfrac{-I}{\langle I \rangle} \right) , I \geq 0 \\ 0, \qquad\qquad \text{otherwise} \end{cases} \tag{2.2}$$

where $\langle I \rangle$ represents the average value of intensity over the N scattering points in the rough surface. To quantify the intensity variations in the speckle pattern a quantity, speckle contrast which is defined as the standard deviation to mean intensity is introduced and is given by

$$C = \frac{\sigma_I}{\langle I \rangle} \tag{2.3}$$

where σ_I represents the standard deviation of the speckle intensity. For a fully developed speckle pattern the theoretical limits of the speckle contrast is between 0 and 1. A speckle contrast of 1 show that there is no blurring in the speckle pattern and gives a clear random pattern while a speckle contrast of 0 indicates complete blurriness in the random speckle pattern (Boas and Dunn, 2010). Recent progress in laser speckle contrast imaging provides new potential applications of

speckle contrast in biomedical optics especially in full field imaging of blood flow (Richards et al., 2013).

2.2. Second order statistics of speckle pattern

Second order statistical properties of the speckle pattern deals with the properties of the speckle at two points, rather than the one point. These second order statistics of the speckle pattern are investigated in terms of the autocorrelation of the speckle field and speckle intensity at two points in space or time.

2.2.1 Autocorrelation of speckle field

Consider the case that a coherent light of wavelength 'λ' illuminating a rough surface and generating a speckle pattern at distance z from the rough surface as shown in Fig. 2.1. On considering the paraxial propagation, the complex amplitude of the speckle field at a position in the detector plane is estimated by Fresnel diffraction integral (Goodman, 2007) and is given as

$$u(x,y;t) = \frac{\exp[jkz]}{j\lambda z} \exp\left[\frac{jk}{2z}\left(x^2+y^2\right)\right] \times$$
$$\int_{-\infty}^{+\infty} \int_{-\infty}^{+\infty} u(\hat{x},\hat{y},t) \exp\left[\frac{jk}{2z}\left(\hat{x}^2+\hat{y}^2\right)\right] \exp\left[\frac{-j2\pi}{\lambda z}\left(x\hat{x}+y\hat{y}\right)\right] d\hat{x}d\hat{y}$$

(2.4)

where $u(\hat{x},\hat{y},t)$ is the complex amplitude of light at the rough surface with $(\hat{x},\hat{y})$ represents the spatial coordinate at this plane at an instant of time t, $k=\dfrac{2\pi}{\lambda}$ the propagation factor and $j=\sqrt{-1}$.

The autocorrelation function of the speckle field at two points in space is given by

$$W(x_1,y_1;x_2,y_2;t) = \left\langle u(x_1,y_1;t)u^*(x_2,y_2;t) \right\rangle$$

(2.5)

where $\langle . \rangle$ represents the ensemble average. On substituting the value of $u(x,y;t)$, Eq. (2.5) modifies to

$$W(x_1, y_1; x_2, y_2; t) = \frac{1}{\lambda^2 z^2} \exp\left[\frac{jk}{2z}\left(x_1^2 + y_1^2 - x_2^2 - y_2^2\right)\right]$$

$$\times \int_{-\infty}^{+\infty}\int_{-\infty}^{+\infty} \int_{-\infty}^{+\infty}\int_{-\infty}^{+\infty} W_S(\hat{x}_1, \hat{y}_1; \hat{x}_2, \hat{y}_2; t)\exp\left[\frac{jk}{2z}\left(\hat{x}_1^2 + \hat{y}_1^2 - \hat{x}_2^2 - \hat{y}_2^2\right)\right]$$

$$\times \exp\left[\frac{-j2\pi}{\lambda z}\left(x_1\hat{x}_1 + y_1\hat{y}_1 - x_2\hat{x}_2 - y_2\hat{y}_2\right)\right]d\hat{x}_1 d\hat{y}_1 d\hat{x}_2 d\hat{y}_2$$

(2.6)

where $W_S(\hat{x}_1, \hat{y}_1; \hat{x}_2, \hat{y}_2; t) = \langle u(\hat{x}_1, \hat{y}_1; t)u^*(\hat{x}_2, \hat{y}_2; t)\rangle$ is the correlation function of the field at the rough scattering surface. On considering the assumption that the correlation extent of the field at the scattering surface is sufficiently small so that it can be represented by a delta function (Goodman, 2007), the correlation function $W_S(\hat{x}_1, \hat{y}_1; \hat{x}_2, \hat{y}_2; t)$ is given by

$$W_S(\hat{x}_1, \hat{y}_1; \hat{x}_2, \hat{y}_2) = \kappa I(\hat{x}_1, \hat{y}_1)\delta(\hat{x}_1 - \hat{x}_2, \hat{y}_1 - \hat{y}_2)$$

(2.7)

where 'κ' is the proportionality constant, $I(\hat{x}_1, \hat{y}_1)$ is the intensity at the scattering surface and $\delta(\hat{x}_1 - \hat{x}_2, \hat{y}_1 - \hat{y}_2)$ is the two dimensional delta function. Substituting Eq. (2.7), the Eq. (2.6) modifies to

$$W(x_1, y_1; x_2, y_2; t) = \frac{\kappa}{\lambda^2 z^2} \exp\left[\frac{jk}{2z}\left(x_1^2 + y_1^2 - x_2^2 - y_2^2\right)\right]$$

$$\times \int_{-\infty}^{+\infty}\int_{-\infty}^{+\infty} I(\hat{x}, \hat{y})\exp\left[\frac{-j2\pi}{\lambda z}\left(\hat{x}(x_1 - x_2) + \hat{y}(y_1 - y_2)\right)\right]d\hat{x}d\hat{y}$$

(2.8)

The quadratic phase factor term preceding the integral can be ignored in most of the practical applications where the modulus of the correlation function is important (Goodman, 2007). On ignoring this quadratic phase factor term, Eq. (2.8) modifies to

$$W(\Delta x, \Delta y; t) = \frac{k}{\lambda^2 z^2} \int_{-\infty}^{+\infty}\int_{-\infty}^{+\infty} I(\hat{x}, \hat{y})\exp\left[\frac{-j2\pi}{\lambda z}\left(\hat{x}\Delta x + \hat{y}\Delta y\right)\right]d\hat{x}d\hat{y}$$

(2.9)

where $\Delta x = x_2 - x_1$ and $\Delta y = y_2 - y_1$. Eq. (2.9) states that the autocorrelation function of the speckle field is equal to the two dimensional Fourier transform of the intensity distribution of the light at the scattering surface and this result is

equivalent to the van Cittert-Zernike theorem of classical coherence theory (Goodman, 2000).

The complex degree of correlation is determined from the autocorrelation function (Goodman, 2007) and is given by

$$\gamma(\Delta x, \Delta y; t) = \frac{W(\Delta x, \Delta y; t)}{W(0,0)} \qquad (2.10)$$

On substituting the value of autocorrelation function from Eq. (2.9), the complex degree of correlation is given by

$$\gamma(\Delta x, \Delta y; t) = \frac{\int\limits_{-\infty}^{+\infty}\int\limits_{-\infty}^{+\infty} I(\hat{x}, \hat{y}) \exp\left[\frac{-j2\pi}{\lambda z}\left(\hat{x}\Delta x + \hat{y}\Delta y\right)\right] d\hat{x} d\hat{y}}{\int\limits_{-\infty}^{+\infty}\int\limits_{-\infty}^{+\infty} I(\hat{x}, \hat{y}) d\hat{x} d\hat{y}} \qquad (2.11)$$

2.2.2 Autocorrelation of speckle intensity

The autocorrelation function of the intensity distribution of a speckle pattern is related to the complex degree of correlation by (Goodman, 2007)

$$\Gamma(\Delta x, \Delta y; t) = \langle I \rangle^2 \left[1 + |\gamma(\Delta x, \Delta y; t)|^2 \right] \qquad (2.12)$$

On substituting the value of $\gamma(\Delta x, \Delta y; t)$, Eq. (2.12) modifies to

$$\Gamma(\Delta x, \Delta y; t) = \langle I \rangle^2 \left[1 + \left| \frac{\int\limits_{-\infty}^{+\infty}\int\limits_{-\infty}^{+\infty} I(\hat{x}, \hat{y}) \exp\left[\frac{-j2\pi}{\lambda z}\left(\hat{x}\Delta x + \hat{y}\Delta y\right)\right] d\hat{x} d\hat{y}}{\int\limits_{-\infty}^{+\infty}\int\limits_{-\infty}^{+\infty} I(\hat{x}, \hat{y}) d\hat{x} d\hat{y}} \right|^2 \right] \qquad (2.13)$$

The Fourier transform of autocorrelation function of speckle intensity distribution represents the power spectral density function and is given by

$$\zeta(v_x, v_y) = \int\limits_{-\infty}^{+\infty}\int\limits_{-\infty}^{+\infty} \Gamma(\Delta x, \Delta y; t) \exp\left[\frac{-j2\pi}{\lambda z}\left(v_x\Delta x + v_y\Delta y\right)\right] d\Delta x d\Delta y \qquad (2.14)$$

On using Eq. (2.13) in Eq. (2.14), the power spectral density relation modifies to

$$\zeta(v_x, v_y) = \langle I \rangle^2 \left[\delta(v_x, v_y) + (\lambda z)^2 \frac{\int\limits_{-\infty}^{+\infty}\int\limits_{-\infty}^{+\infty} I(\hat{x}, \hat{y}) I(\hat{x} + \lambda z v_x, \hat{y} + \lambda z v_y) d\hat{x} d\hat{y}}{\left[\int\limits_{-\infty}^{+\infty}\int\limits_{-\infty}^{+\infty} I(\hat{x}, \hat{y}) d\hat{x} d\hat{y} \right]^2} \right] \quad (2.15)$$

where the zero-frequency power contributed by the average intensity corresponds to the delta function.

2.2.3 Speckle size

The average speckle grain size in a speckle pattern is given by the equivalent area of the normalized covariance function of speckle intensity. The normalized covariance function is related to the autocorrelation of the speckle intensity (Goodman, 2007) and is given by

$$C(\Delta x, \Delta y) = \frac{\Gamma(\Delta x, \Delta y) - \langle I \rangle^2}{\langle I \rangle^2} = |\gamma(\Delta x, \Delta y)|^2 \quad (2.16)$$

Therefore the speckle grain size is given by

$$A_S = \int\limits_{-\infty}^{+\infty}\int\limits_{-\infty}^{+\infty} C(\Delta x, \Delta y) d\Delta x d\Delta y = \int\limits_{-\infty}^{+\infty}\int\limits_{-\infty}^{+\infty} |\gamma(\Delta x, \Delta y)|^2 d\Delta x d\Delta y \quad (2.17)$$

Note that if we are considering a rectangular or circular scattering spot, the speckle grain size is given by

$$A_S = \frac{(\lambda z)^2}{A} = \frac{\lambda^2}{\Omega_s} \quad (2.18)$$

where A is the area of the scattering spot and Ω_s is the solid angle subtended by the scattering spot. These results are valid for a uniformly illuminating scattering spot. If the scattering spot is not uniformly illuminating, by making use of $\gamma(\Delta x, \Delta y)$ from Eq. (2.11), the speckle size is more generally represented as

$$A_S = \left(\lambda z\right)^2 \frac{\displaystyle\int\limits_{-\infty}^{+\infty}\int\limits_{-\infty}^{+\infty} I^2(\hat{x}, \hat{y})\,d\hat{x}d\hat{y}}{\left[\displaystyle\int\limits_{-\infty}^{+\infty}\int\limits_{-\infty}^{+\infty} I(\hat{x}, \hat{y})\,d\hat{x}d\hat{y}\right]^2} \qquad (2.19)$$

2.3. Shaping the speckle pattern using $f - f$ geometry

Recent progress in correlation holography techniques based on the concepts of spatial statistical optics attains new focus on spatial statistics of optical field rather than its temporal statistics (Takeda et al., 2014; Takeda, 2013). The developed techniques have potential applications in synthesizing the optical field with desired statistical properties, correlation imaging and also in coherence and polarization shaping. These techniques utilize the concept of spatial stationarity of the scattered optical field for replacing ensemble average with spatial average under the condition of spatial stationarity and spatial ergodicity of the scattered field. The choice of spatial average permits the analysis of the statistical properties of the instantaneous speckle field or the time frozen speckle field. A conceptual representation of the time frozen speckle field is shown in Fig. 2.2.
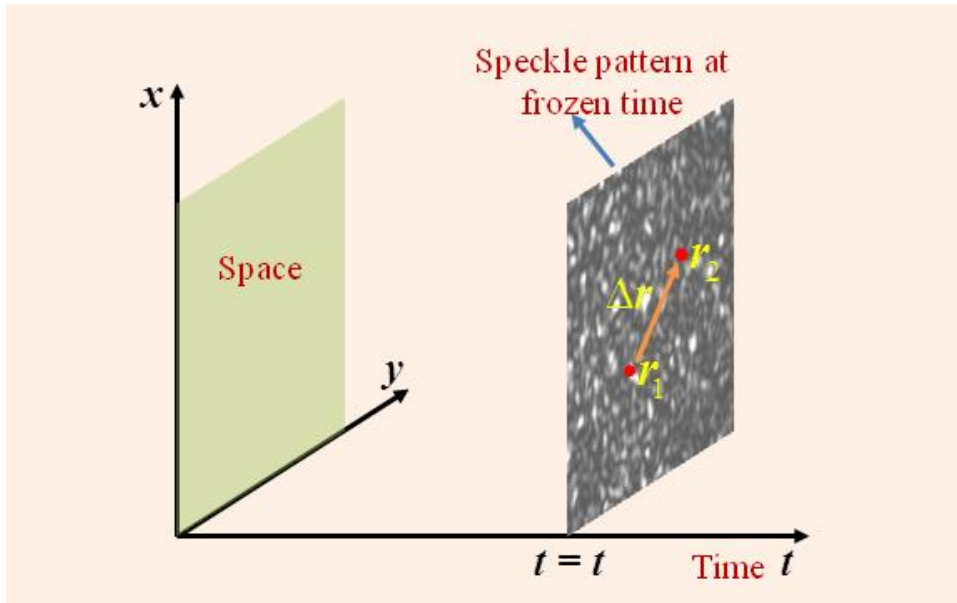
Figure 2.2: A conceptual representation of the space-time distribution of the speckle pattern at a frozen time

In a recent work it is demonstrated that the need of an $f - f$ geometry to realize

18

the perfect spatial stationarity in the scattered field by removing the nonstationary phase factor (Takeda, 2013). The results shows that the Fraunhofer diffraction can make the light from incoherent nonstationary source to have spatial stationarity in the far field. In this section we explain the theoretical basis of shaping the speckle pattern using $f - f$ geometry by maintaining perfect spatial stationarity in the scattered speckle field.

2.3.1 Autocorrelation of speckle field using spatial averaging

Consider a rough scattering surface illuminated with a coherent light of wavelength 'λ' and generates speckle pattern. The $f - f$ geometry is implemented and the speckle pattern is recorded at the Fourier transform plane. A schematic representation of the geometry is shown in Fig. 2.3.
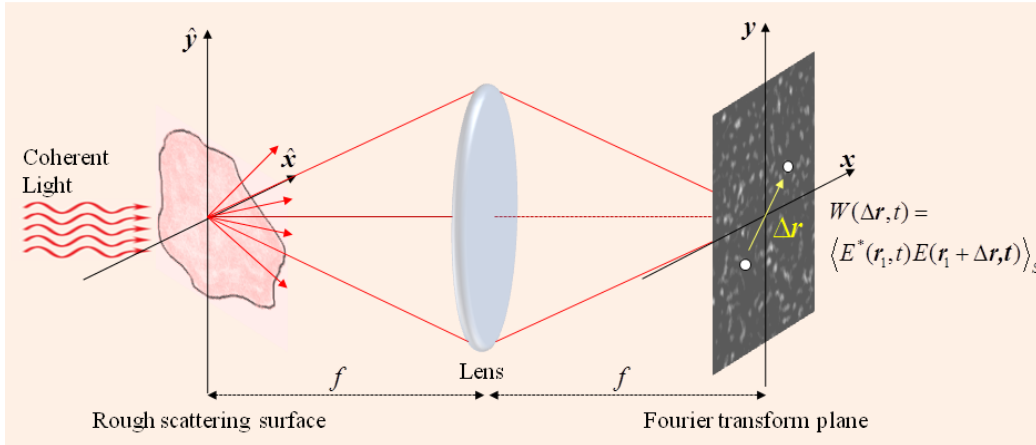
Figure 2.3: Schematic representation of $f - f$ geometry and the formation of speckle pattern at the Fourier transform plane

The scattered optical field reaching the Fourier transform plane is given by

$$E(\boldsymbol{r},t) = \int E(\hat{\boldsymbol{r}},t) \exp(j\varphi(\hat{\boldsymbol{r}})) \exp[-j\frac{2\pi}{\lambda f}\boldsymbol{r}.\hat{\boldsymbol{r}}]d\hat{\boldsymbol{r}} \qquad (2.20)$$

where $\boldsymbol{r}$ and $\hat{\boldsymbol{r}}$ are spatial co-ordinates at the scattering plane and Fourier transform plane respectively for a fixed time $\boldsymbol{t}$, $\varphi(\hat{\boldsymbol{r}})$ is the random phase introduced by the rough scattering surface and f is the focal length of the Fourier transforming lens.

The autocorrelation function of the speckle field at the Fourier transform plane is

given by

$$W(\mathbf{r_1}, \mathbf{r_2}, t) = \left\langle E^*(\mathbf{r_1}, t) E(\mathbf{r_2}, t) \right\rangle \qquad (2.21)$$

where $\langle . \rangle$ represents the ensemble average. Usually in experimental implementation the ensemble average is replaced with the time average by assuming that statistical field is stationary and ergodic in time (Goodman, 2000). However, recently significant practical interests are shown in the direction of replacing ensemble average with space average under the assumption of spatial stationarity and spatial ergodicity (Naik et al., 2011; R. K. Singh et al., 2013; Takeda et al., 2005; Takeda, 2013). Therefore the ensemble average can be replaced with space average on the assumption of spatial stationarity and ergodicity. So the autocorrelation function of the speckle field at the Fourier transform plane modifies to

$$\begin{aligned}
W(\mathbf{r_1}, \mathbf{r_2}) &= \left\langle E^*(\mathbf{r_1}) E(\mathbf{r_2}) \right\rangle_S \\
&= \left\langle E^*(\mathbf{r_1}) E(\mathbf{r_1} + \Delta\mathbf{r}) \right\rangle_S = W(\Delta\mathbf{r})
\end{aligned} \qquad (2.22)$$

where $\langle . \rangle_S$ represents the space average and $\Delta\mathbf{r} = \mathbf{r_2} - \mathbf{r_1}$ for a fixed time t. On substituting the value of $E(\mathbf{r})$ at two spatial points, Eq. (2.22) modifies to

$$\begin{aligned}
W(\Delta\mathbf{r}) &= \int E(\hat{\mathbf{r}}_1) E(\hat{\mathbf{r}}_1 + \Delta r) d\hat{\mathbf{r}}_1 \\
&= \int \left\{ \iint E(\hat{\mathbf{r}}_1) E(\hat{\mathbf{r}}_2) \exp\left[-j\left(\varphi(\hat{\mathbf{r}}_1) - \varphi(\hat{\mathbf{r}}_2) \right) \right] \times \exp\left[-j\frac{2\pi}{\lambda f}(\mathbf{r_2}.\hat{\mathbf{r}}_2 - \mathbf{r_1}.\hat{\mathbf{r}}_1) \right] d\hat{\mathbf{r}}_1 d\hat{\mathbf{r}}_2 \right\} d\mathbf{r_1} \\
&= \int \left\{ \iint E(\hat{\mathbf{r}}_1) E(\hat{\mathbf{r}}_2) \exp\left[-j\left(\varphi(\hat{\mathbf{r}}_1) - \varphi(\hat{\mathbf{r}}_2) \right) \right] \times \exp\left[-j\frac{2\pi}{\lambda f}((\mathbf{r_1} + \Delta r).\hat{\mathbf{r}}_2 - \mathbf{r_1}.\hat{\mathbf{r}}_1) \right] d\hat{\mathbf{r}}_1 d\hat{\mathbf{r}}_2 \right\} d\mathbf{r_1}
\end{aligned}$$

$$(2.23)$$

Taking into account of the delta function resulting from the spatial averaging in the observation plane given by $\int \exp\left[-i\frac{2\pi}{\lambda f}(\hat{\mathbf{r}}_2 - \hat{\mathbf{r}}_1).\mathbf{r_1} \right] d\mathbf{r_1} = \delta(\hat{\mathbf{r}}_2 - \hat{\mathbf{r}}_1)$ and taking $\hat{\mathbf{r}}_1 = \hat{\mathbf{r}}_2 = \hat{\mathbf{r}}$, Eq. (2.23) modifies to

$$W(\Delta\mathbf{r}) = \int E^*(\hat{\mathbf{r}}) E(\hat{\mathbf{r}}) \exp[-j\frac{2\pi}{\lambda f}\Delta\mathbf{r}.\hat{\mathbf{r}}] d\hat{\mathbf{r}} = \int I(\hat{\mathbf{r}}) \exp[-j\frac{2\pi}{\lambda f}\Delta\mathbf{r}.\hat{\mathbf{r}}] d\hat{\mathbf{r}} \qquad (2.24)$$

Eq. (2.24) transforms to the van Cittert-Zernike theorem. Eq. (2.24) states that the autocorrelation of the speckle field based on spatial averaging is related to the Fourier transform of the intensity at the rough scattering surface, which is equivalent to the speckle field autocorrelation in the free space geometry besides the non-stationary phase factor term in the free space geometry. This non-stationary phase factor term limits the perfect spatial stationarity condition of the scattered optical field. The use of an optical system with an ideal Fourier transform lens with focal length f and by considering that the lens has sufficiently large aperture, the perfect spatial stationarity in the scattered field can be realized by removing the non-stationary phase factor term (Takeda, 2013). Thus Eq. (2.24) provides the potential to shape the speckle pattern by a proper choice of the source structure term. The intensity of the source structure term controls the autocorrelation function and thereby a suitable selection of the source structure gives the potential to shape the statistical properties of the optical field in a desired fashion.

2.3.2 Autocorrelation of speckle intensity using spatial averaging

Correlation of intensity fluctuations were made use in a number of techniques and applications starting from the well known Hanbury Brown and Twiss intensity interferometer (Brown and Twiss, 1956, 1957). Autocorrelation of the speckle intensity based on spatial averaging is utilized in photon correlation holography technique to reconstruct three dimensional (3D) object information (Naik et al., 2011). The autocorrelation function of speckle intensity of the scattered field at the Fourier transform plane is given by

$$\Gamma(\Delta \boldsymbol{r}) = \left\langle I(\boldsymbol{r}_1) I(\boldsymbol{r}_2) \right\rangle_S \tag{2.25}$$

where $\left\langle . \right\rangle_S$ is spatial averaging under the assumption of spatial stationarity and spatial ergodicity. The covariance function of the speckle intensity can be defined as

$$C(\Delta \boldsymbol{r}) = \left\langle \Delta I(\boldsymbol{r}_1) \Delta I(\boldsymbol{r}_2) \right\rangle_S \tag{2.26}$$

where $\Delta I(\boldsymbol{r}) = I(\boldsymbol{r}) - \left\langle I(\boldsymbol{r}) \right\rangle$ represents the variation of intensity fluctuations from

its mean value and $I(\boldsymbol{r}) = |E(\boldsymbol{r})|^2$. The covariance function of intensity fluctuations is directly related to the modulus square of the complex correlation function of the scattered field and is given by

$$C(\Delta\boldsymbol{r}) = |W(\Delta\boldsymbol{r})|^2 \qquad\qquad (2.27)$$

The measurement of $C(\Delta\boldsymbol{r})$ can be utilized to recover the amplitude information as it is proportional to the modulus square of the complex coherence function which is used in the photon correlation holographic techniques.

2.4 Vectorial extension of the statistical properties

The vectorial representation of statistical properties of optical field attains significant interest after the unified theory of coherence and polarization of the optical field (Wolf, 2007). Coherence and polarization arise from the same statistical properties of a randomly fluctuating field. Coherence is the correlation of the electric field fluctuations at two points and polarization is the correlation of the vector component of the field at the same point. Recently a significant amount of attention has drawn in the direction of the controlled synthesis of coherence and polarization properties of the randomly fluctuating field and the potential of random speckle pattern as a versatile tool in controlled synthesis. The modulation of coherence and polarization by random phase screens and by using liquid crystal spatial light modulators were demonstrated in recent years (Ostrovsky et al., 2009; Shirai and Wolf, 2004). Vectorial extensions of coherence holography technique were introduced recently which have the potential to control and synthesize the vectorial random fields. (R. K. Singh et al., 2011, 2012). These techniques also provide new ways to apply the polarization fringes in recording and reconstruction of the information. In this section we focus on the extension of the concepts introduced in the previous section to its vectorial regime so that the coherence and polarization properties can be treated simultaneously.

Let us consider the case that the scattered field from a rough surface and the field is Fourier transformed using a lens of focal length f as shown in Fig. 2.3. The statistical properties of the random field at the Fourier transform plane is given by a 2×2 coherence-polarization (CP) matrix (Gori, 1998) given by

$$W(\mathbf{r}_1,\mathbf{r}_2;t_1,t_2) = \begin{pmatrix} \left\langle E_x^*(\mathbf{r}_1,t_1)E_x(\mathbf{r}_2,t_2) \right\rangle & \left\langle E_x^*(\mathbf{r}_1,t_1)E_y(\mathbf{r}_2,t_2) \right\rangle \\ \left\langle E_y^*(\mathbf{r}_1,t_1)E_x(\mathbf{r}_2,t_2) \right\rangle & \left\langle E_y^*(\mathbf{r}_1,t_1)E_y(\mathbf{r}_2,t_2) \right\rangle \end{pmatrix}$$

$$= \begin{pmatrix} W_{xx}(\mathbf{r}_1,\mathbf{r}_2;t_1,t_2) & W_{xy}(\mathbf{r}_1,\mathbf{r}_2;t_1,t_2) \\ W_{yx}(\mathbf{r}_1,\mathbf{r}_2;t_1,t_2) & W_{yy}(\mathbf{r}_1,\mathbf{r}_2;t_1,t_2) \end{pmatrix}$$

(2.28)

where $\langle . \rangle$ represents the ensemble average , $\mathbf{r}_1$ and $\mathbf{r}_2$ are the spatial points at the Fourier transform plane, $E_x(\mathbf{r},t)$ and $E_y(\mathbf{r},t)$ are the orthogonal polarization components for x and y polarization directions respectively and $W_{ij}(\mathbf{r}_1,\mathbf{r}_2,t_1,t_2) = \left\langle E_i^*(\mathbf{r}_1,t_1)E_j(\mathbf{r}_2,t_2) \right\rangle$ with $i=j=x$ or y. This CP matrix describes the spatial coherence and polarization properties as the 2×2 matrix contains the correlation of orthogonal polarization components $E_x(\mathbf{r},t)$ and $E_y(\mathbf{r},t)$. By using the assumption of spatial stationarity and spatial ergodicity we can replace the ensemble average with spatial average at a fixed time t.

The scattered speckle field at the Fourier transform plane is given by

$$E_i(\mathbf{r}) = \int E_i(\hat{\mathbf{r}})\exp(j\varphi_i(\hat{\mathbf{r}}))\exp[-j\frac{2\pi}{\lambda f}\mathbf{r}.\hat{\mathbf{r}}]d\hat{\mathbf{r}} \qquad (2.29)$$

where $\mathbf{r}$ and $\hat{\mathbf{r}}$ are the spatial co-ordinates at the respective planes and $E_i(\hat{\mathbf{r}})$ is the vector component of the field incident on the ground glass, $\varphi_i(\hat{\mathbf{r}})$ is the random phase introduced by the ground glass and λ is the wavelength of light incident on the ground glass.

The elements of CP matrix is given by

$$W_{ij}(\mathbf{r}_1,\mathbf{r}_2) = \left\langle E_i^*(\mathbf{r}_1)E_j(\mathbf{r}_2) \right\rangle_S = \int E_i^*(\mathbf{r}_1)E_j(\mathbf{r}_1+\Delta\mathbf{r})d\mathbf{r}_1 \qquad (2.30)$$

Here $\mathbf{r}_2 = \mathbf{r}_1 + \Delta\mathbf{r}$ and $\langle . \rangle_S$ represents the spatial average as a replacement of ensemble average. On substituting the value of $E_i(\hat{\mathbf{r}})$, Eq. (2.30) modifies to

$$W_{ij}(\Delta\mathbf{r}) = \int I_{ij}(\hat{\mathbf{r}})\exp[-j\frac{2\pi}{\lambda f}\Delta\mathbf{r}.\hat{\mathbf{r}}]d\hat{\mathbf{r}} \qquad (2.31)$$

Here $I_{ij}(\hat{\mathbf{r}}) = E_i^*(\hat{\mathbf{r}})E_j(\hat{\mathbf{r}})$ and the rough surface is assumed to be free from

23

birefringence so that $\varphi_i(\hat{r}) = \varphi_j(\hat{r})$. Also considered $\hat{r}_1 = \hat{r}_2 = \hat{r}$ and made use of the

delta function relation $\int \exp\left[-j\dfrac{2\pi}{\lambda f}(\hat{r}_2 - \hat{r}_1).r_1\right]dr_1 = \delta(\hat{r}_2 - \hat{r}_1)$.

Eq. 2.31 is regarded as the vectorial van Cittert-Zernike theorem based on spatial averaging (R. K. Singh et al., 2013).

The covariance function of the intensity correlation of the scattered field can be directly related to the elements of coherence-polarization (CP) matrix (Hassinen et al., 2011). Thus the covariance function of intensity fluctuations is given by

$$C(r_1, r_2) = \left\langle \Delta I(r_1)\Delta I(r_2)\right\rangle = \sum_{i,j}\left|W_{ij}(r_1, r_2)\right|^2 \tag{2.32}$$

where $i = j = x$ or y. The estimation of CP matrix elements gives a direct access to the generalized Stokes parameters (GSPs) (Korotkova and Wolf, 2005b) and is given by

$$
\begin{aligned}
S_0(r_1, r_2) &= W_{xx}(r_1, r_2) + W_{yy}(r_1, r_2)\\
S_1(r_1, r_2) &= W_{xx}(r_1, r_2) - W_{yy}(r_1, r_2)\\
S_2(r_1, r_2) &= W_{xy}(r_1, r_2) + W_{yx}(r_1, r_2)\\
S_3(r_1, r_2) &= i\left[W_{yx}(r_1, r_2) - W_{xy}(r_1, r_2)\right]
\end{aligned}
\tag{2.33}
$$

The knowledge of the CP matrix elements gives a direct access to coherence polarization properties of the randomly fluctuating field. The degree of coherence of the spatially fluctuating random field is given (R. K. Singh et al., 2013) by

$$\gamma(\Delta r) = \left(\frac{Tr\left[W^*(\Delta r)W(\Delta r)\right]}{Tr\,W(0)Tr\,W(0)}\right)^{1/2} \tag{2.34}$$

The spatial degree of polarization is given by

$$P(0) = \left(1 - \frac{4\det W(0)}{\left[TrW(0)\right]^2}\right)^{1/2} \tag{2.35}$$

Thus the extension of the concepts to vectorial regime has potential applications in the controlled synthesis of coherence and polarization properties of randomly

fluctuating field.

Shaping the laser speckle pattern by controlling the intensity source structure term have a direct impact on the correlation function thereby on the coherence and polarization properties of the scattered field. Thus the use of diffractive optical elements as source structures can synthesize the statistical properties of the scattered field in a desired fashion. Investigations on the developments of experimental techniques to shape and detect the speckle patterns using amplitude and intensity based interferometers are discussed in the following chapters

CHAPTER 3

SYNTHESIS OF LASER SPECKLE
AND ITS ANALYSIS BY USING
FIELD INTERFEROMETERS

The principles of optical interference have been studied for several years and a number of interferometry techniques were build on this basis. Due to high precision, the measurement techniques based on interferometry attains a great deal of attention in imaging, holography, astronomy etc. Developments in the areas of amplitude and intensity based interferometers opens up new ways to measure the correlation of the radiation fields. Advances in speckle interferometry and speckle holography techniques turn the attention to utilize the speckle pattern for various applications (Labeyrie, 1975; Tebaldi, 2004; Weigelt, 1978). Unified theory of coherence and polarization of randomly fluctuating field opens up new opportunities in treating coherence and polarization together in terms of cross spectral density matrix in space-frequency domain or beam coherence-polarization matrix in space-time domain (Gori, 1998; Wolf, 2007, 2003b). Coherence and polarization arise from the same statistical properties of randomly fluctuating field and are correlations among electric field fluctuations at two points and correlation of the vector component of the field at same point respectively. The potential of polarization sensitive interferometer and laser speckle pattern is pointed out in the vectorial coherence holography and Stokes holography (R. K. Singh et al., 2011, 2012; Takeda et al., 2005). In this chapter we focus on the synthesis of speckle pattern using diffractive optics element such as Dammann phase type grating and analysis of speckle pattern by developing field based/polarization sensitive interferometers thereby demonstrating experimental techniques to study the coherence and polarization properties of the statistically fluctuating random field. Initial part of the chapter discusses the design and development of field interferometer capable of single shot detection of complex field and the design of Dammann phase gratings. Later part discusses the use of Dammann grating and implementation of the field interferometer to generate one dimensional (1D) and two dimensional (2D) spatial coherence arrays.

3.1 Field based interferometers

Field based measurement techniques are widely used to detect the interference of complex fields and has the potential to measure the complex coherence function and fringe visibility. The significance of field interferometers is unavoidable in the cases of polarization sensitive measurement techniques and a significant number of works are devoted to develop the polarization sensitive interferometers (de Boer et al., 1999; D. Kim et al., 2014; R. K. Singh et al., 2014; Takeda et al., 2010). In order to obtain a single shot detection of complex field $\left(E(\mathbf{r})\right)$ we designed a field interferometer, which can work in scalar and vectorial domain by inserting angular multiplexing. Since the scalar case i.e. the field with uniform polarization (homogeneous) is a special case of more general vectorial situation. Therefore we initiate the work by developing experimental technique to detect single shot vectorial fields.

The designed experimental set up for the single shot detection of complex field using field interferometer is shown in Fig.3.1. A linearly polarized He-Ne laser beam of wavelength 632.8nm is collimated using a lens (L1) after passing through a spatial filter (SF) arrangement. The beam is made linearly 45^{0} polarized by passing through a half wave plate (HWP) and this beam is introduced into a specially designed polarization interferometer, which can simultaneously measure the orthogonal polarization components of the beam. Non polarizing beam splitter (BS1) splits the beam and the transmitted beam acts as the object arm and reflecting beam acts as the reference arm for the polarization interferometer.
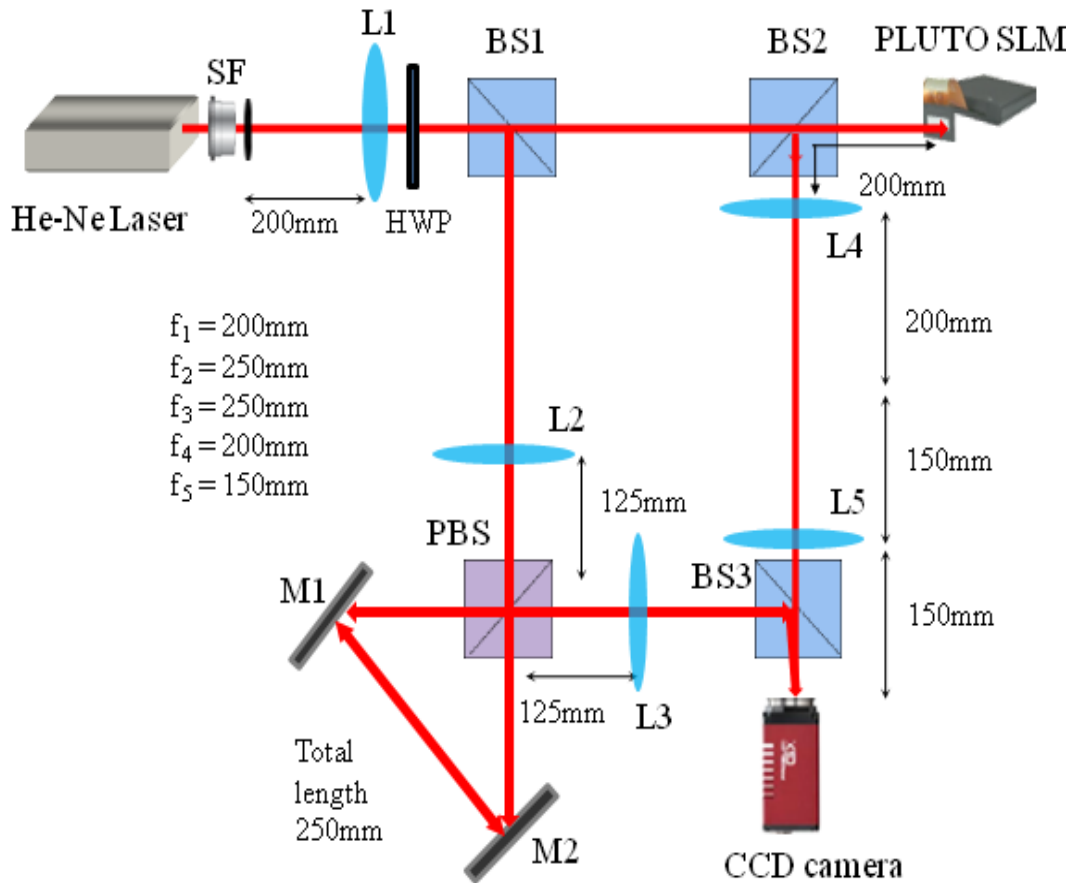
Figure 3.1: Experimental set up for single shot detection of complex field

The beam which is transmitting through BS2 gets reflected from PLUTO type phase SLM from the Holoeye (details of SLM is included in Appendix 3). The SLM is used to introduce the diffractive optical elements in experimental geometry that will discuss in detail in next section. The reflected beam from BS1 is allowed to pass through a telescopic setup, made of two lenses L2 and L3, and a triangular Sagnac geometry. This triangular geometry is used to achieve the angular multiplexing and uses a polarization beam splitter (PBS), which splits the beam into orthogonal polarization components. The tilts in the mirrors M1 and M2 are adjusted to provide different spatial carrier frequencies to the orthogonal polarization components in order to make two different interference fringes for orthogonal polarization components of the light coming from the SLM/object arm. The lenses L4 and L5 constitute a 4f geometry that allows a direct imaging of object in the SLM to the CCD camera. A schematic representation of angular multiplexing by triangular Sagnac geometry is shown in Fig. 3.2. The fringe pattern obtained from the polarization interferometer is captured using a CCD

monochrome camera (Prosilica GX2750). The CCD camera is 14-bit having resolution of 2750×2200 and a pixel pitch of 4.54µm.
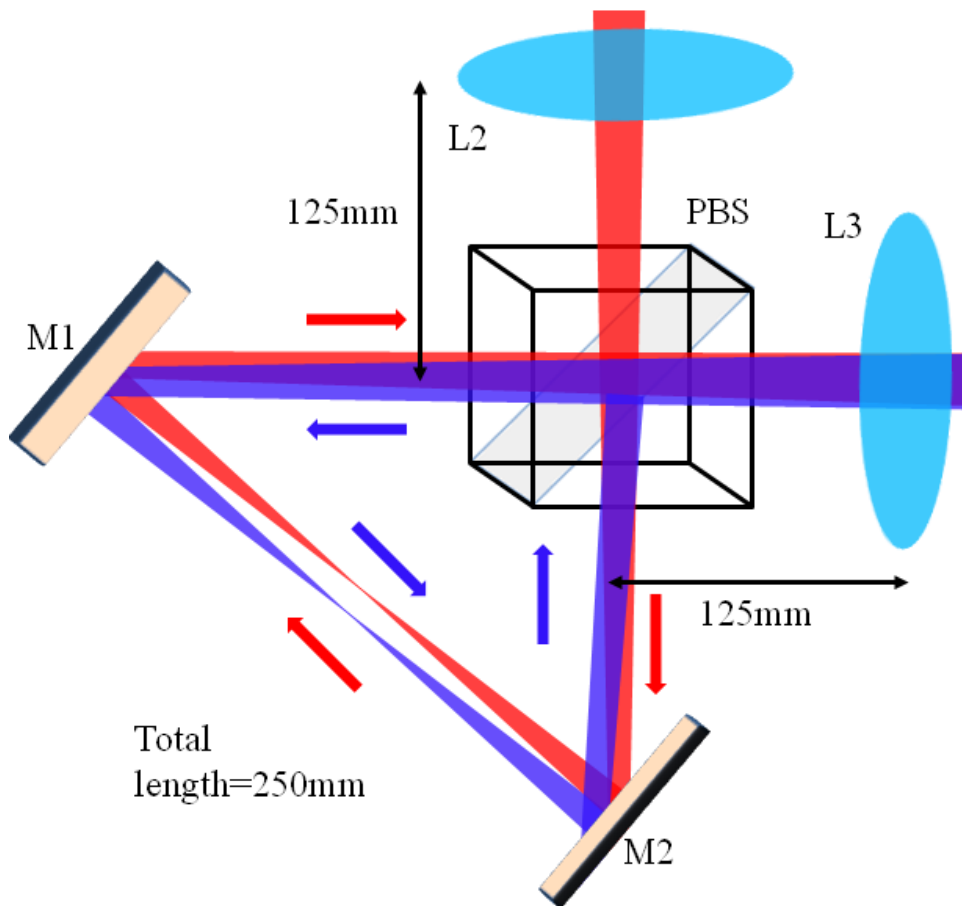
Figure 3.2: Triangular Sagnac geometry representing angular multiplexing

The captured fringe pattern consists of mesh of interference fringes with different spatial carrier frequency for each one of the orthogonal polarization components and is shown in Fig. 3.3(a). Fourier transform of the interference fringes results in the separation of the spectrum of orthogonal polarization components from the dc and its complex conjugate part. Fig. 3.3(b) shows the Fourier transform of the mesh like fringe pattern. The spectrum and its complex conjugate are separated from dc part (blocked in the Fig. 3.3(b) by making a rectangular window) for each of the orthogonal polarization component. The spectrum and its complex conjugate are separated in the Fourier domain diagonally as shown in Fig. 3.3(b) for each of the orthogonal polarization components according to the tilts provided in the mirrors M1 and M2.
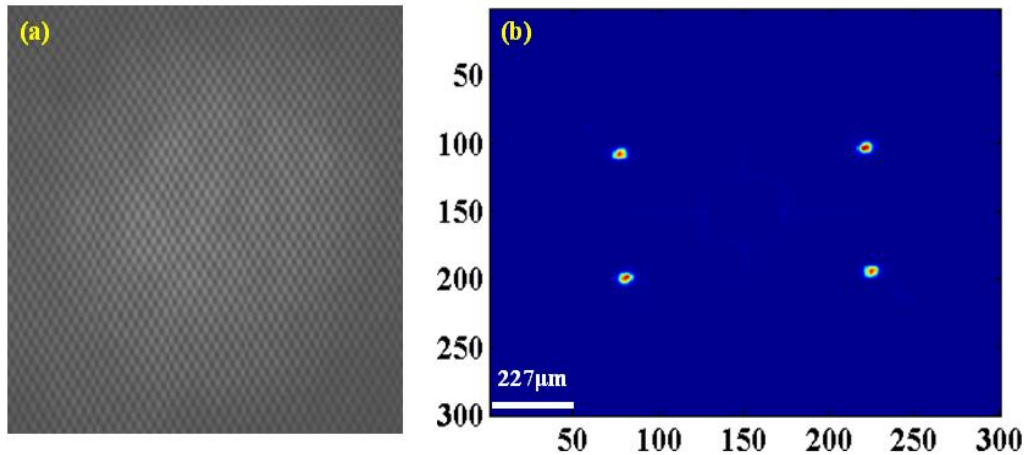
Figure 3.3: (a) Fringe pattern captured by the CCD camera (b) Fourier transform of the fringe pattern (values on X-axis and Y-axis represents the respective pixels).

3.2   Diffractive optical elements

The area of diffractive optics attains a wide attention to researchers due to its broad range of applications. The use of diffractive optical elements gives the flexibility to control and shape the laser beam according to the desired applications. The progresses in high performance dynamically addressable spatial light modulators provide the potential of real time implementation of the diffractive optical elements with computer controlled data. In this section we focus on the design of diffractive optical element such as Dammann phase type grating and its examination using polarization interferometer.

3.2.1 Design of Dammann phase type grating

The diffractive optical elements (DOEs) plays a major role in the tailoring of the beam for desired applications. Various approaches are developed for generation of the array or multiple diffraction spots and significant among which is Dammann grating (Dammann and Görtler, 1971). The Dammann grating is a binary phase grating whose phase transition points are optimized to create diffraction spots with equal intensities and several optimization techniques have been developed to design the Dammann grating with high diffraction efficiency (Krackhardt and Streibl, 1989; Zhou and Liu, 1995; Zou et al., 2010). Recently, a simple procedure to encode the Dammann grating onto a liquid crystal device is

31

presented (Moreno et al., 2010). We used this procedure to design one dimensional (1D) and two dimensional (2D) Dammann grating to encode in spatial light modulator. The grating period is divided into different segments having precise widths with phase shifts of either 0 or π rad. The desired number of diffracted orders of the grating depends on the selection of precise transition points (Zhou and Liu, 1995).

Let us consider a blazed grating with same period as that of the desired Dammann grating which is given as

$$g(x) = \exp\left[i\gamma x\right] \tag{3.1}$$

where $\gamma = \dfrac{2\pi}{d}$ with d as grating period. The Dammann grating function for this period can be represented as a Fourier series as

$$g'(x) = \sum_{n=-\infty}^{\infty} C_n \exp\left[in\gamma x\right] \tag{3.2}$$

Here the values of $|C_n|$ is selected in such a way that these are equal for a set of diffraction orders that will results in equal intensity spots. Using these concepts and by choosing precise transition points (Zhou and Liu, 1995), we designed 1D Dammann gratings with order three (period 80 pixels and total size 600 pixels with pixels size 8μm), order five (period 70 pixels and total size 600 pixels with pixels size 8μm) and order seven (period 95 pixels and total size 600 pixels with pixels size 8μm) and 2D Dammann grating of order three (period 80 pixels and total size 600 pixels with pixels size 8μm). Fig. 3.4 shows the designed 1D and 2D Dammann grating with different orders.
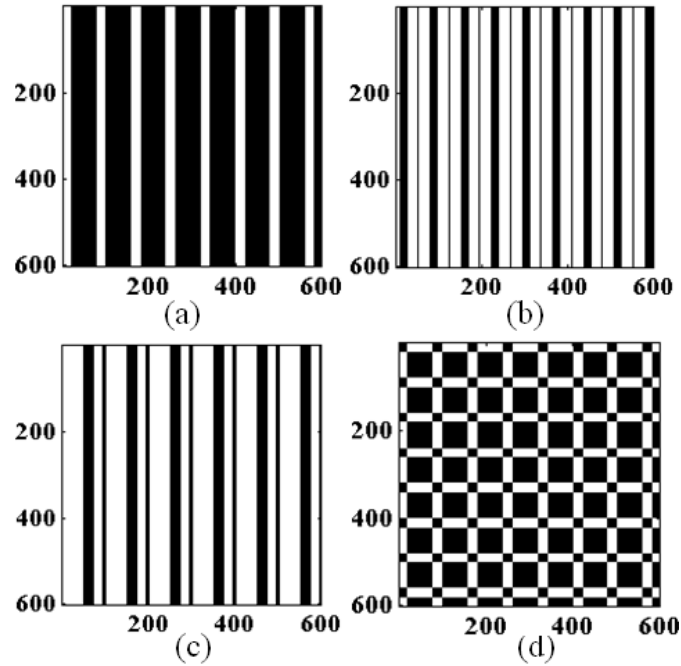
Figure 3.4: Designed Dammann gratings (a) 1D with order three (b) 1D with order five (c) 1D with order seven and (d) 2D with order three (values on X-axis and Y-axis shows the X-pixels and Y-pixels).

3.2.2 Evaluation of Dammann grating using polarization interferometer

The phase structure of the Damman gratings is examined using the polarization interferometer as shown in Fig. 3.1 and by using Fourier fringe analysis approach (Takeda et al., 1982). Role of the polarization interferometer in the analysis of the phase structure and diffraction pattern of the Dammann grating is discussed by utilizing the characteristic feature of Pluto-Holoeye phase only reflective type SLM. The SLM gives modulation to only one of the orthogonal component of the light beam illuminating the liquid crystal display. Physical dimension of the SLM is 1920×1080 with pixel size of 8μm. The designed Dammann grating is introduced in the experimental setup shown in Fig. 3.1 using PLUTO-Holoeye SLM. Fringe pattern obtained from the polarization interferometer is shown in Fig. 3.5(a). The mesh like fringe pattern shows interference of the orthogonal polarization components from the reference arm and the object arm without displaying grating structure in the SLM, i.e the SLM is acting as a mirror. Fig. 3.5(b) shows the effect of the introduction of third order Dammann grating, using SLM, in the interference mesh. Result of the Fourier transform of the interference pattern of Fig. 3.5(b) is shown in Fig. 3.5(c). Result

shows that the Dammann grating is encoded only in the one of the orthogonal polarization of the light, and presence of three spots of equal intensity, as highlighted in the circle of Fig. 3.5(c) for the demonstration purpose, in the frequency plane confirms presence of the grating in the light reflected from the SLM. On the other hand, light from other polarization component does not carry any feature of the grating. Inverse Fourier transform of the filtered spectra gives the phase of the field. This phase of the retrieved field in the grating encoded component gives the Dammann grating structure and is shown in Fig. 3.5(d). Phase variation in Fig. 3.5(d) is between 0 and π which confirms generation of a binary phase type grating.
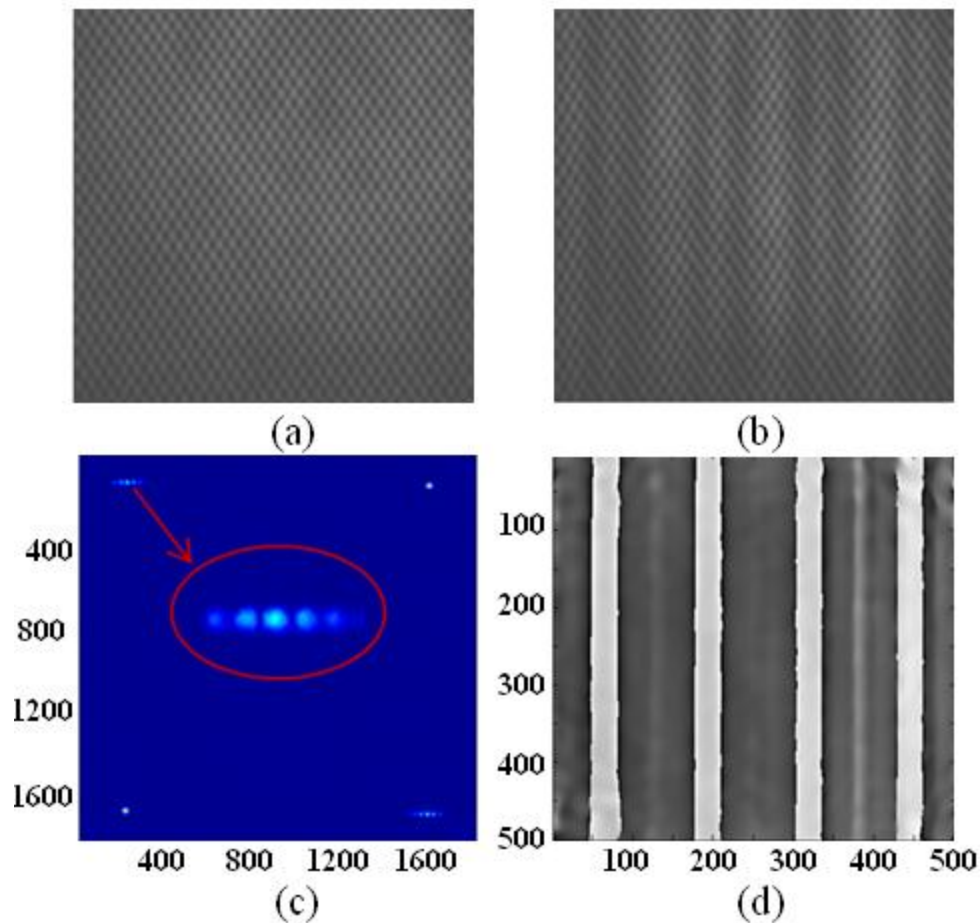
Figure 3.5: (a) Fringe pattern captured by the CCD camera without grating (b) fringe pattern captured by the CCD camera with Dammann grating of order three c) Fourier transform of the fringe pattern showing the diffraction spots and (d) Phase structure of the retrieved grating (values on X-axis and Y-axis shows the X-pixels and Y-pixels).

3.3 Generation of spatial coherence array using Dammann grating

Coherence is one of the fundamental properties of the light and plays important role in interference (Mandel, L Wolf, 1995). Efforts to control and synthesize the coherence has drawn significant attention due to its applications in the field of optical coherence tomography, lithography, profilometry and correlated imaging etc. Light with various kinds of coherence structure are proposed and analyzed in recent years and significant among which are the Gaussian–Schell model beam and spatially varying correlated beams (Chen et al., 2014; Cui et al., 2013; Lajunen and Saastamoinen, 2011; Liang et al., 2014; Tong and Korotkova, 2012b; F. Wang et al., 2013). Experimental generation of spatially varying correlated beams such as elliptical Gaussian Schell model beam and Lagurre Gaussian Schell model beam (F. Wang et al., 2013), rectangular cosine – Gaussian Schell model beam (Liang et al., 2014) and a special correlated partially coherent vector beam (Chen et al., 2014) were reported very recently. The formal analogy between coherence function and optical field has been used to develop an unconventional holography technique, called coherence holography, to shape the spatial coherence of light in a desired fashion (Takeda et al., 2005). In addition to coherence, polarization is another important parameter for the characterization of the light source. Conventionally, coherence and polarization are dealt separately. But recently, importance of the joint effect of polarization and coherence has been recognized and efforts have been made to unify the theory of coherence − polarization. This has played significant role in characterization of many features of the fluctuating electromagnetic field (Gori, 1998; Tervo et al., 2003; Wolf, 2007). Controlled synthesis of coherence of light in the vector fields has also drawn attention and leads to the demonstration of various sources (Santarsiero et al., 2009; Tong and Korotkova, 2012a). Recently, extension of the coherence holography to the vectorial domain is carried out and techniques such as vectorial coherence holography (VCH) (R. K. Singh et al., 2011) and Stokes holography (R. K. Singh et al., 2012) are developed. The VCH generates maximum correlation at the center, i.e. correlation of the fields at the same point, whereas the Stokes holography generates off-axis correlation maxima by making use of the polarization modulation. With emerging interests in the

spatially varying correlation field, developments of experimental methods to generate such beams are important. We propose a new technique for the generation of spatially varying correlation field with multiple high coherence points by using Dammann phase type grating. Though the generation of multiple diffraction spots using Dammann phase type grating is well known, no such attempts have been made to use the Dammann grating for the controlled synthesis of the statistical property of the light. This generates spatial coherence function with equal intensities in transverse correlation.

3.3.1 Shaping the speckle pattern with Dammann grating

Principle of the proposed technique lies in the vectorial van Cittert Zernike theorem which connects vectorial source structure with the spatial coherence – polarization of light in the far field (Gori et al., 2000; R. K. Singh et al., 2013). The Dammann grating is encoded into one of the orthogonal polarization components of the light to control the vectorial source structure thereby shaping the speckle pattern. The monochromatic laser beam encoded with phase grating transmits through a static scattering layer/ground glass which generates a scattered field. The scattered field is Fourier transformed using a lens of focal length f and a conceptual representation of the principle of the technique is shown in Fig 3.6.
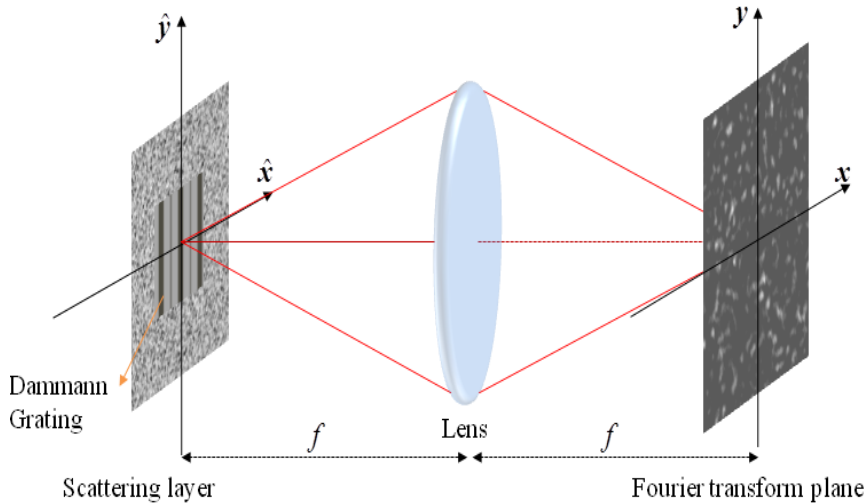
Figure 3.6: Conceptual representation of the principle of the technique

The scattered field on the Fourier transform plane, for a fixed time t, is given by

$$E_j(\boldsymbol{r}) = \int E_j(\hat{\boldsymbol{r}}) \exp\left(i\varphi_j(\hat{\boldsymbol{r}})\right) \exp\left[-i\frac{2\pi \boldsymbol{r}\hat{\boldsymbol{r}}}{\lambda f}\right] d\hat{\boldsymbol{r}} \qquad (3.3)$$

Here $E_j(\hat{r})$ is the complex field incident on the static ground glass with $j = x$ or y and one of the polarization components on the ground glass is encoded with phase grating $g(\hat{r}) = \exp(i\phi(\hat{r}))$ where $\phi(\hat{r})$ is the phase introduced by the Dammann grating, $\hat{r}$ and r are the position vectors in the ground glass plane and Fourier transform plane respectively. $\varphi_j(\hat{r})$ is the random phase introduced by the ground glass and λ is the wavelength of the laser beam. Note that the fixed time t is omitted for brevity. The statistical properties of the transverse vector field are determined by 2×2 coherence − polarization (CP) matrix defined (Gori, 1998)as:

$$W(\boldsymbol{r_1},\boldsymbol{r_2}) = \begin{pmatrix} \left\langle E_x^*(\boldsymbol{r_1})E_x(\boldsymbol{r_2}) \right\rangle & \left\langle E_x^*(\boldsymbol{r_1})E_y(\boldsymbol{r_2}) \right\rangle \\ \left\langle E_y^*(\boldsymbol{r_1})E_x(\boldsymbol{r_2}) \right\rangle & \left\langle E_y^*(\boldsymbol{r_1})E_y(\boldsymbol{r_2}) \right\rangle \end{pmatrix} \tag{3.4}$$

where $\langle...\rangle$ stands for the ensemble average and $E_j(\boldsymbol{r})$ with $j = x$ or y represents the scattered field at the Fourier transform plane. Though both temporal and space averages can be used as replacement of the ensemble average in the experimental implementation. Here, we rely on the space averaging under the assumption that the scattered field is stationary and ergodic in space. Even though the vectorial source (i.e.Dammann grating) which we used in our experiment is a non stationary source we can generate spatially stationary optical fields at observation plane by choosing an appropriate propagation kernel and a perfect optical system(Takeda, 2013). On considering $\boldsymbol{r_2} = \boldsymbol{r_1} + \Delta\boldsymbol{r}$, the elements of the CP matrix are given by

$$W_{jk}(\boldsymbol{r_1},\boldsymbol{r_2}) = \left\langle E_j^*(\boldsymbol{r_1})E_k(\boldsymbol{r_2}) \right\rangle = \left\langle E_j^*(\boldsymbol{r_1})E_k(\boldsymbol{r_1}+\Delta\boldsymbol{r}) \right\rangle \tag{3.5}$$

$$W_{jk}(\Delta\boldsymbol{r}) = \int E_j^*(\boldsymbol{r_1})E_k(\boldsymbol{r_1}+\Delta\boldsymbol{r})d\boldsymbol{r_1}$$

$$= \int \left\{ \iint E_j^*(\hat{r}_1)E_k(\hat{r}_2)\exp\left[-i\left(\varphi_j(\hat{r}_1)-\varphi_k(\hat{r}_2)\right)\right] \times \exp\left[-i\frac{2\pi}{\lambda f}(\boldsymbol{r_2}.\hat{r}_2 - \boldsymbol{r_1}.\hat{r}_1)\right]d\hat{r}_1 d\hat{r}_2 \right\}d\boldsymbol{r_1}$$

$$= \int \left\{ \begin{array}{l} \iint E_j^*(\hat{r}_1)E_k(\hat{r}_2) \times \exp\left[-i\left(\varphi_j(\hat{r}_1)-\varphi_k(\hat{r}_2)\right)\right] \\ \times \exp\left[-i\frac{2\pi}{\lambda f}((\boldsymbol{r_1}+\Delta\boldsymbol{r}).\hat{r}_2 - \boldsymbol{r_1}.\hat{r}_1)\right]d\hat{r}_1 d\hat{r}_2 \end{array} \right\}d\boldsymbol{r_1}$$

$$\tag{3.6}$$

where $W_{jk}(\boldsymbol{r_1},\boldsymbol{r_2})$ with $j,k = x$ or y represents the elements of the CP matrix. The ground glass is assumed to be free from birefringence and both polarization

components experiences same random phase distribution due to the non-birefringence property of the ground glass. i.e. $\varphi_j(\hat{r}) = \varphi_k(\hat{r})$. By making use of the relation $\int \exp\left[-i\dfrac{2\pi}{\lambda f}(\hat{r}_2 - \hat{r}_1).r_1\right]dr_1 = \delta(\hat{r}_2 - \hat{r}_1)$ the elements of the CP matrix given by Eq. (3.6) modifies to

$$W_{jk}(\Delta r) = \int E_j^*(\hat{r})E_k(\hat{r})\exp\left[-i\frac{2\pi}{\lambda f}\Delta r.\hat{r}\right]d\hat{r}$$
$$= \int I_{jk}(\hat{r})\exp\left[-i\frac{2\pi}{\lambda f}\Delta r.\hat{r}\right]d\hat{r}$$

(3.7)

where $I_{jk}(\hat{r}) = E_j^*(\hat{r})E_k(\hat{r})$ represents the intensity term at the static ground glass plane. Eq. (3.7) transforms to vectorial van Cittert-Zernike theorem for electromagnetic field based on spatial averaging. Note that $I_{jk}(\hat{r}) = E_j^*(\hat{r})E_k(\hat{r})$ is a complex quantity which carries Dammann phase type grating imposed on the ground glass plane. When $j = k$, the phase of the complex field cancels out. Whereas, for $j \neq k$, the information is preserved and $I_{jk}(\hat{r})$ becomes a complex quantity which comes into play to control the spatial coherence function. This feature of $I_{jk}(\hat{r})$ is exploited to encode the Dammann grating into the field and generate desired array of the high spatial coherence points.

3.3.2 Experiment

An experimental setup designed for the generation and detection of the complex scattered polarized field is shown in Fig. 3.7. A linearly polarized He-Ne laser beam of wavelength 632.8nm is collimated using a lens L1 after passing through a spatial filter arrangement (SF1). The collimated beam passes through a half wave plate that converts the beam in to a linearly 45^0 polarized beam and the beam is introduced into a specially designed polarization interferometer, which can simultaneously measure the complex orthogonal polarization components of the beam. The transmitted beam from the non polarizing beam splitter (BS1) act as the grating arm and the reflected beam from the beam splitter act as the reference arm of the polarization interferometer. This beam is allowed to pass through a telescopic setup made of two lenses L2 and L3 and a triangular Sagnac polarization interferometer used to achieve the angular multiplexing. The

polarization beam splitter (PBS) splits the beam into two orthogonal polarization components and the mirrors M1 and M2 are adjusted in such a way that it provides different tilts to the orthogonal polarization components. The beam which is transmitted from BS1 passes through the beam splitter BS2 and illuminates the PLUTO spatial light modulator (SLM) from Holoeye (PLUTO–VIS) with 1920×1080 resolution with a pixel pitch of 8.0 µm. The size of the beam which falls on SLM is of 4mm diameter and this SLM introduces a phase variation to only one of the orthogonal polarization component of the incident electric field. The SLM introduces the designed Dammann phase grating into the beam and the complex field encoded with grating is imaged onto the ground glass plane by 4*f* geometry with lenses L4 and L5. The scattered field from the static ground glass is Fourier transformed using a lens L6 that creates a far field at its focal plane. The scattered field from the ground glass and the orthogonal polarization components of the field from the reference arm of the interferometer are combined using a beam splitter BS3 and superimposed on the focal plane of the lens L6. A set of interference fringes along with speckle field with different spatial carrier frequency is generated for each orthogonal polarization component. The speckle pattern obtained from the polarization interferometer is captured using a CCD monochrome camera (Prosilica GX 2750). The CCD camera is 14-bit, with 2750×2200 pixels and a pixel pitch of 4.54µm (details of CCD camera is included in Appendix 3).
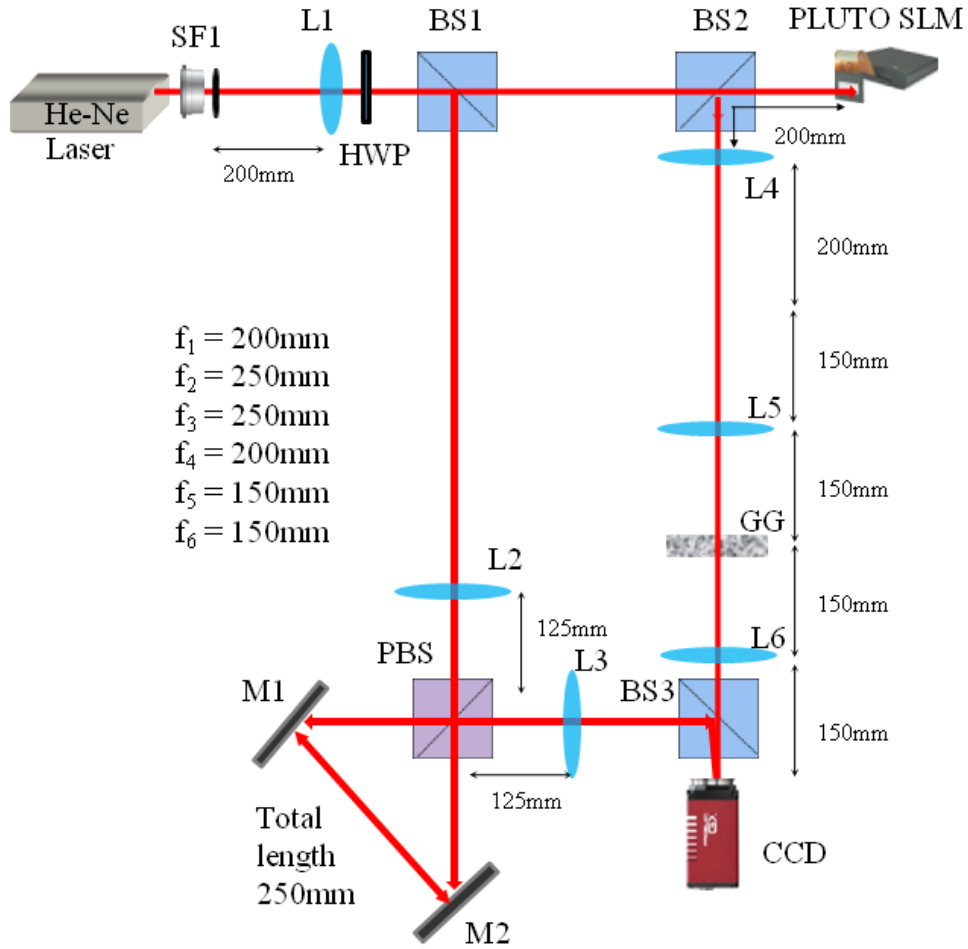
Figure 3.7: Experimental setup for the generation and detection of the complex field of the polarization speckle

We designed Dammann phase type gratings of 1D with fifth order and seventh order and 2D with third order that are shown in Fig. 3.4(a), 3.4(b) and 3.4(c). The designed gratings were introduced in the experimental setup using PLUTO SLM as shown in Fig. 3.7. In our proposed work, this grating shape the vectorial source structure and consequently controls the spatial coherence function in the far field. The complex scattered field of the orthogonal polarization components were detected by the technique for spatial frequency multiplex polarization interferometry and Fourier fringe analysis (Naik, Singh, et al., 2012). By using Fourier fringe analysis technique the complex field for each polarization component of the scattered field is obtained. Under the condition of spatial ergodicity of the scattered field, elements of the CP matrix of the scattered field is obtained by space averaging (R. K. Singh et al., 2011).

3.3.3 Results and Discussion

The experimental results of the amplitudes of orthogonal polarization components of the scattered field and elements of CP matrix of the field are shown in Figs.3.8 ,3.9 and 3.10 for the Dammann phase grating of 1D with order five and seven and 2D with order three respectively. The amplitude distribution of the speckle field of each polarization component of the scattered field in which Dammann phase type grating of order five is encoded in the beam using SLM is shown in Fig. 3.8(a) and 3.8(b). The elements of CP matrix are controlled by the vectorial source structure term $I_{jk}(\hat{r})$ as expressed by Eq. (3.7). Let us consider the case when $j = k = x$ or y, i.e. $I_{xx}(\hat{r})$ or $I_{yy}(\hat{r})$. Due to the complex characteristic of the $I_{jk}(\hat{r})$, the same components of the scattered field will give $I_{jk}(\hat{r}) = E_j^*(\hat{r})E_j(\hat{r}) = |E_j(\hat{r})|^2$. This source distribution consequently results in $W_{xx}(\Delta r)$ and $W_{yy}(\Delta r)$ elements of CP matrix with central intensity point as shown in Fig. 3.8(c) and 3.8(d) for the case of Dammann phase type grating of order five. The central peak of Fig. 3.8(c) and 3.8(d) is explained by Eq. (3.7) which is nothing but Fourier transform of uniform aperture. For the case when $j \neq k$, the vectorial source structure term in Eq. (3.7) gives $I_{jk}(\hat{r}) = E_j^*(\hat{r})E_k(\hat{r})$ i.e. $I_{xy}(\hat{r})$ or $I_{yx}(\hat{r})$ which are complex terms. The correlation of orthogonal components of the scattered field will retain a phase grating effect since one of the components of the scattered field in our experimental arrangement is encoded with a Dammann grating as a result of the characteristic feature of the PLUTO phase only SLM. i.e. $I_{jk}(\hat{r}) = E_j^*(\hat{r})E_k(\hat{r}) = |E(\hat{r})|^2 \exp(-i(\varphi_j(\hat{r}) - \varphi_k(\hat{r}))) \exp(i\phi(\hat{r}))$, where the amplitudes $|E_j(\hat{r})| = |E_k(\hat{r})| = |E(\hat{r})|$. Since $\varphi_j(\hat{r}) = \varphi_k(\hat{r})$, the vectorial source structure term modifies to $I_{jk}(\hat{r}) = |E(\hat{r})|^2 \exp(i\phi(\hat{r}))$. This results into a spatial coherence comb generation in $W_{xy}(\Delta r)$ and $W_{yx}(\Delta r)$ components of the CP matrix as shown in Fig. 3.8(e) and 3.8(f) for the Dammann phase type grating of order five. The spacing between the spatial coherence points can be controlled by the period of phase grating used to shape the vectorial source structure.
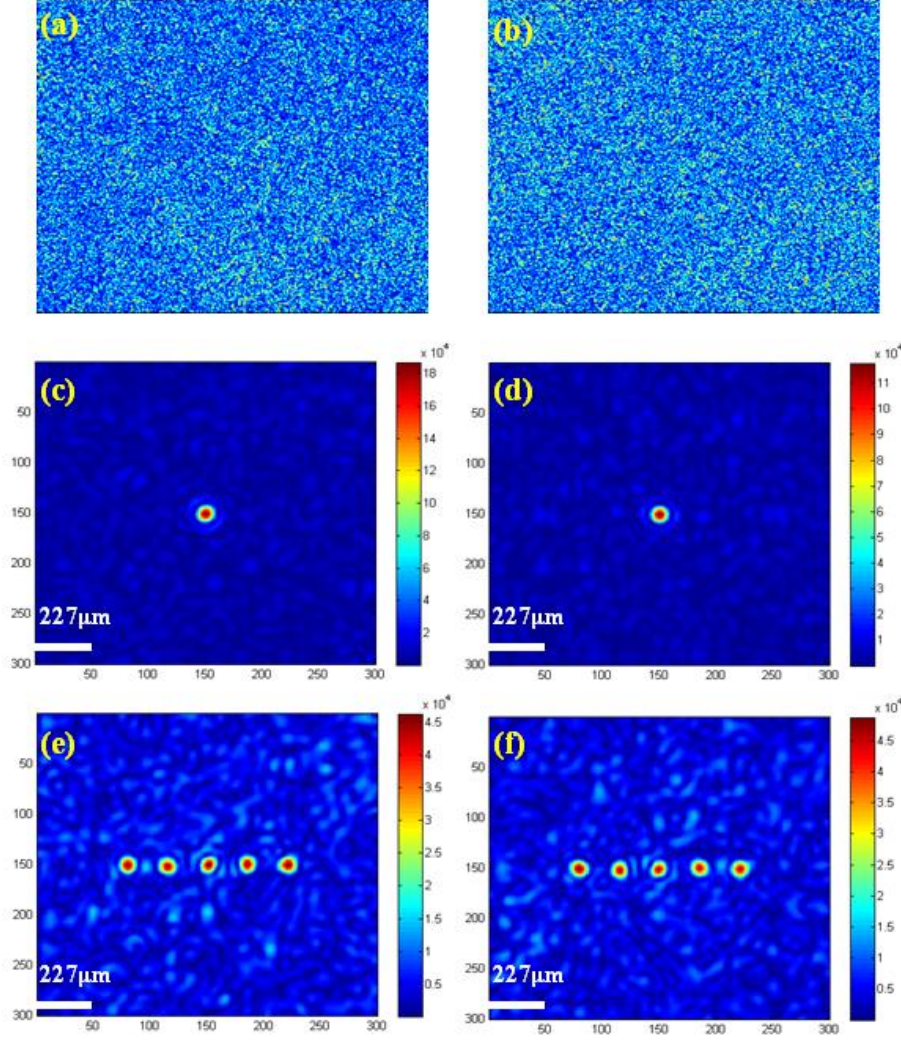
Figure 3.8: Experimental results: (a) & (b) Speckle field of orthogonal polarization components. Amplitude distribution of elements of CP matrix for a fifth order Dammann grating: (c) $W_{xx}(\Delta r)$ (d) $W_{yy}(\Delta r)$ (e) $W_{xy}(\Delta r)$ (f) $W_{yx}(\Delta r)$. The values on X-axis and Y-axis represent the X-pixels and Y-pixels respectively at the CCD plane and the color bar represent the intensity.

We use Dammann phase type grating of order seven to generate a spatial coherence comb of 1-D array of seven equal amplitude points in a similar procedure mentioned previously. The amplitude distribution of the speckle field of each polarization component is shown in Fig. 3.9(a) and 3.9(b). The result of spatial averaging of the same components of the scattered field give $W_{xx}(\Delta r)$ and $W_{yy}(\Delta r)$ elements of the CP matrix as shown in Figs. 3.9(c) and 3.9(d) respectively. Spatial averaging of orthogonal polarization components generate a spatial coherence comb in $W_{xy}(\Delta r)$ and $W_{yx}(\Delta r)$ elements of the CP matrix and results are shown in Figs. 3.9(e) and 3.9(f) respectively. Here the phase grating of order seven shapes the vectorial source structure and generates 1-D array of

42

spatial coherence points with spacing corresponding to the period of phase grating.
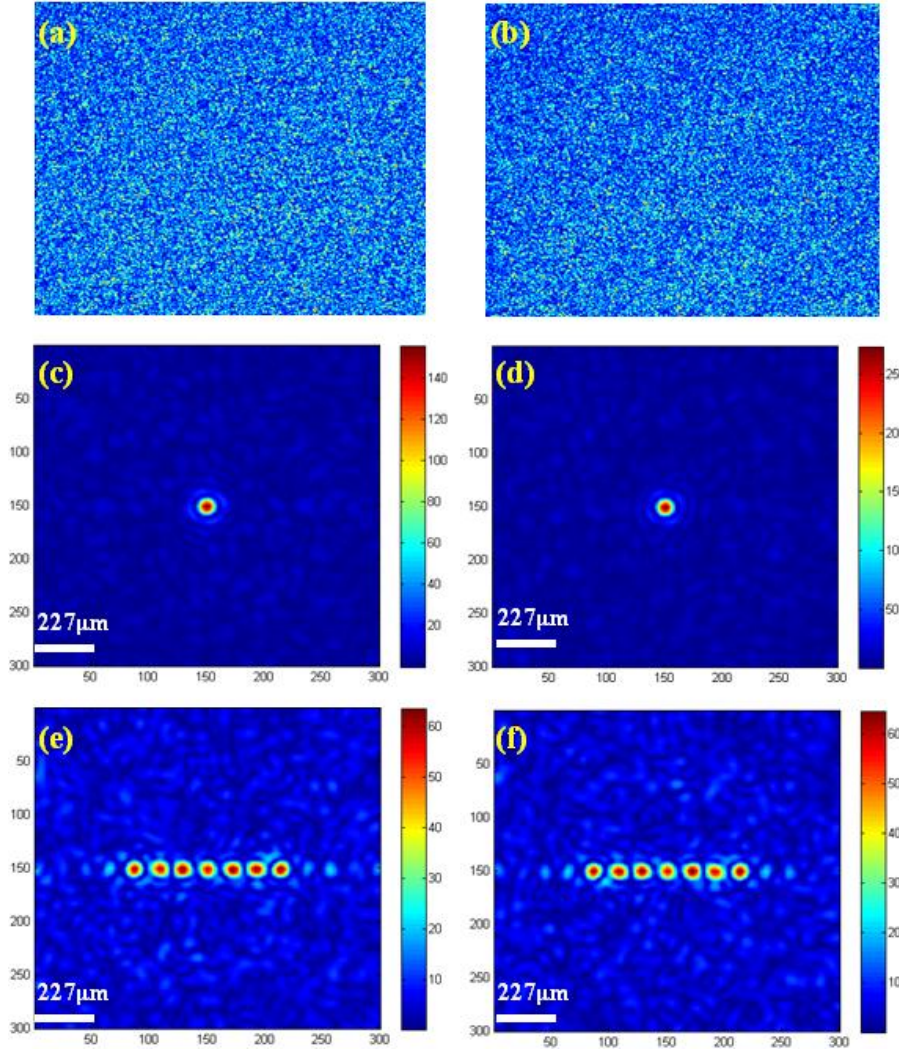
Figure 3.9: Experimental results: (a) & (b) Speckle field of orthogonal polarization components. Amplitude distribution of elements of CP matrix for a seventh order Dammann grating: (c) $W_{xx}(\Delta r)$ (d) $W_{yy}(\Delta r)$ (e) $W_{xy}(\Delta r)$ (f) $W_{yx}(\Delta r)$. The values on X-axis and Y-axis represent the X-pixels and Y-pixels respectively at the CCD plane and the color bar represent the intensity.

In order to generate a 2D array of spatial coherence points we designed 2D Dammann grating of order three and is utilized to shape the vectorial source structure. The CP matrix elements are described by the same procedure described previously. The amplitude distribution of the speckle field of each polarization component is shown in Fig. 3.10(a) and 3.10(b). The result of spatial averaging of the same components of the scattered field give $W_{xx}(\Delta r)$ and $W_{yy}(\Delta r)$ elements of the CP matrix as shown in Figs. 3.10(c) and 3.10(d) respectively. Spatial

averaging of orthogonal polarization components generate a 3×3 spatial coherence array in $W_{xy}(\Delta \boldsymbol{r})$ and $W_{yx}(\Delta \boldsymbol{r})$ elements of the CP matrix and results are shown in Figs. 3.10(e) and 3.10(f) respectively. The use of 2D Dammann phase gratings gives the potential to shape the vectorial source structure and thereby generating a 2D spatial coherence array in the off diagonal elements of the CP matrix.
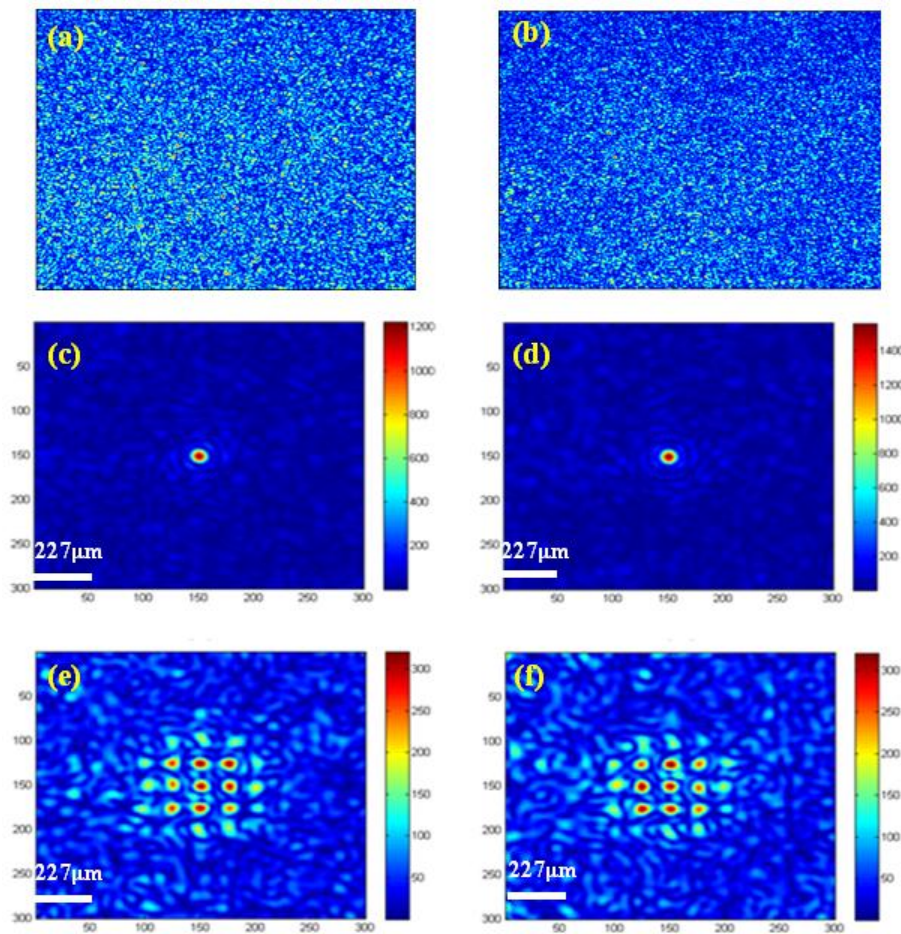
Figure 3.10: Experimental results: (a) & (b) Speckle field of orthogonal polarization components. Amplitude distribution of elements of CP matrix for a third order 2D Dammann grating: (c) $W_{xx}(\Delta \boldsymbol{r})$ (d) $W_{yy}(\Delta \boldsymbol{r})$ (e) $W_{xy}(\Delta \boldsymbol{r})$ (f) $W_{yx}(\Delta \boldsymbol{r})$. The values on X-axis and Y-axis represent the X-pixels and Y-pixels respectively at the CCD plane and the color bar represent the intensity.

3.4 Conclusion

We have experimentally demonstrated a new technique for the generation of spatially varying coherence by demonstrating generation of 1D and 2D spatial

44

coherence arrays with the use of Dammann phase type gratings. The development of field based interferometer using triangular Sagnac geometry allows the single shot detection of the complex scattered field and thereby allow to determine all four elements of CP matrix elements from single detection. Our technique offers a new method to synthesis and analysis of laser speckle pattern and consequently controls the coherence and polarization properties of the fluctuating random field.

CHAPTER 4

ANALYSIS OF LASER SPECKLE
USING INTENSITY
INTERFEROMETERS

Invention of intensity correlation interferometer by Hanbury Brown and Twiss brought a major breakthrough in the correlation based techniques (Brown and Twiss, 1957). Complex field interference methods are useful to measure the two point complex coherence function but also sensitive to fluctuations. On the other hand the intensity interferometer is less sensitive to the fluctuations and measures the fourth order correlation or intensity correlation of the statistically fluctuating random field. For the Gaussian random field, the cross-covariance of the intensity distribution, i.e. fourth order correlation, is proportional to modulus square of the second order correlation. Since the correlation is done electronically after detection of photons as intensity, the intensity interferometers are simpler and free from instability in phase. Usually this interferometer is applied to the temporally fluctuating field; however recent interests are in the direction of using it in spatially fluctuating field where the fluctuations in amplitude and phase for two different spatial points is taken into account. In this section we propose and demonstrate application of intensity based interferometer for analysis of the spatially fluctuating random field. This is carried out by considering different synthesis applications. Firstly we focus on the use of fourth order correlation in combination with speckle holography technique to retrieve the complex coherence function from spatially fluctuating random field. Later we demonstrate the generation of singular point array in the coherence function of spatially fluctuating random field. The random field is generated by three independent random sources places in certain geometry. Finally we extended the idea to vectorial domain by describing a new experimental technique for the determination of generalized Stokes parameters (GSP) or CP matrix elements and demonstrate its application in the synthesis of statistical properties of light field. Note that GSPs are two point extensions of the Stokes parameters and are written as combination of different CP matrix elements.

4.1 Retrieval of complex coherence function using speckle holography

Intensity based correlation approach of the light field gain significant attention in recent years due to its potential applications in characterization of the optical field. Correlation of the field at two different points, known as coherence function, is a complex quantity. This complex coherence function can be measured using interference of the complex fields and modulus of the coherence function is related to the interference fringe visibility. Phase structure of the coherence function is also important in the statistical optics, and in recent developments it is demonstrated that incoherent illumination of a hologram reconstructs the 3-D object as distribution of the spatial complex coherence function (Naik, Ezawa, et al., 2012; Takeda et al., 2005). Complex field interference methods are useful to measure the two point complex coherence function but also sensitive to fluctuations. On the other hand intensity interferometer is less sensitive to the fluctuations. For the Gaussian random field, the cross-covariance of the intensity distribution, i.e. fourth order correlation, is proportional to modulus square of the second order correlation (Mandel and Wolf, 1995). Invention of intensity correlation interferometer by Hanbury Brown and Twiss brought a major breakthrough in the correlation based techniques (Brown and Twiss, 1956). Analysis of the two-detector intensity interferometer was first done by using a classical description of the radiation field. A quantum mechanical interpretation was later given by Glauber (Glauber, 1963).

Propagation of a coherent laser beam through scattering medium generates spatially fluctuating Gaussian field. It is demonstrated that two point correlation of the speckle field in the far field is related to the source structure by a Fourier transform. Mathematically this is similar to the far field diffraction from an incoherent source structure and that has the same spatial structure as the coherent source (Naik et al., 2011; Takeda, 2013). Two point intensity correlation of the speckle field measures modulus square of the complex coherence function but phase information is lost (Naik et al., 2011). Phase structure of the complex coherence function can be retrieved using higher order intensity correlations and

phase retrieval techniques (Barakat, 2000; Bartelt et al., 1984; Ebstein, 1991; Gamo, 1963; Gong and Han, 2010; Marathay et al., 1994). A method based on the two point intensity correlation is also presented for recovery of the modulus and phase of the spatial coherence function of a laser speckle (Ebstein, 1991). In this approach, a random field is measured in at least two separated sub apertures. One is to measure the intensity and relative phase of the light amplitude across a small distance and second aperture is to measure intensity of the speckle. In this section we describe an alternative method to retrieve the complex coherence of the laser speckle by using the intensity correlation with help of off-axis holography technique. Significance of this work lies with its ability to recover the complex coherence of the laser speckle from a single shot intensity distribution. To apply the holography principle, an independent reference speckle with known coherence function is generated and coherently mixed with 'object' speckle field. Here 'object' speckle field corresponds to the random fluctuating field for which spatial coherence needs to be measured. The reference speckle field with known coherence function is synthesized by illuminating an independent scattering surface with an off-axis coherent point source. The coherence function of the reference speckle is a complex quantity with uniform amplitude and linear phase term. The linear phase term of the reference coherence function is attributed to the off-axis illumination and this can be explained by the van Cittert-Zernike theorem. Two speckles, namely object and reference, are coherently superimposed and cross-covariance of intensity distribution of the resultant speckle field is digitally obtained. Here cross-covariance of the intensity is obtained by using spatial averaging by taking advantage of the spatial ergodicity. Interference fringes exist in the cross-covariance of the intensity of the resultant speckle. The complex coherence of the object speckle field is retrieved using the Fourier fringe analysis. Application of this method is demonstrated by experimentally measuring the complex coherence of two different speckle fields at the Fourier plane and accuracy of results is also examined by comparing experimental results with the analytical one.

4.1.1 Complex coherence function from intensity correlation

Illumination of a scattering layer/ground glass by a monochromatic laser beam generates a speckle field. A schematic representation of the generation of speckle

field is shown in Fig. 4.1. The scattered field ($E_O(\boldsymbol{r})$) on the Fourier transform plane for fixed time t, is given by:

$$E_O(\boldsymbol{r}) = \int E_O(\hat{\boldsymbol{r}}) \exp\left(i\varphi(\hat{\boldsymbol{r}})\right) \exp\left[-i\frac{2\pi \boldsymbol{r}\cdot\hat{\boldsymbol{r}}}{\lambda f}\right] d\hat{\boldsymbol{r}} \qquad (4.1)$$

Here, $E_O(\hat{\boldsymbol{r}})$ is the field incident on the ground glass and $\hat{\boldsymbol{r}}$ is position vector on the ground glass plane, $\varphi(\hat{\boldsymbol{r}})$ a random phase introduced by the ground glass, λ the wavelength of the light, f the focal length of the Fourier transforming lens, and fixed time is omitted for brevity. Suffix O stands for 'object' speckle and this is used to distinguish from the reference speckle which will be defined later.
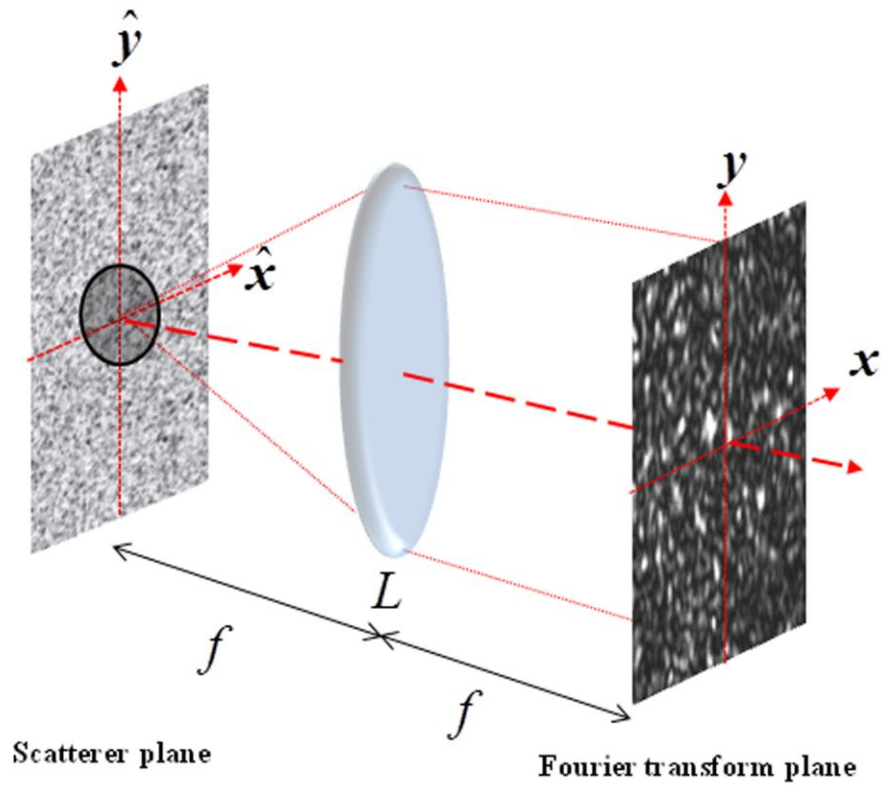
Figure 4.1: Schematic representation of the technique

Considering the situation of stationarity and ergodicity in space for the scattered field at the Fourier transforming plane and noting that $\boldsymbol{r}_2 = \boldsymbol{r}_1 + \Delta\boldsymbol{r}$, a second order correlation property of the speckle field is obtained by spatial averaging with respect to variable $\boldsymbol{r}_1$ over the observation plane, and given (Takeda, 2013) as:

$$W_O(\Delta r) = \left\langle E_O^*(r_1)E_O(r_2) \right\rangle_S = \int E_O^*(r_1)E_O(r_1 + \Delta r)dr_1$$

$$= \int |E_O(\hat{r})|^2 \exp\left[-i\frac{2\pi}{\lambda f}\Delta r \cdot \hat{r}\right]d\hat{r} \tag{4.2}$$

In Eq. (4..2), the integration taken over the observation plane for spatial averaging results in a delta function $\int \exp\left[\dfrac{-2\pi i(\hat{r}_2 - \hat{r}_1).r_1}{\lambda f}\right]dr_1 \propto \delta(\hat{r}_2 - \hat{r}_1)$ and $\langle .. \rangle_S$ is the spatial average as a replacement of the ensemble average for stationary spatially fluctuating field. For a random field obeying Gaussian statistics, there exist a relation between the fourth order correlation and second order correlation, and this is given as

$$C_O(\Delta r) = \left\langle \Delta I_O(r)\Delta I_O(r + \Delta r) \right\rangle_S \propto |W_O(\Delta r)|^2 \tag{4.3}$$

where $C_O(\Delta r)$ is cross- covariance of the intensity $I_O(r)\left[= E_O^*(r)E_O(r)\right]$ and $\Delta I_O(r) = I_O(r) - \langle I_O(r) \rangle$ is the spatial fluctuation of the intensity with respect to its average value. As in Eq. (4.3) the cross – covariance is proportional to modulus square of the second order correlation and phase information is lost. However, this lost phase of the complex coherence function can be retrieved by using a known reference complex coherence function with the help of off- axis holography (Mehtha, 1968). To apply this, we generate a reference speckle pattern and spatial coherence of this field is given as

$$W_R(\Delta r) = \int circ\left(\frac{\hat{r} - \hat{r}_g}{a}\right)\exp\left[-i\frac{2\pi}{\lambda f}\Delta r \cdot \hat{r}\right]d\hat{r} \tag{4.4}$$

Here $\hat{r} = \hat{r}_g$ represents lateral shift of the reference beam of radius 'a' on the ground glass plane. Let us consider coherent addition of the object and reference speckles, the intensity at the Fourier plane is given as

$$I(r) = |E(r)|^2 = |E_O(r) + E_R(r)|^2 \tag{4.5}$$

where $E_R(r)$ is the speckle due to the reference source. Since the resultant intensity is a speckle hologram, the mutual coherence function corresponding to it should

have contributions arising from $|E_O(\boldsymbol{r})|^2$, $|E_R(\boldsymbol{r})|^2$ and the mixed term. The coherence function of the resultant speckle field is

$$
\begin{aligned}
W(\Delta\boldsymbol{r}) &= \left\langle E^*(\boldsymbol{r}_1)E(\boldsymbol{r}_1 + \Delta\boldsymbol{r}) \right\rangle_S \\
&= \left\langle \{E_O(\boldsymbol{r}_1) + E_R(\boldsymbol{r}_1)\}*\{E_O(\boldsymbol{r}_1 + \Delta\boldsymbol{r}) + E_R(\boldsymbol{r}_1 + \Delta\boldsymbol{r})\} \right\rangle_S
\end{aligned}
\tag{4.6}
$$

Since the scatterers used to realize the object- and reference beams are different, we are justified in taking the contribution from the mixed term zero, i.e. $\left\langle E_O^*(\boldsymbol{r}_1)E_R(\boldsymbol{r}_1 + \Delta\boldsymbol{r}) \right\rangle = 0$. Therefore the resultant mutual coherence function for the resultant intensity is

$$
W(\Delta\boldsymbol{r}) = W_O(\Delta\boldsymbol{r}) + W_R(\Delta\boldsymbol{r})
\tag{4.7}
$$

This new holography technique offers solution to the phase problem. The fourth order intensity correlation of the resultant speckle field is given as

$$
\begin{aligned}
\left\langle \Delta I(r)\Delta I(r + \Delta\boldsymbol{r}) \right\rangle &= |W(\Delta\boldsymbol{r})|^2 \\
&= |W_O(\Delta\boldsymbol{r})|^2 + |W_R(\Delta\boldsymbol{r})|^2 + W_O^*(\Delta\boldsymbol{r})W_R(\Delta\boldsymbol{r}) + W_O(\Delta\boldsymbol{r})W_R^*(\Delta\boldsymbol{r})
\end{aligned}
\tag{4.8}
$$

Here $W_O^*(\Delta\boldsymbol{r})$ and $W_R^*(\Delta\boldsymbol{r})$ denote complex conjugate of the coherence functions of the random scattered fields engineered by object and reference source respectively. Interference fringes exist in the cross-covariance of the intensity of the resultant speckle. This interference fringe results due to superposition of the complex coherence of the object and reference speckle fields. The off-axis geometry for superposition of the two speckle fields is important for experimental implementation of the proposed idea. This geometry modulates fringes of the intensity correlation with properly selected carrier frequency in such a way that Fourier spectrum of the 'object' coherence field gets separated from the central background or dc. The complex coherence of the object speckle field is retrieved using the Fourier transform.

4.1.2 Experiment

We developed an experimental strategy equipped with an off- axis holography technique to retrieve the complex coherence function of the speckle fields. The experimental geometry to retrieve the complex coherence function using off-axis holography technique is shown in Fig.4.2.
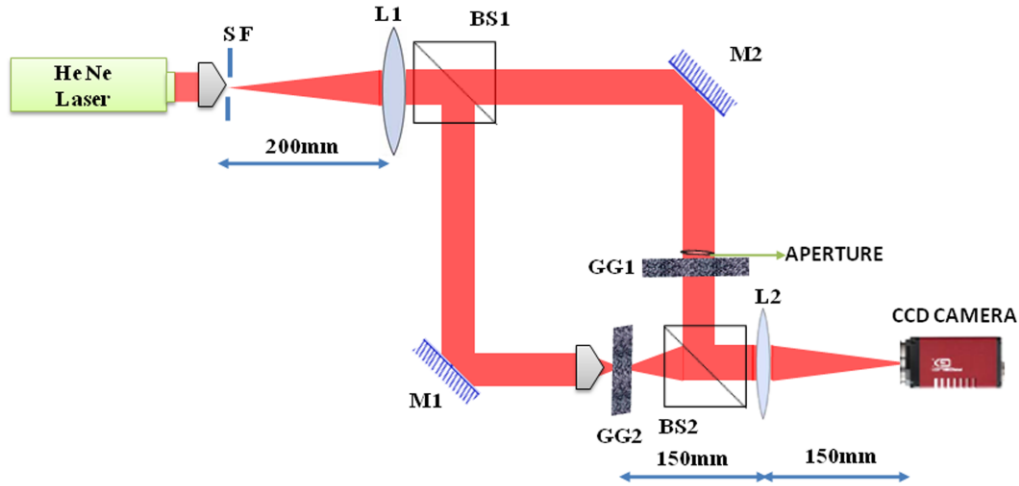
Figure 4.2: Experimental setup for the proposed technique

The proposed experimental setup consists of a Mach - Zehnder interferometer with the object arm (object speckle) controlled by an aperture of specific size. A linearly polarized He-Ne laser beam of wavelength 594.1 nm after spatial filtering and collimation (SF&L1) splits in to two by non polarizing beam splitter (BS1), which constitutes the reference arm and object arm of the interferometer. The beam in the object arm reaches the ground glass (GG1) after passing through aperture of specific size placed very close to the ground glass. The scattered field from GG1 is Fourier transformed using a lens (L2) of focal length 150mm at the camera plane. The reference beam of the interferometer is focused by a microscope objective (MO) of magnification 10X at an off axis point on another ground glass (GG2) and thereby generate a reference speckle field of known coherence function with a linear phase factor. The linear phase factor is introduced to generate a spatial carrier frequency. Both ground glasses GG1 & GG2 are of same GRIT but generate different sizes of speckles due to the size of the illuminating beam. The scattered field from GG2 is also Fourier transformed using lens L2. The two speckle fields from object and reference arms of the interferometer are coherently

superposed and the resultant field is detected in a single shot recording of intensity distribution at the Fourier plane using a CCD monochrome camera (Prosilica GX2750). The CCD camera is 14-bit dynamic range with 2750×2200 pixels and a pixel pitch of 4.54µm. Both ground glasses are static during the recording of the resultant speckle field. Experimental retrieval of the complex coherence function is carried out using the spatial averaging of the two point intensity correlation of the resultant speckle field.

4.1.3 Results and Discussion

The resultant speckle field due to coherent super position of reference and object speckle is recorded by CCD camera and the resultant speckle field is shown in Fig.4.3 for two different cases. The speckle field is controlled by apertures of diameter 1.5 mm and 4.0 mm in the object arm of the interferometer, and the corresponding speckle fields are shown in Fig. 4.3 (a) and 4.3(b) respectively.

(a)   (b)
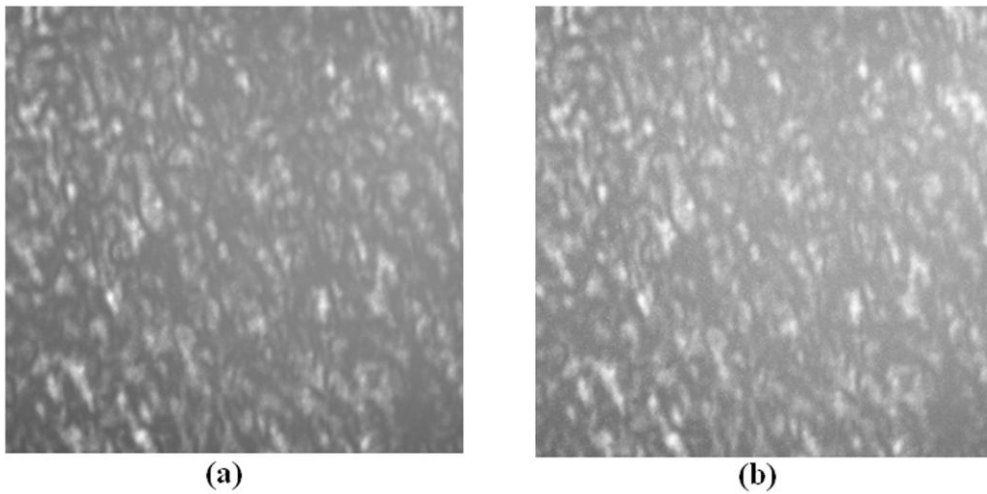
Figure 4.3: Random speckle pattern captured by the CCD camera (a) aperture of diameter 1.5mm (b) aperture of diameter 4.0mm

The cross- covariance of the intensity distribution of the resultant speckle is obtained by spatial averaging under condition of spatial stationarity and ergodicity. This is implemented by taking a portion of the resultant speckle pattern as a matrix $I^m(x, y)$ which represents one realization of the randomly scattered field. Here x and y are the pixel spatial coordinates and take values up to 300×300 pixels. The cross-covariance of the intensity pattern is obtained by correlating $\Delta I^m(x, y)\Delta I^m(0, 0)$ for deferent realization of the speckle patterns and this process

54

is represented as $\sum_{m=1}^{M}\left[\Delta I^m(x,y)\Delta I^m(0,0)\right]/M$. Here, M represents the number of different realizations of the matrix $I^m(x,y)$ produced by the pixel-by-pixel movement of matrix $I^m(x,y)$ over the resultant speckle pattern. We have considered the resultant speckle pattern of size 1200×1200 pixels and two-dimensional scanning of $I^m(x,y)$ over the resultant speckle pattern provides 900×900 different realizations. The fourth-order intensity correlation of the speckle pattern results in interference fringes and is shown in Fig. 4.4. The interference fringe results due to superposition of the complex coherence of the object and reference speckle fields as explained by Eq. 4.8.
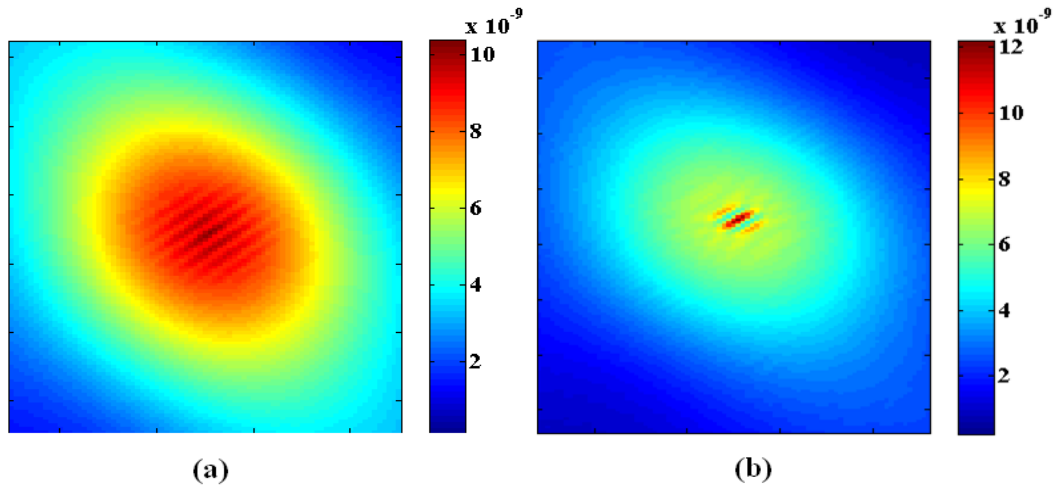
Figure 4.4: Results of fourth order correlation showing interference fringes (a) aperture of diameter 1.5mm (b) aperture of diameter 4.0mm. The color bar represents the intensity.

The use of Fourier fringe analysis technique, separate the spectra from dc part in the spatial frequency domain. High spatial carrier frequency due to linear phase of the reference coherence function plays important role in separation of the frequency spectrum from the dc. Inverse Fourier transform of properly selected and centrally shifted frequency spectrum retrieves the complex coherence function of the speckle field. Results of complex coherence function for apertures of diameter 1.5 mm and 4.0 mm are shown in Fig. 4.5. Amplitude distribution of the complex coherence function of the speckle fields for apertures 1.5 mm and 4.0 mm are shown in Figs. 4.5(a) and 4.5(b) respectively and corresponding phase distributions for 1.5mm and 4.0 mm are shown in Figs. 4.5(c) and 4.5(d)

respectively. The small variation in the phase distribution of the coherence function in Fig. 4.5(c) and 4.5(d) is attributed to the small deviation of the circular aperture from the on-axis position. The complex coherence functions of apertures 1.5mm and 4.0 mm are also analytically evaluated using Eq. (4.2) and considering uniform aperture illumination at GG1 plane, and results are shown in profiles in Fig. 4.6(a) and 4.6(b). Eq. (4.2) is nothing but the van Cittert-Zernike theorem based on spatial averaging under the assumption of spatial stationarity.
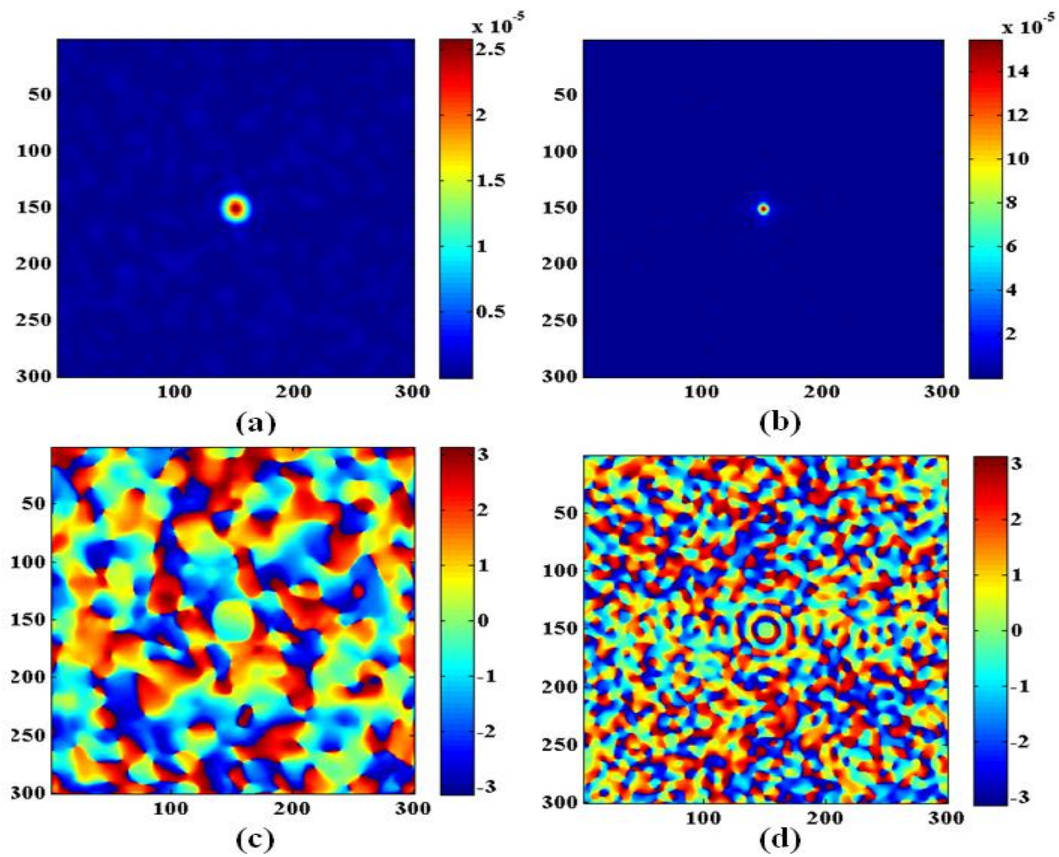
Figure 4.5: Amplitude distribution of complex coherence function (a) aperture of diameter 1.5mm (b) aperture of diameter 4.0mm; Phase distribution of complex coherence function (c) aperture of diameter 1.5mm (d) aperture of diameter 4.0mm. The values on X-axis and Y-axis represent the X-pixels and Y-pixels respectively at the CCD plane and the color bar represent the intensity.
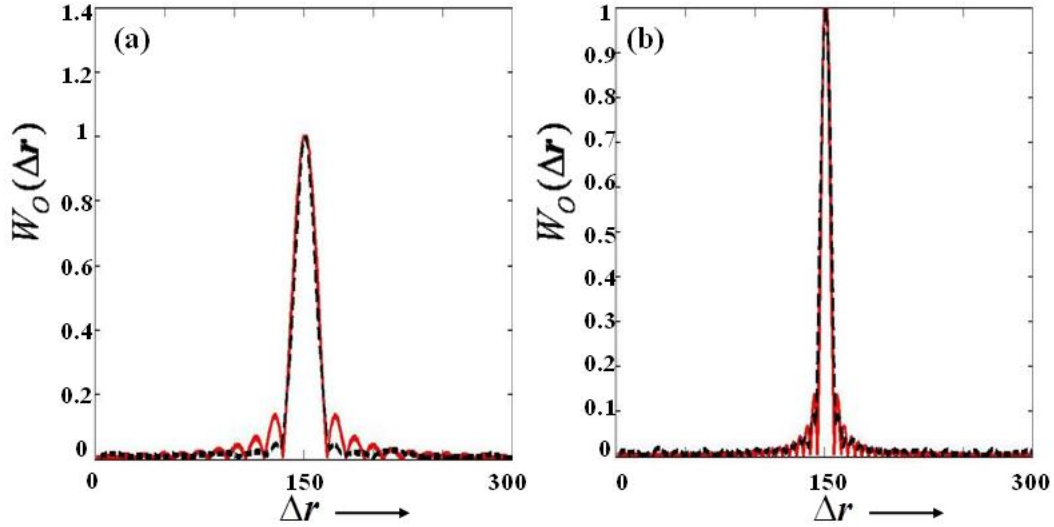
Figure 4.6: Comparison of analytical and experimental plot (a) aperture of diameter 1.5mm (b) aperture of diameter 4.0mm ($\Delta r = 4.54 \mu$m).

The analytical solution of Eq. (4.2) is similar to the far field diffraction pattern of a circular aperture. Red and black colors in the profile of Fig. 4.6 represent analytical and experimental results respectively. The analytical result is evaluated using the uniform aperture illumination on the scattering plane which is different from exact practical situation, and this result into small deviation between analytical and experimental results in outer side lobes.

In summary, we have developed and experimentally demonstrated a method to retrieve the complex coherence function of the speckle field using two point intensity correlation with holographic principle. Application of the proposed method is demonstrated by experimentally measuring the complex coherence function of the laser speckles for two different source apertures. The retrieved complex coherence function of the laser speckle is also compared with the analytical results and good agreement between analytical and experimental results confirms the accuracy of the developed technique.

4.2 Generation of singular point array in spatially fluctuating random field

Phase singularities or optical vortices results from the complete destructive interference of three or more scalar waves on lines known as nodal lines in 3D which when observed on 2D appeared as points. Phase singularity is common in the randomly scattered coherent light and in other complex fields

57

(Freund et al., 1993). Statistics of phase singularities in random optical fields or speckle patterns has drawn considerable interests, and fair amount of literature both theoretical and experimental are available on the subject (Goodman, 2007; O'Holleran et al., 2008; W. Wang et al., 2005). Optical fields are inherently of statistical nature. The phase singularities present in the instantaneous laser speckle washed out due to incoherent nature of the light source and such singularities are referred to as 'hidden singularities'. Statistical parameter such as cross correlation of the light field at two space-time points, known as complex coherence function, plays fundamental role in characterizing the random light field. The complex coherence function obeys wave equation in analogy to the complex optical field (Mandel and Wolf, 1995). This analogy has permitted researchers to extend the area of singular optics from the fully coherent to the incoherent fields. Existence of the coherence vortex has been theoretically and experimentally investigated using different approaches (Berry, 1978; Gbur and Visser, 2003; Schouten et al., 2003; W. Wang et al., 2006; W. Wang and Takeda, 2006). The generation of singularities in light scattered from random phase screen is statistically studied (Berry, 1978). Singularity in the coherence function of the partially coherent beams has been investigated using the Young's interference pattern (Gbur and Visser, 2003; Schouten et al., 2003). The coherence vortices have the degree of coherence equal to zero without fringe visibility. Existence of the coherence vortex can be tested using the interferometric method. The method investigates the local properties of the phase singularities in the spatial coherence function and used in the development of law of conservation for optical coherence (W. Wang et al., 2006; W. Wang and Takeda, 2006). Recently an attempt is made in the direction of generation of coherence vortex array using Mie scattering (Marasinghe et al., 2011). In this section we discuss an experimental technique for the generation of singular point array generation by making use of the intensity interferometer technique.

4.2.1 Singular point array generation

Let us consider scattering of three independent coherent sources from a scattering layer to the Fourier transforming plane of lens. A schematic representation of the scattering of the sources from the scattering layer is shown in

Fig. 4.7. Here independent sources specify full separation of three sources at the scattering plane.
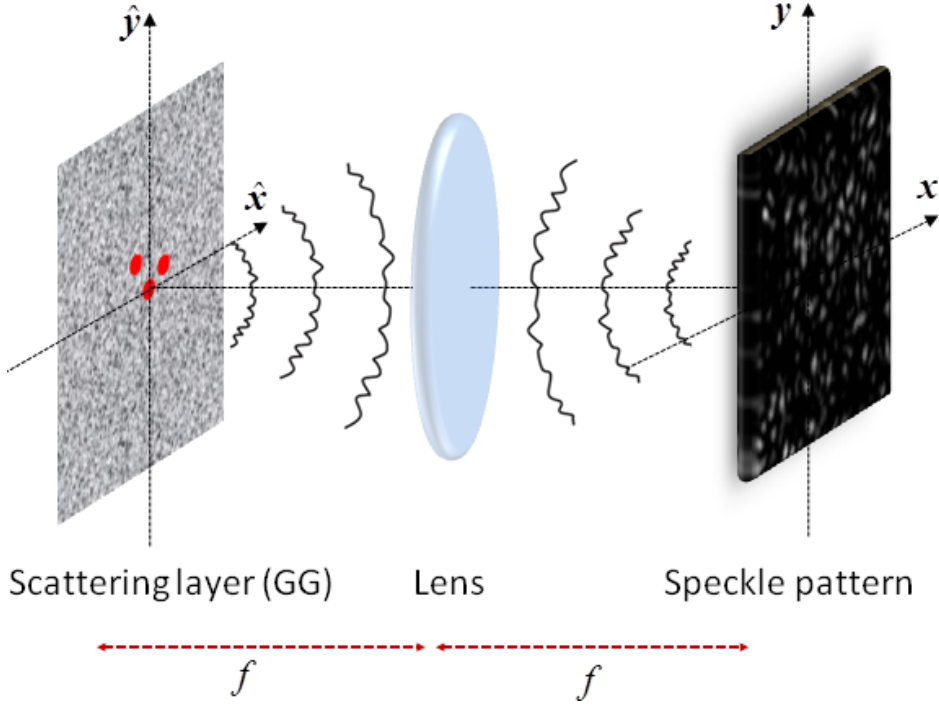
Figure 4.7: Conceptual representation of the proposed technique

The scattered field $(E(r))$ on the Fourier transform plane, for fixed time t, is given by

$$E^m(\boldsymbol{r}) = \int E^m(\hat{\boldsymbol{r}}) \exp\left(i\varphi^m(\hat{\boldsymbol{r}})\right) \exp\left[-i\frac{2\pi \boldsymbol{r}.\hat{\boldsymbol{r}}}{\lambda f}\right] d\hat{\boldsymbol{r}} \tag{4.9}$$

Here, $E^m(\hat{\boldsymbol{r}})$ is ($m^{th} = 1,2,3$) field incident on the scattering layer (ground glass GG) and $\hat{\boldsymbol{r}}$ is position vector on the plane, $\varphi^m(\hat{\boldsymbol{r}})$ a random phase introduced by the ground glass corresponding to the mth source, λ the wavelength of the light, f focal length of the Fourier transforming lens, and the fixed time is omitted for brevity. We have three independent random sources at the ground glass plane and complex field at the Fourier plane is given by

$$E(\boldsymbol{r}) = E^1(\boldsymbol{r}) + E^2(\boldsymbol{r}) + E^3(\boldsymbol{r}) \tag{4.10}$$

Here, $E(r)$ is random complex field which can be obtained numerically using Eq. (4.9). The intensity $\left(I(r) = |E(r)|^2\right)$ allows estimating cross covariance function which is given as $C(r, r + \Delta r) = \langle \Delta I(r) \Delta I(r + \Delta r) \rangle$, where $\langle . \rangle$ is ensemble

averaging and $\Delta I(r) = I(r) - \langle I(r) \rangle$ is fluctuation of the intensity with respect to its mean value.

Experimental implementation of the cross covariance of the intensity can be implemented either using space or temporal averaging under the condition of ergodicity in either space or time. Here we assume ergodicity in space (rather than time) and replace the ensemble averaging by spatial averaging. With this

$$C(\Delta r) = \langle \Delta I(r) \Delta I(r + \Delta r) \rangle_S \tag{4.11}$$

where $\langle . \rangle_S$ denotes the spatial averaging.

Considering Gaussian random field at the Fourier plane, the cross-covariance of the intensity can be explained in second order field correlation as (Naik et al., 2011):

$$C(\Delta r) = |W(\Delta r)|^2 \tag{4.12}$$

From the van Cittert-Zernike theorem, we know that the second order field correlation is connected to the random source structure by a Fourier relation and given as (R. K. Singh et al., 2013):

$$W(\Delta r) = \int I(\hat{r}) \exp\left[-i \frac{2\pi r \hat{r}}{\lambda f} \right] d\hat{r} \tag{4.13}$$

where $I(\hat{r})$ is intensity over the source structure at the scattering plane. The three random sources at the scattering plane are passing through different (independent) portions of the ground glass and can be considered as independent; therefore we are justified in taking contribution from mixed term $\langle E^{m*}(r) E^n(r + \Delta r) \rangle \approx 0$ for $m \neq n$. Under this condition, complex coherence function of the random field is given as;

$$W(\Delta r) = W^1(\Delta r) + W^2(\Delta r) + W^3(\Delta r) \tag{4.14}$$

The complex coherence function of the off-axis circular and uniform source is given as:

$$W^m(\Delta r) = \int circ\left(\frac{\hat{r} - \Delta\hat{r}/2}{a} \right) \exp\left(-i \frac{2\pi}{\lambda f} \Delta r.\hat{r} \right) d\hat{r}$$

$$= 2\pi a^2 \frac{J_1\left(2\pi a \Delta r / \lambda f \right)}{2\pi a \Delta r / \lambda f} \exp\left(-i \frac{\pi}{\lambda f} \Delta r.\Delta\hat{r} \right) \tag{4.15}$$

Here, $m = 1, 2$ and 3 correspond to three sources, a is the radius of the circular aperture and $\Delta\hat{r}/2$ is shift (in our case it is d) of the center of the circular aperture from the optic axis. $J_1(.)$ is Bessel function of the first kind of order one. Eq. (4.15) states that a linear phase term is introduced in the complex coherence function due to an off-axis position of the illuminating aperture at the scattering layer. Generation of the singular point array can be analytically examined using Eq. (4.14) and (4.15) for proper positioning of three sources at the scattering layer plane.

4.2.2 Singular point array detection

An interferometric test is utilized to confirm the generation of singular point array. We considered a reference coherence function with known coherence profile generated from another independent scattering source to superpose with the test field given in Eq. (4.14). Distribution of the reference coherence function is considered as:

$$W^R(\Delta r) = \int circ\left(\frac{\hat{r} - \hat{r}_g}{b}\right)\exp\left(-i\frac{2\pi}{\lambda f}\Delta r.\hat{r}\right)d\hat{r} \tag{4.16}$$

Here radius 'b' is considered to be smaller in comparison to the radius 'a' of the random source as considered in Eq. (4.15). $W^R(\Delta r)$ provide a constant 'reference' wave covering the support of $W(\Delta r)$ to record the 'coherence' interferogram. The position of the circular aperture at the ground glass plane ($\hat{r}_g$) is adjusted in such a way that proper carrier frequency is introduced to the reference coherence function in order to satisfactorily apply the Fourier fringe analysis(Takeda et al., 1982).

$$\left\langle \Delta I^T(r)\Delta I^T(r + \Delta r)\right\rangle_S = \left|W^T(\Delta r)\right|^2$$
$$= \left|W(\Delta r)\right|^2 + \left|W^R(\Delta r)\right|^2 + W^*(\Delta r)W^R(\Delta r) + W(\Delta r)W^{R*}(\Delta r) \tag{4.17}$$

Here, $W^T(\Delta r)$ is the complex coherence function of the resultant speckle of intensity $I^T(r) = E^{T*}(r)E^T(r)$, complex field of resultant field is $E^T(r) = E(r) + E^R(r)$. The 'resultant field' is specifically reserved for interference of all four beams (test and a reference random fields) to distinguish it from the

complex field of Eq. (4.10) which arises due to interference of three random sources described earlier. Reference complex speckle field ($E^R(\boldsymbol{r})$) can be obtained using Eq. (4.9). Reference source is independent from other three previously discussed sources at the ground glass plane. We are justified in taking $\left\langle E^*(\boldsymbol{r})E^R(\boldsymbol{r}+\Delta\boldsymbol{r})\right\rangle \approx 0$ in the derivation of Eq. (4.17).

4.2.3 Experiment

The experimental setup for the proposed technique is shown in Fig. 4.8. A coherent He-Ne laser beam of wavelength λ=632nm, is spatially filtered and collimated by spatial filter assembly (SF) and lens L1. The collimated beam splits into two by a beam splitter (BS1) and forms the two arms of a Michelson interferometer arrangement. The reflected beam from BS1 is further split into two by a beam splitter BS2 and reaches to mirrors M1 and M2. Subsequently, these two reflected beams, from M1 and M2, are focused at the scattering layer by lens L2 of focal length 100mm. A static scattering layer (GG) is located at the focal plane of lens L2. In order to spatially separate two focal spots at the GG plane the mirrors M1 and M2 introduce different tilts. In our experimental geometry, the focal spot of the beam coming from M1 is maintained at the optic axis, whereas beam coming from M2 is focused at a point laterally away from the first one at the GG plane.
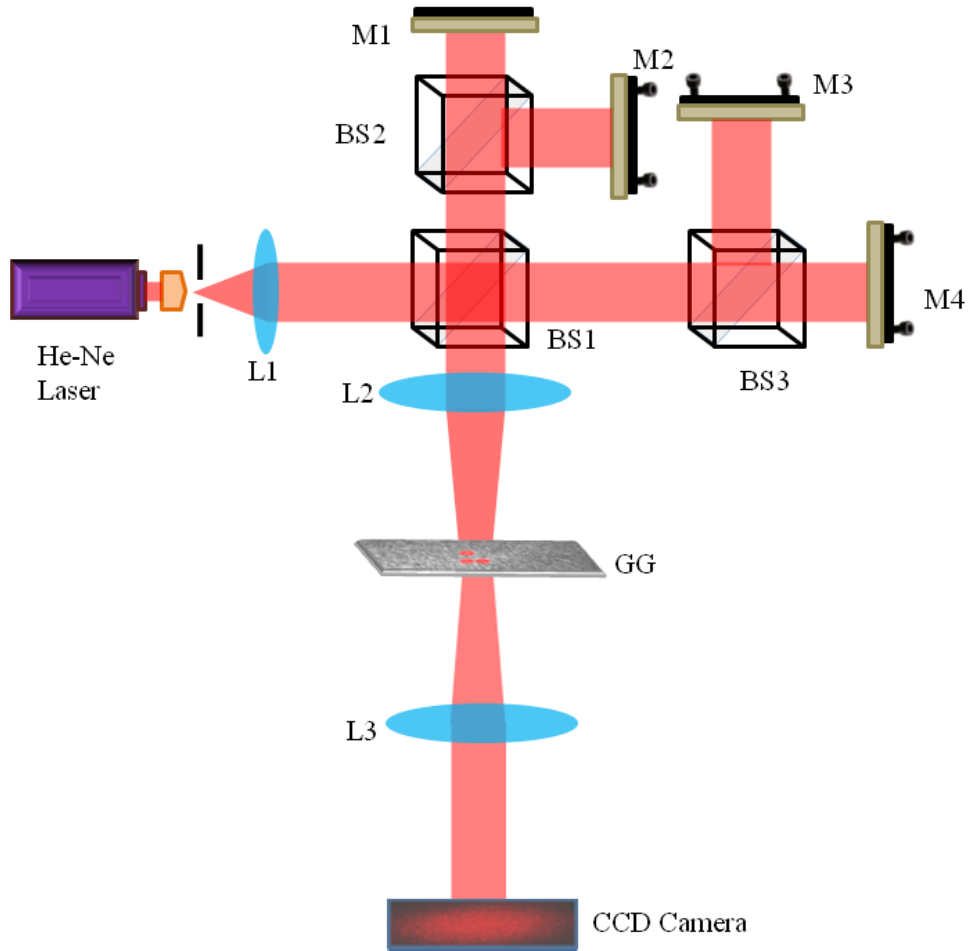
Figure 4.8: Experimental setup for the analysis of laser speckle pattern and generation of singular point array.

The transmitted beam from BS1 again splits into two by a beam splitter BS3. The reflected beam from M3 is focused on GG plane, by giving tilt in such a way that the focal spot is shifted along a direction orthogonal to the previous focal spot. The focal spots of the beams coming from mirrors M1, M2, and M3, make right angle triangle geometry at the GG plane and these positioning in the GG plane is shown in Fig. 4.8 with separation between any two spots *d*. The transmitted beam from BS3 gets reflected from mirror M4 and is used as a testing beam for validating the generation of coherence array. The reference beam from mirror M4 is allowed to illuminate GG in an off-axis position and the size of the focal spot of the reference beam is smaller in comparison with other beams so that an expanded speckle field produced. This provides the proper stretch of the reference coherence function of the reference speckle pattern. The light distribution at the ground glass plane is Fourier transformed at the CCD camera plane by a lens L3 of focal length 200mm,

and the speckle pattern is recorded. The camera is of 14-bit dynamic range, with 2750X2200 pixels and a pixel pitch of 4.54 μm (Prosilica GX2750). Note that generation and testing of the singularities in the coherence function is carried out from a single shot measurement of the speckle pattern and subsequently applying the spatial averaging.

4.2.4 Results and Discussion

The amplitude distribution of the coherence function from the recorded intensity is carried out numerically by estimating the intensity covariance distribution as given in Eq. (4.11) which is related to the three random source structures as explained in Eqs. (4.12)-(4.14). Eq. (4.11) states that from the measured cross-covariance of the intensity $C(\Delta r)$, we can have only modulus square of the complex coherence function, i.e. only amplitude distribution of the complex coherence function as given in Eq. (4.14). The amplitude distribution of the coherence function shows structure of the amplitude nulls. Network of the null in the amplitude distribution, which corresponds to the singular point array, with different densities can be clearly seen in Fig. 4.9. Fig. 4.9(a) is distribution of the coherence function for three random source structures with separation (d) equal to 1.393mm. In this case, a network of coherence vortex array of 5X5 is clearly visible. On the other hand, amplitude distribution in Fig. 4.9(b) corresponds to the source separation 1.591mm and density of the vortex array is 7X7. Though, null amplitude is apparent in the Fig.4.9 but presence of vortex in the coherence function requires confirmation of helical phase structure which can be performed by interferometric method. Here, we use this approach to check the presence of helical phase structure in the complex coherence function.
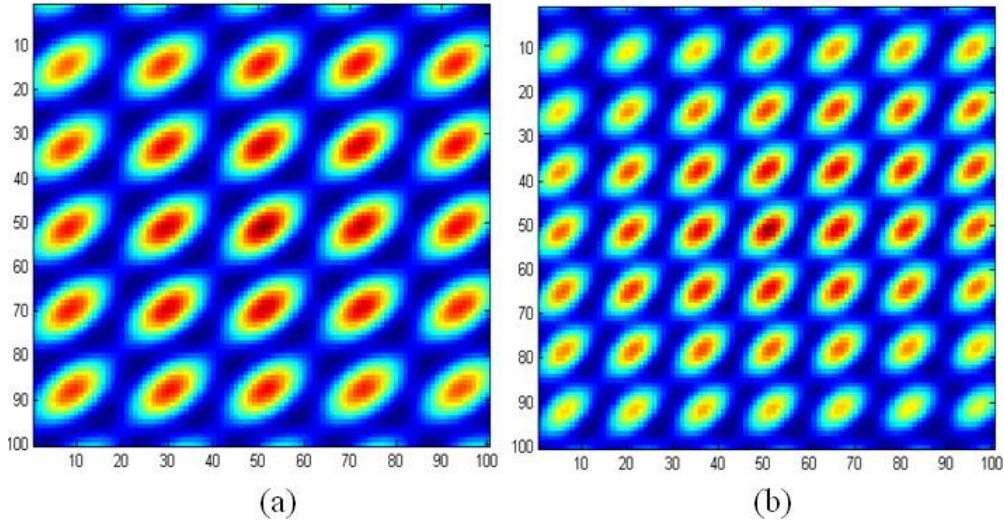
Figure 4.9: Experimental results of amplitude distribution of the coherence vortex array for two different structures of the three independent sources at the ground glass plane (a) 5×5 arrays (b) 7×7 arrays. The values on X-axis and Y-axis represent the X-pixels and Y-pixels respectively at the CCD plane.

The experimental detection of phase structure of the singular point array is performed by interferometric test. The resultant speckle pattern is detected at the camera (CCD) plane and using this data the cross-covariance of the resultant intensity is estimated. This cross covariance represents an interferometric structure due to superposition of the coherence functions. The phase structure of the singular point array is recovered from this interferogram by making use of Fourier fringe analysis technique (Takeda et al., 1982). The Fourier transform of the interferogram separates out the spectra from other terms. The inverse Fourier transform of the centrally positioned spectra reconstructs the desired complex coherence function and the phase structure of the complex coherence function with singular point array is shown in Fig. 4.10. The phase structures of the coherence function with singular point array corresponding to 5×5 and 7×7 array are shown in Figs. 4.10(a) and 4.10(b) respectively. In the interferometric test for the confirmation of singular point array generation we used the assumption of an expanded reference coherence function to fully support the test. But in experimental implementation these have limitation due to the reference beam size at the GG plane, and this may produce residual phase errors of the coherence function and results in a curvature effect as shown in phase structure of Fig. 4.10.
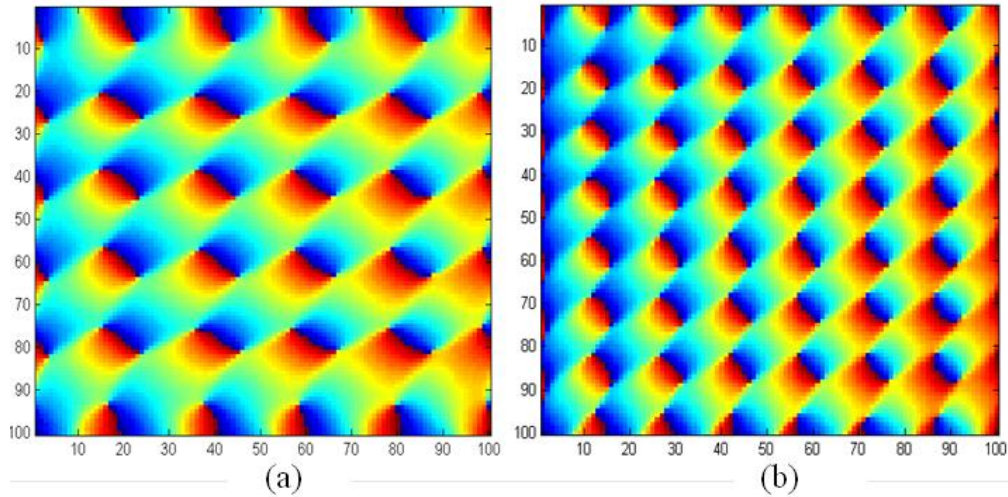
Figure 4.10: Experimental results of phase structure of the coherence function embedded with the coherence vortex array (a) 5×5 arrays (b) 7×7 arrays. The values on X-axis and Y-axis represent the X-pixels and Y-pixels respectively at the CCD plane.

In summary, we have experimentally demonstrated a method to generate singular point array using intensity interferometer technique. This technique provides a simple experimental scheme to produce singular point array with desired densities for a spatially fluctuating random field.

4.3 Experimental determination of Generalized Stokes parameters

Coherence and polarization properties of random electromagnetic beams attain remarkable attention after the introduction of the unified theory of coherence and polarization (Wolf, 2003b). The polarization property of a light wave is usually characterized by four Stokes parameters (Goldstein, 2010) which contain field correlation at one point. Theoretical and experimental advances in generalized Stokes parameters (GSPs) (Ellis and Dogariu, 2004; Korotkova and Wolf, 2005b; Tervo et al., 2009) which characterize the two point vector field correlations attains recent interests in optical coherence theory. Most of the measurement methods described to measure GSPs are based on two pinhole Young's interferometer and require combinations of retarders and polarizers(Kanseri et al., 2009; Roychowdhury and Wolf, 2003; Setälä et al., 2006). Recent efforts to

visualize the complex 2D coherence function (Zhao and Wang, 2014) and generation of beam with special correlation functions (Chen et al., 2014) gives new opportunities to explore the coherence and polarization of randomly fluctuating fields. However field based measurement techniques (R. K. Singh et al., 2014, 2012; Zhao and Wang, 2014) are sensitive to the vibrations. Therefore other alternative techniques are also sought in recent years.

The Hanbury Brown and Twiss intensity interferometer which measures the two point intensity correlation is comparatively less sensitive to the vibrations or external fluctuations (Brown and Twiss, 1956). Recent extension of Hanburry Brown and twiss effect to electromagnetic waves gives potential to relate the intensity correlation with the coherence and polarization properties of the field (Hassinen et al., 2011; Tervo et al., 2003). Very recently a method is suggested to access the two point Stokes parameters (GSPs) from two point intensity correlation (Basso et al., 2014). This method provides the amplitude information of the GSPs, but phase information is lost. Note that phase of GSP is highly significant in imaging applications (R. K. Singh et al., 2013, 2012). In this section, we demonstrate a new experimental technique to measure the complex GSPs by intensity correlation. Basic principle of our technique lies in the relation between fourth order correlation and complex coherence function (Mandel and Wolf, 1995). Our main interest in this work is to experimentally demonstrate the measurement of complex GSPs i.e both amplitude and phase of all the four GSPs. In this technique we utilized the coherent superposition of an independent polarized reference speckle with a polarized object speckle field for which the coherence and polarization property needs to be measured.

4.3.1 Generalized Stokes parameters from intensity correlation

Let us consider a transverse field generated from a random phase screen obeying Gaussian statistics. The orthogonal polarization components are represented as $E_x(\hat{\boldsymbol{r}}, t)$ and $E_y(\hat{\boldsymbol{r}}, t)$ at positions $\hat{\boldsymbol{r}}$ and time t where x and y represents the direction of polarization vector components. The two point intensity correlation of the scattered field can be directly related to the elements of coherence-polarization (CP) matrix elements (Tervo et al., 2003). Thus the two point intensity correlation is given by

$$\Gamma(\boldsymbol{r}_1,\boldsymbol{r}_2,t)=\left\langle\Delta I(\boldsymbol{r}_1,t)\Delta I(\boldsymbol{r}_2,t)\right\rangle=\sum_{i,j}\left|W_{ij}(\boldsymbol{r}_1,\boldsymbol{r}_2,t)\right|^2 \qquad (4.18)$$

where the angular brackets represents the ensemble average, $\Delta I(\boldsymbol{r},t)=I(\boldsymbol{r},t)-\left\langle I(\boldsymbol{r},t)\right\rangle$, $I(\boldsymbol{r},t)=\left|E(\boldsymbol{r},t)\right|^2$ is the intensity at position r and time t and $W_{ij}(\boldsymbol{r}_1,\boldsymbol{r}_2,t)=\left\langle E_i^*(\boldsymbol{r}_1,t)E_j(\boldsymbol{r}_2,t)\right\rangle$ are the elements of CP matrix with $i,j=x$ or y .

Eq. (4.18) shows that $\Gamma(\boldsymbol{r}_1,\boldsymbol{r}_2,t)$ only contains modulus of $W_{ij}(\boldsymbol{r}_1,\boldsymbol{r}_2,t)$ and phase information is lost. To retrieve both amplitude and phase we have developed a new technique with the help of intensity correlation in combination with holography where complex coherence function for the scalar case is recovered with the help of a known reference coherence function. Using similar strategy a reference polarized speckle field generated from an independent scattering layer is coherently superposed with the vectorial field generated from scattering layer for which the coherence and polarization properties needs to be measured. Due to independence of two random phase screens, we are justified to take $\left\langle E_i^R(\boldsymbol{r}_1,t)E_j^O(\boldsymbol{r}_2,t)\right\rangle=0$ Therefore mutual coherence function from the resultant field is given as

$$W_{ij}(\boldsymbol{r}_1,\boldsymbol{r}_2,t)=W_{ij}^R(\boldsymbol{r}_1,\boldsymbol{r}_2,t)+W_{ij}^O(\boldsymbol{r}_1,\boldsymbol{r}_2,t) \qquad (4.19)$$

where $W_{ij}^R(\boldsymbol{r}_1,\boldsymbol{r}_2,t)$ and $W_{ij}^O(\boldsymbol{r}_1,\boldsymbol{r}_2,t)$ represents the complex coherence function of scattered field from reference and object random phase screens. Thus now the two point intensity correlation of the field measured is simply

$$\Gamma(\boldsymbol{r}_1,\boldsymbol{r}_2)=\sum_{ij}\left|\left\langle E_i^*(\boldsymbol{r}_1)E_j(\boldsymbol{r}_2)\right\rangle\right|^2 \qquad (4.20)$$

where $E_i(\boldsymbol{r})=E_i^R(\boldsymbol{r})+E_i^O(\boldsymbol{r})$ is the sum of the polarization components from the reference and object speckle field. The fixed time t is omitted for brevity.

The random field E is allowed to pass through a measurement scheme consist of a quarter wave plate (QWP) with its fast axis rotated by an angle θ with respect to X direction and then filtered by a linear polarizer (LP) in X direction prior to the intensity correlation. A schematic representation of the measurement scheme is shown in Fig. 4.11.
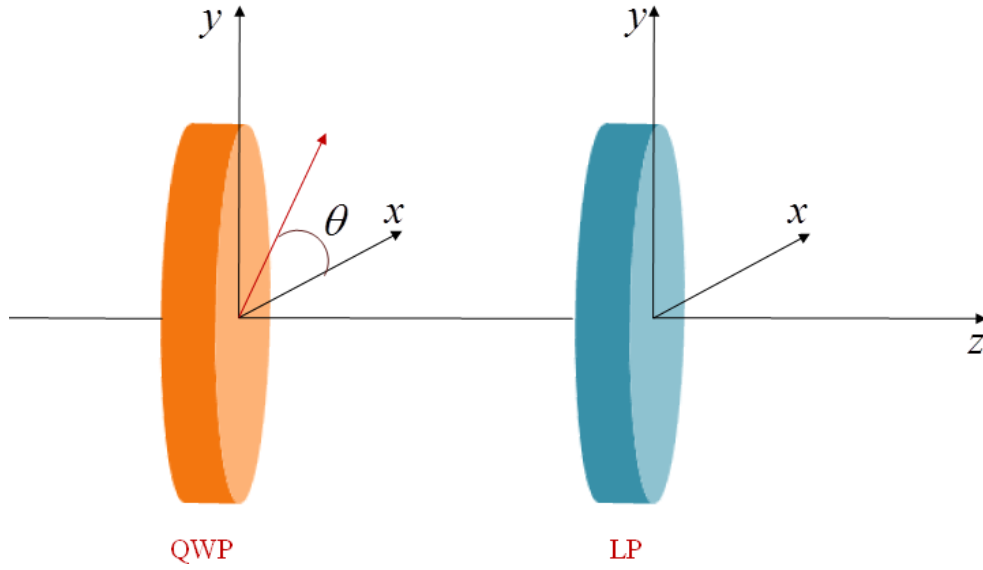
Figure 4.11: Schematic representation of the measurement scheme using a QWP and LP.

The field after the polarization elements is given by

$$
\begin{aligned}
E_{res}(\boldsymbol{r}_1) = & \left[\cos^2\theta + i\sin^2\theta\right]\left(E_x^R(\boldsymbol{r}) + E_x^O(\boldsymbol{r})\right) \\
& + \left[(1-i)\cos\theta\sin\theta\right]\left(E_y^R(\boldsymbol{r}) + E_y^O(\boldsymbol{r})\right)
\end{aligned}
\tag{4.21}
$$

The intensity correlation is the modulus square of the electric field correlation at two spatially separated points. Using Eq. (4.21) and with appropriate trigonometric substitutions the intensity correlation in Eq. (4.20) modifies to

$$
\Gamma(\boldsymbol{r}_1,\boldsymbol{r}_2,\theta) = \frac{1}{4}
\begin{vmatrix}
\left(1+\cos^2 2\theta\right)\left(W_{xx}^R(\boldsymbol{r}_1,\boldsymbol{r}_2) + W_{xx}^O(\boldsymbol{r}_1,\boldsymbol{r}_2)\right) + \\
\left(1-\cos^2 2\theta\right)\left(W_{yy}^R(\boldsymbol{r}_1,\boldsymbol{r}_2) + W_{yy}^O(\boldsymbol{r}_1,\boldsymbol{r}_2)\right) + \\
\left(\dfrac{\sin 4\theta}{2} - i\sin 2\theta\right)\left(W_{xy}^R(\boldsymbol{r}_1,\boldsymbol{r}_2) + W_{xy}^O(\boldsymbol{r}_1,\boldsymbol{r}_2)\right) + \\
\left(\dfrac{\sin 4\theta}{2} + i\sin 2\theta\right)\left(W_{yx}^R(\boldsymbol{r}_1,\boldsymbol{r}_2) + W_{yx}^O(\boldsymbol{r}_1,\boldsymbol{r}_2)\right)
\end{vmatrix}^2
\tag{4.22}
$$

where $W_{ij}^l(\boldsymbol{r}_1,\boldsymbol{r}_2) = \left\langle E_i^{l*}(\boldsymbol{r}_1)E_j^l(\boldsymbol{r}_2)\right\rangle$ with $i = j = x$ or y and $l = R$ or O (See Appendix 1 for detailed derivation).

On introducing the GSPs in terms of CP matrix elements, eq. (4.22) modifies to

$$\Gamma(\Delta\boldsymbol{r},\theta) = \frac{1}{4} \left| \begin{array}{l} \left[S_0(\Delta\boldsymbol{r})\right] + \left[S_1(\Delta\boldsymbol{r})\right]\cos^2 2\theta \\ + \left[S_2(\Delta\boldsymbol{r})\right]\dfrac{\sin 4\theta}{2} + \left[S_3(\Delta\boldsymbol{r})\right]\sin 2\theta \end{array} \right|^2 \qquad (4.23)$$

where $\Delta\boldsymbol{r} = \boldsymbol{r}_2 - \boldsymbol{r}_1$ and we have used the representation $S_k(\boldsymbol{r}_1,\boldsymbol{r}_2) = S_k^R(\boldsymbol{r}_1,\boldsymbol{r}_2) + S_k^O(\boldsymbol{r}_1,\boldsymbol{r}_2)$ with $k = 0,1,2$ and 3 and

$$S_0^l(\Delta\boldsymbol{r}) = W_{xx}^l(\Delta\boldsymbol{r}) + W_{yy}^l(\Delta\boldsymbol{r})$$
$$S_1^l(\Delta\boldsymbol{r}) = W_{xx}^l(\Delta\boldsymbol{r}) - W_{yy}^l(\Delta\boldsymbol{r})$$
$$S_2^l(\Delta\boldsymbol{r}) = W_{xy}^l(\Delta\boldsymbol{r}) + W_{yx}^l(\Delta\boldsymbol{r}) \qquad (4.24)$$
$$S_3^l(\Delta\boldsymbol{r}) = i\left[W_{yx}^l(\Delta\boldsymbol{r}) - W_{xy}^l(\Delta\boldsymbol{r})\right] \text{ with } l = R \text{ or } O$$

Thus the two point intensity correlation measured is direct functions of four GSPs which contains the field from both reference and object arms. By choosing appropriate angles for QWP rotation (i.e θ) such that $\theta_1 = 0°, \theta_2 = 22.5°, \theta_3 = 45°$ and $\theta_4 = 135°$; four intensity correlation results which are the combination of GSPs can be obtained as

$$\Gamma(\Delta\boldsymbol{r},\theta_1) = \frac{1}{4}\left|S_0(\Delta\boldsymbol{r}) + S_1(\Delta\boldsymbol{r})\right|^2$$

$$\Gamma(\Delta\boldsymbol{r},\theta_2) = \frac{1}{4}\left|S_0(\Delta\boldsymbol{r}) + \frac{S_1(\Delta\boldsymbol{r})}{2} + \frac{S_2(\Delta\boldsymbol{r})}{2} + \frac{S_3(\Delta\boldsymbol{r})}{\sqrt{2}}\right|^2$$

$$\Gamma(\Delta\boldsymbol{r},\theta_3) = \frac{1}{4}\left|S_0(\Delta\boldsymbol{r}) + S_3(\Delta\boldsymbol{r})\right|^2 \qquad (4.25)$$

$$\Gamma(\Delta\boldsymbol{r},\theta_4) = \frac{1}{4}\left|S_0(\Delta\boldsymbol{r}) - S_3(\Delta\boldsymbol{r})\right|^2$$

Each of the intensity correlation resulting from the particular rotation of the QWP gives an intensity correlation hologram which results from the coherent superposition of object speckle field with the independent reference speckle field. Experimentally the intensity correlation of each of the speckle pattern corresponding to the rotations of the QWP is performed using spatial average as an effective replacement of ensemble average on the assumption of spatial stationarity and ergodicity of the spatially fluctuating field $\left(\text{i.e. } \Gamma(\Delta\boldsymbol{r},\theta_m) = \left\langle \Delta I(r_1)I(r_1 + \Delta r)\right\rangle_S \text{ with } \Delta r = r_2 - r_1 \text{ and } m = 1,2,3 \text{ and } 4\right)$. This intensity correlation hologram resulting from the different rotations of the QWP

are combinations of the GSPs as given in Eq. (4.25). From these holograms we can recover the complex GSPs of the object field using Fourier transform filtering approach. Fourier transform of the intensity correlation hologram separates the desired spectrum of the field under consideration from other terms. Inverse Fourier transform of the appropriate combinations of the properly filtered and centrally shifted spectra results into the desired GSPs of the field and is given by

$$S_0^O(\Delta\boldsymbol{r}) = 2\Gamma'(\Delta\boldsymbol{r},\theta_3) + 2\Gamma'(\Delta\boldsymbol{r},\theta_4)$$
$$S_1^O(\Delta\boldsymbol{r}) = 4\Gamma'(\Delta\boldsymbol{r},\theta_1) - 2\Gamma'(\Delta\boldsymbol{r},\theta_3) - 2\Gamma'(\Delta\boldsymbol{r},\theta_4)$$
$$S_2^O(\Delta\boldsymbol{r}) = 8\Gamma'(\Delta\boldsymbol{r},\theta_2) - 2(1+\sqrt{2})\Gamma'(\Delta\boldsymbol{r},\theta_3) \quad\quad (4.26)$$
$$\quad\quad -2(1-\sqrt{2})\Gamma'(\Delta\boldsymbol{r},\theta_4) - 4\Gamma'(\Delta\boldsymbol{r},\theta_1)$$
$$S_3^O(\Delta\boldsymbol{r}) = 2\Gamma'(\Delta\boldsymbol{r},\theta_3) - 2\Gamma'(\Delta\boldsymbol{r},\theta_4)$$

where $\Gamma'(\Delta\boldsymbol{r},\theta_m)$ with $m=1,2,3$ and 4 are the inverse Fourier transform of the spectra which is filtered and translated to the origin of the frequency axis and contains only the information about the object field.

4.3.2 Experiment

The experimental implementation of the proposed measurement technique is shown in Fig. 4.12. A linearly polarized He-Ne laser beam of wavelength 632.8 nm (Melles Griot) is filtered using a spatial filter assembly (SF) and collimated using a lens L1 of focal length 200mm. A half wave plate (HWP)converts the linearly polarized collimated beam to a linearly 45^0 beam and this beam passes through a non polarizing beam splitter (BS1) which splits the beam into two, constitutes the two arms of a Mach-Zehnder interferometer.
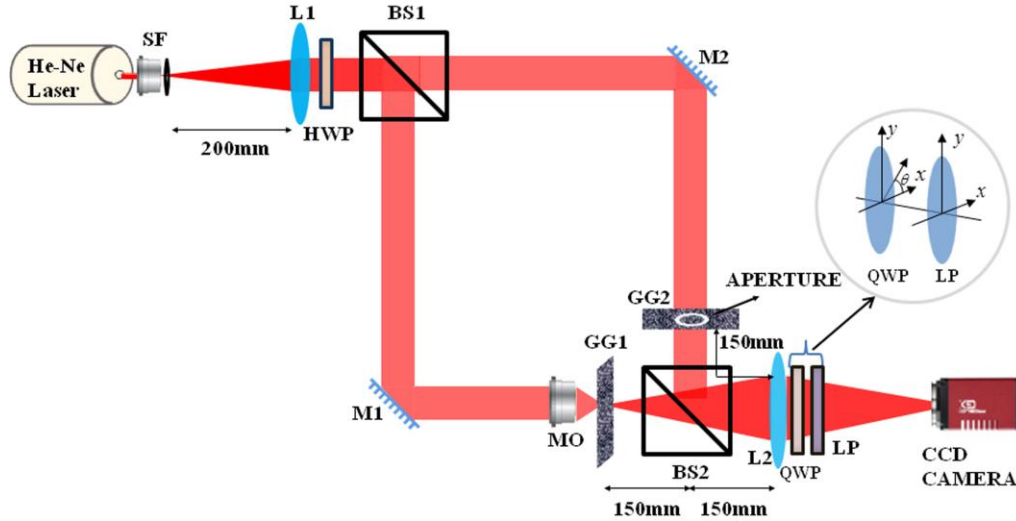
Figure 4.12: Experimental setup for the measurement technique

The reflected beam from BS1 is folded by a mirror M1 and illuminates a random phase screen (GG1) through a microscope objective (MO) which generates an independent reference speckle field. The transmitted beam from BS1 is folded by mirror M2 and illuminates a random phase screen (GG2) through an aperture (circular or annular aperture) which is placed very close to GG2 to constitute the object speckle field. The reference and object speckle field from the two arms of the interferometer are combined using a non polarizing beam splitter (BS2) and Fourier transformed using a common lens L2 of focal length 150 mm. The lens L2 is used in order to fulfill requirement of the spatial stationarity in the spatially fluctuating random field. The resultant speckle field is allowed to pass through a QWP rotated at an angle θ with respect to X direction and filtered by a linear polarizer (LP). Transmission axis of LP is placed in the X direction (shown in inset of Fig.4.12) and field is captured by a monochrome CCD camera. The camera is of 14 bit dynamic range with 2750×2200 pixels and a pixel pitch of 4.54µm (Prosilica GX2750). Both ground glasses are static during the recording of the intensity distribution of the speckle field and intensity is recorded for four different rotation angles of QWP.

4.3.3 Results and Discussion

The optical field to be analyzed which is passing through the random phase screen (GG2) is controlled by aperture and generates the vectorial scattered field which is coherently superposed with the independent vectorial reference speckle field from GG1. Aperture at the plane GG2 shapes coherence-polarization properties of the

random field at the CCD plane. The resultant speckle field for the four combinations of the QWP and LP are recorded using CCD camera. Two point intensity correlations of the speckle intensity at the CCD plane results into holograms corresponding to each of the QWP rotation. By Fourier fringe analysis technique and using Eq. (4.26) the GSPs of the desired optical field is measured. Experimental results of the measured GSPs for a circular aperture as source structures are shown in Fig. 4.13 and Fig. 4.14.
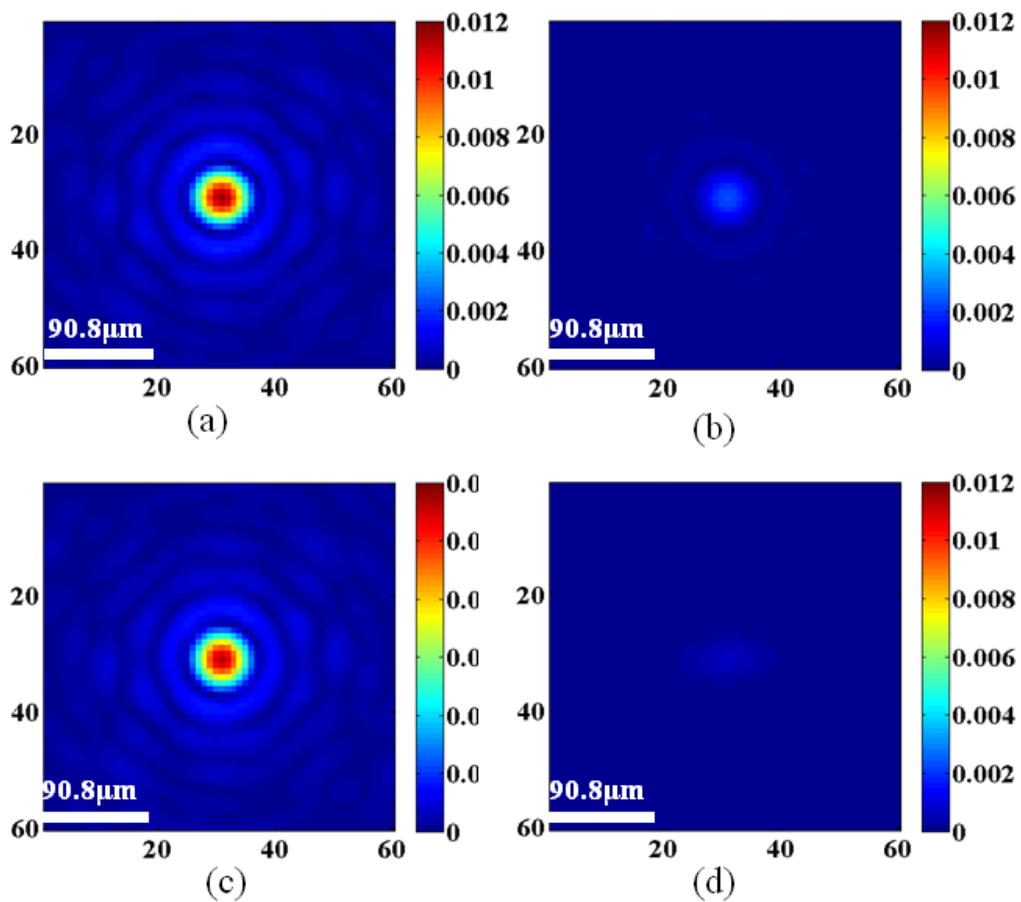
Figure 4.13: Experimental results of amplitude distribution of complex GSPs with circular aperture of 4mm diameter (a) $S_0^O(\Delta r)$ (b) $S_1^O(\Delta r)$ (c) $S_2^O(\Delta r)$ (d) $S_3^O(\Delta r)$ The values on X-axis and Y-axis represent the X-pixels and Y-pixels respectively at the CCD plane and the color bar represent the intensity.

Fig. 4.13(a)-(d) shows the amplitude distribution and Fig. 4.14(a)-(d) shows the phase distribution of complex GSPs for the case of circular aperture of 4mm diameter as source structure. Fig. 4.13(a) represents the amplitude distribution of

$S_0^O(\Delta r)$ and Fig. 4.14(a) represents the corresponding phase distribution. The uniform phase distribution with a zero index value shows the complete retrieval of phase along with its amplitude. Fig. 4.13(b) and 4.14(b) shows the amplitude and phase distribution corresponding to $S_1^O(\Delta r)$. A low intensity value in amplitude distribution as shown in Fig. 4.13(b) shows relative strength of orthogonal x and y component at the scattering plane.
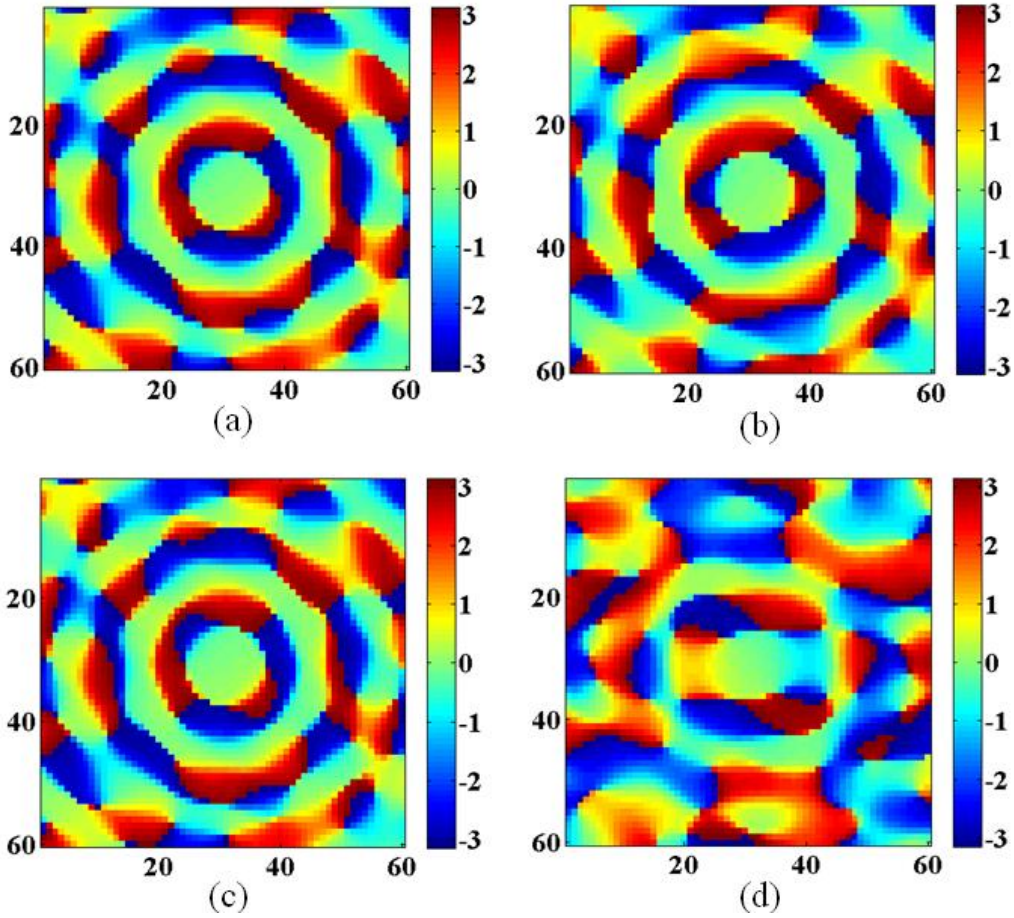
Figure 4.14: Experimental results of phase distribution of complex GSPs with circular aperture of 4mm diameter (a) $S_0^O(\Delta r)$ (b) $S_1^O(\Delta r)$ (c) $S_2^O(\Delta r)$ (d) $S_3^O(\Delta r)$ The values on X-axis and Y-axis represent the X-pixels and Y-pixels respectively at the CCD plane and the color bar represent the phase profile.

The amplitude and phase distribution of $S_2^O(\Delta r)$ are shown in Fig. 4.13(c) and 4.14(c), where the high intensity value in amplitude distribution provides the information of the linear polarization at 45^0 dominates over other polarization state at the random source plane. Fig. 4.13(d) and 4.14(d) corresponds to the amplitude

and phase distribution of $S_3^O(\Delta r)$. A negligible intensity value in amplitude distribution corresponding to Fig. 4.13(d) shows the amount of circular polarization is negligibly small compared with the linear 45^0 polarization state at the random source plane.

Results of amplitude and phase distributions of complex GSPs for an annular aperture with 4mm diameter and an obstruction ratio 0.5 are shown in Fig. 4.15(a)-(d) and Fig. 4.16(a)-(d) respectively.
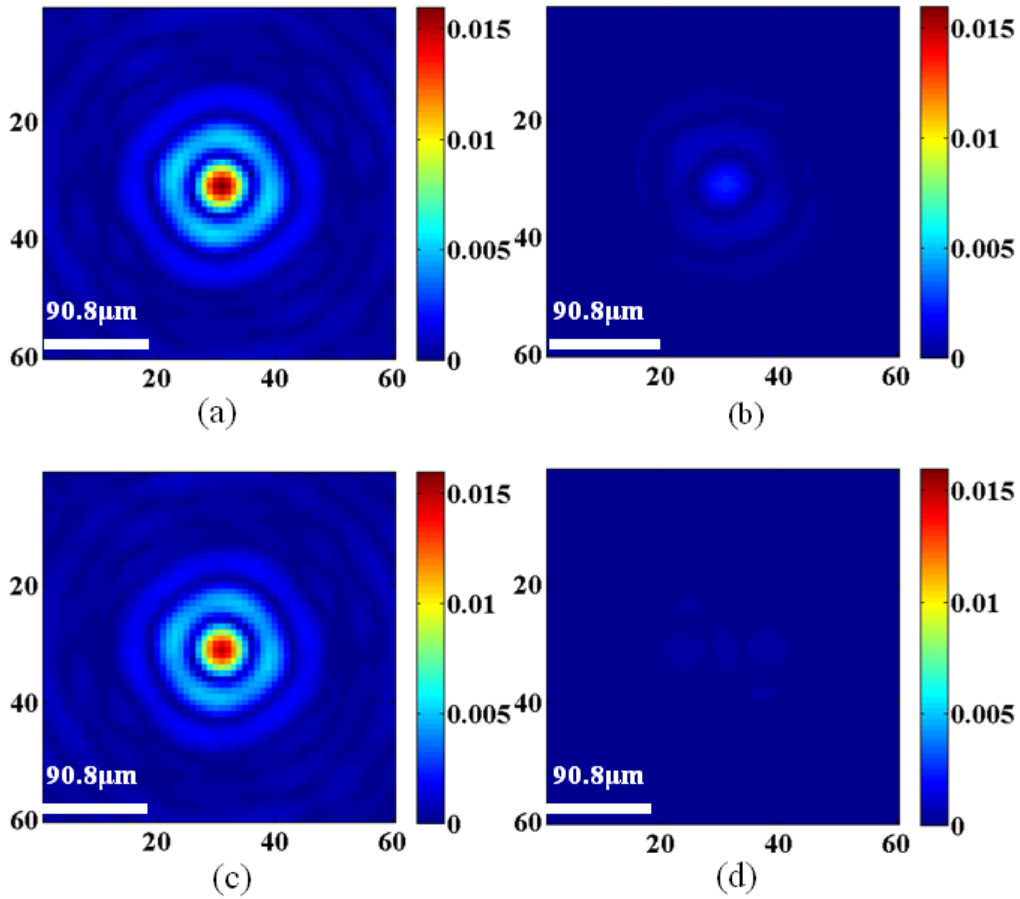
Figure 4.15: Experimental results of amplitude distribution of complex GSPs with circular aperture of 4mm diameter (a) $S_0^O(\Delta r)$ (b) $S_1^O(\Delta r)$ (c) $S_2^O(\Delta r)$ (d) $S_3^O(\Delta r)$ The values on X-axis and Y-axis represent the X-pixels and Y-pixels respectively at the CCD plane and the color bar represent the intensity.

The amplitude distribution has high intensity values for $S_0^O(\Delta r)$ and $S_2^O(\Delta r)$ as shown in Fig. 4.15(a) and 4.15(c) which confirms that linear polarization at 45^0 dominates over other polarization state. The corresponding phase distribution

shown in Fig. 4.16(a) and 4.16(c) shows a uniform distribution of phase with a zero index value. i.e. both amplitude and phase distribution of all the four complex GSPs behaves in a similar way as the circular aperture as source structure except that the complex quantities narrows down and side lobes are dominating due to the obstruction in the annular aperture in comparison with the circular aperture. The experimental results obtained with circular and annular aperture are in well agreement with the analytical results obtained using the van Cittert-Zernike theorem and a profile of amplitude distribution of $S_0^O(\Delta r)$ and $S_2^O(\Delta r)$ is shown in Fig. 4.17(a) and 4.17(b) respectively. The other two GSPs are negligible and not plotted in Fig. 4.17. Red and magenta dotted lines in Fig.4 represent the experimental results and blue and green lines represent the analytical results for circular and annular apertures respectively. Analytical result is evaluated using the Gaussian illuminating beam (with large beam waist) at the scattering plane.
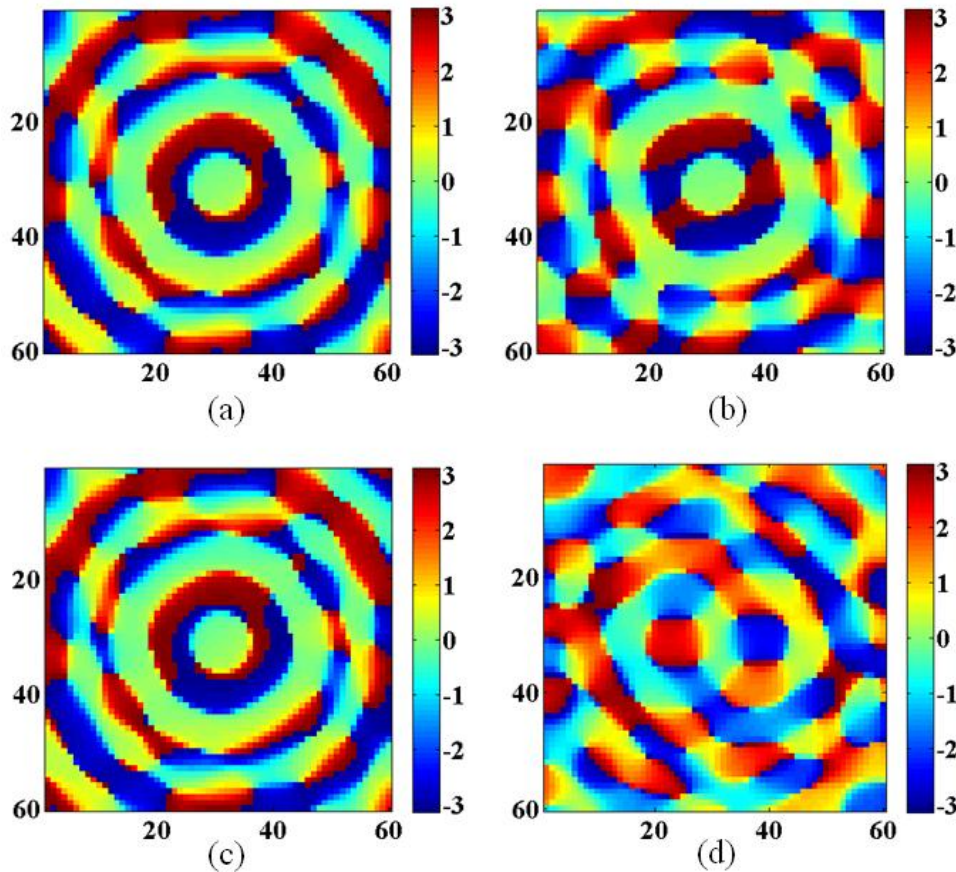
Figure 4.16: Experimental results of phase distribution of complex GSPs with circular aperture of 4mm diameter (a) $S_0^O(\Delta r)$ (b) $S_1^O(\Delta r)$ (c) $S_2^O(\Delta r)$ (d) $S_3^O(\Delta r)$ The values on X-axis and Y-axis represent the X-pixels and Y-pixels respectively at the CCD plane and the color bar represent the phase profile.
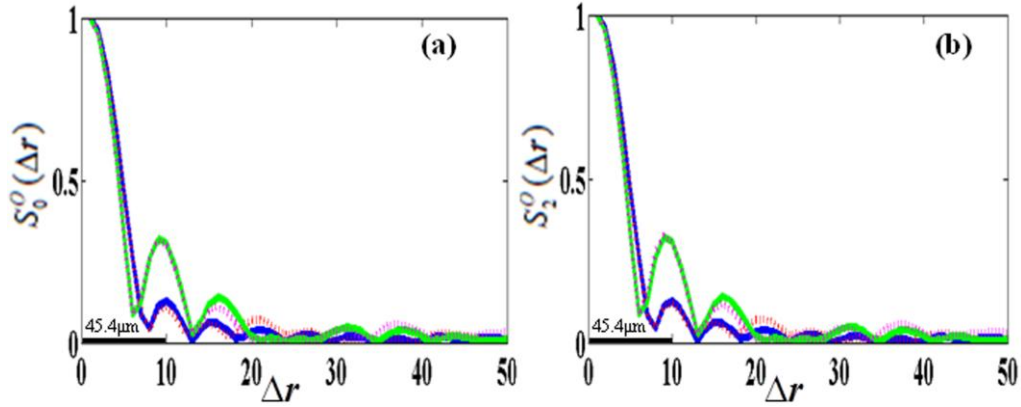
Figure 4.17: Normalized amplitude profiles of the analytical and experimental results of (a) $S_0^O(\Delta r)$ and (b) $S_2^O(\Delta r)$ for the circular and annular apertures ($\Delta r = 4.54 \mu$m).

In summary, an experimental technique is demonstrated for the complete measurement of complex GSPs by making use of vectorial speckle holographic technique in combination with the two-point intensity correlation. The application of the technique is experimentally demonstrated by measuring the complex GSPs using a circular and annular aperture as source structures. The technique is expected to be play crucial role in determining the statistical properties of the random vector field and also in optical imaging.

4.4 Synthesis and analysis of statistical properties of a randomly fluctuating polarized field

Recently a significant amount of attention is drawn in the direction of propagation based polarization changes and controlled synthesis of coherence and polarization properties of randomly fluctuating field due to its application in optical imaging and correlation induced spectral changes. Propagation induced polarization changes in partially coherent optical beams and changes in the state of polarization of an electromagnetic beam on propagation were studied (Agrawal and Wolf, 2000; Korotkova and Wolf, 2005a). Correlation induced changes in coherence and polarization were examined theoretically and experimentally in recent years (Korotkova et al., 2005; Salem and Wolf, 2008; Wolf, 2003a). Modulation of coherence and polarization by random phase screens and by using liquid crystal

spatial light modulator were examined (Ostrovsky et al., 2009; Shirai and Wolf, 2004). An experimental approach for the estimation of degree of coherence of optical waves polarized in the plane of incidence is investigated recently (Angelsky, Hanson, et al., 2009; Angelsky, Zenkova, et al., 2009). A technique for controlling and synthesizing optical fields in vectorial regime with desired coherence-polarization matrix elements is introduced as an extension of coherence holography (R. K. Singh et al., 2011). Synthesis of vector beam with special correlation functions for the efficient control of intensity distribution and degree of polarization on propagation was introduced very recently (Chen et al., 2014).

The use of fourth order correlation or two point intensity correlation for the measurement of coherence and polarization properties of random field gain a significant attraction very recently (Basso et al., 2014; Hassinen et al., 2011; Tervo et al., 2003). Our technique on experimental determination of generalized Stokes parameters using fourth order correlation based on spatial averaging has potential in characterizing the inhomogeneous polarization states. By following approach of vectorial speckle holography and intensity correlation, we propose a method for analysis of statistical properties of synthesized random field using the 2×2 complex coherence-polarization matrix. The synthesis of random field is created by generating inhomogeneous polarization state at the scattering plane with help of a vortex structure. This vortex phase structure is introduced into one of the orthogonal polarization component of the light at the scattering plane.

4.4.1 Synthesis of coherence-polarization properties of the field

The statistical properties of the fluctuating electromagnetic field propagating very close to the z axis in space-time domain is expressed by the beam coherence-polarization (CP) matrix (Gori, 1998) and is given as

$$W(\boldsymbol{r}_1, \boldsymbol{r}_2, t) = \begin{pmatrix} W_{xx}(\boldsymbol{r}_1, \boldsymbol{r}_2, t) & W_{xy}(\boldsymbol{r}_1, \boldsymbol{r}_2, t) \\ W_{yx}(\boldsymbol{r}_1, \boldsymbol{r}_2, t) & W_{yy}(\boldsymbol{r}_1, \boldsymbol{r}_2, t) \end{pmatrix} \tag{4.27}$$

where $W_{ij}(\boldsymbol{r}_1, \boldsymbol{r}_2, t) = \left\langle E_i^*(\boldsymbol{r}_1, t) E_j(\boldsymbol{r}_2, t) \right\rangle$ with $i = j = x$ or y, $E_x(r,t)$ and $E_y(r,t)$ are the orthogonal polarization components of the field at positions $\boldsymbol{r}$ and time t ,asterisk denotes the complex conjugate and the angular brackets represents the ensemble average. The C-P matrix elements can be directly related to the two point

intensity correlation of the fluctuating electromagnetic field by the relation (Hassinen et al., 2011; Tervo et al., 2003)

$$\Gamma(\mathbf{r}_1, \mathbf{r}_2, t) = \langle \Delta I(\mathbf{r}_1, t) \Delta I(\mathbf{r}_2, t) \rangle = \sum_{i,j} \left| W_{ij}(\mathbf{r}_1, \mathbf{r}_2, t) \right|^2 \tag{4.28}$$

where $\Delta I(\mathbf{r}, t) = I(\mathbf{r}, t) - \langle I(\mathbf{r}, t) \rangle$, $I(\mathbf{r}, t) = |E(\mathbf{r}, t)|^2$ is the intensity at position $\mathbf{r}$ and time t. By following approach discussed in previous section, we demonstrated an experimental scheme for the controlled synthesis and analysis of statistical properties of the fluctuating electromagnetic field.

In this technique the resultant coherence function at the observation plane is superposition of coherence functions of reference random field and a synthesized random field. Therefore the resultant coherence function is given by

$$W_{ij}(\mathbf{r}_1, \mathbf{r}_2) = W_{ij}^R(\mathbf{r}_1, \mathbf{r}_2) + W_{ij}^S(\mathbf{r}_1, \mathbf{r}_2) \tag{4.29}$$

where $W_{ij}^R(\mathbf{r}_1, \mathbf{r}_2)$ and $W_{ij}^S(\mathbf{r}_1, \mathbf{r}_2)$ are the complex coherence functions of the reference random field and synthesized random field for fixed time t.

Synthesis of coherence and polarization properties of the randomly fluctuating electromagnetic field is controlled by a circular aperture of specific size which shapes the spatial degree of coherence at the observation plane and a vortex structure in one of the orthogonal polarization components of the fluctuating field. The vortex structure generates an inhomogeneous polarization structure and able to synthesize the spatial degree of coherence and spatial degree of polarization. The generated optical vortices have the singular point where the amplitude vanishes while around the point of singularity the phase varies as an integral multiple of 2π. The wave front of the vortex beam is helical and complex amplitude of the vortex beam for unit topological charge is represented as $\hat{r} \exp\left(-\hat{r}^2/w^2\right) \exp(i\phi)$, where ϕ is the azimuthal angle in transverse plane and w represents the beam waist of Gaussian profile. In our experimental demonstration we used a spiral phase plate to generate the inhomogeneous polarization structure. A schematic representation of topological charge distribution in the spiral phase plate is shown in Fig. 4.18 (detailed specifications of SPP is included in the Appendix 3).

Vortex Geometry

3	2	1
5		4
8	7	6
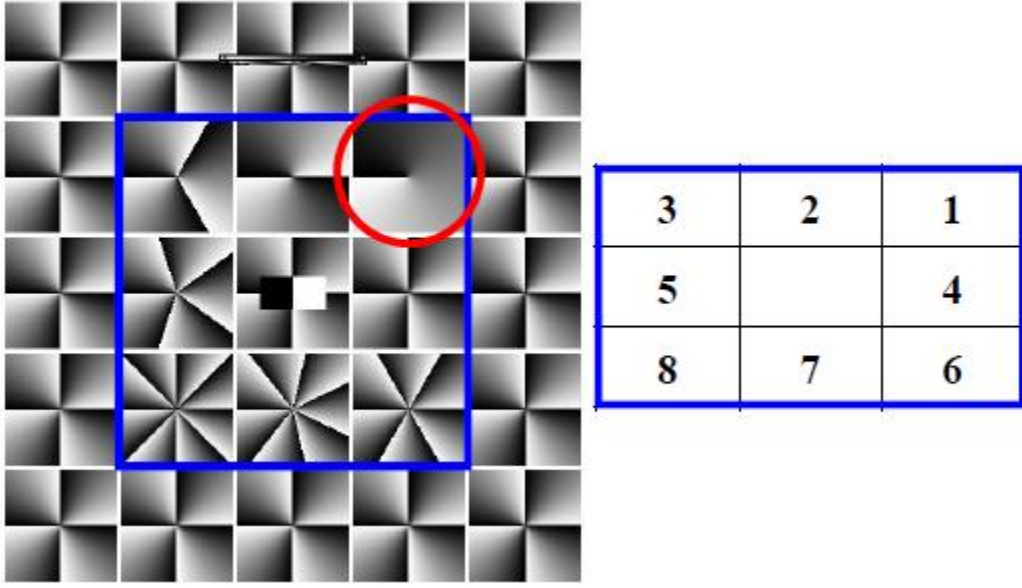
Figure 4.18: A schematic representation of the topological charge distribution in a spiral phase plate (SPP). The highlighted area in red circle is the topological charge 1 which we used in our experiment.

The synthesized CP matrix elements at the Fourier plane is given as

$$W_{ij}^{S}(\Delta \boldsymbol{r}) = \int I_{ij}(\hat{\boldsymbol{r}}) \exp\left[-i\frac{2\pi}{\lambda f}\Delta \boldsymbol{r}.\hat{\boldsymbol{r}}\right] d\hat{\boldsymbol{r}} \qquad (4.30)$$

where $I_{ij}(\hat{\boldsymbol{r}}) = E_i^*(\hat{\boldsymbol{r}})E_j(\hat{\boldsymbol{r}})$ is the vectorial source structure term which determines the synthesize of the randomly fluctuating field in a desired fashion and $\hat{\boldsymbol{r}}$ represents the position vector in the source plane. Eq. (4.30) is nothing but the vectorial van Cittert -Zernike theorem for an electromagnetic field based on spatial averaging(R. K. Singh et al., 2013). Due to the complex nature of the $I_{ij}(\hat{r})$, when $i = j$ the quantity is real and when $i \neq j$ it results in a complex quantity. For the case when one of the orthogonal polarization components generates a vortex beam, $I_{ij}(\hat{\boldsymbol{r}})$ term yields a complex quantity for $i \neq j$. i.e. $I_{ij}(\hat{\boldsymbol{r}}) = |E(\hat{\boldsymbol{r}})|^2 \hat{r} \exp\left(-\hat{r}^2/w^2\right)\exp(i\phi)$ where the amplitudes $|E_i(\hat{\boldsymbol{r}})| = |E_j(\hat{\boldsymbol{r}})| = |E(\hat{r})|$. The synthesized CP matrix elements are determined by the measurement procedure measured in the previous section (a detailed derivation of synthesized CP matrix elements is presented in Appendix 1) and is given by

$$W_{xx}^{S}(\Delta \boldsymbol{r}) = 2\Gamma^{'}(\Delta \boldsymbol{r}, \theta_1)$$

$$W_{yy}^{S}(\Delta \boldsymbol{r}) = 2\Gamma^{'}(\Delta \boldsymbol{r}, \theta_3) + 2\Gamma^{'}(\Delta \boldsymbol{r}, \theta_4) - 2\Gamma^{'}(\Delta \boldsymbol{r}, \theta_1)$$

$$W_{xy}^{S}(\Delta \boldsymbol{r}) = 4\Gamma^{'}(\Delta \boldsymbol{r}, \theta_2) - 2\Gamma^{'}(\Delta \boldsymbol{r}, \theta_1)$$

$$-(1+\sqrt{2}-i)\Gamma^{'}(\Delta \boldsymbol{r}, \theta_3) - (1-\sqrt{2}+i)\Gamma^{'}(\Delta \boldsymbol{r}, \theta_4)$$

(4.31)

$$W_{yx}^{S}(\Delta \boldsymbol{r}) = 4\Gamma^{'}(\Delta \boldsymbol{r}, \theta_2) - 2\Gamma^{'}(\Delta \boldsymbol{r}, \theta_1)$$

$$-(1+\sqrt{2}+i)\Gamma^{'}(\Delta \boldsymbol{r}, \theta_3) - (1-\sqrt{2}-i)\Gamma^{'}(\Delta \boldsymbol{r}, \theta_4)$$

where $\Gamma^{'}(\Delta \boldsymbol{r}, \theta_k)$ with $k = 1, 2, 3$ and 4 represents the inverse Fourier transform of the centrally shifted spectra.

The knowledge of the CP matrix elements gives a direct access to coherence polarization properties of the randomly fluctuating field. The coherence and polarization features of the spatially fluctuating random field is given by the relations (R. K. Singh et al., 2013)

$$\gamma(\Delta \boldsymbol{r}) = \left(\frac{Tr\left[W^{S*}(\Delta \boldsymbol{r})W^{S}(\Delta \boldsymbol{r})\right]}{Tr\ W^{S}(0)Tr\ W^{S}(0)} \right)^{1/2}$$

(4.32)

$$P(0) = \left(1 - \frac{4\det W^{S}(0)}{\left[TrW^{S}(0)\right]^2} \right)^{1/2}$$

(4.33)

where $\gamma(\Delta r)$ is the degree of coherence and $P(0)$ is the spatial degree of polarization.

The relation connecting spatial degree of coherence and spatial degree of polarization is

$$P(0) = \left(2\gamma^2(0) - 1 \right)^{1/2}$$

(4.34)

When degree of coherence $\gamma(0) = 1$, the spatial degree of polarization $P(0) = 1$. i.e. the state of polarization is uniform over the observation plane.

4.4.2 Experiment

An experimental setup devised to synthesize and analyze the statistical properties of the fluctuating electromagnetic field is shown in Fig. 4.19. The experimental setup includes two parts namely synthesis and analysis blocks. Synthesis block (as shown in Fig.4.19 by dotted lines) consists of an inner interferometer to synthesize

the random field in a desired fashion. The analysis block makes use of the speckle interferometric technique and two point intensity correlation based on space averaging. For the measurement of C-P matrix elements a measurement technique based on a quarter wave plate and a linear polarizer is employed in the present experimental demonstration. Description of the experiment is as follows.
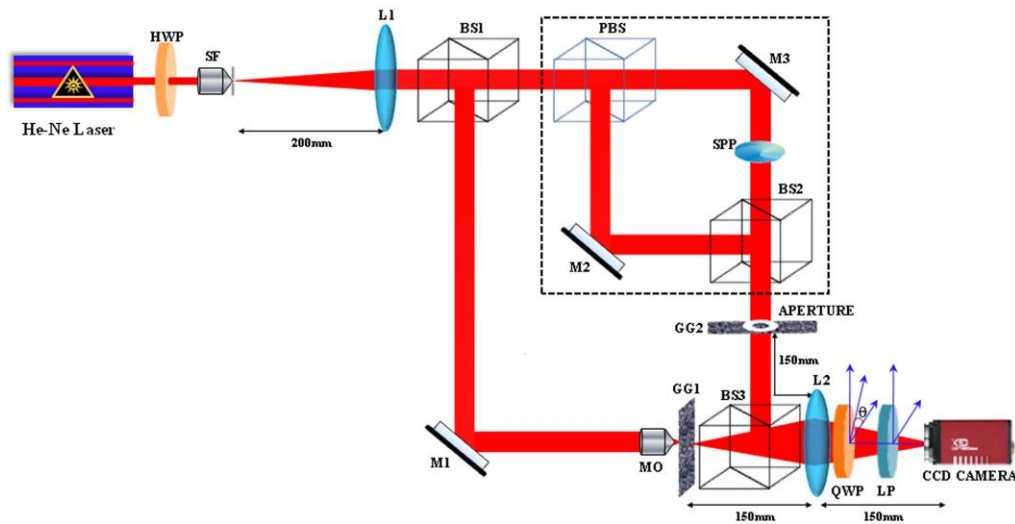
Figure 4.19: Experimental setup for the controlled synthesis and analysis of coherence-polarization properties of the randomly fluctuating field; the synthesis part is shown in dotted block.

A linearly vertically polarized He-Ne laser of wavelength 632.8 nm is oriented linearly 45^0 polarized using a half wave plate (HWP). The beam is filtered using a spatial filter (SF) consisting of a microscope objective and a pinhole combination and collimated with a lens L1 of focal length 200mm. The collimated beam splits into two by a non-polarizing beam splitter BS1 which constitutes the two arms of the Mach-Zehnder type interferometer. The reflected beam from BS1 is folded using a mirror M1and focused to an off axis point on a random phase screen (Ground glass-GG1) using a microscope objective MO of magnification 10X. The scattered field from GG1constitutes the reference arm of the speckle interferometer. The transmitted beam from BS1 splits into orthogonal polarization components using a polarization beam splitter PBS. The reflected and transmitted beams from PBS are folded using mirrors M2 and M3 respectively and combined using a non-polarizing beam splitter BS2. A spiral phase plate SPP is introduced in the transmitted arm from PBS for the controlled synthesis of the statistical properties of the fluctuating electromagnetic field. The SPP is from RPC

photonics, USA and can generate topological charges from one to eight. The fully overlapped orthogonal polarization components from BS2 is allowed to fall on a random phase screen (Ground glass-GG2) controlled by a circular aperture of specific size. Ground glasses GG1 and GG2 with 120 GRIT and generate different sizes of speckle according to the illuminating beam size. Insertion of vortex structure into one of the orthogonal polarization components generates inhomogeneous polarization state at the scattering plane GG2. The speckle field generating from GG2 and GG1 are coherently superposed using a non-polarizing beam splitter BS3 and Fourier transformed using a common lens L2 of focal length 150mm. The resultant scattered field is allowed to pass through a quarter wave plate aligned at an angle θ with X -direction and a linear polarizer filtered in the X-direction. The resultant speckle field intensity are recorded for four specific rotations of the QWP and recorded using a CCD monochrome camera (Prosilica GX 2750). The CCD camera is 14- bit, with 2750×2200 pixels and a pixel pitch of 4.54μm.

4.4.3 Results and Discussion

The controlled synthesis of coherence-polarization properties of the randomly fluctuating field is achieved by using a circular aperture placed very close to the random phase screen and controlling one of the orthogonal component in the object arm of the Mach- Zehnder interferometer with a spiral phase plate having topological charge one. A coherent beam illuminates the ground glass GG2 and generates a random field which is completely coherent and polarized (in a usual sense). The degree of polarization is unity everywhere, though the state of polarization gradually changes from point to point at the observation plane. However, the spatial random fluctuation of such speckle field can be described by replacing ensemble average with spatial average (rather than in time) and the corresponding degree of coherence and the spatial degree of polarization can be defined for such spatially fluctuating fields(R. K. Singh et al., 2013, 2014). The random field is controlled by the aperture at the GG2 plane that shapes the coherence-polarization properties of the field at the CCD plane. Note that this random field is spatially fluctuating in space and a direct relation between source structure and coherence-polarization properties at the CCD plane is given by the vectorial van Cittert-Zernike theorem. Each combination of the QWP and LP gives

speckle field intensity and is captured at the CCD plane. On considering the space average of the resultant intensity at this plane the two point intensity correlations for four different combinations results into holograms. The use of Fourier transform method to intensity correlation hologram and by using Eq. (4.31) the desired C-P matrix elements can be retrieved. In the experimental implementation initially the two orthogonal polarization components are fully overlapped and then controlled by a circular aperture at the GG2 plane.
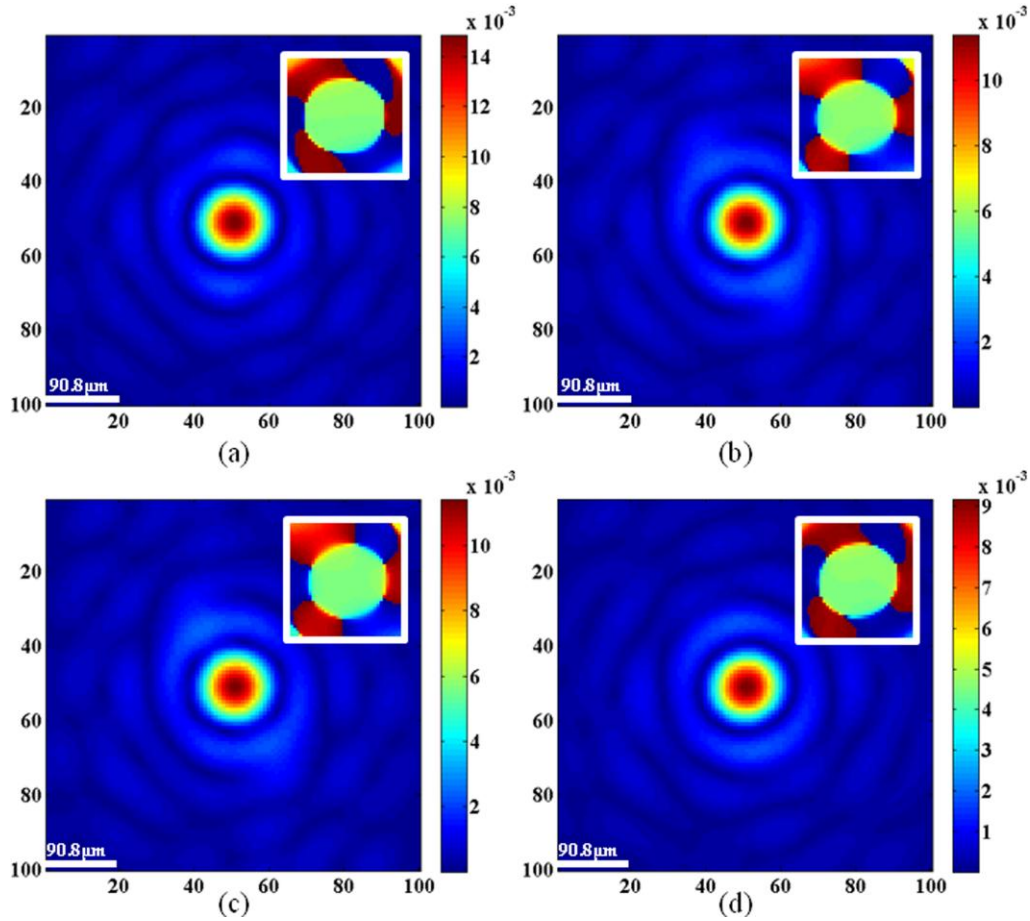
Figure 4.20: Amplitude and phase (shown in inset) distribution of C-P matrix elements for a beam controlled by a circular aperture of 2mm diameter (a) $W_{xx}^{S}(\Delta r)$ (b) $W_{xy}^{S}(\Delta r)$ (c) $W_{yx}^{S}(\Delta r)$ and (d) $W_{yy}^{S}(\Delta r)$. The values on X-axis and Y-axis represent the X-pixels and Y-pixels respectively at the CCD plane and the color bar represent the intensity.

In the second case in one of the orthogonal polarization component in the object arm of the interferometer a SPP with a topological charge one is inserted so that it will generate a vortex beam at this arm. The generation of a vortex beam in this

arm provides the opportunity to synthesize the randomly fluctuating field in a desired fashion according to Eq. (4.30). The amplitude and phase distribution (shown in inset) of synthesized C-P matrix elements for the two different cases are shown in Fig. 4.20 and 4.21 respectively. Fig. 4.20(a)-4.20(d) shows the amplitude distribution and in insets its corresponding phase distribution of C-P matrix elements when the fully overlapping orthogonal polarization components at the GG2 plane is controlled by a circular aperture of 2mm diameter. The circular aperture controls the source structure term $I_{ij}(\hat{r})$ and results in CP matrix elements as given by Eq. (4.30). The uniform phase distribution with a zero index value shown in insets of Fig. 20 explains the full overlapping and thereby negligible phase difference among the orthogonal components of the field.
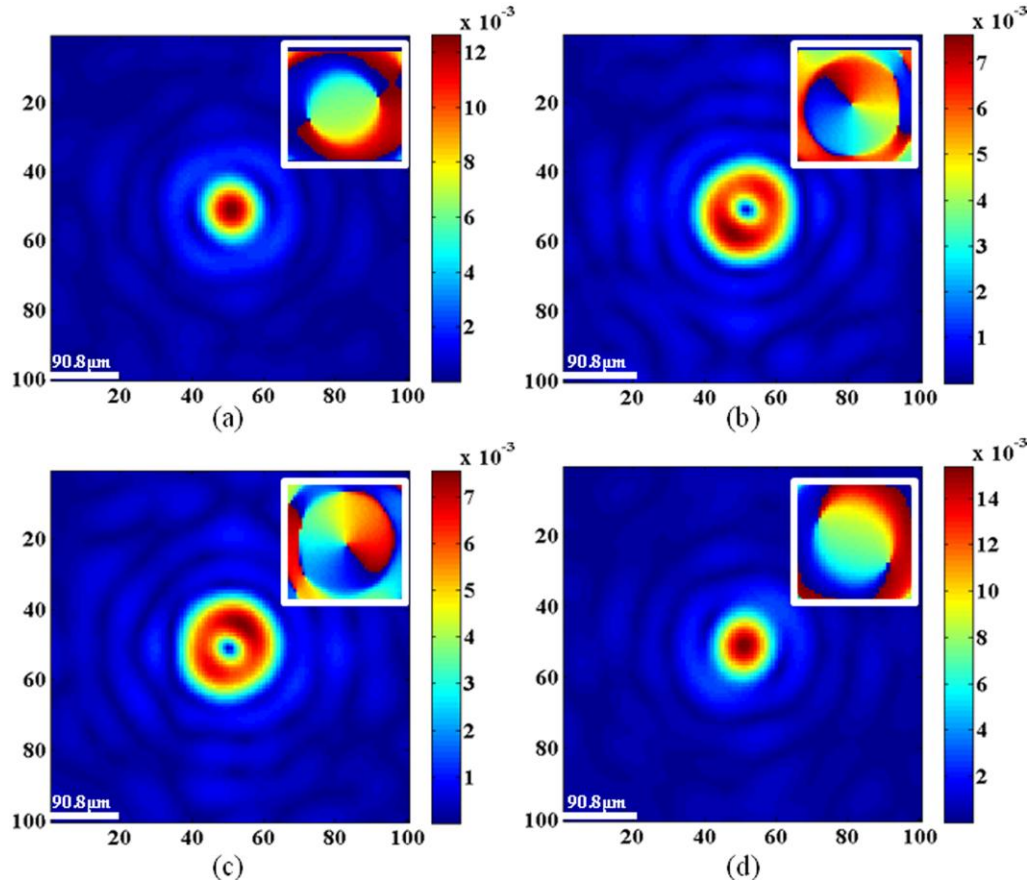
Figure 4.21: Amplitude and phase (shown in inset) distribution of C-P matrix elements for a beam controlled by a circular aperture of 2mm diameter and an SPP is introduced in one of the orthogonal components (a) $W_{xx}^{S}(\Delta r)$ (b) $W_{xy}^{S}(\Delta r)$ (c) $W_{yx}^{S}(\Delta r)$ and (d) $W_{yy}^{S}(\Delta r)$. The values on X-axis and Y-axis represent the X-pixels and Y-pixels respectively at the CCD plane and the color bar represent the intensity.

Insertion of vortex into one of the orthogonal polarization component modifies the source structure term and generates an inhomogeneous polarization state at the GG2 plane. Fig. 4.21(a) and 4.21(d) shows the amplitude distribution and in insets its corresponding phase distribution for the case when $i = j = x$ or y i.e. the diagonal elements $W^S_{xx}(\Delta r)$ and $W^S_{yy}(\Delta r)$ of the C-P matrix. A uniform phase distribution with zero phase value is observed in the diagonal elements of C-P matrix. The off diagonal elements of C-P matrix $W^S_{xy}(\Delta r)$ and $W^S_{yx}(\Delta r)$ i.e. for the case when $i \neq j$ are shown in Fig. 21(b) and 21(c) respectively. It shows the presence of a dark core surrounding by uniform intensity pattern. In insets of Fig. 4.21(b) and 4.21(c) the phase distribution of $W^S_{xy}(\Delta r)$ and $W^S_{yx}(\Delta r)$ are shown. A helicoidal phase structure is clearly visible in the off diagonal elements of the C-P matrix. The generation of a doughnut structure with helicoidal phase structure in off diagonal elements of C-P matrix is attributed to the complex nature of source structure $I_{ij}(\hat{r})$ as given by Eq. (4.30). i.e. the vectorial source structure term $I_{ij}(\hat{r})$ modifies to $I_{ij}(\hat{r}) = |E(\hat{r})|^2 \hat{r} \exp\left(-\hat{r}^2 \middle/ w^2\right) \exp(i\phi)$ and results in a synthesized off diagonal elements of the CP matrix. Generation of the vortex term in the two point correlation function is very significant in order to synthesize the statistical properties of the random field as has been explained.

The degree of coherence and spatial degree of polarization are determined by making use of Eq. (4.32) and Eq. (4.32) respectively. For comparison purpose, both analytical and experimental results are presented in Fig. 4.22 and Fig. 4.23 for two different cases where blue line and red dotted line represent the analytical and experimental results respectively. Fig. 4.22 represents the plot of profile when the fully overlapping beam is controlled by a circular aperture of 2mm diameter at the GG2 plane. The degree of coherence at the centre is expected to be unity and in the experimental result shows a very near unity value (i.e 0.99). The spatial degree of polarization is found to be 0.99 which is very close to the expected unity value which shows the state of polarization is uniform over the observation plane. Fig. 4.23 represents the plot of the profile of degree of coherence when the SPP is introduced in one of the orthogonal component. The presence of vortex beam with unit topological charge in one of the component shapes the off-diagonal elements

of the C-P matrix and there by synthesize the degree of coherence and spatial degree of polarization. The degree of coherence decreases from its unity value to 0.7016 and correspondingly the spatial degree of polarization decreases from unity to an expected zero value. Good agreements between experimental and theoretical results are observed in the plot of the profiles shown in Fig.4.23 and 4.23. A small deviation especially in outer side lobes of theoretical and experimental results in Fig. 22 and Fig. 23 may be attributed to the assumption of uniform aperture illumination on the ground glass GG2.
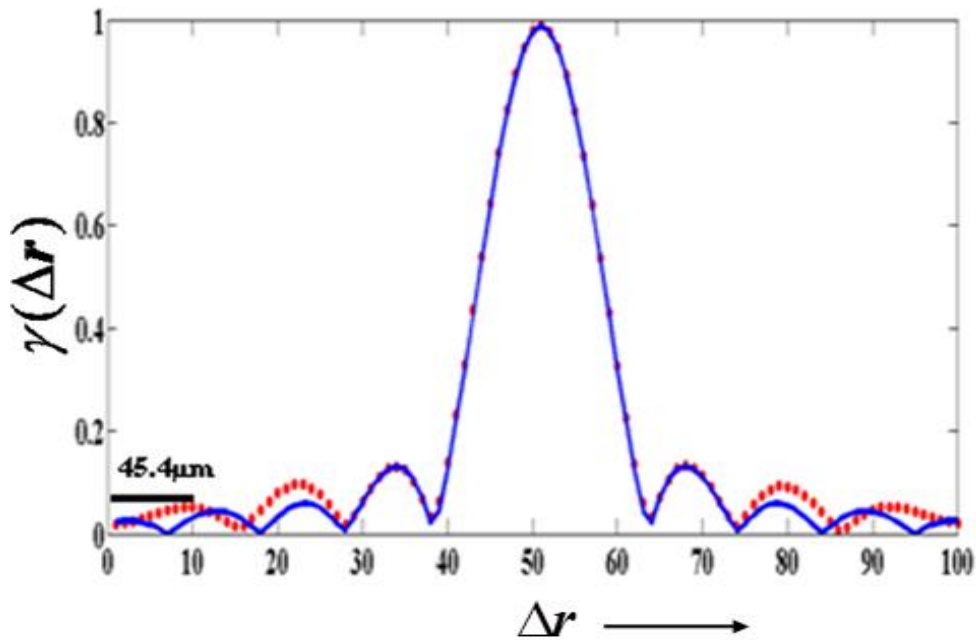
Figure 4.22: Plot of the analytical and experimental profile of degree of coherence for a beam controlled by a circular aperture of diameter 2mm ($\Delta r = 4.54 \mu$m).
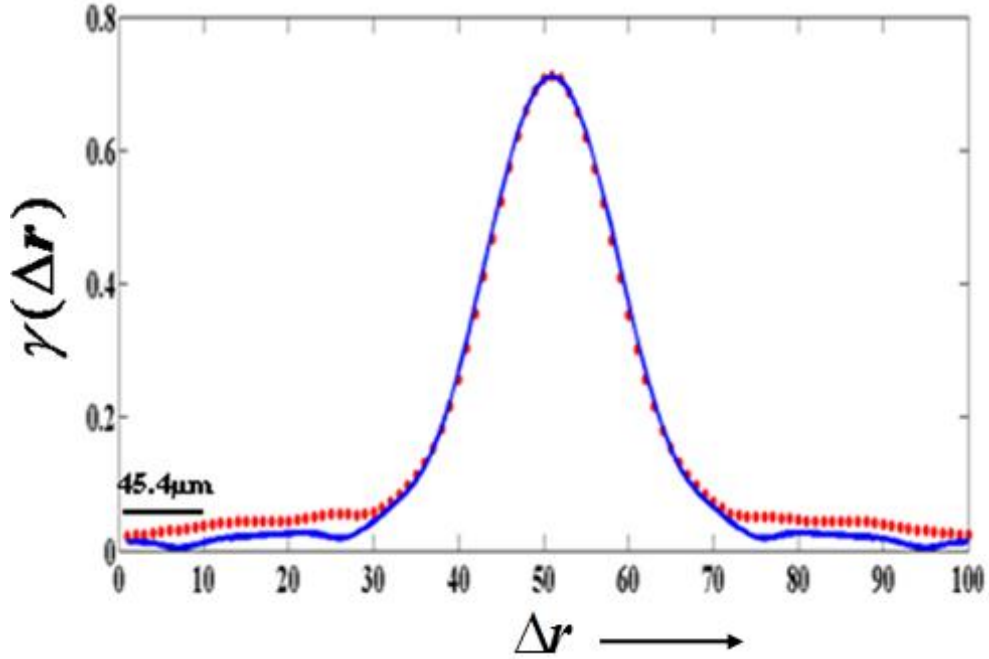
Figure 4.23: Plot of the profile of analytical and experimental results of degree of coherence for a beam controlled by a circular aperture of diameter 2mm and insertion of an SPP with unit topological charge in one of the orthogonal component of polarization ($\Delta r = 4.54 \mu$m).

In summary, an experimental technique is demonstrated for the controlled synthesis and analysis of the statistical properties of a polarized field. The proper selection of the source structure and controlling the orthogonal polarization components of the field with vortex beam provides a good control over the C-P matrix elements. Agreement between experimental and analytical results validates the application of the technique in the controlled synthesis of the statistical properties of the fluctuating electromagnetic field.

4.5 Conclusion

The role of intensity based interferometers in the analysis of laser speckle pattern is discussed and experimentally demonstrated by developing various techniques. Generation of singular point array using fourth order correlation is experimentally demonstrated. A technique for the recovery of complex coherence function using fourth order correlation and speckle holographic approach is proposed and experimentally demonstrated. An extension of the proposed technique to vectorial regime is demonstrated by experimental determination of complex GSPs of the

spatially fluctuating random field. This technique has potential applications in synthesis of coherence and polarization properties of the fluctuating field and also in correlation based imaging. Application of the proposed technique in controlled synthesis of statistical properties of the spatially fluctuating random field is experimentally demonstrated.

CHAPTER 5

IMAGING THROGH SCATTERING MEDIA

Optical imaging through complex scattering media is one of the major technical challenges with important applications in many research fields, ranging from biomedical imaging, astronomical telescopy, and spatially multiplex optical communications. Light propagating through complex scattering layers suffers diffuse scattering due to the inhomogenities of refractive index of the scattering layers which makes it difficult for conventional imaging techniques. The complex valued object information is scrambled in the scattered grainy intensity pattern called the laser speckle. Techniques for extracting information from laser speckles are a tedious process and it starts since the invention of laser. Initial work on coherent propagation of light through scattering media starts from the work of Leith and Upatneik in 1966, where they used a hologram to recover the object information through a scattering medium (Leith and Upatnieks, 1966). A significant number of techniques for imaging through random media based on holographic principles were introduced later (Goodman et al., 1966; Kogelnik and Pennington, 1968; E. Leith et al., 1992). The work by Yaqoob using a phase conjugating crystal made it possible to imaging for biomedical samples (Yaqoob et al., 2008). The methods in which the image is back projected at the position of the object are not have much potential in the case of imaging of objects hidden behind the scattering medium. On the other hand developments in optical coherence tomography arise as a powerful method of imaging which uses only the ballistic light and separates the scattered light (Fercher, 1996; Huang et al., 1991). However for the mediums which produce a large amount of multiple scattering, tomography technique have limitations and the imaging will be a challenge.

Very recently remarkable achievements towards the direction of non-invasive imaging through scattering layers were demonstrated. The technique presented by Bertolotti (2012) uses an angular speckle correlation to image a fluorescent object inside an opaque layer (Bertolotti et al., 2012). The angular scanning of speckle pattern results in a long acquisition time of images and limits

the object to be stationary for the complete acquisition period. The non-invasive single shot imaging technique presented by Katz (2014) capable to overcome the limitation of long acquisition period by capturing the speckle pattern in single-shot but is limited by the actual depth resolved imaging behind the scattering medium and a 3D recovery of object information (Katz et al., 2014). For the complete retrieval of complex valued object information from the autocorrelation function both of these techniques employed a phase retrieval algorithm which can become computationally heavy when dimensions become large and iteration number increases. Moreover, this iterative technique is applied only for the real valued objects.

Holographic methods have remarkable importance in imaging applications, since these methods offer a potential tool to extract both the intensity and phase information. Significant new advances in optical holography, electron holography and X-ray holography open the door to a wide variety of applications by increasing the resolution in comparison with conventional imaging techniques (Lichte and Lehmann, 2008; Tegze and Faigel, 1996; Xu et al., 2001). Atomic scale resolution achieved in electron holography is made utilized in determination of atomic species and interatomic fields (Lichte and Lehmann, 2008). The progress in X-ray holography technique provides new dimensions in crystallographic applications and gives the potential of internal structure imaging in solids (Tegze and Faigel, 1996). Also in the optical domain the recent advances in the holography techniques provide new potential in three dimensional (3D) imaging with high spatial resolution (Kelner and Rosen, 2012; Kreis, 2005; Nomura and Imbe, 2010). In addition, the effort in digital inline holography with numerical reconstruction techniques emerge as a new tool in biological applications and the lateral and depth resolution achieved in 3D imaging gives the potential to overcome limitations in conventional light microscopy (Garcia-Sucerquia et al., 2006; Xu et al., 2001). Recently an angle resolved light scattering measurement is demonstrated by using digital inline holography in combination with Fourier transform light scattering (K. Kim and Park, 2012). However, the use of existing holographic methods is significantly limited when complex scattering media is involved due to the scrambling of optical information into complex speckle patterns. Recovery of holographic information from the speckle field is a challenging task due to the complete scrambling of the information

In this chapter firstly we describe an experimental demonstration of recovery of complex valued object behind the scattering layer using two point intensity correlation and speckle holographic technique. Secondly we propose and experimentally demonstrate the potential of the developed technique in non-invasive true sense single shot imaging through scattering layers by recovering the hologram behind the scattering layer. Finally we extend technique in digital inline holographic non-invasive imaging through scattering layers and demonstrate its potential in depth resolved imaging. Here we use the term true sense single shot because the technique used by Katz et.al is not true sense single shot but its assisted by heavy image processing operation.

5.1 Complex valued object recovery using two point intensity correlation

Recovery of the complex field, i.e. amplitude and phase, of the light is of long standing interest. Holography has provided the means to both record and reconstruct complex wave fronts reflected from or transmitted through objects (M. K. Kim, 2011; Kreis, 2005). However, when the object is highly scattering, the phase and amplitude of light coming from it become fluctuating random fields and generates random speckle pattern that hides any deterministic information bearing components whose recovery is considered to be difficult or impossible. Correlation based technique has been employed to visualize and measure the hidden information of the object (Bartelt et al., 1984; Gamo, 1963; Gong and Han, 2010; Marathay et al., 1994). A recent development in this direction was the construction of Fourier transform holograms corresponding to intensity correlation (Naik et al., 2011; Takeda et al., 2005) wherein computed intensity correlation, i.e. fourth order correlation, is made use of to record the information available in the mutual intensity. In correlation holography techniques, the hologram of a 3-D object is reconstructed using an illumination through a random phase screen (Naik et al., 2011). The random phase-screen scrambles light and generates speckle patterns, from which the 'object' is recovered from the computed spatial covariance function. This works perfectly well to reconstruct amplitude of the object, but is not adequate to recover its phase since the intensity covariance is related to the modulus of the second order correlation (which is the mutual

coherence function). There have been attempts to recover this phase using higher order correlation and phase retrieval techniques (Bartelt et al., 1984; Fienup, 1982; Gamo, 1963; Marathay et al., 1994). A two-point intensity correlation is also tried to recover this phase (Ebstein, 1991).

In this section we describe a two-point intensity correlation strategy that does not make use of a phase retrieval algorithm. The advantage of recovering the object in its entirety, i.e. amplitude and phase, is that even a 3D recovery is possible through holographic reconstruction, usually implemented numerically from a single speckle intensity covariance. Our main objective in this work is to demonstrate experimentally the recovery of a complex coherence function, and through it, the recovery of a complex valued object (including its phase). Since we use holographic recording and recovery using a random phase screen, we can demonstrate retrieval of object information hidden behind a scattering medium. In our experimental approach we coherently add a 'reference' speckle from an independent scattering layer with the speckle pattern resulting from the hologram (through illumination from a scattering layer). Therefore what we record is a 'speckle hologram'. From this speckle hologram we demonstrate the reconstruction of the complex coherence function by numerically back-propagating the estimate of the cross-covariance of the recorded intensity fluctuation.

5.1.1 Implementation of the technique

Implementation of our proposed technique is shown in Fig. 5.1. An object beam is combined with a reference beam, a tilted plane wave, (plane I in Fig. 5.1) realizing overall complex amplitude

$$E_H(\hat{\boldsymbol{r}}) = E_O(\hat{\boldsymbol{r}}) + a(\hat{\boldsymbol{r}}), \tag{5.1}$$

where $\hat{\boldsymbol{r}}$ is transverse spatial coordinate on the plane I. The object and reference fields distributions at the recording plane are denoted by $E_O(\hat{\boldsymbol{r}})$ and $a(\hat{\boldsymbol{r}}) = |a(\hat{\boldsymbol{r}})| \exp[-i2\pi\hat{a}\hat{\boldsymbol{r}}]$, respectively. Tilt of the reference beam is denoted in terms of the spatial frequency $|\hat{\alpha}| = \sin(2\theta/\lambda)$, , where 2θ is tilt of the reference wave. The intensity of the hologram at the plane I is given by

$$I_H(\hat{\boldsymbol{r}}) = \left|E_O(\hat{\boldsymbol{r}})\right|^2 + \left|a(\hat{\boldsymbol{r}})\right|^2 + E_O^*(\hat{\boldsymbol{r}})a(\hat{\boldsymbol{r}}) + E_O(\hat{\boldsymbol{r}})a^*(\hat{\boldsymbol{r}}). \qquad (5.2)$$
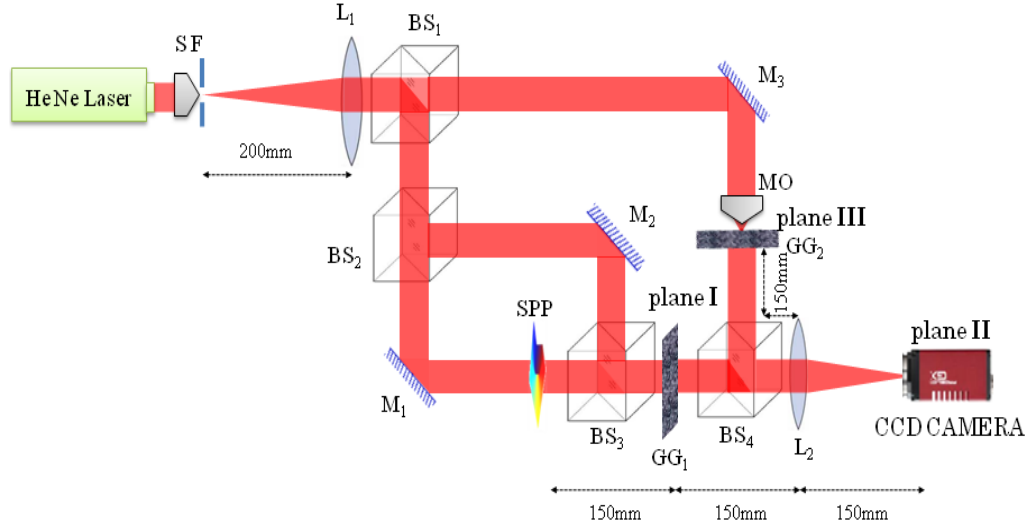
Figure 5.1: Experimental implementation of the proposed technique

We use this intensity distribution corresponding to a hologram and apply an experimental strategy to retrieve the complex coherence function of the speckle field shaped by the hologram from a single shot measurement of the intensity distribution. A linearly polarized He-Ne laser beam of wavelength 594.1nm is filtered and collimated by a spatial filter lens assembly (SF&L_1). The collimated beam is split into two and folded by mirrors M_1 and M_3 and recombined by a non-polarizing beam splitter BS_4 forming a Mach-Zehnder interferometer. The beam reflected from BS_1 is split into two by another non-polarizing beam splitter BS_2 to make a Mach-Zehnder interferometer within the first to record the hologram corresponding to the phase object generated by the spiral phase plate (SPP) with a tilted reference beam (Eq. (5.1)). (The SPP is from the RPC photonics, USA, and can generate vortices with topological charge varying from one to eight. Details are included in the Appendix 3). The topological charge of the vortex beam represents accumulated phase variation around the point of phase singularity in order of integral multiple of 2π. The complex amplitude of the vortex beam is expressed as $r^m \exp\left[-r^2/w^2\right]\exp(im\varphi)$, where φ is the azimuthal angle on the transverse plane, w represents the 'size' of the Gaussian profile, and m is topological charge of the vortex. The object beam reflected off mirror M_1 and containing the vortex phase information is combined with the reference beam

coming from mirror M$_2$ with the help of the beam splitter BS$_3$. The combined beam is scrambled using a static scattering layer/ground glass screen GG$_1$ (plane I) placed at distance of 150mm from SPP. We note that the hologram is not recorded on GG$_1$ but scrambled and scattered off. The 'hologram' beam from GG$_1$ is combined with a reference beam (generated by the off-axis point source obtained with the help of a microscope objective MO focusing light onto a static ground glass plate, GG$_2$,denoted as plane III in Fig. 5.1) with the help of the beam splitter BS$_4$. The light distributions at the ground glass plates GG$_1$ and GG$_2$ are Fourier transformed by the lens L$_2$ of focal length 150mm, onto the monochrome CCD camera. The camera is of 14-bit dynamic range, with 2750×2200 pixels and a pixel pitch of 4.54μm (Prosilica GX2750). The resultant speckle field intensity is our data which is recorded using the camera. Both the ground glasses are static during the recording of the resultant speckle intensity.

5.1.2 Recovery of the wave front

In our experiment, we have not recorded a hologram, but instead allowed the combined complex wave to propagate through ground glass. The complex amplitude immediately behind the ground glass, expressed as $\exp[i\phi(\hat{r})]$, with $\phi(\hat{r})$ being the random phase, is

$$\tilde{E}(\hat{r}) = E_H(\hat{r})\exp[i\phi(\hat{r})].\tag{5.3}$$

We employ a lens L$_1$ in Fig.5.1 to Fourier transform the complex field given in Eq. (5.3), and the complex field at the Fourier transform plane, which is plane II in Fig. 5.1, is given as

$$E_H(\boldsymbol{r}) = \int E_H(\hat{r})\exp[i\phi(\hat{r})]\exp\left(-i\frac{2\pi}{\lambda f}\boldsymbol{r}.\hat{r}\right)d\hat{r}.\tag{5.4}$$

Here $\boldsymbol{r}$ is the transverse spatial co-ordinate at plane II, f is the focal length of lens L$_1$ and λ is the illumination wavelength. The intensity available at the plane II is $I_H(\boldsymbol{r}) = E_H^*(\boldsymbol{r})E_H(\boldsymbol{r})$, which allows us to estimate the covariance function corresponding to $I_H(\boldsymbol{r})$ which is. $C_H(\boldsymbol{r},\boldsymbol{r}+\Delta\boldsymbol{r}) = \langle\Delta I_H(\boldsymbol{r})\Delta I_H(\boldsymbol{r}+\Delta\boldsymbol{r})\rangle$, Here $\langle.\rangle$

represents ensemble average and $\Delta I_H(\mathbf{r}) = I_H(\mathbf{r}) - \langle I_H(\mathbf{r}) \rangle$ is the spatial fluctuation of the intensity with respect to its average value.

We assume the complex amplitude is a realization of a spatially stationary random field and therefore its covariance function, $C_H(\mathbf{r}, \mathbf{r} + \Delta \mathbf{r})$,, depends on the difference coordinate $\Delta \mathbf{r}$,. Moreover, the random field is assumed to be ergodic with respect to the spatial coordinates, and therefore ensemble averaging can be achieved through averaging over patches of speckle at different spatial locations as discussed in our previous demonstrations. With this

$$C_H(\mathbf{r}, \mathbf{r} + \Delta \mathbf{r}) = \langle \Delta I_H(\mathbf{r}) \Delta I_H(\mathbf{r} + \Delta \mathbf{r}) \rangle_S , \tag{5.5}$$

where $\langle \ \rangle_S$ denotes spatial averaging.

Assuming that the random field, such as laser speckle in our case, obeys Gaussian statistics the fourth order correlation available in $C_H(\Delta \mathbf{r})$ can be expressed in terms of its second order correlation $W_H(\Delta \mathbf{r})$, as

$$C_H(\Delta \mathbf{r}) \propto |W_H(\Delta \mathbf{r})|^2 \tag{5.6}$$

From van Cittert-Zernike theorem(R. K. Singh et al., 2013) we know that $W_H(\Delta \mathbf{r})$, is related to the intensity $I_H(\hat{\mathbf{r}})$, at plane I through a Fourier transform:

$$W_H(\Delta \mathbf{r}) = \int I_H(\hat{\mathbf{r}}) \exp\left(-i \frac{2\pi}{\lambda f} \hat{\mathbf{r}}.\Delta \mathbf{r} \right) d\hat{\mathbf{r}}. \tag{5.7}$$

We would like to point out that the accuracy of recovery of the 'object', using Eq.(5.7) is dependent on the validity of assumptions of spatial stationarity and Gaussian statistics used in Eqs.(5.5) and (5.6). The quality of full-field reconstruction is questionable if spatial stationarity is ensured only in patches in the Fourier plane, i.e., plane II in Fig. 5.1. Deterioration of reconstruction resulting from deviation from the spatial stationarity has pointed out (Takeda, 2013). The spatial resolution achieved in the reconstruction is also limited owing to the cap imposed on the spatial finesse of the hologram by the finite correlation length of the random phase screen used in the experiment (as the smallest resolvable

distance is dictated by correlation length of the scatterer) even though we assume the random screen to be delta correlated. In case this assumption of 'ideal' phase screen is valid, the resolution of the recovered object depends only on the size of the hologram and f number of the Fourier transforming lens used.

From Eq. (5.6) it is obvious that from the measured $C_H(\Delta r)$, we can only have the modulus of $W_H(\Delta r)$ directly. This means that for a full recovery of the object the lost phase in $W_H(\Delta r)$ has to be retrieved. Here, we used the holographic approach that we used to recover the complex coherence function as discussed in section 4.2. For this, at plane II we introduce a 'speckle field' coherent with respect to $W_H(\Delta r)$. This makes the intensity at plane II correspond to a hologram given by

$$I(\boldsymbol{r}) = \left| E_H(\boldsymbol{r}) + E_R(\boldsymbol{r}) \right|^2, \tag{5.8}$$

where $E_R(\boldsymbol{r})$ is the speckle field from the reference source. Since the intensity is a hologram, the mutual coherence function corresponding to it should have contributions arising from $\left| E_H(\boldsymbol{r}) \right|^2$, $\left| E_R(\boldsymbol{r}) \right|^2$ and the mixed term (all computable invoking Eq. 5.7). However, since the ground glasses used to realize the object- and reference beams are different, we are justified in taking the contribution from the mixed term zero, i.e. $\left\langle E_H^*(\boldsymbol{r}) E_R(\boldsymbol{r}_1 + \Delta r) \right\rangle = 0$. Therefore the resultant mutual coherence function from the resultant intensity at plane II is

$$W(\Delta \boldsymbol{r}) = W_H(\Delta \boldsymbol{r}) + W_R(\Delta \boldsymbol{r}), \tag{5.9}$$

This 'speckle holography' technique offers a solution to the phase problem hidden in Eq. (5.6). In other words, if the mutual coherence function from a reference speckle pattern is available, that arising from an 'object' speckle pattern can be determined. In this work, we recover the complex coherence function of the laser speckle arising out of an object hidden behind a random phase screen and employ this for the recovery of the hidden object, both amplitude and phase.

Since the 'reference' beam is at $\hat{r} = \hat{r}_g$ is introduced by an off-axis source of radius 'a' (at plane III in Fig. 5.1), $W_R(\Delta r)$ is given by

$$W_R(\Delta r) = \left\langle E_R(r) E_R^*(r + \Delta r) \right\rangle_S = \int circ\left(\frac{\hat{r} - \hat{r}_g}{a}\right) \exp\left[-i\frac{2\pi}{\lambda f}\hat{r}.\Delta r\right] d\hat{r}. \qquad (5.10)$$

When '$\hat{r} = \hat{r}_g$' is small $W_R(\Delta r)$ effectively provides a constant 'reference' wave covering the support of $W_H(\Delta r)$ to record the hologram $\left|W(\Delta r)\right|^2$

$$\left|W(\Delta r)\right|^2 = \left|W_H(\Delta r)\right|^2 + \left|W_R(\Delta r)\right|^2 + W_H(\Delta r) \times W_R^*(\Delta r) + W_H^*(\Delta r) W_R(\Delta r). \qquad (5.11)$$

From this hologram we can recover the complex coherence function of the object speckle, i.e. $W_H(\Delta r)$ and it's conjugate $W_H^*(\Delta r)$. We recall that $\left|W(\Delta r)\right|^2$ is obtained from the overall intensity covariance function, $C(\Delta r)$ obtained from the measured intensity. We 'reconstruct' the desired complex coherence function from the hologram $\left|W(\Delta r)\right|^2$ numerically using Fourier transform operation.

5.1.3 Results and Discussions

The reconstruction of the complex coherence function and through it the complex phase structure of the vortex object, from the recorded speckle intensity is carried out numerically by first estimating the intensity covariance distribution $C(\Delta r) = \left\langle \Delta I(r) \Delta I(r + \Delta r) \right\rangle$. The resultant speckle fields recorded by the CCD camera for three vortices with topological charges m = 3, 6 and 8 are shown in Figs. 5.2(a)-5.2(c) respectively.
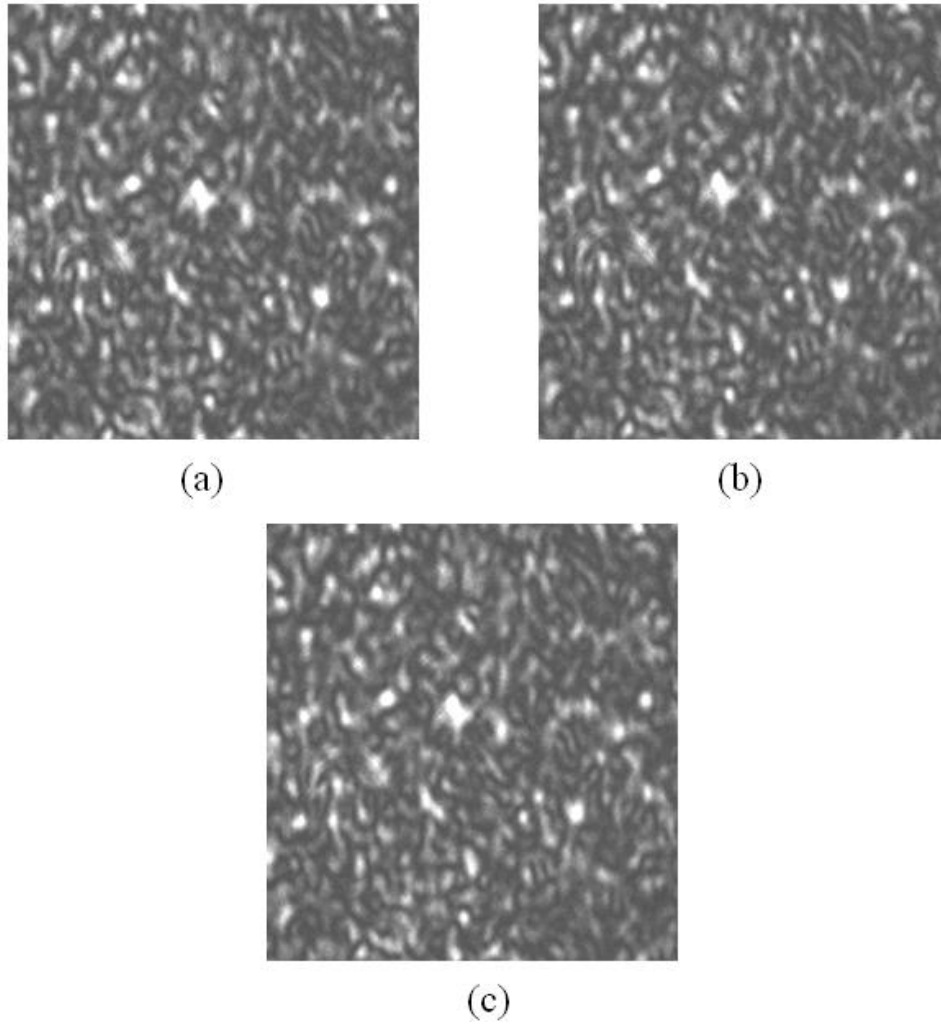
Figure 5.2: Resultant speckle intensities recorded by the CCD camera, (a) for vortex charge 3 (b) for vortex charge 6 (c) for vortex charge 8.

Information of the vortex is completely scrambled into the speckle pattern. Results of the cross-covariance of the intensity for corresponding three speckle fields are shown in Figs. 5.3(a)-5.3(c). Fig. 5.3(a) and 5.3(b) are results for vortex with charge three and six respectively, whereas Fig. 5.3(b) is for topological charge eight. Presence of fringe patterns in Figs. 5.3(a)-5.3(c) can be explained on the basis of Eq. (5.11).
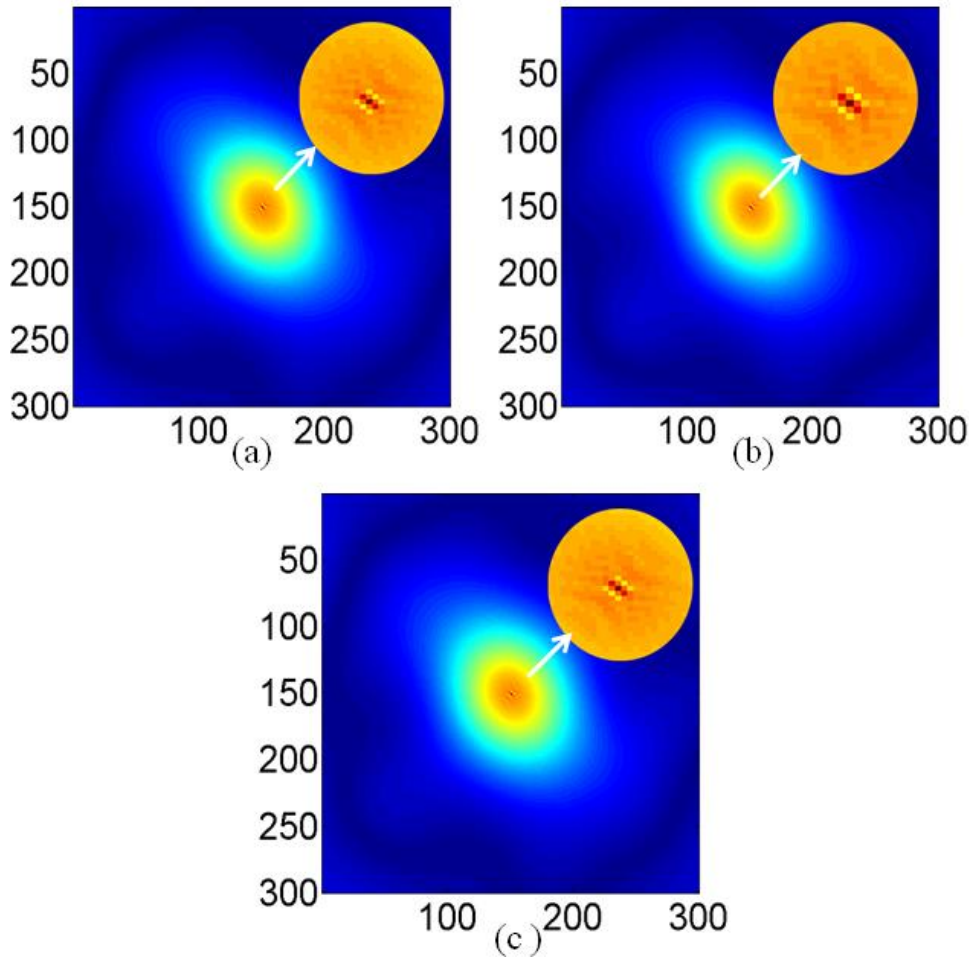
Figure 5.3: Results of space averaged cross-covariance function from the recorded speckle intensities, (a) for vortex charge 3 (b) for vortex charge 6 (c) for vortex charge 8. The arrows point out the magnified interference fringes of the cross-covariance of the intensity correlation. The values on X-axis and Y-axis represent the X-pixels and Y-pixels respectively at the CCD plane.

By the use of Fourier fringe analysis approach, the Fourier spectra are separated on the basis of the spatial carrier frequency. By making sure that the high spatial carrier frequency introduced by tilt in the reference coherence function is large enough, the interference terms can be separated in the frequency plane. The Fourier spectra of the cross-covariance of the intensity snapshots are shown in Fig. 5.4(a) -5.4(c) for three values of topological charge set in the SPP at 3, 6 and 8. We note that the strong central frequency content in Fig. 5.4 is digitally suppressed to highlight the presence of the fork structure in the Fourier spectral plane. Presence of this fork structure confirms encoding of the vortex in the hologram. Extra lines in the fork grating provide information on topological charge of the vortex. For

example three extra lines in the fork structure of the Fig. 5.4(a) show that topological charge of the vortex is three. We would like to emphasize and highlight here that these fork structure exists in the distribution of intensity correlation rather than that at direct intensity. This is very important feature to distinguish physical properties of deterministic and non-deterministic light sources. The structure in Figs. 5.4(a)-5.4(c) can be numerically back propagated, using digital holographic principles, to retrieve the phase object at the SPP.
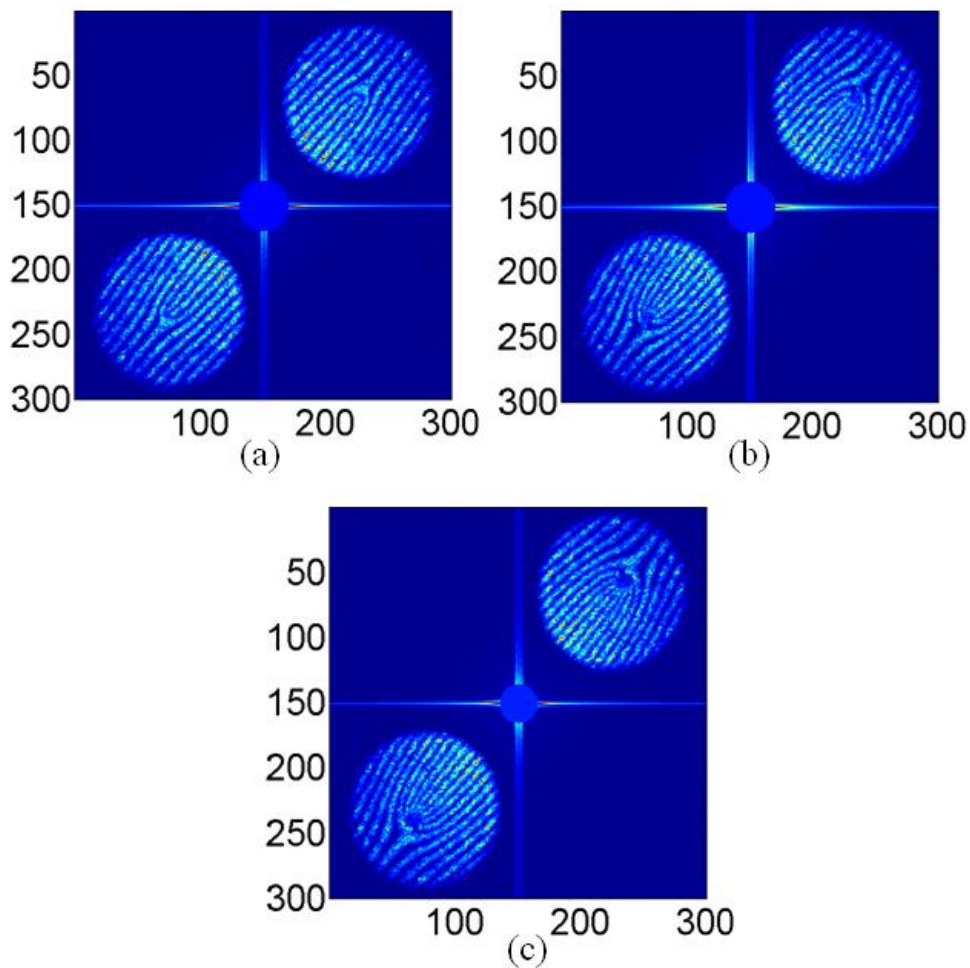
Figure 5.4: Fourier transform of the cross-covariance distributions of the vortex object, (a) for vortex charge 3 (b) for vortex charge 6 (c) for vortex charge 8. The values on X-axis and Y-axis represent the X-pixels and Y-pixels respectively at the ground glass plane (plane I).

However, in the present work our aim is only to reconstruct the complex coherence function of the scattered field at the Fourier plane. Since we have retrieved the complex coherence function, it also contains the phase of the object encoded in the hologram. This information is retrieved through inverse Fourier transforming the

centrally shifted first order components from Figs. 5.4(a) to 5.4(c) and the results are shown in Figs. 5.5 (a) to 5.5(c) respectively. Fig. 5.5(a) shows the vortex of topological charge 3 and it's conjugate. Figs. 5.5 (b) and 5.5(c) are for charges 6 and 8 respectively. The corresponding phase structures of the reconstructed vortices are also shown in Figs. 5.5(a) to 5.5(c) in insets.
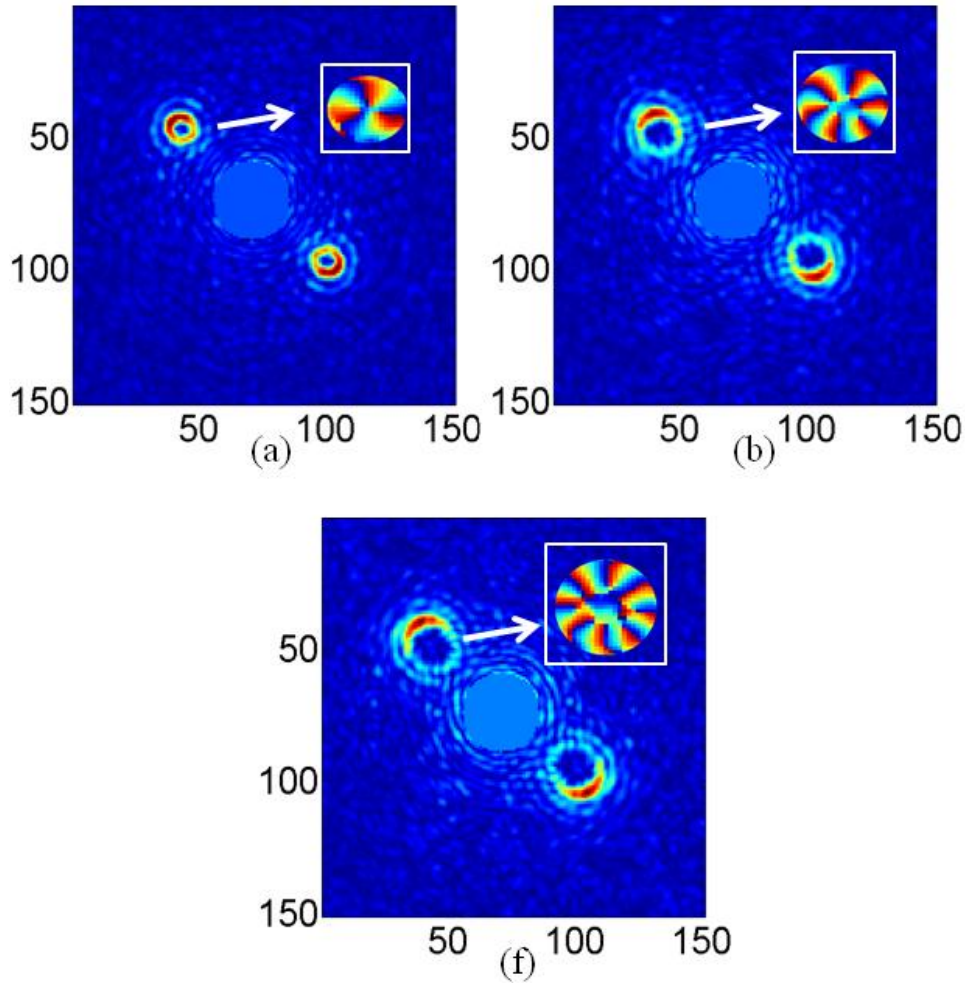
Figure 5.5: Inverse Fourier transforms of the centrally shifted fork grating for each of the case of the vortex object used, which corresponds to the reconstructed complex coherence function, (a) for vortex charge 3 (b) for vortex charge 6 (c) for vortex charge 8. The reconstructed (enlarged) phase structure corresponding to each of the amplitude distribution is shown in the insets by arrow. The values on X-axis and Y-axis represent the X-pixels and Y-pixels respectively at the ground glass plane (plane I).

In summary, we have recovered the wave front form spatially fluctuating random fields using two point intensity correlation and speckle holography

technique in a single-shot record of an intensity distribution. Application of this technique for the reconstruction of complex field of the object lying behind a random phase screen is presented. Image distribution of the object structure is demonstrated as a distribution of the complex coherence function. The proposed method is expected to play an important role in extending holography to record and reconstruct objects hidden in turbid media, in other words, to engineer time reversal imaging through a scattering medium.

5.2 Depth resolved 3D imaging through scattering layers

Imaging systems with 3D imaging capability has a significant interest in recent years due to its potential applications in various fields such as microscopy, optical coherence tomography, medical imaging etc. The strength of holography and digital holography in 3D imaging are exploited in many recent works in biomedical related imaging techniques. The presence of a scattering layer or an inhomogeneous medium significantly affects the performance of the conventional imaging techniques and suffers from the formation of complex speckle pattern. Recent interests are in the direction of efficient use of this complex speckle pattern for imaging purpose. A non-invasive imaging through a scattering layer has been performed using angular speckle correlation and phase retrieval methods (Bertolotti et al., 2012). More recently, an improved approach based on speckle autocorrelation was proposed, which utilizes the ergodic property of speckle patterns in diffusive regime (Katz et al., 2014). This circumvents the requirement of lengthy angular scanning procedures and hence reduces the measurement time significantly. Unfortunately, the aforementioned techniques do not provide three-dimensional (3D) imaging capability and thus the actual depth resolved recovery of the object behind the scattering medium remains as a technical challenge. This limitation of depth reconstruction for the techniques based on the speckle memory effect is mainly owing to the inability to measure the full phase space.

In this section we describe a non-invasive single-shot imaging method that allows the 3D reconstruction of objects behind a scattering medium by making use

of the strategy developed for complex valued object recovery from two point intensity correlation. In order to retain the depth reconstruction capability, the imaging technique must retrieve the complete object field information (both amplitude and phase) at the plane of scattering media. Thus, we propose and experimentally demonstrate a coherent 3D imaging method based on the concepts of speckle holography together with two-point intensity correlation (or speckle correlation). Here, we demonstrate that the combination of the principles of holographic imaging and two-point intensity correlation can provide a foundation for 3D imaging through turbid media. To illustrate the potential of our method, we experimentally validate the imaging of a real world objects hidden behind the random scattering plane.

5.2.1 Principle of the imaging technique

The principle of the technique lies in the recovery of complex coherence function and subsequently the illuminating structure at the scattering plane by making use of interference of coherence waves and two point intensity correlation. The complex coherence function in the far field is connected with the intensity of the source structure at the scattering plane by a Fourier transform relation (the van Cittert-Zernike theorem) (Mandel and Wolf, 1995). Therefore, this relationship can be exploited to develop a new imaging technique through random scattering medium by recovering the hologram information behind the scattering layer. Note that in this section, we are concentrating on recovery of hologram rather than the object as distribution of complex coherence function at the camera plane. Since the actual object information is encoded in this hologram, the wave front due to object can be reconstructed from this hologram, which is further utilized in retrieving the depth resolved images. The complex amplitude of the object at different depths is obtained by performing a beam propagation operation based on the angular spectrum method (Goodman, 1996). Let us consider a situation where a hologram lies behind a scattering layer. A schematic representation of the obstruction of hologram by a scattering layer and the proposed imaging technique is shown in Fig.5.6.
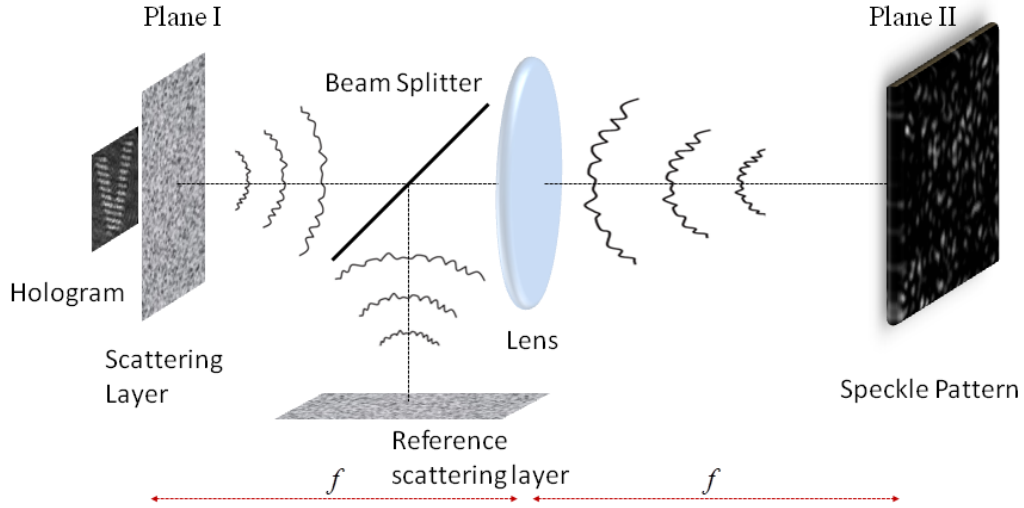
Figure 5.6: Schematic representation of the proposed imaging technique.

$$I_H(\hat{r}) = |U(\hat{r})|^2 \qquad (5.12)$$

where $U(\hat{r})$ is the complex field reaching the scattering layer (plane I).

The generated hologram at the plane I is obstructed by a scattering layer (Ground glass diffuser) and the holographic information is scrambled due to the scattering from the diffuser. Digital recording of the scattered field from the diffuser does not recover the complete information of the object but it gives a random speckle pattern. The random speckle pattern carries the hologram information but is completely scrambled. The scattered field from the scattering layer (plane I) is Fourier transformed using a lens of focal length f. The complex coherence of the scattered field at the Fourier plane (plane II) is given by (R. K. Singh et al., 2013)

$$W_H(\Delta r) = \int I_H(\hat{r}) e^{-i\frac{2\pi}{\lambda f}(\Delta r.\hat{r})} d\hat{r} \ , \qquad (5.13)$$

where $\hat{r}$ and $\Delta r = r_2 - r_1$ are the transverse spatial coordinate in plane I and II, respectively, λ is the wavelength of the light source and f is the focal length of the lens. The Eq. (5.13) states that it is possible to retrieve the hologram information through a Fourier transform relation experimentally from the complex coherence function.

From the intensity distribution at the detector plane $\left(I_H(\boldsymbol{r}) \equiv U(\boldsymbol{r})U^*(\boldsymbol{r})\right)$, the intensity cross-variance function or the fourth order correlation function can be estimated and is given by

$$C_H(\Delta\boldsymbol{r}) = \left\langle \Delta I_H(\boldsymbol{r})\Delta I_H(\boldsymbol{r}+\Delta\boldsymbol{r})\right\rangle_S, \qquad (5.14)$$

where $\langle.\rangle_S$ represents the spatial averaging as a replacement of ensemble averaging and $\Delta I_H(\boldsymbol{r}) = I_H(\boldsymbol{r}) - \left\langle I_H(\boldsymbol{r})\right\rangle$. This fourth order correlation function can be expressed in terms of the second order correlation function on the assumption that the scattered field follows Gaussian statistics as

$$C_H(\Delta\boldsymbol{r}) \propto \left|W_H(\Delta\boldsymbol{r})\right|^2. \qquad (5.15)$$

Loss of phase information of the coherence function can be compensated by applying coherence interference approach given by

$$\left|W(\Delta\boldsymbol{r})\right|^2 = \left|W_H(\Delta\boldsymbol{r}) + W_R(\Delta\boldsymbol{r})\right|^2, \qquad (5.16)$$

where $W(\Delta\boldsymbol{r})$ and $W_R(\Delta\boldsymbol{r})$ are the complex correlation functions of the resultant speckle field and reference speckle field respectively. Thus the two point intensity correlation of the speckle field at plane II results in a fringe pattern and by using Fourier transform method of fringe analysis and employing van Cittert-Zernike theorem the digital hologram at plane I can be recovered.

5.2.2 Experimental Implementation

An experimental setup is designed and implemented as shown in Fig. 5.7. A coherent laser beam of wavelength 632.8 nm is spatial filtered (L_1 &A_1) and collimated using lens L_2. This collimated beam splits into two beams by a non-polarizing beam splitter (BS_1) and acts as the two arms of a Mach Zehnder type interferometer. The reflected beam from BS2 is used to illuminate the object and considered as the object arm of the interferometer. The reflected beam from BS_1 again splits into two by another non-polarizing beam splitter BS_2. The reflected and transmitted beam from BS_2 is used to generate an off-axis hologram of the specified object used in our experimental demonstration. These two beams were folded by the mirrors M_1 and M_2 and made to superpose using another non-polarizing beam splitter BS_3 and the generated off-axis hologram is allowed to

illuminate the ground glass diffuser (GG_1) through an aperture (A_2) of specific size. The hologram is completely scattered by the diffuser and generates complex speckle patterns. The transmitted beam form BS1 is folded by the mirror M3 and illuminates another independent ground glass diffuser (GG2) through a microscope objective (MO). The MO is used to generate a point source illumination on GG2 to achieve an independent reference speckle pattern. The speckle patterns from the two diffusers GG1 and GG2 are combined using another non-polarizing beam splitter BS4 and the resultant speckle pattern is Fourier transformed using a common lens L3 of focal length 150mm. The resultant speckle field is captured by a CCD camera (Prosilica GX 2750). The camera is of 14-bit dynamic range, with 2750×2200 pixels and a pixel pitch of 4.54μm.
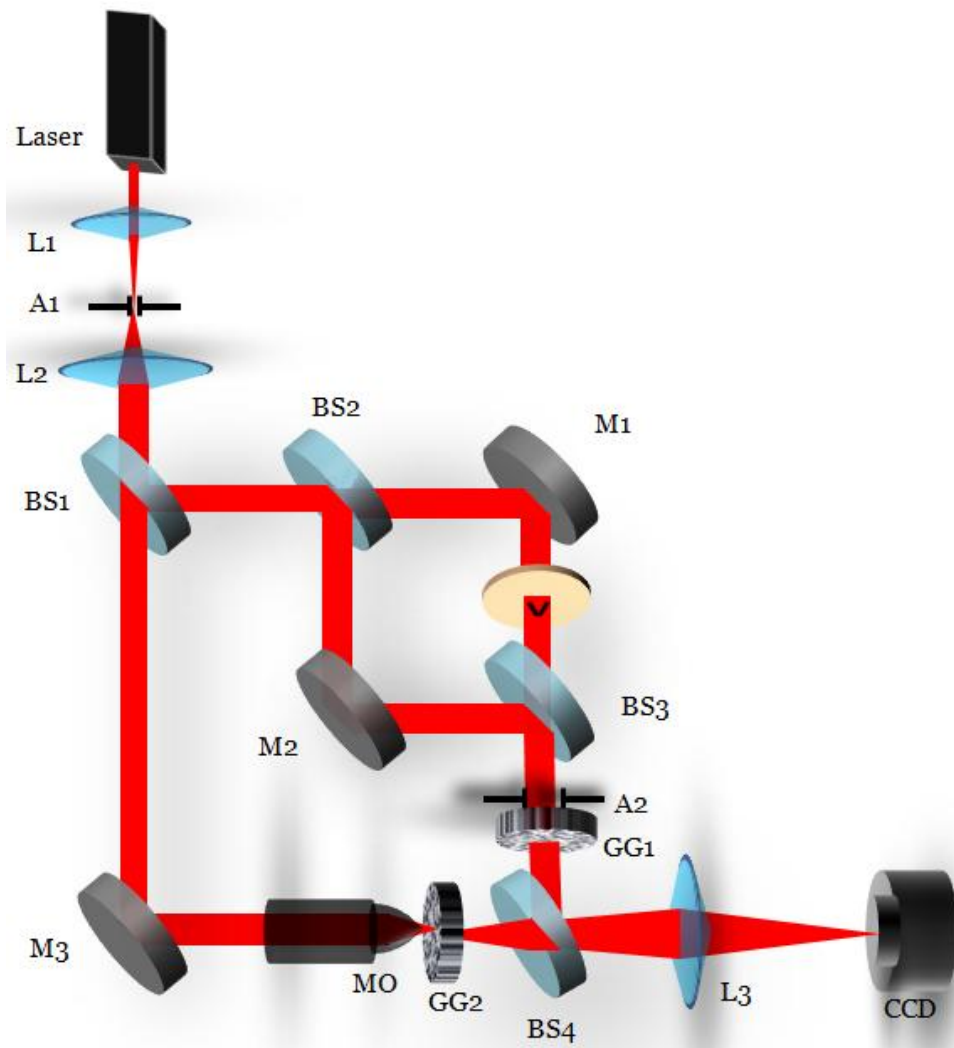
Figure 5.7: Experimental setup for the imaging technique.

5.2.3 Generation of an off-axis hologram

To investigate the applicability of the proposed imaging technique to real world objects, an off-axis hologram is generated as shown in the schematic representation of Fig.5.8. The objects (letter "V" and "L") are created in a transparency and it is placed at a distance of 155 mm from the ground glass diffuser. A hologram of the desired object is created by using a coherent beam illumination on the object and using an off-axis holographic geometry developed by Mach-Zehnder type interferometer as shown in Fig. 5.7. The generated hologram is allowed to illuminate the ground glass diffuser which obstructs the hologram and scrambles the holographic information into complex speckle patterns.
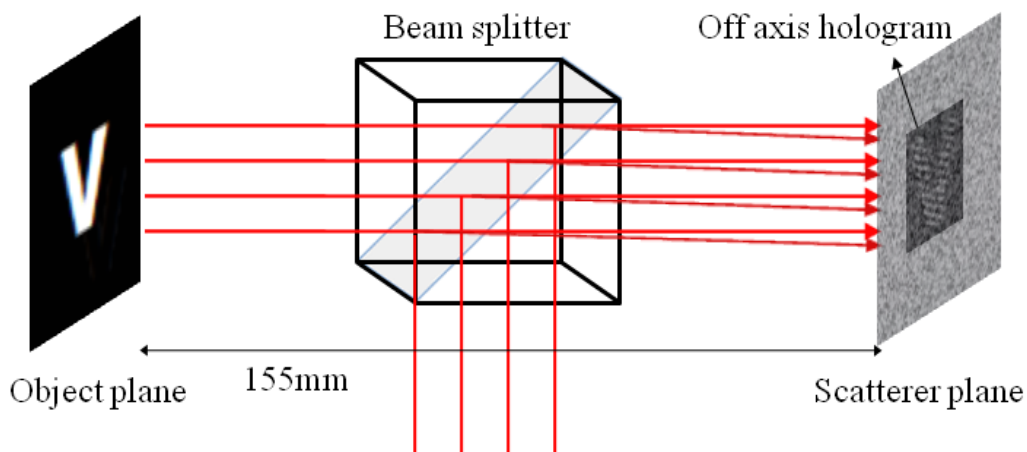
Figure 5.8: Schematic representation of the generation of an off-axis hologram.

5.2.4 Results and Discussion

The resultant speckle field from object and reference part is captured by a CCD camera (Prosilica GX 2750) for an off-axis hologram (of letter "V") and is shown in Fig. 5.9(a). The resultant speckle pattern captured by the CCD camera completely hides the holographic information and only the random speckle patterns are visible. The two point intensity correlation of the resultant speckle field under spatial averaging condition yields a coherence wave hologram at the Fourier transform plane. This hologram is the result of the coherent superposition of the correlation functions from the object and reference contributions of the speckle field. The coherence wave hologram resulting from the two point intensity

correlation is shown in Fig. 5.9(b). Fig. 5.9(b) clearly shows the presence of fringes which results from the superposition of tilted reference speckle field with hologram speckle field. Using Fourier transform method of fringe analysis technique(Takeda et al., 1982), the complex coherence function of the hologram field can be retrieved. The Fourier transform of the coherence wave hologram obtained from the two point intensity correlation function is shown in Fig. 5.9(c). Due to the presence of the off-axis reference speckle pattern, Fourier transform of Eq. 5.16 reconstructs the hologram at an off-axis location as highlighted in Fig. 5.9(c) with red circle. Fig. 5.9(c) clearly represents the separation of spectrum, its complex conjugate and dc in Fourier domain due to the presence of off-axis reference speckle pattern. The desired information (highlighted in red circle in fig. 5.9(c)) is filtered and this hologram is centered for further processing. This Fourier filtering process also removes the effect of $W_R(\Delta r)$ term of Eq. 5.16.

(a)

(b)   (c)
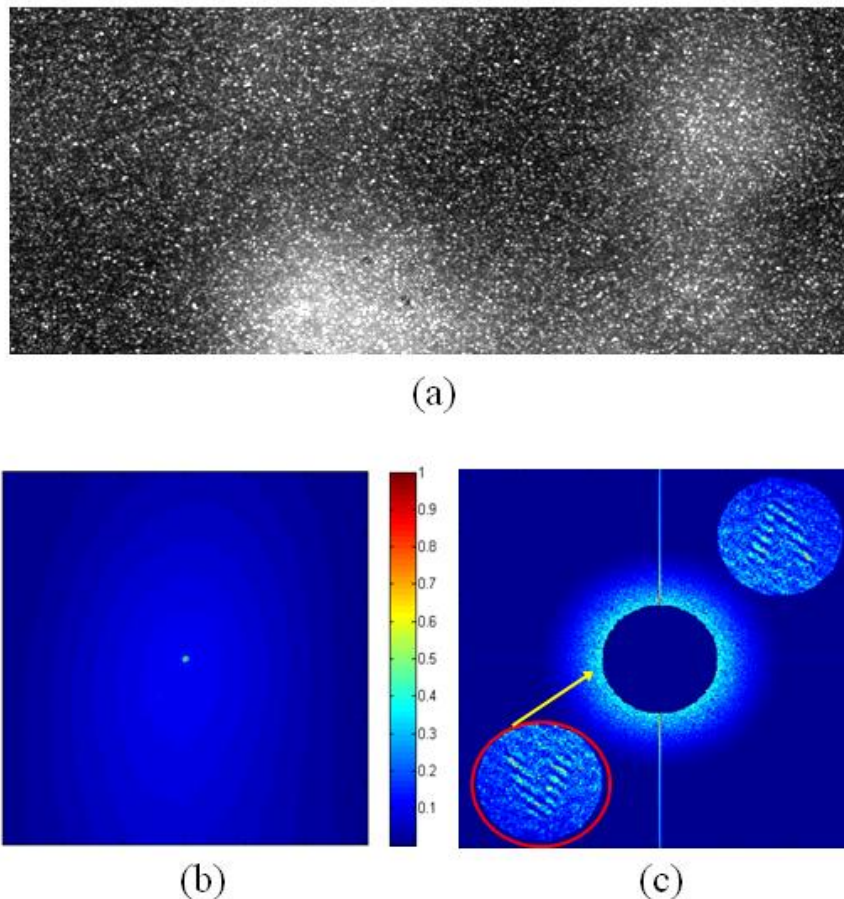
Figure 5.9: (a) Random speckle pattern captured by the CCD camera (b) Coherence wave hologram resulting from the two point intensity correlation of the speckle field, and (c) Fourier transform operation on the coherence wave hologram. The color bar represents the intensity.

$v=6.02, \eta=0.86$
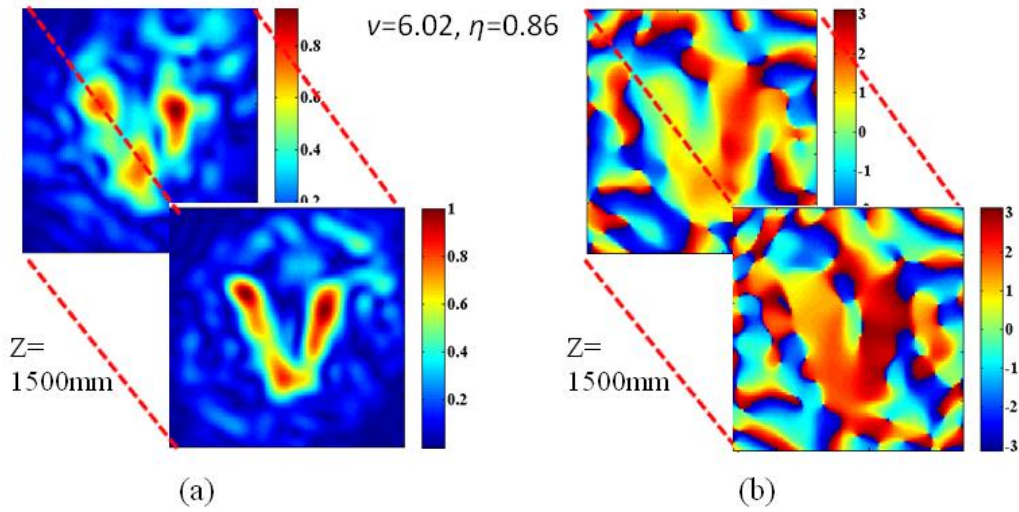
Figure 5.10: Reconstructed amplitude and phase information through a scattering layer; (a) reconstructed amplitude information of the object at a distance 155mm from scattering medium and its defocused information at z= 1500mm from object plane; the color bar represents the intensity (b) reconstructed phase information of the object at a distance 155mmfrom scattering medium and its defocused information at z=1500mm from object plane; the color bar represents the phase profile. *Visibility (v)* and *Reconstruction Efficiency (η)* values at the actual depth are shown just above the figure.

These retrieved holograms are then utilized to reconstruct the object at desired plane. A Fourier transformation process on the reconstructed hologram will separates the desired information from the dc part. Inverse Fourier transform of the centrally shifted spectrum will retrieve the complex amplitude information. This complex amplitude contains the information of the object. The retrieved complex amplitude can be further propagated using angular spectrum method of beam propagation to reconstruct the object 'V' (See Appendix 2). Fig. 5.10 shows the depth resolved amplitude and phase information of the object at two different planes behind the scattering layer. The in-focus image appearing in Fig. 5.10(a) shows the complete amplitude information recovery at the exact plane i.e. 155mm behind the scattering layer. In order to show the depth resolved imaging capability we recovered the object information at a plane 1500mm behind the object plane. The recovered information is shown in the back plane in Fig. 5.10(a), where the information is completely out of focus. The corresponding recovered phase information at two different planes behind the scattering layer is shown in Fig.

5.10(b). The results corresponding to a different object "L" of dimension 5mm×4mm are also shown in Fig. 5.11 and 5.12. The reconstruction of the object with full amplitude and phase information confirms the fact that the proposed method can faithfully image through an opaque scattering layer.
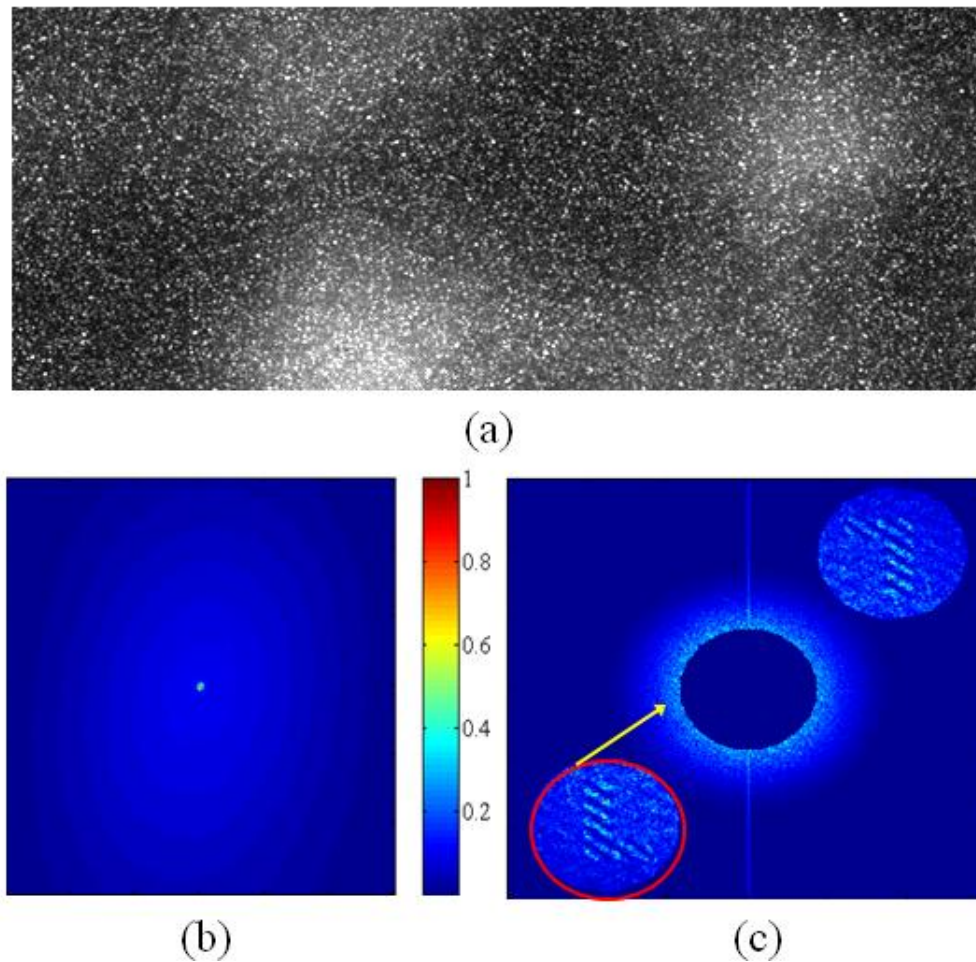
Figure 5.11: (a) Random speckle pattern captured by the CCD camera (b) Coherence wave hologram resulting from the two point intensity correlation of the speckle field, and (c) Fourier transform operation on the coherence wave hologram. The color bar represents the intensity.
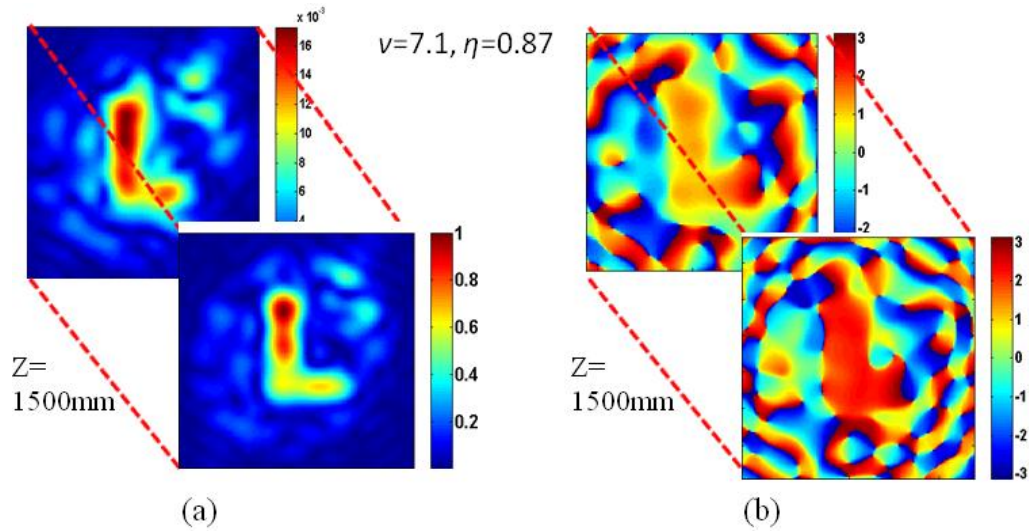
Figure 5.12: Reconstructed amplitude and phase information through a scattering layer; (a) reconstructed amplitude information of the object at a distance 155mm from scattering medium and its defocused information at z= 1500mm from object plane; the color bar represents the intensity (b) reconstructed phase information of the object at a distance 155mmfrom scattering medium and its defocused information at z=1500mm from object plane; the color bar represents the phase profile. *Visibility (v)* and *Reconstruction Efficiency (η)* values at the actual depth are shown just above the figure.

The reconstruction quality of the recovered objects is analyzed by considering two parameters: visibility *(v)* and reconstruction efficiency *(η)*. The visibility of the object reconstruction is defined as the extent to which the reconstruction of the image is distinguishable from the background noise. It is measured as the ratio of the average image intensity level in the region corresponding to the signal region to the average background intensity level. A global threshold approach is used to identify the signal region. The calculated visibility values for the images shown in Figs. 5.10(a) and 5.12(a) are 6.02 and 7.1 respectively. The reconstruction efficiency *(η)* can be defined as the ratio of measured power in the signal region of the image to the sum of the measured powers in signal and background regions. The *η* values for the two different objects are 0.86 and 0.87 respectively.

In summary, we have experimentally demonstrated a single-shot 3D imaging technique through a highly scattering medium by utilizing the concepts of speckle holography in combination with two point intensity correlation. The demonstrated technique has the unique ability to retrieve the complex field behind a scattering

medium resulting into the reconstruction of actual position of the object. Thus the imaging technique provides the potential to implement the 3D complex field imaging through an opaque scattering medium for wide range of applications.

5.3 Imaging through scattering layer using digital in-line holography

Digital inline holography with numerical reconstruction techniques emerge as a new tool in biological applications, where the lateral and depth resolution achieved in 3D imaging gives the potential to overcome limitations in conventional light microscopy (Garcia-Sucerquia et al., 2006; Xu et al., 2001). The dynamic scattering from biological tissues and live cells were investigated by using a new technique called Fourier transform light scattering which have the potential to study the tissue optical properties, cell type characterization, and dynamic structure of cell membranes (Ding et al., 2008). Recently a technique employing the principle of digital inline holography and Fourier transform light scattering technique is introduced to measure the angle resolved light scattering of transparent micrometer-sized objects (K. Kim and Park, 2012). Even though these techniques have unique position in biological applications, it is not able to give a non-invasive imaging through the scattered medium where the complete information of the object is scrambled in to a speckle pattern. Techniques for microscopic imaging and quantitative phase contrast imaging of objects in turbid media by digital holography is demonstrated by exploiting the Doppler frequency shift experienced by the photons scattered by the flowing colloidal particles (Paturzo et al., 2012). Breakthrough achievements in non-invasive imaging through scattering layers were demonstrated by Katz (2014) and Bertolotti (2012) by using autocorrelation and phase retrieval techniques (Bertolotti et al., 2012; Katz et al., 2014). Even though these techniques has the potential of real time imaging, it is limited by the depth resolved imaging and 3D recovery of object information. To resolve depth imaging issue behind the random scattering medium, we developed an off-axis holography, discussed in previous section. We recovered the off-axis hologram behind the random scattering medium by

retrieving the complex coherence function and thereby the complete amplitude and phase information. However, recording the off-axis hologram behind the scatterer is not always feasible.

In this section we experimentally demonstrate a non-invasive single-shot imaging technique to recover the complex valued objects lying behind the scattering layer by using the principles of inline (Gabor type) holography in combination with the two point intensity correlation. This technique utilizes the randomness of the speckle pattern to recover the inline hologram and thereby provides a depth resolved information of the object behind the scattering layer. The recovery of the digital inline hologram from the complex correlation function gives the opportunity to use the numerical propagation techniques to recover the complex object information at desired plane behind the scattering medium. To demonstrate the potential of the proposed technique, imaging of various objects at different depths behind the scattering layer were illustrated.

5.3.1 Principle of the technique

The principle of the technique lies in the recovery of the in-line hologram from the complex speckle pattern by making use of the intensity correlation in combination with the speckle holographic approach. Illumination of an object (reflecting or transmitting type) with coherent light generates scattered light. When the scattered beam from the object is small in compared to the unscattered one, the holographic diffraction is dominant and it results into the formation of an inline (or Gabor type) hologram (Gabor, 1948; Garcia-Sucerquia et al., 2006; Kreis, 2005). A direct digital recording of this in-line hologram and the use of advanced numerical techniques have the potential to recover the complex information of the object. However, the presence of a scattering layer in the path of the hologram restricts the use of conventional imaging techniques due to the scattering from the layer and the formation of complex speckle patterns. To overcome this difficulty we made use of the combination of numerical propagation technique with intensity correlation holography approach. A schematic representation of the formation of in-line hologram and its obstruction by a scattering layer is shown in Fig. 5.13.
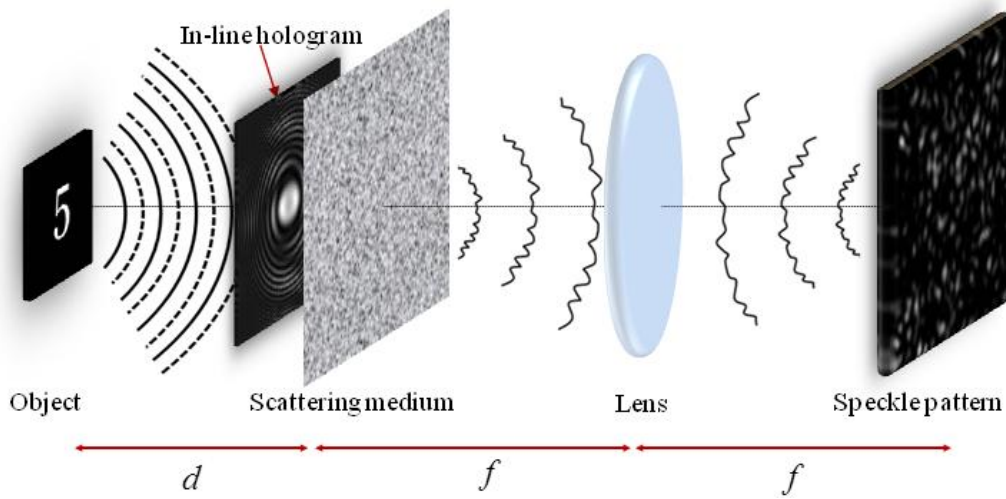
Figure 5.13: Schematic representation of the formation of an in-line hologram and its obstruction by a scattering layer.

Let us consider a complex valued object located at a distance, *d*, behind a random medium. The wave amplitude reaching the scattering layer located at a distance *d* from the object is given by

$$U(\hat{r}) = U_r(\hat{r}) + U_s(\hat{r}), \tag{5.17}$$

where $\hat{r}$ is the spatial coordinates at an instant of time t, $U_r(\hat{r}, t)$ is the unscattered wave and $E_s(\hat{r}, t)$ is the scattered wave. This holographic diffraction from the object produces an in-line hologram and the corresponding intensity just behind the scattering layer is given by

$$I(\hat{r}) = |U_r(\hat{r})|^2 + |U_s(\hat{r})|^2 + U_r^*(\hat{r})U_s(\hat{r}) + U_r(\hat{r})U_s^*(\hat{r}). \tag{5.18}$$

The first two terms in the right hand side of Eq. (5.18) represent the intensity of the unscattered and scattered beam, respectively. Third and fourth terms represent the intensity terms of real and virtual images in the in-line hologram. This inline hologram is obstructed by an inhomogeneous complex scattering layer. A schematic representation of the formation of inline hologram and its obstruction by the scattering layer is shown in Fig.5.13. The holographic information is completely scrambled by the scattering layer and direct recording yield only the complex speckle pattern. We use our developed technique of speckle holographic approach in combination with the two point intensity correlation to retrieve the

116

complex coherence function from the random speckle pattern (discussed in section 5.1).

An independent reference speckle pattern is generated from a known independent scattering medium and allows superposing with the speckle pattern from the random inhomogeneous medium. The two point intensity correlation of this resultant random field at the Fourier plane results into a coherence hologram given by

$$\Gamma(\Delta r) = \left| W_H(\Delta r) + W_R(\Delta r) \right|^2 , \tag{5.19}$$

where $W_H(\Delta r)$ and $W_R(\Delta r)$ are complex correlation functions of resultant, object and reference speckle field respectively. The complex coherence function of the object field $W_H(\Delta r)$ can be retrieved from Eq. 5.19 by applying digital process. The complete retrieval of complex correlation function at the Fourier plane provides the inline hologram at the scattering plane and given as:

$$I(\hat{\boldsymbol{r}}) = \int W(\Delta \boldsymbol{r}, t) \exp\left[-i\frac{2\pi}{\lambda f}(\Delta \boldsymbol{r}.\hat{\boldsymbol{r}}) \right] d\hat{\boldsymbol{r}} , \tag{5.20}$$

where $I(\hat{\boldsymbol{r}})$ is the intensity corresponding to the source structure which contains the digital inline hologram information of the complex valued object located at distance d from the scattering layer. The digital inline hologram recovered at the scattering layer gives the potential to retrieve the depth-resolved reconstruction of complex-valued object information using numerical techniques. Generally the inline holograms suffered from twin image problem and this degrades the quality of the reconstructed image (Kreis, 2005). To eliminate the virtual image or the out of focus image formed in the inline hologram, the recovered digital hologram was numerically propagated to a conjugate plane $z = d$ from the recovered hologram plane by Rayleigh-Sommerfield back propagation (K. Kim and Park, 2012) (Details included in Appendix 2). By proper identification of the edge of the out of focus image, the inside region of the image is replaced with the average value of the background or outside the edge. The resulting field is then back propagated to the desired plane ($z = -d$) where the real object or in focus object is present. Thus, the complex field retrieved allows the complete reconstruction i.e. both amplitude

117

and phase information of the object at the desired plane thereby providing a depth resolved imaging of the object hidden behind the random inhomogeneous medium.

5.3.2 Experimental Implementation

In order to demonstrate the applicability of our proposed imaging technique to various objects we implemented separate experimental geometry for both reflecting type and transmitting type objects.

5.3.2.1 Reflecting object

Experimental implementation of the imaging technique for a reflecting type object is shown in Fig. 5.14. A linearly polarized He-Ne laser beam with the wavelength of 632.8nm is spatial filtered using a microscope objective (L1) and a pin hole (A1) combination. The filtered beam is collimated using a lens (L2) of focal length 150mm and is using as the input beam to a Mach-Zehnder type interferometer. The collimated beam is divided in to two by a beam splitter (BS1). The reflected beam from BS1 illuminates a reflective type SLM through a beam splitter BS3 and polarizer (P) combination. Reflective type objects were introduced in the experimental setup using a reflective type spatial light modulator (SLM. The spatial light modulator used in the experimental implementation is LC-R 720 (reflective) from Holoeye. It is based on LCOS micro display with a resolution of 1280×768 pixels with a pixel pitch of 20μm (Details are included in Appendix 3).The object that to be imaged is displayed in the SLM and the reflected beam from SLM carries the object information. The reflected beam from the SLM carries the object information and suffers a holographic diffraction and forms an inline hologram and illuminates the scattering layer (Ground glass diffuser-GG1) at a specific distance from the object. This scattered light carries the holographic information but is completely scrambled in the speckle pattern. The transmitted beam from BS1 acting as the reference arm of the Mach-Zehnder interferometer is used to generate the known independent reference speckle pattern. This beam is folded by a mirror M2 then illuminates an independent ground glass GG2 through a microscope objective MO, thereby generating an independent reference speckle pattern. The beam from MO is pointed to fall in GG2 in an off axis position in order to provide a suitable spatial carrier frequency in the reference speckle pattern. The speckle patterns from the two arms of the interferometer are combined using a non-polarizing beam splitter BS2. The combined field is Fourier

transformed using a lens L3 of focal length 75mm. The resultant field at the Fourier transform plane is captured by a high resolution CCD monochrome camera (Prosilica GX 2750). The camera is of 14 bit with 2750×2200 pixels and a pixel pitch of 4.54µm. The high resolution and large total pixel size of the CCD camera allows us to implement spatial averaging technique by replacing the ensemble averaging, thereby provides the potential to develop a single–shot imaging technique.
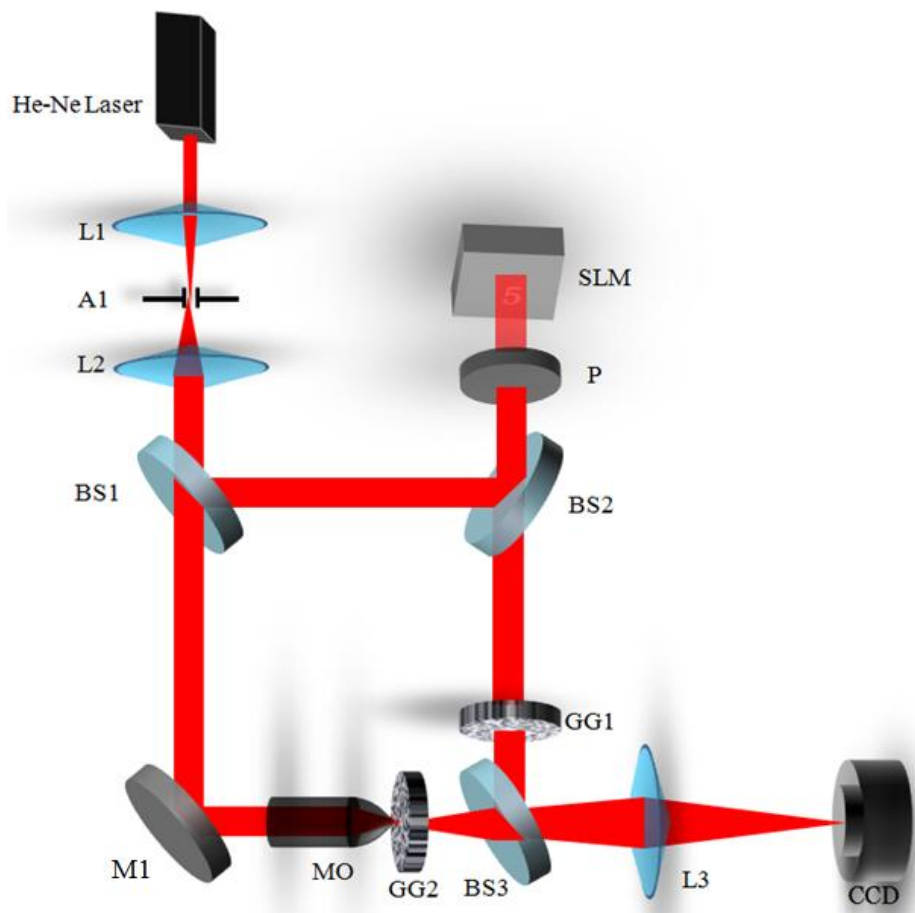
Figure 5.14: Experimental implementation of the imaging technique for a reflecting type object.

5.3.2.1 Transmitting object

Further to implement the experimental technique to transmitting type object we modified the experimental geometry by replacing the SLM and beam splitter BS3-polaizer P combination with a mirror M2 to make it as a simple Mach- Zehnder type interferometer. The beam folded from mirror M2 illuminates the transmitting type object and suffers a holographic diffraction and generates an in-line hologram. This in-line hologram scatters from the scattering layer (GG1) and

superimpose with the reference speckle field from the diffuser GG2. The resultant speckle field is Fourier transformed using a common lens of focal length L3 and captured by a CCD camera.
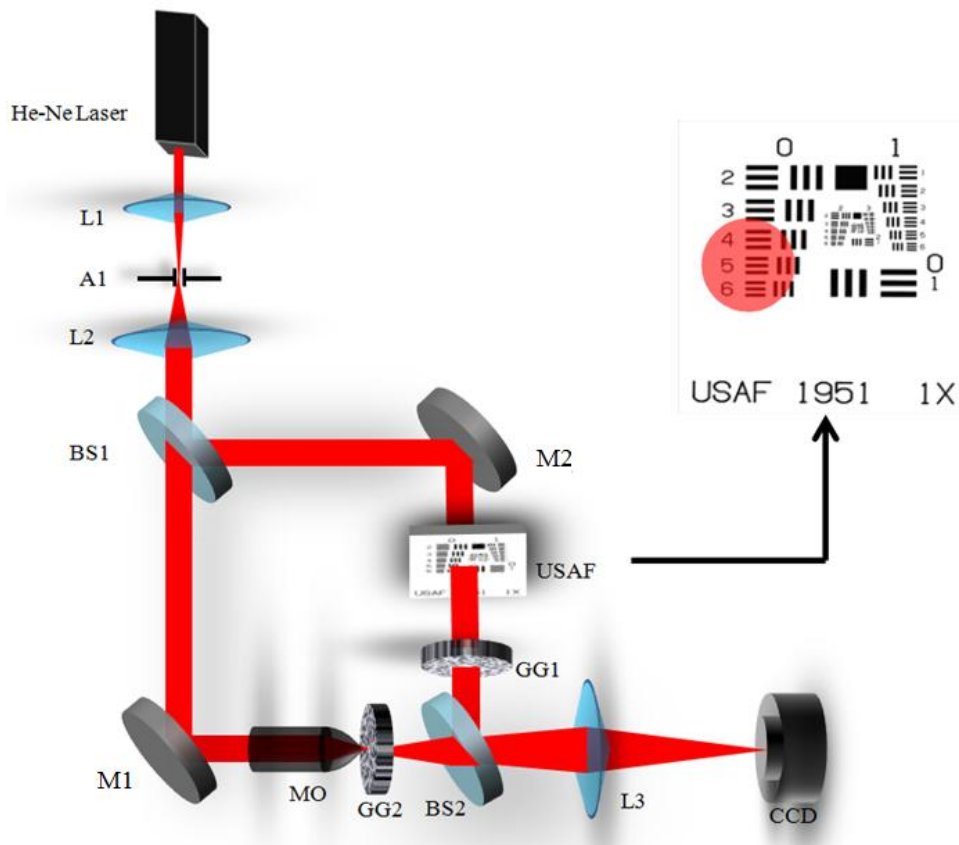
Figure 5.15: Experimental implementation of the imaging technique for a transmitting type object.

5.3.3 Results and Discussion

For the experimental demonstration of the imaging technique initially we implemented the experimental geometry for reflecting type objects and the objects were introduced in the experiment using the reflective SLM. The SLM is illuminated by a He-Ne laser source and the random speckle pattern is recorded at the Fourier transform plane using CCD camera. An object '5' of dimension $\sim 0.94\,mm \times 0.54\,mm$ is inserted in the experimental setup using the SLM at a distance of 288mm behind the ground glass diffuser acting as scattering layer (GG1). The holographic diffraction of the object on propagation results the

120

formation of an in-line hologram. The size of the in-line hologram is controlled by an aperture of size 5mm placed very near the GG1. The size of the aperture is chosen in such a way that the speckle grain size at the recording plane is larger than two CCD pixels in order to meet the sampling criterion. Figure 5.16(a) shows the recorded intensity of resultant speckle image at the CCD plane. The recorded pattern has no visible relation with the object displayed in the SLM. Two point intensity correlation of these resultant speckle pattern using spatial averaging approach results into a coherence wave hologram at the CCD plane as described in Eq. (5.19) that contains the second order correlation function, $W_H(\Delta r, t)$. The coherence wave hologram resulting from the two point intensity correlation is shown in Fig. 5.16 (b). The use of Fourier transform method of fringe analysis can yield the desired complex coherence function at the CCD plane. The Fourier transform of the coherence wave hologram is shown in Fig. 5.16(c). The spectrum, its complex conjugate and the dc are separated in Fourier domain. The separation of the spectrum can be controlled by the position of the off-axis point in the reference speckle field. Inverse Fourier transform of the centrally shifted spectrum gives the desired complex coherence function at the CCD plane. The intensity $I(\hat{r}, t)$ of the digital inline hologram at the scattering plane can be recovered from the complex coherence function by making use of the van Cittert-Zernike theorem described in Eq. (5.20).
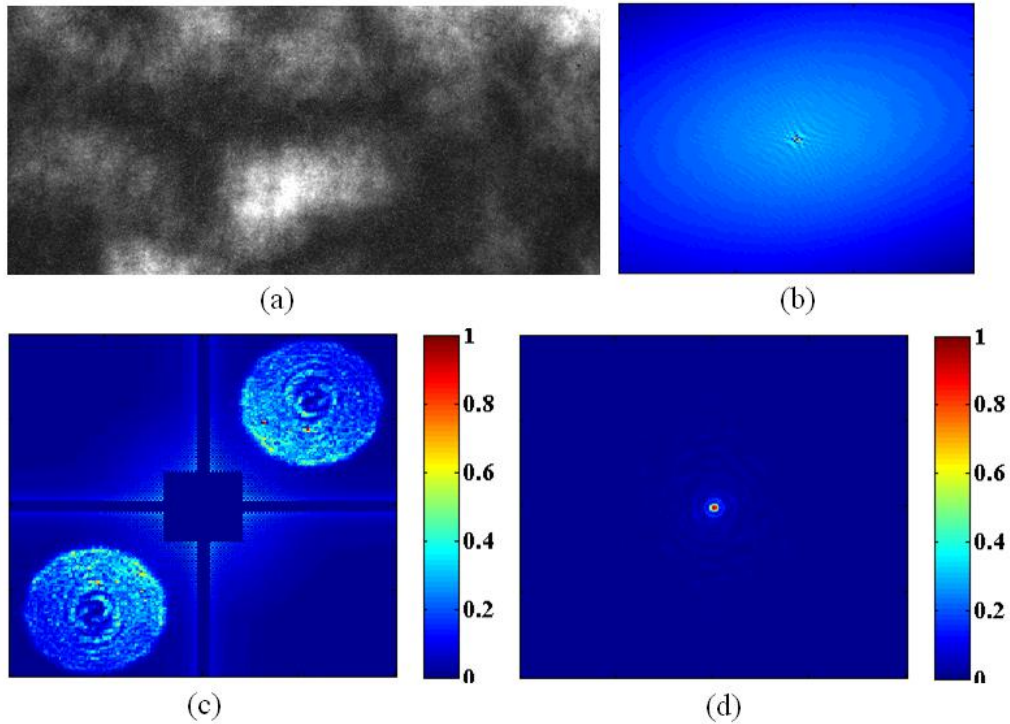
Figure 5.16: (a) Random speckle pattern captured by the CCD camera, (b) coherence wave hologram resulting from the two point intensity correlation, (c) Fourier transform of coherence wave hologram and (d) Recovered complex coherence function at the CCD plane; the color bar represents the intensity.

The recovered in-line hologram from the complex coherence function is shown in Fig. 5.17(a). By using Rayleigh-Sommerfield back propagation and twin image removal as explained in the above section, the complex-valued object information at the desired plane from the scattering medium can be reconstructed from the recovered inline hologram. Fig. 5.17 (b) and 5.17(c) shows the reconstructed amplitude and phase distribution of the object '5' at a distance of 288mm behind the scattering medium. In order to check the reconstruction capability of our imaging technique, we did direct imaging of the object i.e. without scattering layer at a distance of 288mm from the object. The direct imaging results are shown in Fig. 5.18. Fig. 5.18(a) represents the directly recorded in-line hologram at a distance of 288mm from the SLM plane. Fig. 5.18 (a) and 5.18(b) represents the recovered amplitude and phase distribution for the direct imaging case.
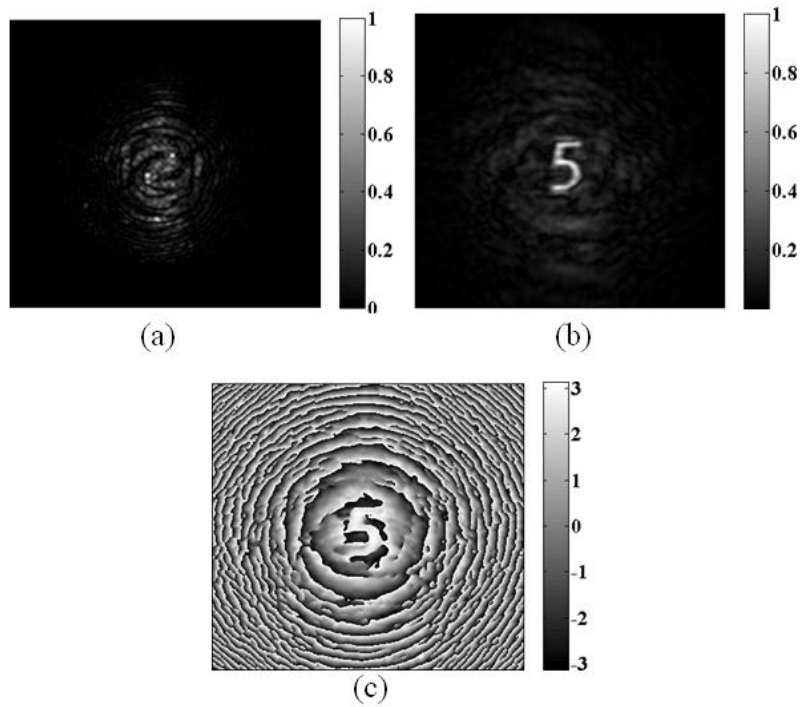
Figure 5.17: (a) Recovered in-line hologram with scattering layer (b) & (c) recovered amplitude and phase distribution at 288mmbehind the scattering layer respectively. The grey scale intensity and phase variation is shown in the respective bar representation.
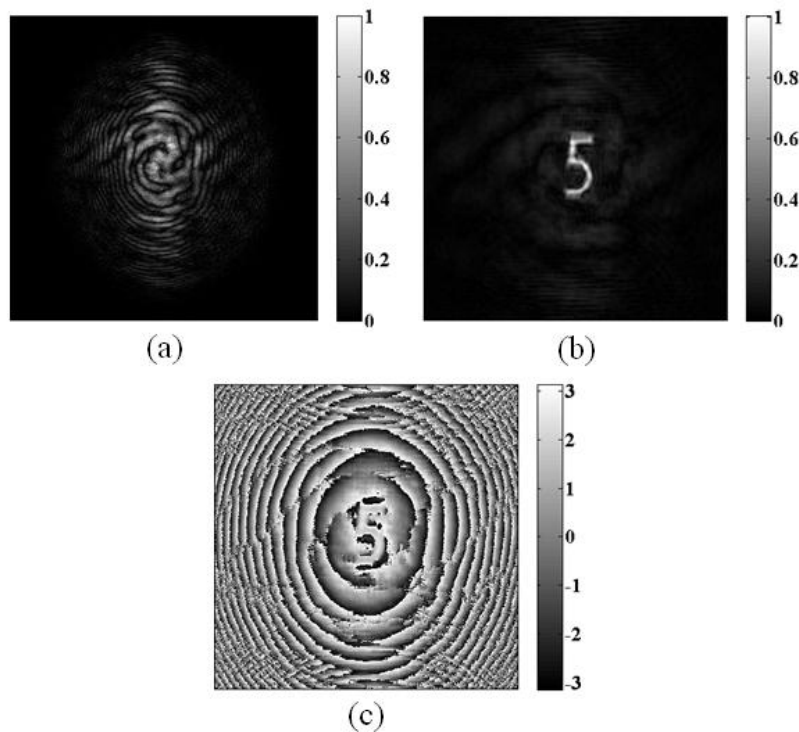
Figure 5.18: (a) Recovered in-line hologram without scattering layer (direct imaging) (b) & (c) recovered amplitude and phase distribution at 288mm from CCD plane respectively. The grey scale intensity and phase variation is shown in the respective bar representation.

The visibility and reconstruction efficiency parameters for the reconstructed image of object '5' with and without scattering medium are evaluated using the same way as described in the previous section. The reconstruction parameters v and η are 15.6218 and 0.9398, respectively for with scattering medium and 16.2050 and 0.9419, respectively for without scattering medium. A good agreement between imaging through scattering layer and a direct in-line hologram imaging shows the potential of the proposed imaging technique. Further to demonstrate the reconstruction capability of the imaging technique at various z-planes behind the scattering medium, a different object 'V' of dimension $\sim 0.8mm \times 0.8mm$ is displayed at various planes behind the scattering medium. The complex amplitude recovered at various planes behind the scattering medium from 100 mm to 600mm with an interval of 100mm is shown in Fig. 5.19. The reconstruction parameters for various planes behind the scattering medium for the cases with and without scattering medium are estimated and are shown in Table. 5.1. It is clear from Fig. 5.19 and Table 5.1 that the quality of reconstruction is deteriorated for short and long distances between the object and the scatterer. When an object is too far from the scatterer, high spatial frequency components are not able to reach the limited size scatterer window and thus to the detector which leads to the deterioration of the reconstructed image quality. Also in short distances, the diffraction pattern of the object reaching the scatterer plane is very narrow and thus it is difficult to fulfill the requirement of delta function correlation at the scatterer plane and leads to deterioration of the image quality. This feature is very much similar to the reconstruction of in-line hologram in the free space.

Z planes (mm)	With Scattering Medium		Without Scattering Medium	
	Visibility(v)	Reconstruction Efficiency(η)	Visibility(v)	Reconstruction Efficiency(η)
100	12.7282	0.9272	16.9175	0.9442
200	17.6150	0.9463	19.7889	0.9519
300	17.8059	0.9468	22.4323	0.9573
400	15.8655	0.9407	16.1322	0.9416
500	13.7838	0.9324	14.6849	0.9362
600	12.5867	0.9264	13.7917	0.9323

Table 5.1: Reconstruction parameters of object V for different planes behind the scattering medium and without the scattering medium

124
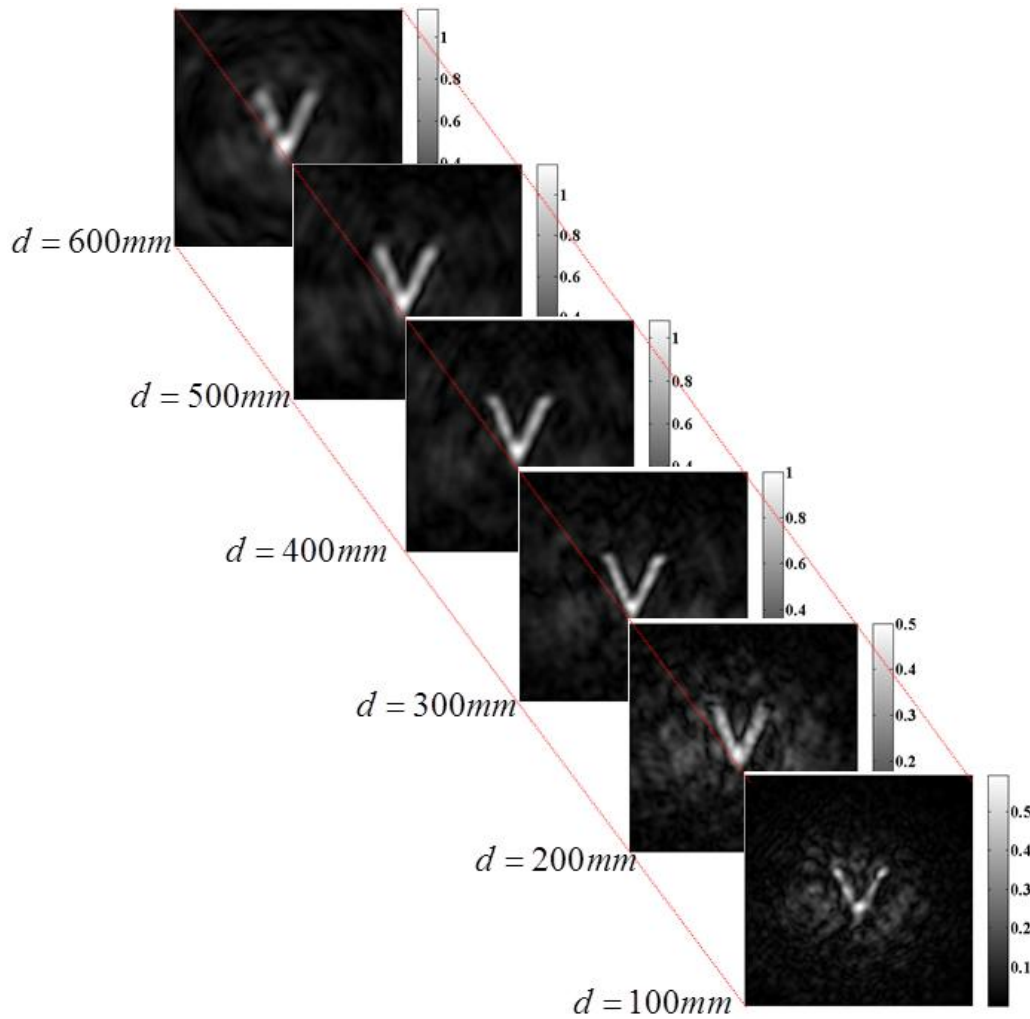
Figure 5.19: Recovered amplitude information at various planes behind the scattering layer.

Furthermore to check the capability of the technique in transmitting type object imaging, we use a transmitting type object as our samples for experimental illustration. A USAF 1951 resolution chart is laying 50mm behind the scattering medium GG1. The experimental geometry is modified as shown in Fig. 5.15. The resultant speckle field is recorded by the CCD camera. Experimental results are shown in Fig. 5.20 and 5.21 for two different cases where the beam illuminates group 0 and group 1 area of the USAF resolution chart. The resultant speckle field recorded at the CCD plane is shown in Fig. 5.20(a) and 5.21(a) for group 0 and group 1 area of USAF resolution chart respectively. The corresponding reconstructed amplitude distributions at a distance 50mm behind the scattering medium are shown in Fig. 5.20(b) and 5.21(b) and the phase distributions are shown in Fig. 5.20(c) and 5.21(c) respectively. Reconstruction quality of the

recovered images is estimated by measuring the reconstruction parameters. The visibility for the retrieved image for group 0 and group 1 area of USAF resolution chart are found to be 18.9183 and 14.7490, respectively and the corresponding reconstruction efficiency are 0.9498 and 0.9365, respectively. A good extent of recovery of both amplitude and phase distribution at actual depth behind the scattering medium shows the potential of the technique in depth resolved imaging of real world objects through scattering medium.

(a)

(b)   (c)
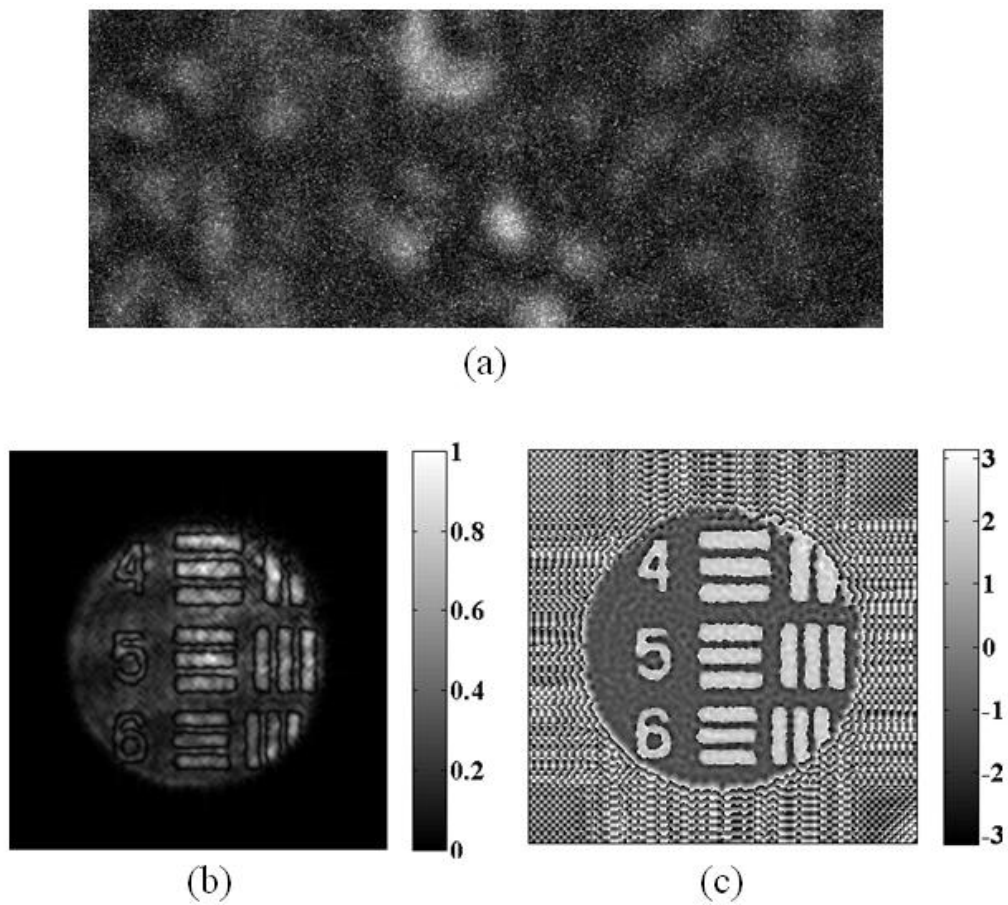
Figure 5.20: (a) Random speckle pattern recorded by the CCD camera (b) & (c) recovered amplitude and phase distribution at 50mm behind the scattering layer for group 0 area of USAF chart respectively. The grey scale intensity and phase variation is shown in the respective bar representation.

(a)

(b)   (c)
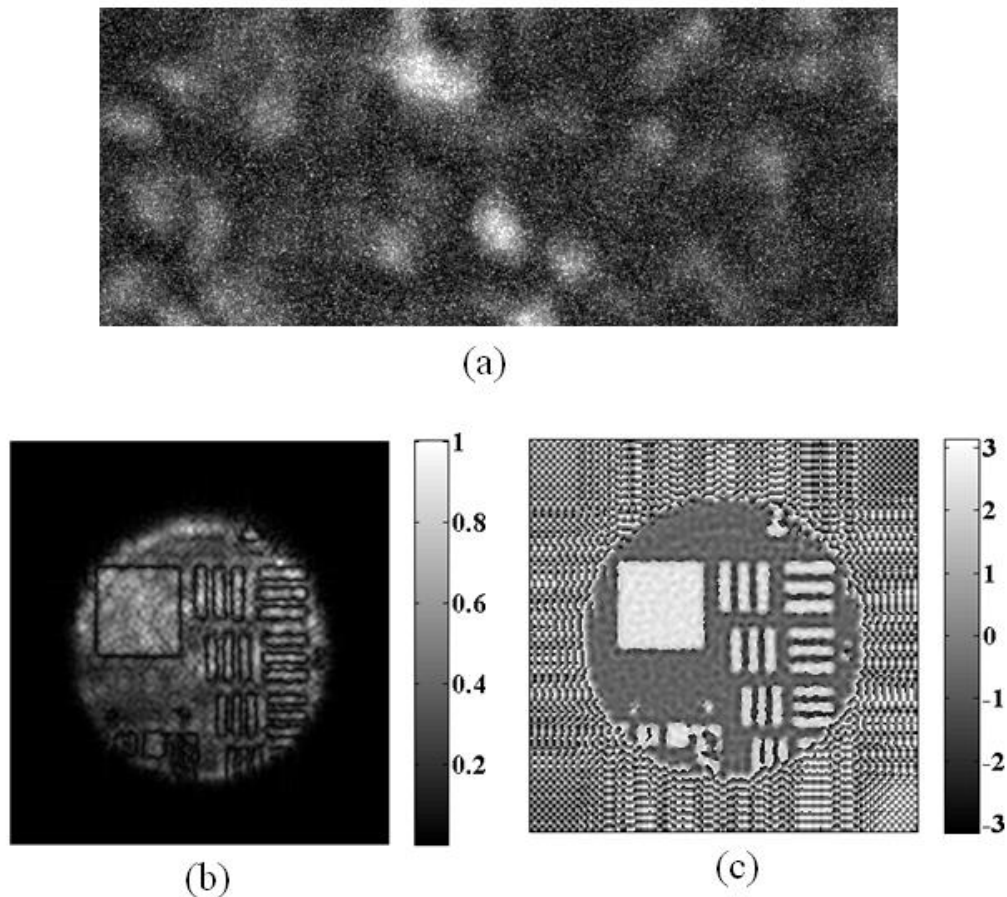
Figure 5.21: (a) Random speckle pattern recorded by the CCD camera (b) & (c) recovered amplitude and phase distribution at 50mm behind the scattering layer for group 1 area of USAF chart respectively. The grey scale intensity and phase variation is shown in the respective bar representation.

Further to demonstrate the potential of the imaging technique in imaging of micron scale objects behind the scattering medium and to test the strength in biological application we used micron sized polystyrene beads as our sample objects. The polystyrene beads are immersed in Olympus immersion oil and sandwiched between two cover slips. The sample is placed at a distance of 70mm behind the scatterer plane. The polystyrene beads are randomly distributed between the cover slips and it forms aninline hologram at the scatterer plane. This inline hologram illuminates the scatterer and generates the random speckle pattern. As mentioned in the above case the inline hologram at the scatterer plane is recovered from the random speckle pattern using two point intensity correlation and complex coherence function. Recorded speckle intensity pattern at the CCD plane is shown in Fig. 5.22(a). The amplitude and phase distribution obtained for a set of polystyrene beads which are randomly distributed between two cover slips are

shown in Fig. 5.22(b) and 5.22(c) respectively. An efficient depth resolved recovery of both amplitude and phase distribution of polystyrene beads explains the possibility of implementing the technique in imaging through turbid media and biomedical related applications.
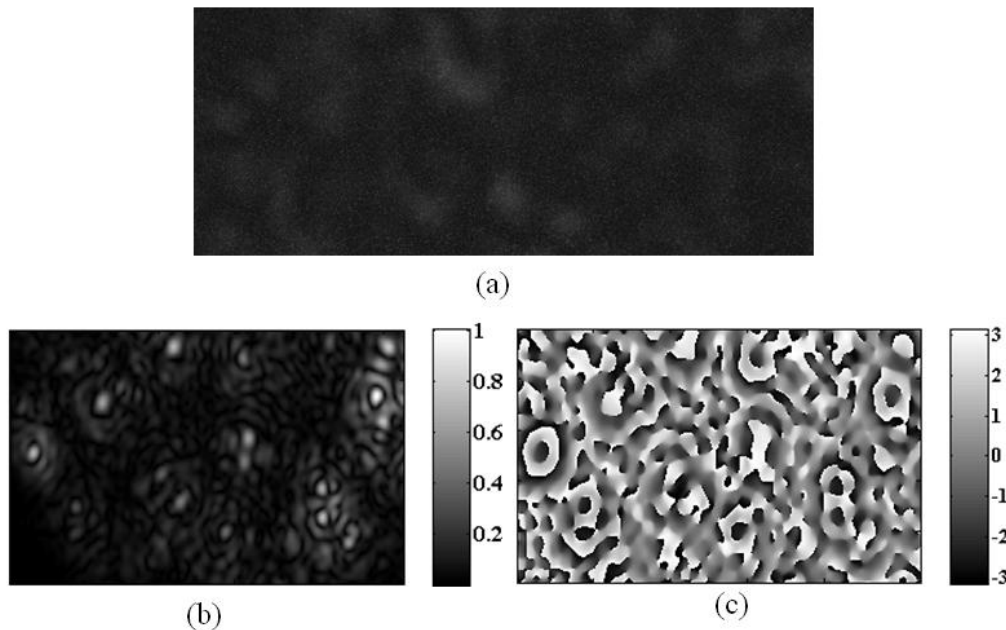
Figure 5.22: (a) Random speckle pattern recorded by the CCD camera (b) & (c) recovered amplitude and phase distribution at 70mm behind the scattering layer for poly styrene beads respectively. The grey scale intensity and phase variation is shown in the respective bar representation.

In summary, we experimentally demonstrated a non-invasive single-shot imaging technique through complex scattering layers using digital inline holographic principle. The retrieval of complex correlation function from the single-shot speckle pattern by employing the two point intensity correlation provides the potential to recover the inline hologram at the scattering plane. Experimental description of the recovery of amplitude and phase of different reflecting and transmitting type objects were demonstrated and a quantitative analysis of reconstruction is performed.

5.4   Conclusion

We proposed and experimentally demonstrated techniques that have unique potential in imaging through complex scattering layers. The randomness of the speckle pattern and speckle holographic approach is effectively exploited to recover the complex correlation function of the speckle field. The recovery of the complex correlation function provided the potential to use the well established van Cittert-Zernike theorem in our experimental strategy. The use of spatial averaging as a replacement of ensemble averaging provides the uniqueness of single-shot non-invasive imaging that effectively reduces the time consumption.

CHAPTER 6
CONCLUSIONS AND FUTURE
WORK

6.1 Conclusions

Shaping and analysis of laser speckle pattern and the effective utilization of their randomness are the key investigations presented in the thesis. Active shaping approach for shaping the laser speckle size has been developed and successfully demonstrated. Some of these significant shaping technique applied are based on the use of diffractive optical elements such as hologram, phase gratings, Dammann gratings, apertures etc. The developed experimental techniques for the controlled shaping of correlation function find applications in optical manipulation and optical imaging. The correlation is not a directly observable quantity and its analysis required interferometric approach. Therefore to test the active speckle (or coherence) shaping, we developed and applied both amplitude and intensity based interferometers and discussed their advantages. To get benefit of single-shot correlation analysis, we rely on the spatial averaging (rather than temporal averaging) and demonstrated application of spatial stationarity feature of random fields in different applications ranging from characterization to imaging. This implementation of spatial averaging in experimental techniques gives the potential of a single-shot imaging and thereby reduces the experimental complexity.

The investigations and development of new experimental techniques capable of treating coherence and polarization together by shaping the speckle pattern provides new potential in polarization sensitive studies. The development of polarization sensitive interferometer and efficient execution of diffractive optical element such as Dammann phase type grating by phase only SLM provides the potential to control the orthogonal polarization components of the fluctuating field. This potential is effectively implemented to generate uniform array of spatial coherence points both in 1D and 2D with desired spacing. This technique offers a new method to synthesis and analysis of laser speckle pattern and consequently controls the coherence and polarization properties of the spatially fluctuating random field. The HBT interferometer based two point intensity correlation is effectively combined with speckle holographic approach to retrieve the complex

information of the random field in scalar and vectorial cases. Generation of singular point array with desired densities is efficiently demonstrated in spatially fluctuating random field by utilizing the concepts of two point intensity correlation and spatial average approach. A new experimental technique for the determination of generalized Stokes parameters or coherence-polarization matrix elements is experimentally demonstrated by making use of the speckle holographic approach in combination with the intensity correlation. This technique is expected to play a crucial role in determining the statistical properties of the vectorial random field and in optical imaging. Applicability of this technique is demonstrated in the controlled synthesis of coherence and polarization properties of random light field.

The potential of the synthesized correlation function is efficiently applied in the optical imaging through random scattering layers. The speckle holographic approach in combination with two point intensity correlation is exploited to recover the complex valued object lying behind the scattering layer. Experimental demonstrations were presented for the recovery of image distribution of the object structure as a distribution of the complex coherence function. The reconstruction of complex coherence function from random speckle pattern gives the opportunity to recover the hologram of objects hidden by the scattering layers. A single-shot imaging technique is demonstrated for the recovery of an off-axis hologram hidden by a scattering layer and the technique has unique ability to retrieve the complex field behind a scattering medium resulting into the reconstruction of actual position of the object. Thus the imaging technique provides the potential to implement the 3D complex field imaging through an opaque scattering medium for wide range of applications. Further to demonstrate the applicability of the technique to more real time situation where the holographic diffraction is dominant, the recovery of in-line hologram through scattering layer is presented. Experimental demonstrations are presented for depth resolved imaging of reflecting type and transmitting type object hidden by the scattering layer. Thus our developed technique has a remarkable achievement in true non-invasive and depth resolved 3D imaging through complex scattering layers, thereby have robust practical applications in biomedical imaging, imaging through turbid media, astronomy etc.

6.2 Future Work

Recent interests in the spatial statistical optics are effectively exploited in the present thesis by making use of the randomness of the speckle pattern for the controlled synthesis of coherence and polarization properties of the spatially fluctuating field and in imaging through the scattering layer. Experimental demonstrations presented in the thesis based on spatial statistics provide potential to explore new possibilities in emerging field of spatial statistical optics. Some of the future scopes the present work is as follows

- Recent interests in special correlation functions can be experimentally implemented by utilizing the polarization sensitive interferometer technique developed for shaping and analysis of speckle pattern. Using this technique more diffractive optical elements can be effectively employed for the controlled shaping of the speckle pattern.

- Effective implementation of the HBT interferometer technique for the determination of GSPs or C-P matrix elements give potential to investigate the propagation induced changes in coherence and polarization properties of the spatially fluctuating random field. This experimental technique may find applications in imaging of polarization sensitive objects especially in biomedical fields.

- Non-invasive single-shot imaging technique through scattering layer can be implemented for more biomedical samples and its possibility of real time implementation can be explored further to develop this technique as a potential tool in biomedical imaging.

- Applying the developed correlation based imaging approach for reconstruction of the object sandwiched between random scattering medium or embedded into the scattering medium.

REFERENCES

1. Agrawal, G. P., and Wolf, E. (2000). Propagation-induced polarization changes in partially coherent optical beams. *J. Opt. Soc. Am. A*, *17*(11): 2019–2023.

2. Angel, L., Tebaldi, M., Bolognini, N., and Trivi, M. (2000). Speckle photography with different pupils in a multiple-exposure scheme. *Journal of the Optical Society of America A: Optics and Image Science, and Vision*, *17*(1): 107–119.

3. Angel, L., Tebaldi, M., Trivi, M., and Bolognini, N. (2001). Properties of speckle patterns generated through multiaperture pupils. *Optics Communications*, *192*: 37–47.

4. Angel, L., Tebaldi, M., Trivi, M., and Bolognini, N. (2002). Phase-object analysis with a speckle interferometer. *Opt. Lett.*, *27*(7): 506–508.

5. Angelsky, O. V., Hanson, S. G., Zenkova, C. Y., Gorsky, M. P., and Gorodyns'ka, N. V. (2009). On polarization metrology (estimation) of the degree of coherence of optical waves. *Optics Express*, *17*(18): 15623–15634.

6. Angelsky, O. V., Zenkova, C. Y., Gorsky, M. P., and Gorodyns'ka, N. V. (2009). Feasibility of estimating the degree of coherence of waves at the near field. *Applied Optics*, *48*(15): 2784–2788.

7. Barakat, R. (2000). Imaging via the van Cittert Zernike theorem using triple-correlations. *Journal of Modern Optics*, *47*(10): 1607–1621.

8. Bartelt, H., Lohmann, A. W., and Wirnitzer, B. (1984). Phase and amplitude recovery from bispectra. *Applied Optics*, *23*(18): 3121–3129.

9. Basso, G., Oliveira, L., and Vidal, I. (2014). Complete characterization of partially coherent and partially polarized optical fields. *Optics Letters*, *39*(5): 1220–1222.

10. Berry, M. V. (1978). Disruption of wavefronts: statistics of dislocations in incoherent Gaussian random waves. *Journal of Physics A: Mathematical and General*, *11*(1): 27–37.

11. Bertolotti, J., van Putten, E. G., Blum, C., Lagendijk, A., Vos, W. L., and Mosk, A. P. (2012). Non-invasive imaging through opaque scattering layers. *Nature*, *491*(7423): 232–234.

12. Boas, D. a, and Dunn, A. K. (2010). Laser speckle contrast imaging in

biomedical optics. *Journal of Biomedical Optics*, *15*(1): 011109.

13. Briers, D., Duncan, D. ., Hirst, E., Kirkpatrick, S. ., Larsson, M., Steenbergen, W., Thopson, O. B. (2013). Laser speckle contrast imaging: theoretical and practical limitations. *Journal of Biomedical Optics*, *18*(6):

14. Broky, J., Ellis, J., and Dogariu, A. (2008). Identifying non-stationarities in random EM fields: are speckles really disturbing? *Optics Express*, *16*(19): 14469–14475.

15. Brown, R. H., and Twiss, R. Q. (1956). Correlation between Photons in two Coherent Beams of Light. *Nature*, *177*(4497): 27–29.

16. Brown, R. H., and Twiss, R. Q. (1957). Interferometry of the Intensity Fluctuations in Light. I. Basic Theory: The Correlation between Photons in Coherent Beams of Radiation. *Proceedings of the Royal Society A: Mathematical, Physical and Engineering Sciences*, *242*(1230): 300–324.

17. Carswell, A. I., and Pal, S. R. (1980). Polarization anisotropy in lidar multiple scattering from clouds. *Applied Optics*, *19*(24): 4123–4126.

18. Carter, W. H., and Wolf, E. (1977). Coherence and radiometry with quasihomogeneous planar sources. *Journal of the Optical Society of America*, *67*(6): 785–796.

19. Chen, Y., Chen, H., Dilworth, D., Leith, E., Lopez, J., Shih, M., Vossler, G. (1993). Evaluation of holographic methods for imaging through biological tissue. *Applied Optics*, *32*(23): 4330–4336.

20. Chen, Y., Wang, F., Liu, L., Zhao, C., Cai, Y., and Korotkova, O. (2014). Generation and propagation of a partially coherent vector beam with special correlation functions. *Physical Review A*, *89*: 013801.

21. Choi, Y., Yang, T. D., Fang-Yen, C., Kang, P., Lee, K. J., Dasari, R. R., … Choi, W. (2011). Overcoming the diffraction limit using multiple light scattering in a highly disordered medium. *Physical Review Letters*, *107*(2): 1–4.

22. Cui, S., Chen, Z., Zhang, L., and Pu, J. (2013). Experimental generation of nonuniformly correlated partially coherent light beams. *Optics Letters*, *38*(22): 4821–4824.

23. Curry, N., Bondareff, P., Leclercq, M., van Hulst, N. F., Sapienza, R., Gigan, S., and Grésillon, S. (2011). Direct determination of diffusion properties of random media from speckle contrast. *Optics Letters*, *36*(17): 3332–3334.

24. Dainty, J. C. (1970). Some Statistical Properties of Random Speckle Patterns in Coherent and Partially Coherent Illumination. *Optica Acta: International Journal of Optics*.17(10): 761-772.

25. Dainty, J. C. (1984). *Laser Speckle and Related Phenomena* (Vol. 1). New York: Springer.

26. Dammann, H., and Görtler, K. (1971). High-efficiency in-line multiple imaging by means of multiple phase holograms. *Optics Communications*, *3*(5): 312–315.

27. Davis, M. A., Kazmi, S. M. S., and Dunn, A. K. (2014). Imaging depth and multiple scattering in laser speckle contrast imaging. *Journal of Biomedical Optics*, *19*(8): 086001.

28. de Boer, J. F., Milner, T. E., and Nelson, J. S. (1999). Determination of the depth-resolved Stokes parameters of light backscattered from turbid media by use of polarization-sensitive optical coherence tomography. *Optics Letters*, *24*(5): 300–302.

29. Ding, H., Wang, Z., Nguyen, F., Boppart, S. a., and Popescu, G. (2008). Fourier transform light scattering of inhomogeneous and dynamic structures. *Physical Review Letters*, *101*(23): 1–4.

30. Ebstein, S. M. (1991). Recovery of spatial-coherence modulus and phase from complex field correlations: fourth-order correlation interferometry. *Journal of the Optical Society of America A*, *8*(9): 1442–1449.

31. Ellis, J., and Dogariu, A. (2004). Complex degree of mutual polarization. *Optics Letters*, *29*(6): 536–538.

32. Feng, S., Kane, C., Lee, P. A., and Stone, A. D. (1988). Correlations and Fluctuations of Coherent Wave Transmission through Disordered Media. *Physical Review Letters*, *61*(7): 834–837.

33. Fercher, A. F. (1996). Optical oherence tomography, *1*(2):, 157–173.

34. Fienup, J. R. (1982). Phase retrieval algorithms: a comparison. *Applied Optics*, *21*(15): 2758–2769.

35. Freund, I., Rosenbluh, M., and Feng, S. (1988). Memory effects in propagation of optical waves through disordered media. *Physical Review Letters*, *61*(20): 2328–2331.

36. Freund, I., Shvartsman, N., and Freilikher, V. (1993). Optical dislocation networks in highly random media. *Optics Communications*, *101*(3-4): 247–

264.

37. Gabor, D. (1948). A new microscopic principle. *Nature*. 4098: 777-778

38. Gamo, H. (1963). Triple correlator of photoelectric fluctuations as a spectroscopic tool. *Journal of Applied Physics*, *34*(4): 875–876.

39. Garcia-Sucerquia, J., Xu, W., Jericho, S. K., Klages, P., Jericho, M. H., and Kreuzer, H. J. (2006). Digital in-line holographic microscopy. *Applied Optics*, *45*(5): 836–850.

40. Gbur, G., and Visser, T. D. (2003). Coherence vortices in partially coherent beams. *Optics Communications*, *222*(1-6): 117–125.

41. Ghabbach, a, Zerrad, M., Soriano, G., and Amra, C. (2014). Accurate metrology of polarization curves measured at the speckle size of visible light scattering, *22*(12): 14594–14609.

42. Glauber, R. J. (1963). The Quantum Theory of Optical Coherence. *Physical Review*, *130*(6): 2529–2539.

43. Goldstein, D. (2010). *Polarized Light, Third Edition*. New York: Marcel Dekker.

44. Gong, W., and Han, S. (2010). Phase-retrieval ghost imaging of complex-valued objects. *Physical Review A - Atomic, Molecular, and Optical Physics*, *82*: 023828.

45. Goodman, J. W. (1976). Some fundamental properties of speckle. *Journal of the Optical Society of America*, *66*(11): 1145–1150.

46. Goodman, J. W. (1996). Introduction to Fourier Optics. New York: McGraw-Hill.

47. Goodman, J. W. (2000). *Statistical Optics*. New Jersy: Wiley-Interscience.

48. Goodman, J. W. (2007). Speckle phenomena in Optics: Theory and Applications.

49. Goodman, J. W., Huntley, W. H., Jackson, D. W., and Lehmann, M. (1966). Wavefront reconstruction imaging through random media. *Applied Physics Letters*, *8*: 311–313.

50. Gori, F. (1998). Matrix treatment for partially polarized, partially coherent beams. *Optics Letters*, *23*(4): 241–243.

51. Gori, F., Santarsiero, M., Borghi, R., and Piquero, G. (2000). Use of the van Cittert-Zernike theorem for partially polarized sources. *Optics Letters*, *25*(17): 1291–1293.

52. Hassinen, T., Tervo, J., Setälä, T., and Friberg, a T. (2011). Hanbury Brown-Twiss effect with electromagnetic waves. *Optics Express*, *19*(16): 15188–95.

53. Huang, D., Swanson, E. A., Lin, C. P., Schuman, J. S., Stinson, W. G., Chang, W., … et al. (1991). Optical coherence tomography. *Science*, *254*(5035): 1178–1181.

54. Kanseri, B., Member, S., Rath, S., Kandpal, H. C., The, A., and Bcp, B. C. (2009). Determination of the Beam Coherence-Polarization Matrix of a Random Electromagnetic Beam, *45*(9): 1163–1167.

55. Katz, O., Heidmann, P., Fink, M., and Gigan, S. (2014). Non-invasive real-time imaging through scattering layers and around corners via speckle correlations. *Nature Photonics*, *8*(10): 784–790.

56. Kelner, R., and Rosen, J. (2012). Spatially incoherent single channel digital Fourier holography. *Optics Letters*, *37*(17): 3723–5.

57. Kim, D., Seo, Y., Jin, M., Yoon, Y., Chegal, W., Cho, Y. J., Magnusson, R. (2014). Stokes vector measurement based on snapshot polarization-sensitive spectral interferometry. *Optics Express*, *22*(14): 17430–17439.

58. Kim, K., and Park, Y. (2012). Fourier transform light scattering angular spectroscopy using digital inline holography. *Optics Letters*, *37*(19): 4161–4163.

59. Kim, M. K. (2011). *Digital Holographic Microscopy. Principles, Techniques, and Applications* (Vol. 162).

60. Kirkpatrick, S. J., and Cipolla, M. J. (2000). High resolution imaged laser speckle strain gauge for vascular applications. *J Biomed Opt*, *5*(1): 62–71.

61. Kodono, H., Asakura, T., and Takai, N. (1987). Roughness and correlation-length determination of rough-surface objects using the speckle contrast. *Applied Physics B*, *44*: 167–173.

62. Kogelnik, H., and Pennington, K. (1968). Holographic imaging through a random medium. *Josa*, *58*(February): 273–274.

63. Korotkova, O., Hoover, B. G., Gamiz, V. L., and Wolf, E. (2005). Coherence and polarization properties of far fields generated by quasi-homogeneous planar electromagnetic sources. *Journal of the Optical Society of America. A,* *22*(11): 2547–2556.

64. Korotkova, O., and Wolf, E. (2005a). Changes in the state of polarization of a random electromagnetic beam on propagation. *Optics Communications*, *246*(1-3): 35–43.

65. Korotkova, O., and Wolf, E. (2005b). Generalized Stokes parameters of

random electromagnetic beams. *Optics Letters*, *30*(2): 198-200.

66. Krackhardt, U., and Streibl, N. (1989). Design of dammann-gratings for array generation. *Optics Communications*, *74*(1-2): 31–36.

67. Kreis, T. (2005). *Handbook of Holographic Interferometry*. Weinheim: Wiley-VCH.

68. L. EK, N.-E. M. (1971). Detection of the nodal lines and the amplitude of vibration by speckle interferometry. *Optics Communications*, *2*(9): 419–424.

69. Labeyrie, A. (1975). Interference fringes obtained on vega with two optical telescopes. *The Astrophysical Journal*, *196*: L71–L75.

70. Lajunen, H., and Saastamoinen, T. (2011). Propagation characteristics of partially coherent beams with spatially varying correlations. *Optics Letters*, *36*(20): 4104–4106.

71. Leader, J. C. (1980). Similarities and distinctions between coherence theory relations and laser scattering phenomena. *Optical Engineering*, *19*(4): 593–601.

72. Leith, E., Chen, C., Chen, H., Chen, Y., Dilworth, D., Lopez, J., … Vossler, G. (1992). Imaging through scattering media with holography. *Journal of the Optical Society of America A*, *9*(7): 1148–1153.

73. Leith, E. N., and Upatnieks, J. (1963). Wavefront Reconstruction with Continuous-Tone Objects. *Journal of the Optical Society of America*, *53*(12): 1377–1381.

74. Leith, E. N., and Upatnieks, J. (1964). Wavefront Reconstruction with Diffused Illumination and Three-Dimensional Objects. *Journal of the Optical Society of America*, *54*(11): 1295–1301.

75. Leith, Emmett N, Upatnieks, J. (1966). Holographic imagery through diffusing media. *J. Opt. Soc. Am.*, *56*(4): 523.

76. Li, J., Yao, G., and Wang, L. V. (2002). Degree of polarization in laser speckles from turbid media: implications in tissue optics. *Journal of Biomedical Optics*, *7*(3): 307–312.

77. Liang, C., Wang, F., Liu, X., Cai, Y., and Korotkova, O. (2014). Experimental generation of cosine-Gaussian-correlated Schell-model beams with rectangular symmetry. *Optics Letters*, *39*(4): 769–772.

78. Lichte, H., and Lehmann, M. (2008). Electron holography—basics and applications. *Reports on Progress in Physics*, *71*(1): 016102.

79. Liu, C. Y. C., and Lohmann, A. W. (1973). High resolution image formation through the turbulent atmosphere. *Optics Communications*, *8*(4): 372–377.

80. Lowenthal, S., and Joyeux, D. (1971). Speckle removal by a slowly moving diffuser associated with a motionless diffuser. *Journal of the Optical Society of America*, *61*(7): 847–851.

81. Maiman, T. H. (1960). Stimulated Optical Radiation in Ruby. *Letters to Nature*.

82. Mandel, L Wolf, E. (1995). Optical Coherence and Quantum Optics. New York: Cambridge University.

83. Manni, J. G., and Goodman, J. W. (2012). Versatile method for achieving 1% speckle contrast in large-venue laser projection displays using a stationary multimode optical fiber. *Optics Express*, *20*(10): 11288–11315.

84. Marasinghe, M. L., Paganin, D. M., and Premaratne, M. (2011). Coherence-vortex lattice formed via Mie scattering of partially coherent light by several dielectric nanospheres. *Optics Letters*, *36*(6): 936–938.

85. Marathay, A. S., Hu, Y., and Shao, L. (1994). Second-, Third-, and Fourth-Order Intensity Correlations. *Optical Engineering*, *33*(10): 3265–3271.

86. Mehta, D. S., Naik, D. N., Singh, R. K., and Takeda, M. (2012). Laser speckle reduction by multimode optical fiber bundle with combined temporal, spatial, and angular diversity. *Applied Optics*, *51*(12): 1894–904.

87. Mehtha, C. L. (1968). New approach to the phase problem in optical coherence theory. *Journal of Optical Society of America*, *58*(9): 1233–1234.

88. Moreno, I., Davis, J. a, Cottrell, D. M., Zhang, N., and Yuan, X.-C. (2010). Encoding generalized phase functions on Dammann gratings. *Optics Letters*, *35*(10): 1536–1538.

89. Mosk, A. P., Lagendijk, A., Lerosey, G., and Fink, M. (2012). Controlling waves in space and time for imaging and focusing in complex media. *Nature Photonics*, *6*(5): 283–292.

90. Naik, D. N., Ezawa, T., Singh, R. K., Miyamoto, Y., and Takeda, M. (2012). Coherence holography by achromatic 3-D field correlation of generic thermal light with an imaging Sagnac shearing interferometer. *Optics Express*, *20*(18): 19658–19669.

91. Naik, D. N., Singh, R. K., Ezawa, T., Miyamoto, Y., and Takeda, M. (2011). Photon correlation holography. *Optics Express*, *19*(2): 1408–1421.

92. Naik, D. N., Singh, R. K., Itou, H., Brundavanam, M. M., Miyamoto, Y., and

Takeda, M. (2012). Single-shot full-field interferometric polarimeter with an integrated calibration scheme. *Optics Letters*, *37*(15): 3282–4.

93. Nomura, T., and Imbe, M. (2010). Single-exposure phase-shifting digital holography using a random-phase reference wave. *Optics Letters*, *35*(13): 2281–2283.

94. O'Holleran, K., Dennis, M., Flossmann, F., and Padgett, M. (2008). Fractality of Light's Darkness. *Physical Review Letters*, *100*: 053902.

95. Ohtsubo, J., and Asakura, T. (1975). Statistical properties of speckle intensity variations in the diffraction field under illumination of coherent light. *Optics Communications*, *14*(1): 30–34.

96. Ostrovsky, A. S., Martínez-Niconoff, G., Arrizón, V., Martínez-Vara, P., Olvera-Santamaría, M. a, and Rickenstorff-Parrao, C. (2009). Modulation of coherence and polarization using liquid crystal spatial light modulators. *Optics Express*, *17*(7): 5257–5264.

97. Paturzo, M., Finizio, A., Memmolo, P., Puglisi, R., Balduzzi, D., Galli, A., and Ferraro, P. (2012). Microscopy imaging and quantitative phase contrast mapping in turbid microfluidic channels by digital holography. *Lab on a Chip*, *12*(17): 3073–3076.

98. Pecora, R. (1985). *Dynamic Light Scattering; Applications of Photon Correlation Spectroscopy*. New York: Plenum Press.

99. Porcello, L. J., Massey, N. G., Innes, R. B., and Marks, J. M. (1976). Speckle reduction in synthetic-aperture radars. *Journal of the Optical Society of America*, *66*(11): 1305–1344.

100. Redding, B., Choma, M. a, and Cao, H. (2011). Spatial coherence of random laser emission. *Optics Letters*, *36*(17): 3404–3406.

101. Redding, B., Choma, M. A., and Cao, H. (2012). Speckle-free laser imaging using random laser illumination. *Nat Photon*, *6*(6): 355–359.

102. Réfrégier, P., Zerrad, M., and Amra, C. (2012). Coherence and polarization properties in speckle of totally depolarized light scattered by totally depolarizing media. *Optics Letters*, *37*(11): 2055–2057.

103. Richards, L. M., Kazmi, S. M. S., Davis, J. L., Olin, K. E., and Dunn, A. K. (2013). Low-cost laser speckle contrast imaging of blood flow using a webcam. *Biomedical Optics Express*, *4*(10): 2269–2283.

104. Ridgen, J.D. Gordon, E. I. (1962). The granularity of scattered optical maser

light. *Proc. IRE*, *50*: 2367–2368.

105. Roychowdhury, H., and Wolf, E. (2003). Determination of the electric cross-spectral density matrix of a random electromagnetic beam. *Optics Communications*, *226*: 57–60.

106. Salem, M., and Wolf, E. (2008). Coherence-induced polarization changes in light beams. *Optics Letters*, *33*(11): 1180–1182.

107. Santarsiero, M., Borghi, R., and Ramírez-Sánchez, V. (2009). Synthesis of electromagnetic Schell-model sources. *J. Opt. Soc. Am. A*, *26*(6): 1437–1443.

108. Schmidt, M. K., Aizpurua, J., Zambrana-Puyalto, X., Vidal, X., Molina-Terriza, G., and Sáenz, J. J. (2015). Isotropically Polarized Speckle Patterns. *Physical Review Letters*, *114*: 113902.

109. Schmitt, J. M., Xiang, S. H., and Yung, K. M. (1999). Speckle in optical coherence tomography. *Journal of Biomedical Optics*, *4*(1): 95–105.

110. Schneiderman, A. M., Kellen, P. ., and Miller, M. G. (1975). laboratory-simulated speckle interferometry. *J. Opt. Soc. Am.*, *65*(11): 1287–1291.

111. Schouten, H. F., Gbur, G., Visser, T. D., and Wolf, E. (2003). Phase singularities of the coherence functions in Young's interference pattern. *Opt Lett*, *28*(12): 968–970.

112. Setälä, T., Tervo, J., and Friberg, A. T. (2006). Contrasts of Stokes parameters in Young's interference experiment and electromagnetic degree of coherence. *Optics Letters*, *31*(18): 2669-2671.

113. Shih, Y. C., Davis, A., Hasinoff, S. W., Durand, F., Shih, Y., Davis, A., Freeman, W. T. (2012). Laser speckle photography for surface tampering detection. In *IEEE Conference on Computer Vision and Pettern recognition*.

114. Shirai, T., and Wolf, E. (2004). Coherence and polarization of electromagnetic beams modulated by random phase screens and their changes on propagation in free space. *Journal of the Optical Society of America A*, *21*(10): 1907–1916.

115. Singh, A. K., Naik, D. N., Pedrini, G., Takeda, M., and Osten, W. (2014). Looking through a diffuser and around an opaque surface: a holographic approach. *Optics Express*, *22*(7): 7694–7701.

116. Singh, R. K., Naik, D. N., Itou, H., Brundabanam, M. M., Miyamoto, Y., and Takeda, M. (2013). Vectorial van Cittert-Zernike theorem based on spatial averaging: experimental demonstrations. *Optics Letters*, *38*(22): 4809–

4812.

117. Singh, R. K., Naik, D. N., Itou, H., Miyamoto, Y., and Takeda, M. (2011). Vectorial coherence holography. *Optics Express*, *19*(12): 11558–67.

118. Singh, R. K., Naik, D. N., Itou, H., Miyamoto, Y., and Takeda, M. (2012). Stokes holography. *Optics Letters*, *37*(5): 966–968.

119. Singh, R. K., Naik, D. N., Itou, H., Miyamoto, Y., and Takeda, M. (2014). Characterization of spatial polarization fluctuations in scattered field. *Journal of Optics*, *16*(10): 105010.

120. Soriano, G., Zerrad, M., and Amra, C. (2014). Enpolarization and depolarization of light scattered from chromatic complex media. *Optics Express*, *22*(10): 12603–12613.

121. Sorrentini, J., Zerrad, M., and Amra, C. (2009). Statistical signatures of random media and their correlation to polarization properties. *Optics Letters*, *34*(16): 2429–2431.

122. Takai, N., and Asakura, T. (1983). Displacement measurement of speckles using a 2-D level-crossing technique. *Appl. Opt.*, *22*(22): 3514–3519.

123. Takeda, M. (2013). Spatial stationarity of statistical optical fields for coherence holography and photon correlation holography. *Opt. Lett.*, *38*(17): 3452–3455.

124. Takeda, M., Ina, H., and Kobayashi, S. (1982). Fourier-transform method of fringe-pattern analysis for computer-based topography and interferometry. *Journal of the Optical Society of America*, *72*(1): 156–160.

125. Takeda, M., Wang, W., Duan, Z., and Miyamoto, Y. (2005). Coherence holography. *Optics Express*, *13*(23): 1–5.

126. Takeda, M., Wang, W., Duan, Z., Miyamoto, Y., and Rosen, J. (2008). Coherence Holography and Spatial Frequency Comb for 3-D Coherence Imaging. *Image (Rochester, N.Y.)*, 3–5.

127. Takeda, M., Wang, W., and Hanson, S. G. (2010). Polarization speckles and generalized stokes vector wave: a review. In *Proc. of SPIE: Optical Metrology* (Vol. 7387, p. 73870V).

128. Takeda, M., Wang, W., and Naik, D. inesh N. (2009). Coherence holography: a thought synthesis and analysis of optical coherence fields. In *Fringe 2009*.

129. Takeda, M., Wang, W., Naik, D. N., and Singh, R. K. (2014). Spatial

Statistical Optics and Spatial Correlation Holography: A Review. *Optical Review*, *21*(6): 849–861.

130. Tchvialeva, L., Dhadwal, G., Lui, H., Kalia, S., Zeng, H., McLean, D. I., and Lee, T. K. (2013). Polarization speckle imaging as a potential technique for in vivo skin cancer detection. *Journal of Biomedical Optics*, *18*(6): 061211.

131. Tebaldi, M. (2004). Speckle interferometric technique to assess soap films. *Optics Communications*, *229*: 29–37.

132. Tebaldi, M., Angel, L., Trivi, M., and Bolognini, N. (2003). Phase-object detection by use of double-exposure fringe-modulated speckle patterns. *Journal of the Optical Society of America. A, Optics, Image Science, and Vision*, *20*(1): 116–129.

133. Tebaldi, M., Toro, L. A., Trivi, M., and Bolognini, N. (2000). New multiple aperture arrangements for speckle photography. *Optics Communications*, *182*(1-3): 95–105.

134. Tegze, M., and Faigel, G. (1996). X-ray holography with atomic resolution. *Nature*, *380*(6569): 49–51.

135. Tervo, J., Setala, T., and Friberg, A. (2003). Degree of coherence for electromagnetic fields. *Optics Express*, *11*(10): 1137–1143.

136. Tervo, J., Setälä, T., Roueff, A., Réfrégier, P., and Friberg, A. T. (2009). Two-point Stokes parameters: interpretation and properties. *Optics Letters*, *34*(20): 3074–3076.

137. Tong, Z., and Korotkova, O. (2012a). Electromagnetic non-uniformly correlated beams. *J. Opt. Soc. Am. A*, *29*(10): 2154–2158.

138. Tong, Z., and Korotkova, O. (2012b). Nonuniformly correlated light beams in uniformly correlated media. *Optics Letters*, *37*(15): 3240–3242.

139. Tran, T.-K.-T., Chen, X., Svensen, Ø., and Akram, M. N. (2014). Speckle reduction in laser projection using a dynamic deformable mirror. *Optics Express*, *22*(9): 11152–11166.

140. Vellekoop, I. M., and Aegerter, C. M. (2010). Scattered light fluorescence microscopy: imaging through turbid layers. *Optics Letters*, *35*(8): 1245–1247.

141. Volpe, G., Kurz, L., Callegari, A., Volpe, G., and Gigan, S. (2014). Speckle optical tweezers: micromanipulation with random light fields. *Optics Express*, *22*(15): 18159–18167.

142. Vry, U., and Fercher, A. F. (1986). Higher-order statistical properties of speckle fields and their application to rough-surface interferometry. *J. Opt. Soc. Am. A*, *3*(7): 988–1000.

143. Wang, F., Liu, X., Yuan, Y., and Cai, Y. (2013). Experimental generation of partially coherent beams with different complex degrees of coherence. *Optics Letters*, *38*(11): 1814–1816.

144. Wang, W., Duan, Z., Hanson, S. G., Miyamoto, Y., and Takeda, M. (2006). Experimental study of coherence vortices: Local properties of phase singularities in a spatial coherence function. *Physical Review Letters*, *96*: 073902.

145. Wang, W., Hanson, S. G., Miyamoto, Y., and Takeda, M. (2005). Experimental investigation of local properties and statistics of optical vortices in random wave fields. *Physical Review Letters*, *94*: 103902.

146. Wang, W., Hanson, S. G., and Takeda, M. (2009). Statistics of polarization speckle: theory versus experiment. *Ninth International Conference on Correlation Optics, Proceedings of SPIE*, *7388*: 738803.

147. Wang, W., and Takeda, M. (2006). Coherence current, coherence vortex, and the conservation law of coherence. *Physical Review Letters*, *96*: 223904.

148. Wang, Y., Meng, P., Wang, D., Rong, L., and Panezai, S. (2013). Speckle noise suppression in digital holography by angular diversity with phase-only spatial light modulator. *Optics Express*, *21*(17): 19568–19578.

149. Weigelt, G. . (1978). Speckle holography measurements of the stars Zeta Cancri and ADS 3358. *Applied Optics*, *17*(17): 2660–2662.

150. Wolf, E. (2003a). Correlation-induced changes in the degree of polarization, the degree of coherence, and the spectrum of random electromagnetic beams on propagation. *Optics Letters*, *28*(13): 1078–1080.

151. Wolf, E. (2003b). Unified theory of coherence and polarization of random electromagnetic beams. *Physics Letters, Section A: General, Atomic and Solid State Physics*, *312*(5-6): 263–267.

152. Wolf, E. (2007). *Introduction to the Theory of coherence and Polarization of Light*. Cambridge University.

153. Xu, W., Jericho, M. H., Meinertzhagen, I. a., and Kreuzer, H. J. (2001). Digital in-line holography for biological applications. *Proceedings of the National Academy of Sciences of the United States of America*, *98*(20):

11301–11305.

154. Yamaguchi, I. (1987). Advances in the laser speckle strain gauge. In *SPIE Photomechanics and Speckle Metrology* (Vol. 814, pp. 141–148).

155. Yaqoob, Z., Psaltis, D., Feld, M. S., and Yang, C. (2008). Optical phase conjugation for turbidity suppression in biological samples. *Nature Photonics*, *2*(2): 110–115.

156. Yu, H., Park, J., Lee, K., Yoon, J., Kim, K., Lee, S., and Park, Y. (2015). Recent advances in wavefront shaping techniques for biomedical applications. *Current Applied Physics*, *15*(5): 632–641.

157. Zerrad, M., Luitot, C., Berthon, J., and Amra, C. (2014). Optical systems for controlled specular depolarization, *39*(24): 6919–6922.

158. Zerrad, M., Sorrentini, J., Soriano, G., and Amra, C. (2010). Gradual loss of polarization in light scattered from rough surfaces: electromagnetic prediction. *Optics Express*, *18*(15): 15832–15843.

159. Zerrad, M., Tortel, H., Soriano, G., Ghabbach, A., and Amra, C. (2015). Spatial depolarization of light from the bulks : electromagnetic prediction. *Opt. Express*, *23*(7): 8246–8260.

160. Zhao, J., and Wang, W. (2014). Experimental study of spatial coherence diffraction based on full-field coherence visualization. *J. Opt. Soc. Am. A*, *31*(10): 2217–2222.

161. Zhou, C., and Liu, L. (1995). Numerical study of Dammann array illuminators. *Applied Optics*, *34*(26): 5961–5969.

162. Zou, H., Zhu, W. H., Gong, J. F., Zhang, K. X., and Xie, H. Y. (2010). The study of various Dammann grating. *2010 Symposium on Photonics and Optoelectronic, SOPO 2010 - Proceedings*, (5): 0–3.

APPENDIX 1

DETERMINATION OF GSPs AND CP MATRIX ELEMENTS

An Experimental scheme is developed for the determination of GSPs or CP matrix elements by making use of the measurement scheme consist of a QWP and LP combination and two point intensity correlation. A detailed derivation of measurement scheme and GSPs or CP matrix elements is presented in this section.

A 1.1 Measurement scheme using QWP and LP

A measurement scheme consists of a QWP with its fast axis at an angle θ with respect to the horizontal direction (X-axis) and a LP filtered in the horizontal direction is used for the determination of the GSPs or C-P matrix elements. A schematic representation of the measurement scheme is shown in Fig. A1.1.
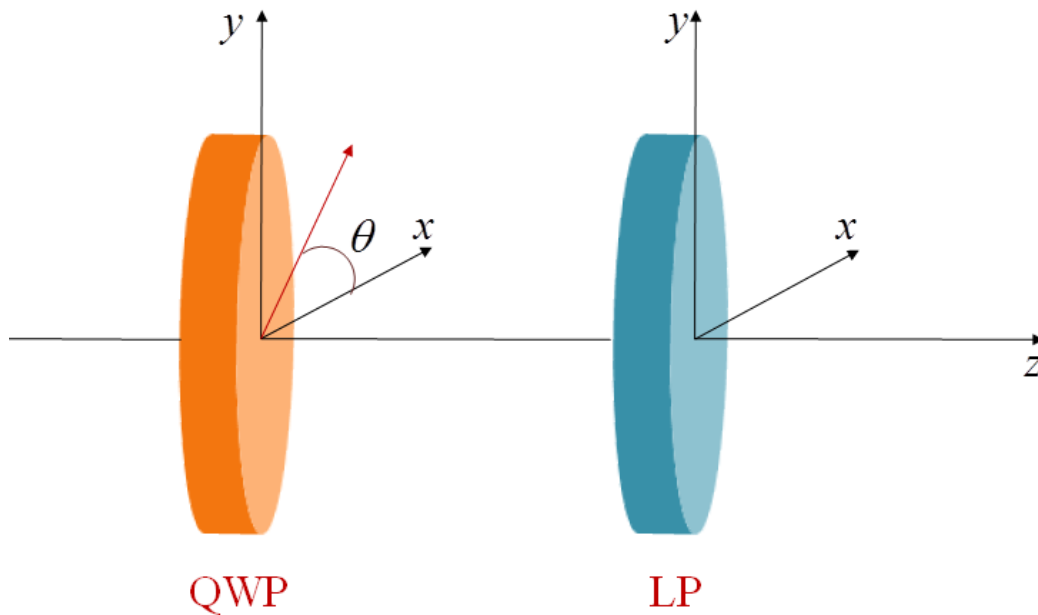

Figure A.1: Schematic representation of the measurement scheme consist of a QWP and LP

A QWP is an optical devise consist of a birefringent material such that the light associated with larger index of refraction is retarded by $\pi/2$ in phase ($(\lambda/4)$) with respect to that associated with smaller index of refraction. Let us consider the case

of a QWP with its fast axis at an angle θ with respect to the X-direction, and then the optical field at the output of the wave plate can be written as

$$
\begin{pmatrix} E'_x(\boldsymbol{r}) \\ E'_y(\boldsymbol{r}) \end{pmatrix} = R(-\theta)QR(\theta)\begin{pmatrix} E_x(\boldsymbol{r}) \\ E_y(\boldsymbol{r}) \end{pmatrix}
$$
$$
= \begin{pmatrix} \cos\theta & -\sin\theta \\ \sin\theta & \cos\theta \end{pmatrix}\begin{pmatrix} 1 & 0 \\ 0 & i \end{pmatrix}\begin{pmatrix} \cos\theta & \sin\theta \\ -\sin\theta & \cos\theta \end{pmatrix}\begin{pmatrix} E_x(\boldsymbol{r}) \\ E_y(\boldsymbol{r}) \end{pmatrix},
$$

(A1.1)

where $\boldsymbol{r}$ is the spatial co-ordinates, $R(\theta) = \begin{pmatrix} \cos\theta & \sin\theta \\ -\sin\theta & \cos\theta \end{pmatrix}$ is the transmission matrix for the rotation of the incident vector of the wave plate, θ is the rotation angle of the QWP and $Q = \begin{pmatrix} 1 & 0 \\ 0 & i \end{pmatrix}$ is the matrix representation of QWP with its fast axis along X-direction.

When the QWP with its fast axis at an angle θ with respect to the X-direction and LP filtered in X-direction, the optical field at the output of this optical combination is given by

$$
\begin{pmatrix} E'_x(\boldsymbol{r}) \\ E'_y(\boldsymbol{r}) \end{pmatrix} = \begin{pmatrix} 1 & 0 \\ 0 & 0 \end{pmatrix}\begin{pmatrix} \cos\theta & -\sin\theta \\ \sin\theta & \cos\theta \end{pmatrix}\begin{pmatrix} 1 & 0 \\ 0 & i \end{pmatrix}\begin{pmatrix} \cos\theta & \sin\theta \\ -\sin\theta & \cos\theta \end{pmatrix}\begin{pmatrix} E_x(\boldsymbol{r}) \\ E_y(\boldsymbol{r}) \end{pmatrix}
$$
$$
= \begin{pmatrix} 1 & 0 \\ 0 & 0 \end{pmatrix}\begin{pmatrix} \cos^2\theta + i\sin^2\theta & (1-i)\sin\theta\cos\theta \\ (1-i)\sin\theta\cos\theta & \sin^2\theta + i\cos^2\theta \end{pmatrix}\begin{pmatrix} E_x(\boldsymbol{r}) \\ E_y(\boldsymbol{r}) \end{pmatrix},
$$

(A1.2)

where $\begin{pmatrix} 1 & 0 \\ 0 & 0 \end{pmatrix}$ is the matrix representation of the LP filtering in the X-direction.

Then the resultant field at the output of this optical combination for a rotation angle θ of the QWP is given by

$$
E'_x(\boldsymbol{r}) = (\cos^2\theta + i\sin^2\theta)E_x(\boldsymbol{r}) + ((1-i)\sin\theta\cos\theta)E_y(\boldsymbol{r}).
$$

(A1.3)

A 1.2 Determination of GSPs

The resultant field reaching the measurement scheme consisting of polarization elements (QWP and LP) is the contribution from reference and the

object speckle field $\left(i.e.\ E_i(\boldsymbol{r}) = E_i^R(\boldsymbol{r}) + E_i^O(\boldsymbol{r})\right)$. The field after the polarization elements can be determined by utilizing Eq. A1. 3 and is given by

$$E_{res}(\boldsymbol{r}_1) = \left[\cos^2\theta + \mathrm{i}\sin^2\theta\right]\left(E_x^R(\boldsymbol{r}) + E_x^O(\boldsymbol{r})\right)$$
$$+ \left[(1-\mathrm{i})\cos\theta\sin\theta\right]\left(E_y^R(\boldsymbol{r}) + E_y^O(\boldsymbol{r})\right) \tag{A1.4}$$

The intensity correlation of the two spatially separated points is the modulus square of this resultant field and is given by

$$\Gamma(\boldsymbol{r}_1, \boldsymbol{r}_2, \theta) = \left|\left\langle E_{res}^*(\boldsymbol{r}_1) E_{res}(\boldsymbol{r}_2)\right\rangle\right|^2$$

$$= \frac{1}{4}\left| \begin{array}{l} \left(1+\cos^2 2\theta\right)\left(W_{xx}^R(\boldsymbol{r}_1,\boldsymbol{r}_2) + W_{xx}^O(\boldsymbol{r}_1,\boldsymbol{r}_2)\right) + \\ \left(1-\cos^2 2\theta\right)\left(W_{yy}^R(\boldsymbol{r}_1,\boldsymbol{r}_2) + W_{yy}^O(\boldsymbol{r}_1,\boldsymbol{r}_2)\right) + \\ \left(\dfrac{\sin 4\theta}{2} - \mathrm{i}\sin 2\theta\right)\left(W_{xy}^R(\boldsymbol{r}_1,\boldsymbol{r}_2) + W_{xy}^O(\boldsymbol{r}_1,\boldsymbol{r}_2)\right) + \\ \left(\dfrac{\sin 4\theta}{2} + \mathrm{i}\sin 2\theta\right)\left(W_{yx}^R(\boldsymbol{r}_1,\boldsymbol{r}_2) + W_{yx}^O(\boldsymbol{r}_1,\boldsymbol{r}_2)\right) \end{array} \right|^2 \tag{A1.5}$$

where

$$W_{xx}^l(\boldsymbol{r}_1,\boldsymbol{r}_2) = \left\langle E_x^{l*}(\boldsymbol{r}_1)E_x^l(\boldsymbol{r}_2)\right\rangle, W_{xy}^l(\boldsymbol{r}_1,\boldsymbol{r}_2) = \left\langle E_x^{l*}(\boldsymbol{r}_1)E_y^l(\boldsymbol{r}_2)\right\rangle,$$

$$W_{yx}^l(\boldsymbol{r}_1,\boldsymbol{r}_2) = \left\langle E_y^{l*}(\boldsymbol{r}_1)E_x^l(\boldsymbol{r}_2)\right\rangle \text{ and } W_{yy}^l(\boldsymbol{r}_1,\boldsymbol{r}_2) = \left\langle E_y^{l*}(\boldsymbol{r}_1)E_x^l(\boldsymbol{r}_2)\right\rangle \text{ with } l = R \text{ or } O$$

On introducing the GSPs in terms of CP matrix elements, Eq. A1.5 modifies to

$$\Gamma(\Delta\boldsymbol{r}, \theta) = \frac{1}{4}\left| \begin{array}{l} \left[S_0(\Delta\boldsymbol{r})\right] + \left[S_1(\Delta\boldsymbol{r})\right]\cos^2 2\theta \\ + \left[S_2(\Delta\boldsymbol{r})\right]\dfrac{\sin 4\theta}{2} + \left[S_3(\Delta\boldsymbol{r})\right]\sin 2\theta \end{array} \right|^2 \tag{A1.6}$$

where $\Delta\boldsymbol{r} = \boldsymbol{r}_2 - \boldsymbol{r}_1$ and considered the replacement of ensemble average with spatial average under the condition of spatial stationarity and ergodicity. Here we have used the representation $S_k(\Delta\boldsymbol{r}) = S_k^R(\Delta\boldsymbol{r}) + S_k^O(\Delta\boldsymbol{r})$ with $k = 0, 1, 2$ and 3 and

$$S_0^l(\Delta\boldsymbol{r}) = W_{xx}^l(\Delta\boldsymbol{r}) + W_{yy}^l(\Delta\boldsymbol{r})$$
$$S_1^l(\Delta\boldsymbol{r}) = W_{xx}^l(\Delta\boldsymbol{r}) - W_{yy}^l(\Delta\boldsymbol{r})$$
$$S_2^l(\Delta\boldsymbol{r}) = W_{xy}^l(\Delta\boldsymbol{r}) + W_{yx}^l(\Delta\boldsymbol{r})$$
$$S_3^l(\Delta\boldsymbol{r}) = \mathrm{i}\left[W_{yx}^l(\Delta\boldsymbol{r}) - W_{xy}^l(\Delta\boldsymbol{r})\right] \text{ with } l = R \text{ or } O \tag{A1.7}$$

By choosing appropriate angles for QWP rotation (i.e θ) such that $\theta_1 = 0°, \theta_2 = 22.5°, \theta_3 = 45°$ and $\theta_4 = 135°$; four intensity correlation results which are the combination of GSPs can be obtained as

$$\Gamma(\Delta\boldsymbol{r},\theta_1) = \frac{1}{4}\left|S_0(\Delta\boldsymbol{r}) + S_1(\Delta\boldsymbol{r})\right|^2$$

$$\Gamma(\Delta\boldsymbol{r},\theta_2) = \frac{1}{4}\left|S_0(\Delta\boldsymbol{r}) + \frac{S_1(\Delta\boldsymbol{r})}{2} + \frac{S_2(\Delta\boldsymbol{r})}{2} + \frac{S_3(\Delta\boldsymbol{r})}{\sqrt{2}}\right|^2$$

$$\Gamma(\Delta\boldsymbol{r},\theta_3) = \frac{1}{4}\left|S_0(\Delta\boldsymbol{r}) + S_3(\Delta\boldsymbol{r})\right|^2 \qquad \text{(A1.8)}$$

$$\Gamma(\Delta\boldsymbol{r},\theta_4) = \frac{1}{4}\left|S_0(\Delta\boldsymbol{r}) - S_3(\Delta\boldsymbol{r})\right|^2$$

On bringing the intensity correlation functions to right hand side of the equation, Eq.A1.8 modifies to

$$\left|S_0(\Delta\boldsymbol{r}) + S_1(\Delta\boldsymbol{r})\right|^2 = 4\Gamma(\Delta\boldsymbol{r},\theta_1)$$

$$\left|S_0(\Delta\boldsymbol{r}) + \frac{S_1(\Delta\boldsymbol{r})}{2} + \frac{S_2(\Delta\boldsymbol{r})}{2} + \frac{S_3(\Delta\boldsymbol{r})}{\sqrt{2}}\right|^2 = 4\Gamma(\boldsymbol{r}_1,\boldsymbol{r}_2,\theta_2)$$

$$\left|S_0(\Delta\boldsymbol{r}) + S_3(\Delta\boldsymbol{r})\right|^2 = 4\Gamma(\Delta\boldsymbol{r},\theta_3) \qquad \text{(A1.9)}$$

$$\left|S_0(\Delta\boldsymbol{r}) - S_3(\Delta\boldsymbol{r})\right|^2 = 4\Gamma(\Delta\boldsymbol{r},\theta_4)$$

Due to the superposition of the speckle field from object and reference field, the two point intensity correlation results into an intensity correlation hologram. Therefore each of the intensity correlation results for the particular rotations of the QWP are intensity correlation holograms. Fourier transform operation on the hologram results into a spectrum, its complex conjugate and the dc term. On filtering out the desired spectrum and moving it to the centre and performing inverse Fourier transform operation modifies Eq. A1.9 to

$$S_0^O(\Delta\boldsymbol{r}) + S_1^O(\Delta\boldsymbol{r}) = 4\Gamma'(\Delta\boldsymbol{r},\theta_1)$$

$$S_0^O(\Delta\boldsymbol{r}) + \frac{S_1^O(\Delta\boldsymbol{r})}{2} + \frac{S_2^O(\Delta\boldsymbol{r})}{2} + \frac{S_3^O(\Delta\boldsymbol{r})}{\sqrt{2}} = 4\Gamma'(\Delta\boldsymbol{r},\theta_2)$$

$$S_0^O(\Delta\boldsymbol{r}) + S_3^O(\Delta\boldsymbol{r}) = 4\Gamma'(\Delta\boldsymbol{r},\theta_3) \qquad \text{(A1.10)}$$

$$S_0^O(\Delta\boldsymbol{r}) - S_3^O(\Delta\boldsymbol{r}) = 4\Gamma'(\Delta\boldsymbol{r},\theta_4)$$

where $\Gamma'(\Delta \boldsymbol{r}, \theta_m)$ with $m = 1, 2, 3$ and 4 are the inverse Fourier transform of the spectra which is filtered and translated to the origin of the frequency axis.

From Eq. A1.10 GSPs of the object field can be determined and is given by

$$
\begin{aligned}
S_0^O(\Delta \boldsymbol{r}) &= 2\Gamma'(\Delta \boldsymbol{r}, \theta_3) + 2\Gamma'(\Delta \boldsymbol{r}, \theta_4) \\
S_1^O(\Delta \boldsymbol{r}) &= 4\Gamma'(\Delta \boldsymbol{r}, \theta_1) - 2\Gamma'(\Delta \boldsymbol{r}, \theta_3) - 2\Gamma'(\Delta \boldsymbol{r}, \theta_4) \\
S_2^O(\Delta \boldsymbol{r}) &= 8\Gamma'(\Delta \boldsymbol{r}, \theta_2) - 2(1 + \sqrt{2})\Gamma'(\Delta \boldsymbol{r}, \theta_3) \\
&\quad - 2(1 - \sqrt{2})\Gamma'(\Delta \boldsymbol{r}, \theta_4) - 4\Gamma'(\Delta \boldsymbol{r}, \theta_1) \\
S_3^O(\Delta \boldsymbol{r}) &= 2\Gamma'(\Delta \boldsymbol{r}, \theta_3) - 2\Gamma'(\Delta \boldsymbol{r}, \theta_4)
\end{aligned}
\tag{A1. 11}
$$

A 1.3 Determination of CP matrix elements

A similar procedure is used to derive the CP matrix elements and is used in the synthesis of coherence and polarization properties of the field. On recalling Eq. A1.5 and the object field is modified and represented as synthesized (object arm is used for the synthesis of the desired field) field Eq. A1. 5 can be written as

$$
\begin{aligned}
\Gamma(\boldsymbol{r}_1, \boldsymbol{r}_2, \theta) &= \left| \left\langle E_{res}^*(\boldsymbol{r}_1) E_{res}(\boldsymbol{r}_2) \right\rangle \right|^2 \\
&= \frac{1}{4} \left|
\begin{aligned}
&\left(1 + \cos^2 2\theta\right)\left(W_{xx}^R(\boldsymbol{r}_1, \boldsymbol{r}_2) + W_{xx}^S(\boldsymbol{r}_1, \boldsymbol{r}_2)\right) + \\
&\left(1 - \cos^2 2\theta\right)\left(W_{yy}^R(\boldsymbol{r}_1, \boldsymbol{r}_2) + W_{yy}^S(\boldsymbol{r}_1, \boldsymbol{r}_2)\right) + \\
&\left(\frac{\sin 4\theta}{2} - i\sin 2\theta\right)\left(W_{xy}^R(\boldsymbol{r}_1, \boldsymbol{r}_2) + W_{xy}^S(\boldsymbol{r}_1, \boldsymbol{r}_2)\right) + \\
&\left(\frac{\sin 4\theta}{2} + i\sin 2\theta\right)\left(W_{yx}^R(\boldsymbol{r}_1, \boldsymbol{r}_2) + W_{yx}^S(\boldsymbol{r}_1, \boldsymbol{r}_2)\right)
\end{aligned}
\right|^2
\end{aligned}
\tag{A1. 12}
$$

By choosing appropriate angles for QWP rotation (i.e θ) such that $\theta_1 = 0°, \theta_2 = 22.5°, \theta_3 = 45°$ and $\theta_4 = 135°$; four intensity correlation results which are the combination of CP matrix elements can be obtained as

$$\Gamma(\mathbf{r}_1,\mathbf{r}_2,\theta_1) = \frac{1}{4}\left|2W_{xx}(\Delta\mathbf{r})\right|^2$$

$$\Gamma(\mathbf{r}_1,\mathbf{r}_2,\theta_2) = \frac{1}{4}\left|\begin{array}{l}\frac{3}{2}W_{xx}(\Delta\mathbf{r})+\left(\frac{1}{2}-\frac{i}{\sqrt{2}}\right)W_{xy}(\Delta\mathbf{r})\\[4pt]+\left(\frac{1}{2}+\frac{i}{\sqrt{2}}\right)W_{yx}(\Delta\mathbf{r})+\frac{1}{2}W_{yy}(\Delta\mathbf{r})\end{array}\right|^2 \tag{A1. 13}$$

$$\Gamma(\mathbf{r}_1,\mathbf{r}_2,\theta_3) = \frac{1}{4}\left|W_{xx}(\Delta\mathbf{r})-i\left(W_{xy}(\Delta\mathbf{r})-W_{yx}(\Delta\mathbf{r})\right)+W_{yy}(\Delta\mathbf{r})\right|^2$$

$$\Gamma(\mathbf{r}_1,\mathbf{r}_2,\theta_4) = \frac{1}{4}\left|W_{xx}(\Delta\mathbf{r})+i\left(W_{xy}(\Delta\mathbf{r})-W_{yx}(\Delta\mathbf{r})\right)+W_{yy}(\Delta\mathbf{r})\right|^2$$

On bringing the intensity correlation functions to right hand side of the equation, Eq.A1.13 modifies to

$$\left|2W_{xx}(\Delta\mathbf{r})\right|^2 = 4\Gamma(\mathbf{r}_1,\mathbf{r}_2,\theta_1)$$

$$\left|\frac{3}{2}W_{xx}(\Delta\mathbf{r})+\left(\frac{1}{2}-\frac{i}{\sqrt{2}}\right)W_{xy}(\Delta\mathbf{r})+\left(\frac{1}{2}+\frac{i}{\sqrt{2}}\right)W_{yx}(\Delta\mathbf{r})+\frac{1}{2}W_{yy}(\Delta\mathbf{r})\right|^2 = 4\Gamma(\mathbf{r}_1,\mathbf{r}_2,\theta_2)$$

$$\left|W_{xx}(\Delta\mathbf{r})-i\left(W_{xy}(\Delta\mathbf{r})-W_{yx}(\Delta\mathbf{r})\right)+W_{yy}(\Delta\mathbf{r})\right|^2 = 4\Gamma(\mathbf{r}_1,\mathbf{r}_2,\theta_3)$$

$$\left|W_{xx}(\Delta\mathbf{r})+i\left(W_{xy}(\Delta\mathbf{r})-W_{yx}(\Delta\mathbf{r})\right)+W_{yy}(\Delta\mathbf{r})\right|^2 = 4\Gamma(\mathbf{r}_1,\mathbf{r}_2,\theta_4)$$

$$(A1.14)$$

On applying the Fourier transform filtering approach as discussed in the previous section the Eq. A1. 14 modifies to

$$W_{xx}^{S}(\Delta\mathbf{r}) = 2\Gamma'(\mathbf{r}_1,\mathbf{r}_2,\theta_1)$$

$$\frac{3}{2}W_{xx}^{S}(\Delta\mathbf{r})+\left(\frac{1}{2}-\frac{i}{\sqrt{2}}\right)W_{xy}^{S}(\Delta\mathbf{r})+\left(\frac{1}{2}+\frac{i}{\sqrt{2}}\right)W_{yx}^{S}(\Delta\mathbf{r})+\frac{1}{2}W_{yy}^{S}(\Delta\mathbf{r}) = 4\Gamma'(\mathbf{r}_1,\mathbf{r}_2,\theta_2)$$

$$W_{xx}^{S}(\Delta\mathbf{r})-i\left(W_{xy}^{S}(\Delta\mathbf{r})-W_{yx}^{S}(\Delta\mathbf{r})\right)+W_{yy}^{S}(\Delta\mathbf{r}) = 4\Gamma'(\mathbf{r}_1,\mathbf{r}_2,\theta_3)$$

$$W_{xx}^{S}(\Delta\mathbf{r})+i\left(W_{xy}^{S}(\Delta\mathbf{r})-W_{yx}^{S}(\Delta\mathbf{r})\right)+W_{yy}^{S}(\Delta\mathbf{r}) = 4\Gamma'(\mathbf{r}_1,\mathbf{r}_2,\theta_4)$$

$$(A1.15)$$

From Eq. A1.15 the CP matrix elements of the synthesized field are given by

$$W_{xx}^S(\Delta \boldsymbol{r}) = 2\Gamma'(\Delta \boldsymbol{r}, \theta_1)$$

$$W_{yy}^S(\Delta \boldsymbol{r}) = 2\Gamma'(\Delta \boldsymbol{r}, \theta_3) + 2\Gamma'(\Delta \boldsymbol{r}, \theta_4) - 2\Gamma'(\Delta \boldsymbol{r}, \theta_1)$$

$$W_{xy}^S(\Delta \boldsymbol{r}) = 4\Gamma'(\Delta \boldsymbol{r}, \theta_2) - 2\Gamma'(\Delta \boldsymbol{r}, \theta_1)$$

$$-(1+\sqrt{2}-i)\Gamma'(\Delta \boldsymbol{r}, \theta_3) - (1-\sqrt{2}+i)\Gamma'(\Delta \boldsymbol{r}, \theta_4)$$

$$W_{yx}^S(\Delta \boldsymbol{r}) = 4\Gamma'(\Delta \boldsymbol{r}, \theta_2) - 2\Gamma'(\Delta \boldsymbol{r}, \theta_1)$$

$$-(1+\sqrt{2}+i)\Gamma'(\Delta \boldsymbol{r}, \theta_3) - (1-\sqrt{2}-i)\Gamma'(\Delta \boldsymbol{r}, \theta_4)$$

(A1. 16)

APPENDIX 2

WAVE PROPAGATION TECHNIQUES

Wave propagation techniques have remarkable importance in holography based imaging techniques. In this section we describe some of the wave propagation techniques that play a crucial role in the object reconstruction from holograms.

A2.1. Rayleigh-Sommerfeld formulation of wave propagation

The Kirchhoff formulation of diffraction theory found to be inconsistent, since the theory implies that the field is zero everywhere behind the aperture which contradicts the physical situation. By using a different choice of the Green's function, Sommerfeld removed this inconsistency and the corresponding results are called Rayleigh-Sommerfeld diffraction formulation. Let us first consider the field immediately behind the screen given by Kirchhoff as

$$U(P_1) = \frac{1}{4\pi} \iint_{S_1} \left(\frac{\partial U}{\partial n} G - U \frac{\partial G}{\partial n} \right) ds \qquad (A2.1)$$

where U is the complex function of the position and $G = \frac{\exp(jkr)}{r}$ is the Green's function, r is the length of the position vector and S_1 is the surface immediately behind the aperture. Sommerfeld proved that the assumptions of boundary conditions imposed by Kirchhoff are inconsistent and he modified the theory by making use of Green's functions. A schematic representation showing the Rayleigh-Sommerfeld diffraction formulation is shown in Fig. A2. 1.
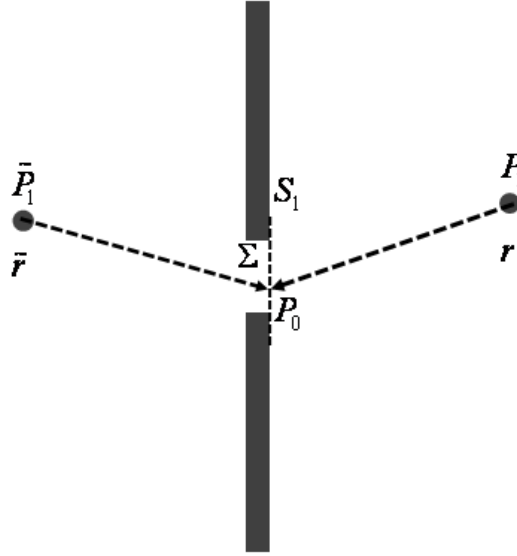
Figure A2.1: Schematic representation of Rayleigh-Sommerfeld diffraction formulation

An alternate Green's function that meets the requirement is proposed of two identical point sources at two sides of the aperture which oscillating with 180^0 phase difference. This Green's function is given by

$$G_- = \frac{\exp(jkr)}{r} - \frac{\exp(jk\tilde{r})}{\tilde{r}} \tag{A2. 2}$$

On substituting the Green's function G_- instead of G in Eq. A2.1, the field contribution at the point P_1 is given by

$$U(x, y, z) = \frac{1}{j\lambda} \iint_\Sigma U(\hat{x}, \hat{y}, 0) \frac{\exp(jkr)}{r} \cos\theta \, dxdy \tag{A2. 3}$$

where Σ is the aperture surface, $U(\hat{x}, \hat{y}, 0)$ is the field at the aperture , r is the length of the position vector from aperture to the observation point and θ is the angle to the surface normal. Eq. A2.3 is the Rayleigh-Sommerfeld diffraction formula and can be executed for the determination of field distribution at different planes behind the source aperture.

A2.2. Angular spectrum method of wave propagation

Angular spectrum method of wave propagation is useful to determine the field amplitude at any other point or any parallel plane by adding the contributions

of plane waves during the propagation. Let us consider a field $U(x, y; 0)$ at $z = 0$, then the Fourier transform of the field distribution is given by

$$A(f_X, f_Y; 0) = \iint U(x, y; 0) \exp\left[-j2\pi\left(f_X x + f_y y\right)\right] dx dy \qquad \text{(A2. 4)}$$

On considering Fourier decomposition of $U(x, y; 0)$, the angular spectrum representation of the field $U(x, y; 0)$ is given by

$$A\left(\frac{\alpha}{\lambda}, \frac{\beta}{\lambda}; 0\right) = \iint U(x, y; 0) \exp\left[-j2\pi\left(\frac{\alpha}{\lambda} x + \frac{\beta}{\lambda} y\right)\right] dx dy \qquad \text{(A2. 5)}$$

where $\dfrac{\alpha}{\lambda} = f_X, \dfrac{\beta}{\lambda} = f_Y$. Eq. A2.5 is derived by considering the direction cosines (α, β, γ) and is related by $\alpha = \lambda f_X, \beta = \lambda f_Y$ and $\gamma = \sqrt{1 - \alpha^2 - \beta^2}$.

The propagation of angular spectrum of $U(x, y; 0)$ across any plane at a distance z is given by

$$A\left(\frac{\alpha}{\lambda}, \frac{\beta}{\lambda}; z\right) = \iint U(x, y; z) \exp\left[-j2\pi\left(\frac{\alpha}{\lambda} x + \frac{\beta}{\lambda} y\right)\right] dx dy \qquad \text{(A2. 6)}$$

The field distribution at the corresponding plane z is given by

$$U(x, y; z) = \iint A\left(\frac{\alpha}{\lambda}, \frac{\beta}{\lambda}; z\right) \exp\left[j2\pi\left(\frac{\alpha}{\lambda} x + \frac{\beta}{\lambda} y\right)\right] d\frac{\alpha}{\lambda} d\frac{\beta}{\lambda} \qquad \text{(A2. 7)}$$

This field distribution $U(x, y; z)$ must have to satisfy the Helmholtz equation

$$\nabla^2 U + k^2 U = 0 \qquad \text{(A2. 8)}$$

So an elementary solution of this equation is given by

$$A\left(\frac{\alpha}{\lambda}, \frac{\beta}{\lambda}; z\right) = \iint A\left(\frac{\alpha}{\lambda}, \frac{\beta}{\lambda}; 0\right) \exp\left[j\frac{2\pi}{\lambda} \sqrt{1 - \alpha^2 - \beta^2} z\right] \qquad \text{(A2. 9)}$$

When the direction cosines satisfy $\alpha^2 + \beta^2 < 1$, the effect of propagation over the distance z is a change of the relative phase of the various components of the angular spectrum. Then the field distribution at a distance z can be obtained by

inverse Fourier transforming Eq. A2.9 and is given by

$$U(x, y; z) = \iint A\left(\frac{\alpha}{\lambda}, \frac{\beta}{\lambda}; 0\right) \exp\left[j\frac{2\pi}{\lambda} \sqrt{1 - \alpha^2 - \beta^2} \, z \right]$$
$$\times circ\left(\sqrt{\alpha^2 + \beta^2}\right) \exp\left[j2\pi\left(\frac{\alpha}{\lambda} x + \frac{\beta}{\lambda} y\right) \right] d\frac{\alpha}{\lambda} d\frac{\beta}{\lambda}$$

(A2. 10)

where the *circ* function controls the region of integration. Eq.A2. 10 can be effectively implemented numerically for the determination of field distribution at various planes parallel to the aperture plane.

APPENDIX 3

The experimental demonstrations presented in the thesis utilize a number of optical components and devises. The technical details of the optical components and devises are presented here.

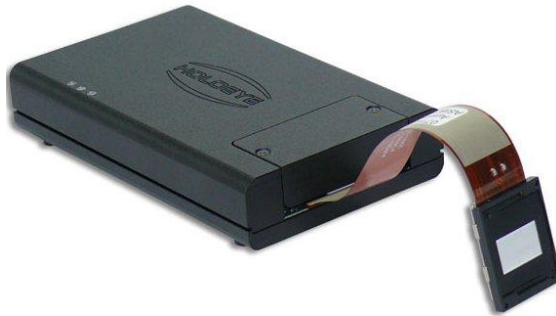## Spatial Light Modulator (SLM):

- **PLUTO Phase only SLM**

Figure A3.1: Photograph of Pluto phase only SLM

Display type: Reflective LCOS (Phase only)
Resolution: 1920 x 1080
Pixel pitch: 8.0 µm
Active area: 15.36 x 8.64 mm (0.7″ Diagonal)
Addressing: 8 Bit (256 Grey Levels)
Signal formats: DVI – HDTV Resolution
Frame rate: 60 Hz

- **LC-R 720 SLM**

Figure A3.2: Photograph of LC-R 720 SLM

Display type: Reflective LCOS (Twisted Nematic)
Resolution: 1280 x 768
Pixel pitch: 20.0 µm
Active area: 25.6 x 15.4 mm (1.18″ Diagonal)
Addressing: 8 Bit (256 Grey Levels)
Signal formats: DVI – WXGA Resolution
Frame rate: 180 Hz
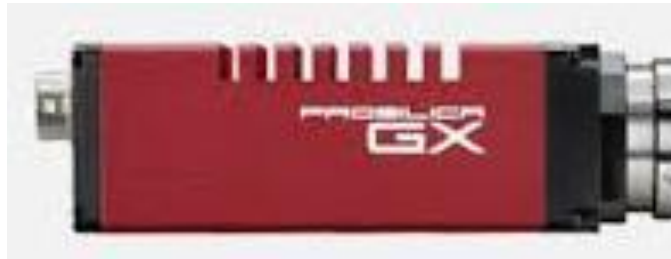
CCD Monochrome camera:

- **Prosilica GX 2750**

Figure A3.3: Photograph of CCD monochrome camera

Resolution: 2750 × 2200
Sensor: Sony ICX694
Sensor type: CCD Progressive
Cell size: 4.54 µm
Lens mount: C (adjustable)
Frame rate: 20 fps
ADC: 14 Bit
On-board FIFO: 128 M byte

Spiral Phase Plate: VPP-m633 (RPC Photonics, USA)

Vortex Geometry
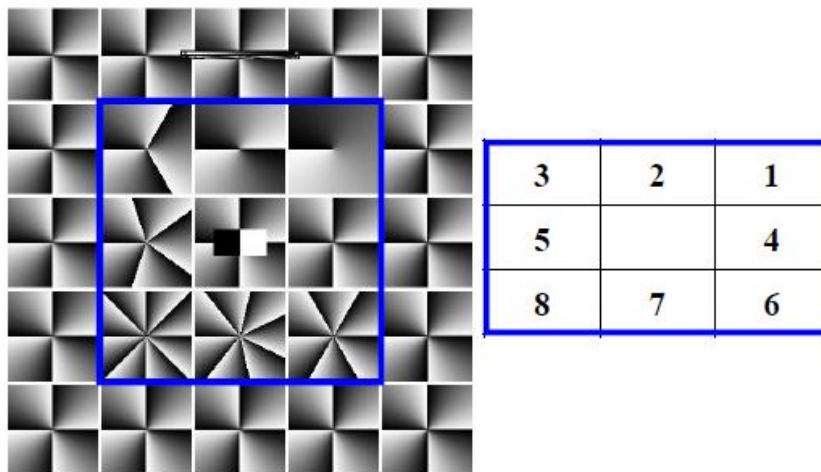
3	2	1
5		4
8	7	6

Figure A3.4: Vortex geometry in spiral phase palte-VPP-m633; highlighted area shows the different topological charge position.

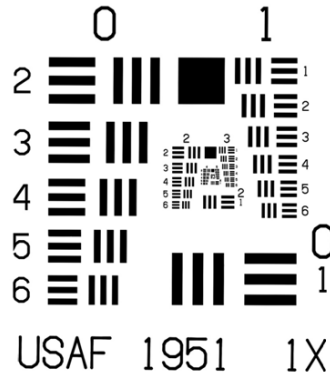## USAF Resolution chart: USAF 1951 1X (Edmund Optics)

Figure A3.5: USAF 1951 1X Resolution chart.

LASERS:

- **He-Ne Laser systems-CVI Melles Griot**
    - 25-LHP-928-230:

      Wavelength-633nm

      CW output power: 35.0mW

      Polarization: Linear>500:1
    - 25-LHP-925-230:

      Wavelength-633nm

      CW output power: 17.0mW

      Polarization: Linear>500:1
    - 25-LYP-173-230:

      Wavelength-594.1nm

      CW output power: 5.0mW

      Polarization: Linear>500:1

Ground Glass Diffusers: Thor Labs

- DG20-120-MD: 2" with 120 GRIT

Wave Plates: Thorlabs

- Quarter Wave plate: AQWP05M-600 (400-800nm)
- Half Wave plate: AHWPO5M-600 (400-800nm)

Polarizer: Thorlabs

- Mounted Linear Polarizer: 12.5mm, SM05, 500-720nm

Non-polarizing Beam Splitter: Edmund Optics

- CMI-BSO13 (50:50)

Polarization Beam Splitter: Edmund Optics

- CMI-PBS251 (50:50)

Lenses: Thorlabs

- Achromatic Doublet, F=750mm AC508-75A
- Achromatic Doublet, F=100mm AC508-100A
- Achromatic Doublet, F=150mm AC508-150A
- Plano convex lens, F=100mm, N-BK7, LA1050-A
- Biconvex lens, F=100mm, N-BK7, LB1630-A
- Biconvex lens, F=150mm, N-BK7, LB1374-A
- Biconvex lens, F=200mm, N-BK7, LB1199-A

Mirrors: Thorlabs

- Dielectric high quality mirrors (50.8mm)-BB2-E02
- Dielectric high quality mirrors (25.4mm)-BB1-E02
- Aluminium protected mirror (25.4mm)-PF10-03-G01
- Aluminium protected mirror (25.4mm)-PF20-03-G01

Spatial Filter Assembly: New port

- Three axis spatial filter-M-900

Microscope Objective: New port

- M-20X
- M-40X

High Energy Pinhole Aperture: New port

- 10 micron- 900PH-10
- 15 micron-900PH-15

LIST OF PUBLICATIONS BASED ON THE THESIS

PUBLISHED

1   **Vinu, R.V**. Sharma, M. K. Singh, R.K. and Senthilkumaran, P. (2014). Generation of spatial coherence comb using Dammann grating. *Optics Letters,* 39(8): 2407-2409.

2   Singh, R.K. **Vinu, R.V**. and Anandraj, S. M. (2014). Recovery of complex valued objects from two-point intensity correlation measurement. *Applied Physics Letters,* 104: 111108/1-4.

3   Singh, R.K. **Vinu, R.V**. and Anandraj, S. M. (2014). Retrieving complex coherence from two-point intensity correlation using holographic principle. *Optical Engineering,* 53: 104102/1-5.

4   **Vinu, R.V**. and Singh, R.K. (2015). Experimental determination of generalized Stokes parameters, *Optics Letters,* 40(7): 1227-1230.

5   **Vinu, R.V**. and Singh, R.K. (2015). Synthesis of statistical properties of randomly fluctuating polarized field. *Applied Optics,* 54 (21): 6491-6497.

6   Soni, N.K. **Vinu R.V**. and Singh, R.K. (2016) Imaging behind the scattering medium by polarization modulation. *Optics Letters,* **41**(5): 906-909.

COMMUNICATED/UNDER PREPARATION

1   **Vinu, R.V**. Gaur, C. Khare, K. and Singh, R.K. Sparsity assisted approach for imaging from laser speckle. (Submitted SPIE-photonics West-2017).

2   **Vinu, R.V**. and Singh, R.K. Determining helicity and topological charge of a coherent vortex beam from laser speckle. (Communicated).

3   Somkuwar, A. S. Das, B. **Vinu, R.V**. Park, Y. and Singh, R.K. (2016). Non-invasive single-shot 3D imaging through a scattering layer using speckle interferometry. arXiv:1511.04658.

4 **Vinu, R.V**. Kim, K. Somkuwar, A. S. Park, Y. and Singh, R.K. Digital in-line holographic non-invasive imaging through complex scattering layers. arXiv:1603.07430.

5 **Vinu, R.V**. Senthilkumaran, P. and Singh, R.K. Singular points array in spatially fluctuating random field. (To be communicated).

CONFERENCE PAPERS

1 **Vinu, R.V**. Sharma, M. K. Singh, R.K. and Senthilkumaran, P. (2013). Evaluation of Dammann grating using polarization interferometer. Conference proceedings (IEEE Xplore).

2 **Vinu, R.V**. Sharma, M. K. Singh, R.K. and Senthilkumaran, P. (2014).Synthesis of 2-D spatial coherence array. Conference proceedings (OSA).

3 **Vinu, R.V**. Sharma, M. K. Singh, R.K. and Senthilkumaran, P. (2014). Generation of off-axis intensity maximum in transverse spatial correlation. International Conference on Optics and Optoelectronics (ICOL) – Dehradun, India.

4 **Vinu, R.V**. and Singh, R.K. (2014). Experimental detection of coherence-polarization matrix. Conference on Recent trends in Information Optics & Quantum Optics (IOQO) - IIT Patna, India.

5 **Vinu, R.V**. and Singh, R.K. (2015). A new method to measure coherence-polarization of light using fourth order correlation. International Conference on Optics and Photonics (ICOP) - Kolkata University, India.

6 **Vinu, R.V**. and Singh, R.K. (2015). Correlation holography for imaging through random media. World Congress on Microscopy: Instrumentation, Techniques and Applications in Life Sciences and Materials Sciences. (WCM 2015) - Mahatma Gandhi University, Kerala, India (Invited Talk).

7 **Vinu, R.V**. and Singh, R.K. (2016). Object recovery from diffused light. Optics & Photonics International Congress (BISC-16). Yokohama, Japan.